Étude de l'accélération des rayons cosmiques par les ondes de choc des restes de supernovae dans les superbulles galactiques

Gilles Ferrand

THÈSE

présentée par

Gilles Ferrand

en vue de l'obtention du

doctorat de l'Université de Toulouse

délivré par

Université Toulouse III - Paul Sabatier

UFR : Physique Chimie Automatique
discipline : astrophysique des hautes énergies

Étude de l'accélération des rayons cosmiques par les ondes de choc des restes de supernovae dans les superbulles galactiques

---

soutenue le 18 décembre 2007

devant le jury composé de :

Jean-François Olive,	professeur, CESR, Univ. Toulouse III,	**président**
Etienne Parizot,	professeur, APC, Univ. Paris VII,	**rapporteur**
Donald Ellison,	professeur, North Carolina State University,	**rapporteur**
Andrei Bykov,	professeur, Ioffe Institute,	**examinateur**
Fabien Casse,	maître de conférences, APC, Univ. Paris VII,	**examinateur**
Alexandre Marcowith,	chargé de recherche, LPTA, Univ. Montpellier II,	**directeur**

THESIS

submitted by

Gilles Ferrand

in fulfillment of the requirements for the degree of

Doctor of the University of Toulouse

delivered by

University Toulouse III - Paul Sabatier

school: UFR Physique Chimie Automatique
speciality: high-energy astrophysics

Study of the Acceleration of Cosmic-Rays by Supernova Remnant Shock Waves in Galactic superbubbles

---

defended on the 18th of December 2007
before a jury composed of:

Jean-François Olive,	Professor, CESR, Univ. Toulouse III,	**President**
Etienne Parizot,	Professor, APC, Univ. Paris VII,	**Reviewer**
Donald Ellison,	Professor, North Carolina State University,	**Reviewer**
Andrei Bykov,	Professor, Ioffe Institute,	**Examinator**
Fabien Casse,	Associate Professor, APC, Univ. Paris VII,	**Examinator**
Alexandre Marcowith,	Associate Scientist, LPTA, Univ. Montpellier II,	**Advisor**

Contents

List of Figures

Merci

à tous les enseignants qui m'ont permis d'être maître de mes choix à Nantes et à Paris,

à tous les enseignants, chercheurs et étudiants qui m'ont ouvert la voie vers l'astro à Paris et à Toulouse,

à tous les chercheurs et autres personnels du CESR qui m'ont accueilli dans leur labo, soutenu dans mon travail, et aidé pour la suite,

à tous les irlandais qui m'ont accueilli par deux fois à Dublin,

à celui qui m'a guidé durant ces trois années,

à tous les thésards et assimilés avec qui j'ai vécu ce moment particulier de ma vie et qui sont devenus mes amis,

à mes parents sans qui de telles études n'auraient pas été possibles,

à ma grand-mère Marie et mon grand-père François qui sont partis au début de cette aventure.

Acknowledgments

I wish to thank Alexandre Marcowith for supervising my PhD and Turlough Downes for sharing his knowledge on numerical simulations. I also thank Peter Duffy and Stephen O'Sullivan for helping me with the development of the code presented here.

I thank Thomas Jones for useful comments on my paper. I also thank Don Ellison and Etienne Parizot for their careful review of my manuscript, as well as the other members of my jury Andrei Bykov, Fabien Casse, Jean-François Olive for attending my defence.

This work has been partly funded by the Egide and Enterprise Ireland *Ulysses* programme, and by the *COSMOGRID* project, funded under the Programme for Research in Third Level Institutions (PRTLI) administered by the Irish Higher Education Authority under the National Development Plan and with partial support from the European Regional Development Fund.

The code presented here has been mostly developed on the *soleil* supercomputer of the French *CALMIP* collaboration located in Toulouse and on the *rowan* supercomputer of the Irish *COSMOGRID* collaboration located in Dublin.

Introduction [fr]

Il y a un siècle les scientifiques ont identifié un nouveau type de messagers venant de l'espace : les rayons cosmiques. Ce rayonnement est en fait constitué de particules (essentiellement des protons) de très haute énergie (jusqu'à 10^{20} eV, une énergie macroscopique) qui bombardent la Terre en permanence. Ces particules interagissent parfois avec notre corps, provoquant éventuellement des mutations cellulaires : elles sont l'une des sources de mutations aléatoires dans la théorie de l'évolution de Darwin. C'est en général la seule raison pour laquelle l'homme de la rue en a (parfois) entendu parler. Pour l'astrophysicien professionnel, comprendre ces particules est absolument nécessaire, quand on sait qu'elles remplissent toute la Galaxie avec une densité d'énergie du même ordre de grandeur que la lumière des étoiles ou le champ magnétique. Elles jouent un rôle clé dans de nombreux domaines de l'astrophysique, de la chimie des petites échelles jusqu'à la dynamique des grandes échelles, avec la production d'une grande partie de l'émission haute énergie de l'univers.

Dans cette thèse nous nous intéressons à la *production* des rayons cosmiques : quels sont les mécanismes d'accélération, où sont les sources ? Nous nous restreignons ici aux rayons cosmiques dits *galactiques*, ceux qui sont bien confinés par le champ magnétique de la Galaxie et qui y sont probablement produits. On pense que leurs sources principales sont les restes de supernovae (RSNs). Les supernovae libèrent de grandes quantités d'énergie, notamment d'énergie cinétique sous la forme d'un choc qui balaye le milieu interstellaire ; et on a identifié un mécanisme, appelé *accélération diffusive par onde de choc* (ADOC), qui permet à un tel choc d'accélérer efficacement des particules ambiantes jusqu'à de très hautes énergies – grâce à la présence d'un champ magnétique turbulent qui fait diffuser les particules. Ce modèle standard a permis de comprendre les grandes lignes de la production des rayons cosmiques, mais il rencontre toujours d'importantes difficultés lorsqu'on s'intéresse aux détails. L'une des raisons pour lesquelles l'ADOC a été rapidement populaire est qu'elle explique naturellement la formation de spectres en loi de puissance (comme observé) ; toutefois ce résultat n'est valide qu'en régime linéaire, alors qu'il est bien connu maintenant que la rétroaction des rayons cosmiques produit des chocs modifiés (avec un précurseur) et des spectres modifiés (concaves). L'ADOC est un mécanisme très efficace et en fait inévitable, cependant il n'est toujours pas du tout certain que les RSNs (isolés) peuvent réellement accélérer les rayons cosmiques galactiques jusqu'aux cassures observées dans leur

spectre (le *genou* vers 10^{15} eV et la *cheville* vers 10^{17} eV). La composition observée des rayons cosmiques est en accord avec celle du milieu interstellaire moyen, néanmoins elle comporte un certain nombre d"'anomalies". Enfin il y a des preuves observationnelles de l'accélération d'électrons dans les RSNs, mais toujours pas de détection directe de protons de haute énergie dans ces objets.

Nous restons convaincus que les rayons cosmiques (au moins galactiques) sont intimement liés aux *étoiles massives*. Mais nous remarquons que l'ADOC a été principalement développée dans le cadre des supernovae isolées – les plus faciles à observer et à modéliser – alors qu'en général les étoiles massives naissent, vivent et meurent en groupes (les *associations OB*), de sorte que les supernovae explosent en fait avec une forte corrélation spatiale et temporelle. Les explosions et les vents des étoiles massives creusent de vastes bulles chaudes et peu denses autour des associations OB, appelées *superbulles*. C'est donc dans ces environnements particuliers que la plupart des supernovae explose. On sait déjà que cela a des conséquences importantes sur la composition des rayons cosmiques. Dans cette thèse nous poursuivons l'exploration de la production des rayons cosmiques dans les superbulles, en étudiant l'idée que les explosions *collectives* de supernovae induisent probablement des effets spécifiques.

Pour mener cette étude nous réalisons des simulations numériques, car la rétroaction des rayons cosmiques sur le choc rend le problème *non-linéaire* et quasiment inabordable analytiquement. En nous appuyant sur des méthodes connues, nous avons développé un nouveau code (nommé Marcos pour *Machine à accélérer les rayons cosmiques*). Ce code fonctionne en 1D et est restreint aux chocs parallèles du fait que nous ne gérons pas explicitement le champ magnétique. Notre approche consiste à coupler les lois de l'hydrodynamique décrivant le choc avec le transport cinétique des rayons cosmiques. La difficulté numérique majeure est la vaste gamme d'échelles spatiales et temporelles à résoudre, ce qui nous a conduits à implémenter une technique de grille adaptative. Le coût des problèmes réalistes étant toujours très élevé, nous avons également parallélisé notre code (dans la dimension "énergie").

Cette thèse est structurée en trois parties. Dans la première partie nous décrivons la physique de l'accélération des rayons cosmiques : nous rappelons la phénoménologie générale des rayons cosmiques, nous présentons l'ADOC en détails, et nous nous concentrons sur l'accélération par chocs multiples. Dans la seconde partie nous décrivons comment nous étudions ce problème à l'aide de simulations numériques : nous présentons le couplage des rayons cosmiques avec le choc, nous discutons la nécessité de bien résoudre toutes leurs échelles, et nous présentons nos premiers résultats sur l'accélération non-linéaire par chocs successifs (voir aussi un début d'extension en géométrie sphérique en annexe). Dans la troisième partie nous décrivons comment tout cela s'applique dans les superbulles : nous rappelons leurs propriétés essentielles, nous discutons la production des rayons cosmiques en leur sein (présentant nos premiers résultats sur le rôle d'une population pré-existante de rayons cosmiques en amont du choc), et nous passons en revue l'émission haute énergie associée.

Introduction [en]

One century ago scientists identified a new kind of messenger coming from space: *cosmic-rays*. This radiation actually consists of particles (mostly protons) of very high energy (up to 10^{20} eV, a macroscopic energy) which constantly bombard the Earth. These particles sometimes interact with our bodies, eventually leading to cell mutations: they are one source of the random mutations involved in Darwin's theory of evolution. That's usually the only reason why the layman has (sometimes) heard about them. For the professional astrophysicist, the understanding of these particles is mandatory, as they fill the whole Galaxy with an energy density of the same order as the star light or the magnetic field. Cosmic-rays play a key role in many fields of astrophysics, from small-scale chemistry to large-scale dynamics, including the production of a large part of the high-energy radiation of the Universe.

In this thesis we are mostly interested in the *production* of cosmic-rays: what are the acceleration mechanisms, where are the sources? We will restrict ourselves here to so-called *Galactic cosmic-rays*, the ones which can be confined by the Galactic magnetic field and are probably produced in the Galaxy. Their main sources are commonly believed to be supernova remnants (SNRs). Supernovae release large amounts of energy, in particular in the form of kinetic energy as a strong shock propagating in the interstellar medium; and scientists have identified an efficient mechanism, known as *diffusive shock acceleration* (DSA), by which shocks can accelerate ambient particles up to very high energies – thanks to the presence of magnetic turbulence off which particles diffuse. This standard model manages to give us the global picture of cosmic-ray production, however it still faces some important difficulties when attention is paid to the details. The main reason why DSA has evoked great enthusiasm is that it naturally explains the formation of power-law spectra (in agreement with the observations), however this result holds in the test-particle regime only, and it is well known now that cosmic-ray back-reaction leads to modified shocks (with a precursor) and modified spectra (concave ones). DSA is a very efficient and actually unavoidable acceleration process, however it is still very uncertain whether (isolated) SNRs can really accelerate Galactic cosmic-rays up to the observed breaks in their spectrum (the *knee* around 10^{15} eV and the *ankle* around 10^{17} eV). The composition of cosmic-rays broadly agrees with the standard interstellar medium composition, however there are a few composition "anomalies". And there is now strong observational support for the

acceleration of electrons in SNRs, however there is still no direct unambiguous detection of highly energetic protons in these objects.

We still believe that cosmic-rays (at least Galactic ones) are closely linked to *massive stars*. However we note that DSA has been mostly studied in the context of single (that is isolated) supernovae – the easiest to observe and to model – whereas most massive stars are born, live and die in groups (called *OB associations*), so that supernovae actually explode with high spatial and temporal correlations. The explosions and the winds of massive stars blow big hot tenuous bubbles around OB associations, known as *superbubbles*. It is in this very particular environment that most supernovae actually explode. It is already known that this has important effects on the composition of cosmic-rays. In this thesis we further investigate cosmic-ray production inside superbubbles, addressing the idea that *collective* explosions of supernovae probably lead to specific acceleration effects.

To carry out this study we resort to numerical simulations, as the cosmic-ray back-reaction on the shock makes the problem *non-linear*, and almost intractable analytically. Relying on known techniques, we have developed a new code, named Marcos for *Machine à Accélérer les Rayons COSmiques* (the French for "cosmic-ray accelerating machine"). The code works in one space dimension and is restricted to parallel shocks as we don't explicitly deal with the magnetic field. Our approach consists of coupling the laws of hydrodynamics describing the shock and the kinetic transport of cosmic-rays. We note that the major numerical difficulty is the very extended range of space- and time-scales to resolve properly, which led us to implement an Adaptive Mesh Refinement technique (AMR). Realistic problems are still computationally expensive, so that we have also parallelized the code (in the energy dimension).

This thesis is composed of three parts. In the first part we describe the physics of cosmic-ray acceleration: we recall the general cosmic-ray phenomenology, present the diffusive shock acceleration mechanism in some detail, and focus on acceleration by multiple shocks. In the second part we describe how we address this problem by the means of numerical simulations: we present the coupling of cosmic-rays with the shock, discuss the need to resolve all their scales well, and present our first results of non-linear acceleration by repeated shocks (see also a first step towards the extension to spherical geometry in the appendix). In the third part we describe how all this applies to the context of superbubbles: we recall the basics of these objects, discuss cosmic-rays production in these environments (showing our first results on the role of pre-existent upstream cosmic-rays on the acceleration mechanism), and finally review their associated high-energy emission.

Part I

Cosmic-Ray Acceleration

Particles coming from space, much more energetic than the ones created in our best accelerators, are routinely detected on Earth. Called cosmic-rays, they still evoke many questions a century after their discovery (chapter 1). Scientists have unveiled an efficient acceleration mechanism, called diffusive shock acceleration (DSA), which is thought to be at work in supernova remnant blast waves (chapter 2). Although a wealth of evidence has been accumulated in favor of this scenario, the direct connection between Galactic cosmic-rays and supernova remnants has not yet been firmly proved. A number of questions are still open, and the more we detail the physics of the DSA model the more complex the situation becomes. An important aspect is the non-linearity of the interplay between the accelerated cosmic-rays and the underlying interstellar medium – so that numerical simulations are a tool of choice (part II). In this work we are also particularly interested in the effect of acceleration by multiple shocks (chapter 3), a mechanism relevant in various environments, most notably into superbubbles (part III).

Chapter 1

Cosmic-Rays

Cosmic-rays are highly energetic particles pervading the Universe. In this chapter we briefly review the history of their discovery, the main results of their observation, and the basics of their production theory.

1.1 History

Cosmic-rays have been discovered one century ago, which is both a quite late discovery given their central role in astrophysics and a quite old discovery given all the problems their understanding still raises. Their story has been told in many places, the introductions of Paul (2004) and Degrange (2004) make a short review and the reference book of Longair (1991) goes in much more details.

1.1.1 Discovery

The study of cosmic-rays started in the early twentieth century[1]. At that time ionizing radiations were studied with electroscopes. A few people realized that their electroscopes were always spontaneously discharging even if they were protected from any visible radiation. They concluded that some kind of unknown ionizing radiation was present at the Earth surface, and supposed that it was coming from the Earth interior[2]. But when Wulf made precise measurements on top of the Eiffel Tower, he observed that the discharging rate was decreasing more slowly with altitude than expected. To get a definitive answer, Hess made several balloon experiments from 1911 to 1913. He measured that above 1.5 km and up to 5 km the ionization rate steadily rises, proving that the ionization source is not *into* but *above* the Earth - most probably in space.

[1] Although they have been indirectly observed for ages by humans, as they contribute to aurora when interacting with the Earth magnetic field at the poles.

[2] Which was a sound hypothesis, as radioactivity had just been discovered, and as today we know that the activity of the planet core indeed produces a gamma radiation.

Before trying to identify the actual sources (see section 1.3.1.1), the big issue was to figure out what this radiation actually was. This was the subject of vigorous discussions in the 1920s, opposing most notably Millikan, convinced that cosmic-rays were photons (it is him who coined the term "cosmic-rays"), and Compton, convinced that they were charged particles. The discovery of the influence of the Earth magnetic field on cosmic-rays between 1927 and 1933 proved that most of them are indeed charged – and thus are not photons, but matter. In 1938 Auger discovered "air showers" of particles, interpreted as the result of the impact of a very energetic particle (a cosmic-ray) on the Earth atmosphere. But not until the 1960s (see section 1.1.3) were scientists able to measure precisely the composition and energy of cosmic-rays (see section 1.2).

1.1.2 Particle Physics

Not only cosmic-rays proved to be particles, but they teached us what particles are really made of: the science of *particle physics* greatly developed in the 1930s and 1940s through the study of the cosmic radiation. In cosmic-rays were found the positron (Anderson, 1932), the charged muons (Anderson & Neddermeyer, 1937), the charged pions (Powell, 1947), etc.

In the 1930s the first human-made accelerators of particles were hardly reaching a few MeV[3]. Today they reach the TeV[4]. Although (impressively) 6 orders of magnitudes better, this is still at least 8 orders of magnitudes too short to compete with astrophysical sources... It is then no surprise that cosmic-rays are the center of a new and vibrant interdisciplinary field, known as "astroparticle" physics.

1.1.3 Observations

We give here a short review – which doesn't try to be exhaustive – of the way cosmic-rays have been observed in the last 50 years, from space and from the ground, with direct and indirect method.

1.1.3.1 Detection of Highly-Energetic Particles

The conquest of space after World War II made it possible to detect directly cosmic-rays in space. In 1965 and 1966 the Russian satellites Proton I and II measured their energy spectrum up to 10^{14} eV. From 1979 to 1981 the American satellite HEAO-3 measured their composition, followed since 1991 by the ACE mission. Experiments in balloon (as first did Hess) are also still in use,

[3]The electron-volt is defined as the energy gained by an electron accelerated by an electric potential of 1V, that is $1\,\mathrm{eV} = 1.6 \times 10^{-19}\,\mathrm{J}$. Common multiples are $1\,\mathrm{MeV} = 10^6\,\mathrm{eV}$ (mega), $1\,\mathrm{GeV} = 10^9$ eV (giga), $1\,\mathrm{TeV} = 10^{12}$ eV (tera), $1\,\mathrm{PeV} = 10^{15}$ eV (peta), $1\,\mathrm{EeV} = 10^{18}$ eV (exa), $1\,\mathrm{ZeV} = 10^{21}$ eV (zetta).

[4]The LHC (Large Hadron Collisioner) being built by the CERN in Geneva will allow face-on collisions of protons of 7 TeV.

such as the BESS mission. All this experiments rely on various techniques of particle and nuclear physics to collect particles and measure their energy, charge, mass, composition... The detectors are either gas-filled devices (proportional counters, Geiger counters, spark chambers) either solid state devices (semiconductors, scintillation detectors, crystals). They can be used up to energies of roughly 10^{15} eV.

Above this limit cosmic-rays are detected through the secondary particle showers they generate in the atmosphere (following Auger's work). This approach, developed since the 1950s, actually consists in using the Earth atmosphere itself as a detector. In that case one can either detect the secondary particles on the ground, as done by AGASA in Japan since 1990 and by Kascade in Europe since 1996, either detect the Cherenkov light induced by those supraluminous particles, as done by HiRes in the USA since 1994. The Auger observatory being currently built by an international collaboration in the Argentina pampa combines the two techniques on a giant surface of 3000 km^2.

1.1.3.2 Detection of Highly-Energetic Photons

The progresses made in the observation of cosmic-rays are closely connected to the development of high-energy astrophysics, as high energy radiation is often the signature of high energy particles (and is sometimes observed thanks to the same kind of techniques). Accelerated protons produce γ-ray lines through various nuclear interactions (excitation, spallation, radioactive decay) and a γ continuum through collision on interstellar protons (pionisation). Accelerated electrons produce a γ-ray line through annihilation with positrons and a X to γ continuum through "collisions" with interstellar nuclei (Bremsstrahlung) and with ambient photons (inverse Compton).

X-astronomy started in the 1960s and rose in the 1970s (with the Uhuru and Einstein satellites). γ-astronomy started in the 1970s (with the SAS II and COS-B satellites) and rose in the 1990s (with the CGRO satellite). Today the sky is extensively observed from space in X-rays by XMM-Newton, Chandra and Suzaku and in γ-rays by INTEGRAL, Swift, Agile (and soon GLAST).

More recently (since the end of the 1980s) γ-astronomy has developed on the ground, relying on the same technique used for very high energy cosmic-rays, that is detecting the air shower induced by very energetic photons. After the first attempts of the Whipple Observatory, HEGRA, CAT, CANGAROO, a new generation of observatories has risen: MAGIC, VERITAS, HESS (since 2002).

To end this section we would like to note, first that high-energy radiation of course can't be totally reduced to cosmic-ray physics, and second that cosmic-rays produce important radiation at the other end of the spectrum too: the synchrotron emission from accelerated electrons in magnetized environments has been observed since the contruction of the first big radiotelescopes in the early 1950s (see section 2.5.1.1).

1.2 Phenomenology

We describe here the main results of the observation of cosmic-rays over the last 40 years (more details can be found in Parizot (2005) and references therein). Cosmic-rays are a new kind of messengers for astrophysics[5]. As photons they can be distinguished by their energy (1.2.1), but contrary to photons they can't[6] be associated with their sources because of their diffusion on the Galactic magnetic field (1.2.3). However, cosmic-rays carry a specific information: their composition (1.2.2).

1.2.1 Spectrum

The best known characteristic of the cosmic radiation is certainly its energy spectrum, shown in figure 1.1. It's an almost perfect power-law $dN/dE \propto E^{-s}$ over at least 12 orders of magnitudes in energy and 32 orders of magnitude in flux, which we regard as one of the most striking discoveries in astrophysics. It is worth to note that this power-law spectrum is the signature of a *non-thermal* phenomenon: which physical process can maintain this out of equilibrium radiation in all the Universe over such ranges of energies? Looking more precisely we see a few features which of course are of great importance in such a regular spectrum.

At low energies the spectrum is deformed because of the Sun's influence: charged particles up to a few GeV are repelled by the magnetized solar wind. This phenomenon called solar modulation prevents us to measure the Galactic cosmic-rays flux and composition at low energies.

From 10 GeV to a few PeV the spectrum is a power-law of logarithmic slope $s = 2.7$. Around 100 GeV the flux is of roughly 1 particle per m^2 per month. This is historically the part of the cosmic-radiation which has been studied in more details.

Around 3-5 PeV occurs a famous break in the spectrum, called the "knee". The spectrum softens to $s = 3.0$. This is more clearly seen when multiplying the cosmic-rays flux by E^3 as done in figure 1.2. The flux is now roughly 1 particle per m^2 per year. The exact reason of this quite sudden break is still unknown. One might suggest that it connects two different populations, but such a scenario seems unlikely as the spectrum is steepening. A hardening of the spectum can be naturally explained by the existence of a second population which is dominated by the first component at low energies because of its lower normalization but eventually dominates above some energy because of its steeper slope. But a steepening of the spectrum requires a precise double fine-tuning: the second component has to start exactly at the energy at which the first component stops (otherwise, being steeper, it should dominate below too), and exactly at the same normalization in flux (otherwise one would see

[5]Together with neutrinos and gravitational waves.

[6]But maybe at very high energies.

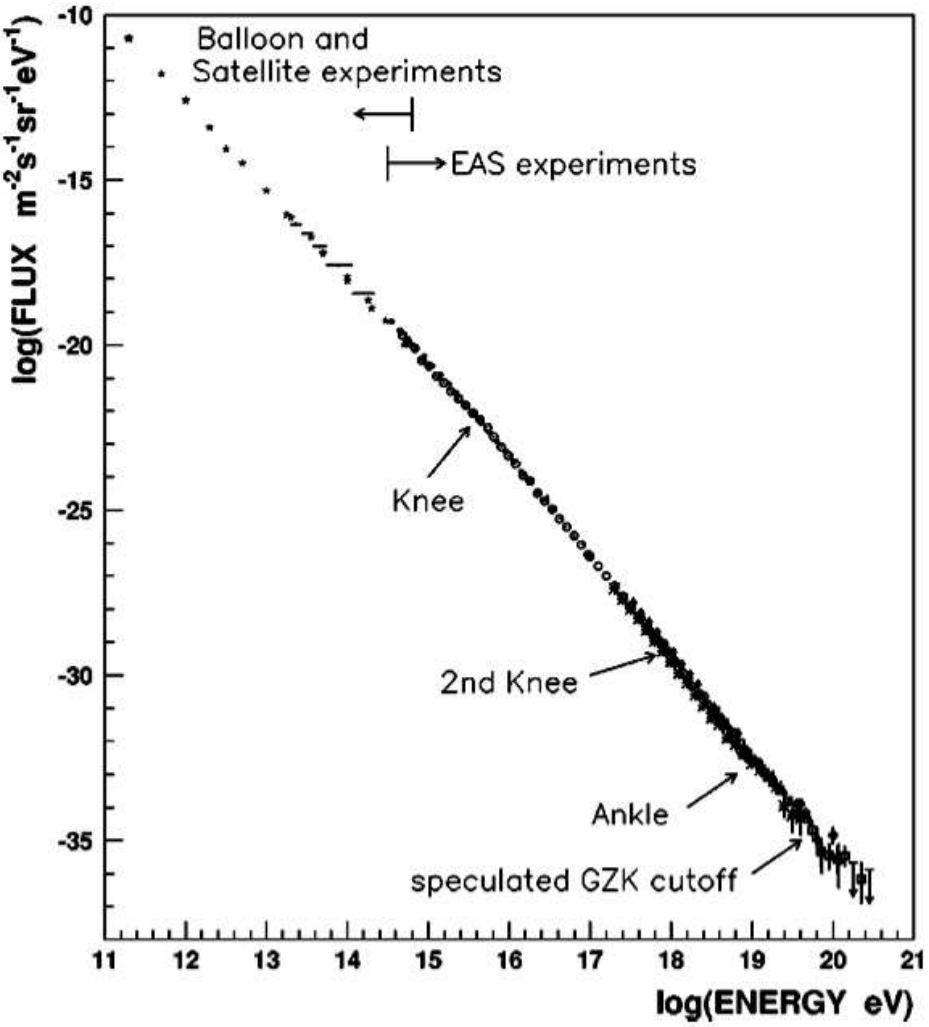

Figure 1.1: Observed differential energy spectrum of primary cosmic-rays. (figure from Nagano and Watson (2000), data compiled by Simon Swordy)

some kind of step in the spectrum, not just a slope change). It seems thus more natural to consider that the knee corresponds to a change in a single population – but is it a change in the acceleration mechanism (at the source) or in the propagation (from the source to us)? Or does it point to a change in physics at high energies, which would distort our interpretation of the spectrum? A few people have also proposed that such a feature in the spectrum is simply the mark of an individual local source – masking the actual Galactic spectrum. To end this short discussion on this open topic, we note that the precise position of the knee is expected to be at different energies for different kind of particles, and that an important point yet uncertain is whether this depends on the charge Z or on the mass A of the nucleons.

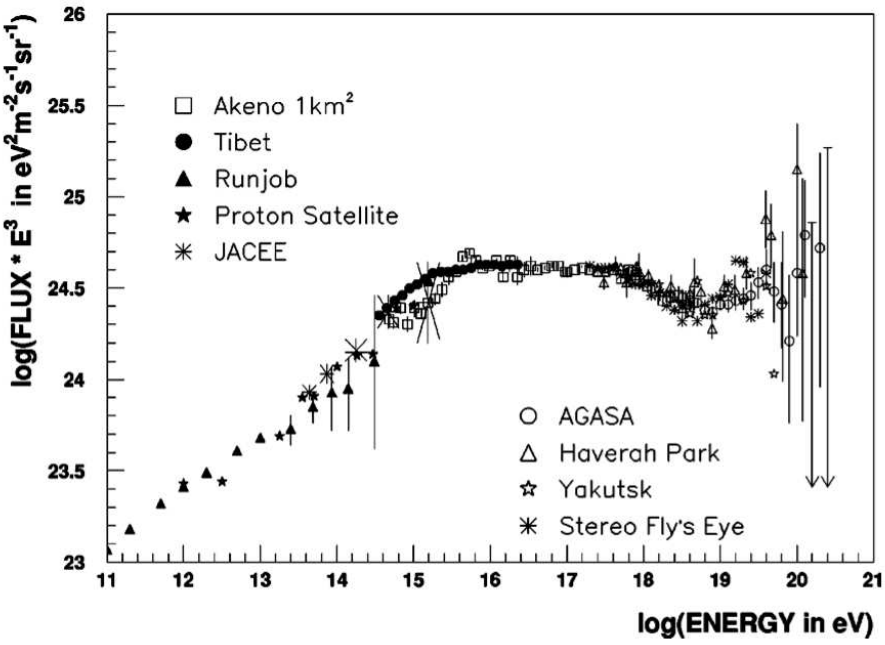

Figure 1.2: Observed differential energy spectrum of primary cosmic-rays (the flux has been multiplied by E^3 to highlight the spectrum features).
(figure from Nagano and Watson (2000))

The $s = 3.0$ power-law extends to about 0.5 EeV, where the spectrum softens again to $s = 3.3$. This feature called the "second knee" has been identified more recently. Around 3 EeV the spectrum hardens back to $s = 2.7$. This is called the "ankle". The flux is now only 1 particle per km^2 per year. Protons of 10^{19} eV have a Larmor radius in the typical mean Galactic magnetic field of 3 μG of 3 kpc, which is higher than the width of the Galactic disk. Thus cosmic-rays of energies above the ankle can't be confined within the Galaxy. This basic observation is the reason why this region of the spectrum is believed to mark the transition between a Galactic population and an extra-galactic population of cosmic-rays[7][8].

Cosmic-rays have been detected up to 300 EeV, that is roughly 50 J, that is a macroscopic energy – in a microscopic particle. But such very high energy

[7] As previously explained there is then no problem to interpret the hardening of spectrum, however note that the connection of the fluxes is not that obvious: there is *a priori* no reason why the extra-galactic component flux should be at the same level as the Galactic one precisely at the energy at which the Galactic component stops.

[8] It has been shown recently that the actual shape of the ankle as seen on figure 1.2 can be explained as a propagation effect for extra-galactic cosmic-rays, the "pair production dip". In that case the transition to Galactic cosmic-rays would actually occur at the second knee. A magnetic horizon effect could provide the required low-energy cut-off of extra-galactic cosmic-rays and allow a transition at this energy (see eg the lecture of Lemoine (2006)).

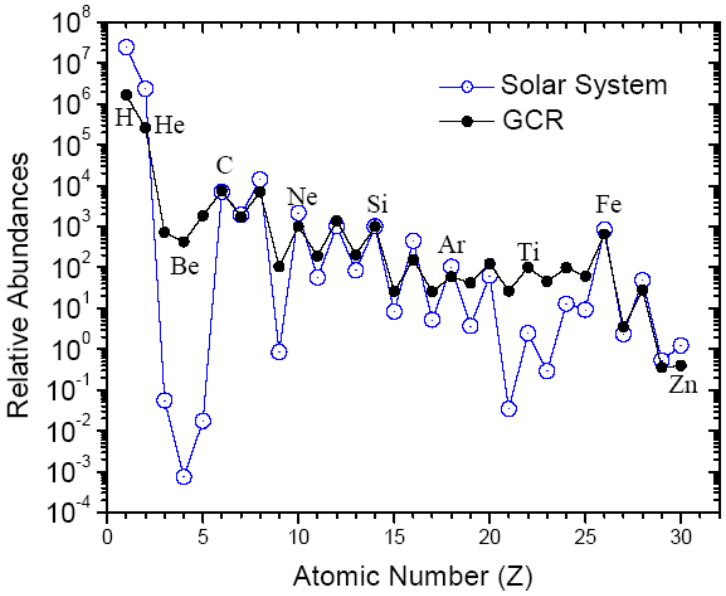

Figure 1.3: Relative abundances of the different chemical elements in the Galactic cosmic radiation and in the solar system.
(figure from Israel (2004))

events are very rare: the flux is now roughly 1 particle per km^2 per century... Thus as seen on figure 1.2 errors bars explode and one can't make firm conclusions. One important question that has lead to a tremendous amount of work is the question of how the spectrum ends. Since 1966 Greisen and independently Zatsepin and Kuzmin have realized that cosmic-rays of energies above roughly 10^{20} eV will be quickly destroyed by their interaction with the photons of the (ubiquitous) cosmic background (for instance cosmic-rays of 2×10^{20} eV can't travel more than 50 Mpc, which drastically limits the number of possible extra-galactic sources). Hence the expectation of a sudden break in the spectrum, called the GZK cut-off. This cut-off has been reported by the HiRes experiment, but not by the AGASA one. Recently the first results of the Auger observatory have given strong support in favour of the GZK cut-off (eg Yamamoto 2007).

1.2.2 Composition

The composition of cosmic-rays up to roughly 1 GeV has been extensively studied. They are made of 1% of electrons and 99% of nucleons. Nucleons are made of roughly 89% of protons, 10% of Helium nuclei, and 1% of heavier elements. The relative abundances of these elements are shown on figure 1.3. As one can see the cosmic-rays composition is similar to the solar system's one, so that it seems that cosmic-rays are made of quite standard interstellar medium. There are however a few important differences, on which we shall

say more in section 8.1. The most visible ones are (i) the overabundance of heavy elements compared to Hydrogen and Helium and (ii) the overabundance of three light elements: Lithium (Li), Beryllium (Be), Boron (B) – commonly referred to as LiBeB – which are produced in flight by cosmic-rays through *spallation* processes (breaking of heavy nuclei during collisions). To be more precise Meyer et al. (1997) and Ellison et al. (1997) have shown that volatility and mass-to-charge ratio are the two key parameters to discuss the composition of cosmic-rays. Among the volatile elements, the abundance enhancements relative to solar increase with mass, which most likely reflects a mass-to-charge dependence of the acceleration efficiency. The more refractory elements seem systematically overabundant relative to the more volatile ones, and in a quasi–mass-independent fashion, which suggests that (charged) grains are accelerated before being stripped of their material. These observations are fully consistent with the hypothesis of cosmic-rays originating from a mixture of interstellar gas and dust.

Note that figure 1.3 shows the abundances observed at the Earth. We have to model propagation effects (see section 1.3.2) to infer the source composition. Note also that all these precise data have been obtained for quite low energy cosmic-rays. Important efforts are currently being made do determine the composition around the knee, but the measures are still difficult to interpret. At very high energies (at the ankle and above) the composition is simply unknown (there is a pending controversy between models relying on protons only and models relying on heavier nuclei).

Although cosmic-ray composition is not the aspect we've been directly working on in this thesis, we would like to stress that the proper understanding of cosmic-rays origin requires assembling the information coming from their three spectral dimensions (energy, mass, and direction if avalaible).

1.2.3 Isotropy

We know thanks to propagation studies (see section 1.3.2) that cosmic-rays of low energy collected on the Earth have crossed a *grammage* of 5-10 g/cm^2, which is roughly 3 orders of magnitudes higher than the mean surface density of the Galaxy. Thus cosmic-rays don't follow straight paths in the Galaxy. We have already encountered the reason why when discussing the nature of the ankle: being charged particles cosmic-rays are deflected by magnetic fields. We shall say more on this process in section 2.1.2, for now it's sufficient to say that resonant interactions between cosmic-rays and magnetic fields lead to sizeable and almost random changes in the direction of flight of cosmic-rays, so that cosmic-rays actually perform a random walk in the Galaxy. This seems coherent with the very small observed anisotropy of the cosmic radiation (shown on figure 1.4): no more than a few percents up to the ankle and

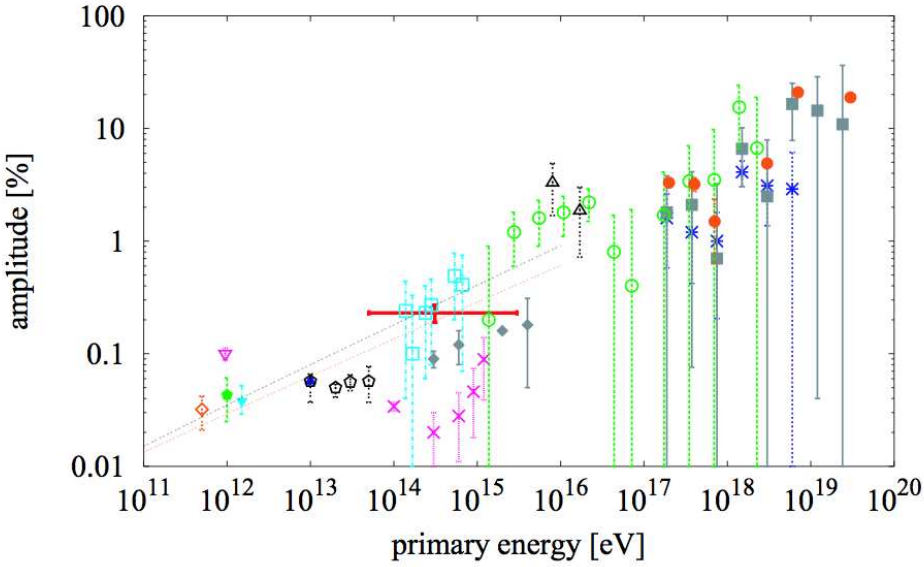

Figure 1.4: Anisotropy of the cosmic radiation.
This figure (from Iyono 2005) shows the amplitude of the first harmonic of the arrival local sidereal time of cosmic-rays (different symbols and colours correspond to different experiments).

well below 1% below the knee [9]. Therefore one cannot associate Galactic cosmic-rays arriving on Earth with their sources: at low energies one can't do "proton astronomy". At very high energies however particles are more rigid (they are less deflected by magnetic fields) so that one may hope detecting individual sources – provided one has sufficient statistics (very recently the Pierre Auger Collaboration (2007) reported a correlation of the highest energy cosmic-rays with extragalactic sources)[10].

1.3 Standard Model of Galactic Cosmic-Rays

From now on we will focus on so-called Galactic cosmic-rays (GCR), that is cosmic-rays of energies up to about the ankle (a few 10^{18} eV)[11]. It is commonly thought, although not firmly established, that GCRs are accelerated by the shocks of supernova remnants (SNR)[12]. This link was made quite early because

[9] Although the distribution of possible sources in the Galaxy such as supernova remnants has a very sharp profile.

[10] The AGASA experiments had already reported a few multiplets of events that seem statistically extremely unlikely to be coincidences

[11] Regarding very high energy cosmic-rays the whole bestiary of high-energy extra-galactic sources is invoked (black holes, neutron stars, gamma ray bursts,...), not to say about the top-down scenarios that propose that cosmic-rays are not actually accelerated but originate from the decay of very energetic (yet undiscovered) particles.

[12] In the Galaxy pulsars and micro-quasars are also possible sites of acceleration.

of the power requirements for the acceleration of cosmic-rays: when Baade and Zwicky introduced the concept of supernova in 1934 they noted that their huge energy release could be the engine of cosmic-ray acceleration. And around 1950 Fermi found the theoretical mechanism that can actually explain how magnetized shocks can efficiently accelerate charged particles, which is the basics of the so-called *diffusive shock acceleration* process (DSA), which we will study in details in chapter 2. As we will see this mechanism produces fairly easily a power-law spectrum in energy $dN/dE \propto E^{-s}$, with a slope s which has the great quality of being universal as it depends only on the shock compression ratio r (according to $s = (r+2)/(r-1)$) which in the limit of strong shocks is always $r = 4$ (see section 2.1.1.2), giving a slope $s = 2$. Corrected from propagation effects which make the spectrum steeper (see section 1.3.2.1), this is encouragingly close to the observed value of $s = 2.7 - 3$ [13]. In the remaining of this introductory chapter we will simply give the global astrophysical picture of the standard model for the acceleration of Galactic cosmic-rays (see also the courses of Marcowith (2007a) and Achterberg (1998)).

1.3.1 Origin

1.3.1.1 Sources: the SNR Hypothesis

The first argument for SNRs as the sources of cosmic-rays has been the energy budget. The measured local energy density of cosmic-rays is about $\epsilon_{\rm cr} = 1\,{\rm eV/cm^3}$ [14]. Maintaining this density uniformly in the Galaxy volume $V_{\rm gal}$ over the cosmic-rays residence time $t_{\rm cr,gal}$ requires a power $P_{\rm cr} = \epsilon_{\rm cr} \times V_{\rm gal}/t_{\rm cr,gal}$. Our Galaxy can be described as a disk of height 500 pc and of radius 15 kpc thus a volume $V_{\rm gal} \simeq 350$ kpc^3. From propagation studies (see section 1.3.2) one can estimate $t_{\rm cr,gal} \simeq 10$ My (at 1 GeV). Therefore the required power is $P_{\rm cr} \simeq 10^{41}$ erg/s. The power delivered by supernovae in the Galaxy is $P_{\rm sn} = E_{\rm sn} \times \nu_{\rm sn}$ where $E_{\rm sn} = 10^{51}$ erg is the typical energy release of a supernova and $\nu_{sn} \simeq 3$ per century is the estimated supernova rate in our Galaxy, so that $P_{sn} \simeq 10^{42}$ erg/s. Thus powering the cosmic-rays in the Galaxy only requires transferring roughly 10% of the supernovae energy, which is not only plausible but expected from DSA studies[15]. Hence the idea that cosmic-rays are actually particles of the interstellar medium swept up by supernova remnants shock waves, which is consistent with their observed standard composition. This scenario is supported by the observation of non-thermal multi-wavelength radiation from SNRs, which is interpreted as the emission of accelerated particles (see section 2.5.1).

[13] But all that stands in the *linear* regime, which as we will see in section 2.3 cannot hold.

[14] This is also roughly the energy density in the magnetic field, as well as in the visible light and in the cosmic microwave background.

[15] However we note that (i) this only means that supernovae *can* power cosmic-rays and (ii) this is just a rough order of magnitude calculation.

1.3.1.2 Acceleration: the Electromagnetic Field at Work

Even if SNR shocks carry the power required to produce cosmic-rays, shocks won't accelerate particles by simply pushing them. Another ingredient is required, namely the magnetic field. The only force that can actually accelerate (charged) particles from the thermal pool to very high energies is the Lorentz force $\mathbf{F} = \mathrm{q}\,(\mathbf{E} + \mathbf{v} \times \mathbf{B})$[16]. We recall that in astrophysical environments $< \mathbf{E} >= \mathbf{0}$ as the ionized gas is almost perfectly conductor[17], so that only the $\mathbf{B}$ field remains, which can't work. However transitory induced $\mathbf{E}$ fields can develop, as the result of variable magnetic fields, for instance in magneto-hydrodynamic waves or in bigger moving magnetized structures.

The maximum energy achievable by a particle in an electromagnetic accelerator depends on the field strength as well as on the accelerator size and age. An upper limit is obtained by requesting the Larmor radius of the particle $r_L = E/qBc$ to be smaller than the accelerator size R, which gives $E_{\max} = q\,Bc\,R = Z\,B_{\mu\mathrm{G}}\,R_{\mathrm{pc}} \times 10^{15}\,\mathrm{eV}$ (Hillas 1984). This is simply the work done by the induced electric field Bc over the distance R. For a SNR extending over a few pc in a typical magnetic field of a few μG this gives a maximum energy above the knee. But Lagage and Cesarsky (1983) have made a more detailled calculation taking into account the evolution of the SNR (see section 2.1.1.3) which gives $E_{\max} = Z\,B_{\mu\mathrm{G}} \times 10^{14}\,\mathrm{eV}$, that is below the knee in a typical magnetic field (but B is probably amplified, see section 2.1.2.3). And anyway Galactic sources such as SNRs should actually reach the ankle, that is around 10^{18} eV. Thus the maximum achievable energy is still a problematic issue of the standard model of acceleration of GCRs by (isolated) SNRs.

1.3.2 Propagation

Although in this thesis we are mostly interested by the acceleration mechanisms at the source, we present briefly the main aspects of the propagation of cosmic-rays in the Galaxy, as the correct description of this process is clearly mandatory to get a complete understanding of the cosmic radiation (see the review of Strong et al. (2007)).

1.3.2.1 The Cosmic-Rays Travel in our Galaxy

After their escape from the accelerator cosmic-rays are still subject to various processes altering their energy. Charged particle lose energy mainly through Coulombian interactions (which can be modelled as continuous losses). Heavy nuclei can also collide with interstellar nuclei of hydrogen or helium (which has to be modelled as "catastrophic" losses), forming secondary nuclei in flight (we have already seen the case of the LiBeB in 1.2.2). The quantitative study

[16] A particle can gain energy by falling in a gravitational potential, but to escape it will lose all the energy stored.

[17] But in very particular electric machines such as neutron stars and accreting black holes.

of the observed secondary over primary ratios (such as [B/C]) gives precious information on the cosmic-rays diffusion in the Galaxy. It allows to derive their grammage that is the mean column density of matter they have crossed during their travel to the Earth: $X_{\rm cr} = 5 - 10\,{\rm g/cm^2}$. Knowing the actual size (height ~ 500 pc, radius ~ 15 kpc) and matter density (of the order of 1 proton per ${\rm cm^3}$) of the Galaxy this allows to derive the time spent by cosmic-rays in the Galaxy $t_{\rm cr} \simeq 10^7$ yr and the distance they have travelled when they escape it $L_{cr} \simeq 1$ Mpc. Such high values are possible, as already explained in 1.2.3, because cosmic-rays perform a random walk on the Galactic magnetic field. Before escaping the Galaxy they do N steps of typical length λ (mean free path), travelling an integrated length $L_{\rm cr} = N \times \lambda$ but a net distance of only $d_{\rm cr} \simeq \sqrt{N} \times \lambda$ (taking for $d_{\rm cr}$ the height of the Galactic disk one gets more than 1 million steps of size of a few tenths of parsec).

Valuable information can also be obtained from radioactive clocks. Some secondaries contain radioactive isotopes, such as the ^{10}Be which has a half-time of 1.6 million years. Cosmic-rays contain about 3% ^{10}Be with respect to its stable isotopes ^{7}Be and ^{9}Be, whereas calculations of spallation reactions predict a ratio of 10%, showing that a significant fraction of the ^{10}Be must have decayed. This yields an estimate of the cosmic-rays lifetime in our Galaxy in agreement with the previous one.

1.3.2.2 Back to the Source Spectrum

To end this section we want to discuss briefly how the power-law spectrum of the cosmic radiation observed on Earth is related to the spectrum at the sources. In the most simplified model of cosmic-rays transport in the Galaxy, called the *leaky box,* one considers that particles are injected by sources at a given differential rate $Q_{\rm inj}(E)$ and escape the Galaxy in a time $\tau_{\rm esc}(E)$ also dependent on their energy. In that case the equilibrium spectrum of cosmic-rays in the Galaxy is simply $N(E) = Q_{\rm inj}(E) \times \tau_{\rm esc}(E)$. As both the injection rate and the escape time are believed to be power-laws (that is $Q_{\rm inj} \propto E^{-\alpha}$ and $\tau_{\rm esc} \propto E^{-\delta}$) the resultant spectrum is naturally a power-law too, of index $s = \alpha + \delta$. The question is now to adjust α and δ to get the observed $s = 2.7$ below the knee. This is possible in at least two ways. Some propagation calculations suggest $\delta = 0.6$, which implies $\alpha = 2.1$, in good agreement with the DSA model (which gives indeed $\alpha \simeq 2.1$ when one takes into account the SNR evolution, see section A.5). However more recent and detailled propagation calculations have obtained $\delta = 0.36$, which is particularly interesting as theoretically such an index naturally derives from magnetic field turbulence of Kolmogorov type. But in that case one needs $\alpha = 2.35$, which doesn't fit any more in the standard DSA process. More observations at high energies and more work on MHD turbulence are required to get a definitive answer.

References

Achterberg, A. (1998). Cosmic Ray Physics - Sources of energetic particles in the universe. Nova Autumn School.

Degrange, B. (2004). Particules de haute énergie dans l'univers. Ecole de Dolomieu.

Ellison, D. C., Drury, L. O., and Meyer, J.-P. (1997). Galactic Cosmic Rays from Supernova Remnants. II. Shock Acceleration of Gas and Dust. ApJ, 487:197–217.

Hillas, A. M. (1984). The Origin of Ultra-High-Energy Cosmic Rays. ARA&A, 22:425–444.

Israel, M. (2004). An Overview of Cosmic-Ray Elemental Composition. ACE news 83.

Iyono, A. e. a. (2005). The Cosmic Ray Anisotropy Observed by the Large Area Air Shower Experiments. In *International Cosmic Ray Conference*, volume 6 of *International Cosmic Ray Conference*, pages 101–104.

Lagage, P. O. and Cesarsky, C. J. (1983). The maximum energy of cosmic rays accelerated by supernova shocks. A&A, 125:249–257.

Lemoine, M. (2006). Propagation of ultra-high energy cosmic rays in the Universe. Ecole de Gif sur les rayons cosmiques de haute énergie.

Longair, M. (1991). *High Energy Astrophysics*, volume 1: Particles, Photons and their Detection. Cambridge University Press.

Marcowith, A. (2007a). Les supernovae comme sources des rayons cosmiques I. Les supernovae isolées [brouillon]. Ecole de Gif sur les rayons cosmiques de haute énergie.

Meyer, J.-P., Drury, L. O., and Ellison, D. C. (1997). Galactic Cosmic Rays from Supernova Remnants. I. A Cosmic-Ray Composition Controlled by Volatility and Mass-to-Charge Ratio. ApJ, 487:182–196.

Nagano, M. and Watson, A. A. (2000). Observations and implications of the ultrahigh-energy cosmic rays. *Reviews of Modern Physics*, 72:689–732.

Parizot, E. (2005). Rayons cosmiques et rayonnement du cosmos. HDR.

Paul, J. (2004). Une brêve histoire des rayons cosmiques. In Parizot, E., Marcowith, A., Tatischeff, V., Pelletier, G., and Salati, P., editors, *Physique et astrophysique du rayonnement cosmique (Ecole CNRS de Goutelas XXVI)*, pages 1–6.

Pierre Auger Collaboration, T. (2007). Correlation of the Highest-Energy Cosmic Rays with Nearby Extragalactic Objects. *Science*, 318:938–943.

Strong, A. W., Moskalenko, I. V., and Ptuskin, V. S. (2007). Cosmic-Ray Propagation and Interactions in the Galaxy. *Annual Review of Nuclear and Particle Science*, 57:285–327.

Yamamoto, Y. (2007). The UHECR spectrum measured at the Pierre Auger Observatory and its astrophysical implications. In *ICRC'07 proceedings (pre-conference edition)*.

Chapter 2

Diffusive Shock Acceleration

Diffusive shock acceleration (DSA) at supernova remnant (SNR) blast waves is the favoured production mechanism for the production of Galactic cosmic-rays (GCR). The theoretical grounds of the model lie in the early ideas of Fermi (1949, 1954). The DSA model in SNRs itself has been developed independently in the late 1970s by Krymskii (1977), Axford et al. (1978), Bell (1978a, 1978b), Blandford and Ostriker (1978) (see Drury 1983 for a comprehensive review). It can naturally explain the formation of a power-law spectrum by a shock wave (and with a remarkable universal slope). However, it has been soon realised that the acceleration process can actually be so efficient that the cosmic-rays back-react on the shock dynamics, requiring a more involved *non-linear* analysis (see the reviews of Jones and Ellison (1991) and Malkov and Drury (2001)).

In this chapter we will first review the physical ingredients of the DSA mechanism (namely shock waves and magnetic waves), before deriving the well-known linear results of the theory. We will then show how the particles back-reaction modify this simple picture. We will also discuss the delicate problem of *injection* of particles in the accelerator (that is, how does the DSA mechanism get initialized?). Finally we will present the various observations supporting the DSA theory at SNR shocks (looking for both linear and non-linear acceleration evidence).

2.1 Ingredients

As can be seen from its name, diffusive shock acceleration requires two ingredients: a shock, that is a velocity jump, and diffusion centers, which are actually magnetic field waves. In this section we recall the physics of these objects and the way they manifest in astrophysics, particularly in SNRs.

2.1.1 Shock Waves

Shocks are ubiquitous in the universe: they are observed in all environments and at all scales. The closest one is the Earth's bow shock which is our best laboratory (thanks to *in situ* spacecraft observations) for studying astrophysical shocks. Energetic particles have been detected and successfully modeled using the DSA process (see Ellison et al. (1990) and references therein). The solar system hosts other kind of shocks where particle acceleration is observed or inferred: solar flares, interplanetary travelling shocks (resulting from this flares), cometary shocks, and the solar wind termination shock[1]. Shocks are common companions of stars in their late phases: accreting shocks in compact objects, pulsar wind termination shocks, and of course supernova remnant shocks. Shocks are also present at galactic scales, such as the Galactic wind termination shock, shocks associated with active galactic nuclei (AGN), and shocks in extra-galactic jets. At cosmological scales shocks are present in the early cosmological flows and in today's clusters of galaxies.

2.1.1.1 Definition

A shock forms when something material propates in a medium at a speed higher than the reaction speed of this medium. The natural travelling speed of a perturbation in a medium of density ρ and pressure P is the sound speed

$$c_s = \sqrt{\frac{\partial P}{\partial \rho}}. \tag{2.1}$$

With the usual polytropic equation of state

$$P \propto \rho^\gamma \tag{2.2}$$

this simply reads

$$c_s = \sqrt{\frac{\gamma P}{\rho}} = \sqrt{\gamma \bar{m} k_B T} \tag{2.3}$$

where T is the medium temperature, $\bar{m}$ is its mean atomic mass, and k_B the Boltzmann constant. If something travels at a higher speed, sound waves steepen to form a shock wave, that is a sharp discontinuity in the hydrodynamical profiles. The shock compresses and heats the medium, therefore raising the sound speed, so that the medium can actually respond to the perturbation. Thus a shock transfers macroscopic ordered velocity (kinetic energy) into microscopic unordered velocity (heat). The strength of the shock is measured by the ratio of its proper speed over the local sound speed

$$M_s = \frac{v_s}{c_s} \tag{2.4}$$

called the Mach number (shocks form for $M_s > 1$, that is supersonic flows).

[1] Which has probably been crossed by the two Voyager spacecrafts in 2004 and 2006.

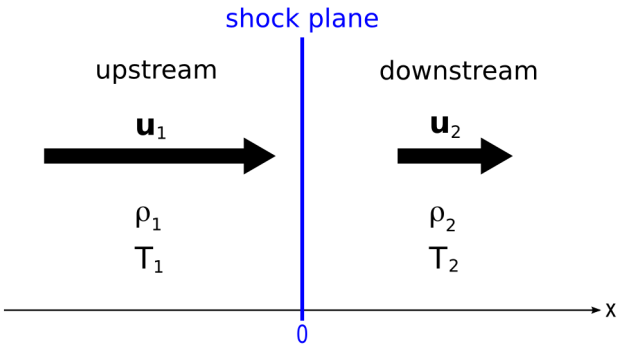

Figure 2.1: Simple picture of a shock front (in the shock front).

A very simple sketch of a planar shock is given in figure 2.1. The shock is represented as a discontinuity at $x = 0$, separating upstream ($x < 0$, noted 1) and downstream ($x > 0$, noted 2) states. The velocities are measured here in the shock rest frame, so that the flow falls on the shock and continues downstream at lower speed. In the presence of an electromagnetic field this simple picture is a bit more complicated. Lets consider the point of intersection of a magnetic field line and the shock front. If this point moves at subluminal speed it is possible to do a change of frame to make the shock stationary, and it turns out that in this special frame (called the de Hoffman and Teller frame) the electric field vanishes and the plasma flows along the magnetic field lines (both upstream and downstream). The shock configuration is then given by the upstream orientation of **B** with respect to the shock normal: one distinguishes "perpendicular shocks" where **B** is perpendicular to the shock normal (that is parallel to the shock front) and "parallel shocks" where **B** is parallel to the shock normal (that is perpendicular to the shock front). If the point of intersection moves at superluminal speed (a case we won't consider therafter) this change of frame is not possible but one can still find a particular frame (called the perpendicular frame) where the shock is stationary (and where both the electric and magnetic field lie normal to each other).

2.1.1.2 The Discontinuity

For a given upstream state the downstream state is entirely determined by the shock Mach number: the two states are linked by the so called Rankine-Hugoniot[2] relations. These three jump conditions express simply the continuity of the mass, momentum and energy fluxes at the shock interface (in its rest frame). They can be expressed as:

[2]Who discovered them in 1889.

$$r = \frac{u_1}{u_2} = \frac{\rho_2}{\rho_1} = \frac{(\gamma+1)M_s^2}{(\gamma-1)M_s^2+2} \quad \rightarrow \quad \frac{\gamma+1}{\gamma-1} \tag{2.5}$$

$$\frac{P_2}{P_1} = \frac{2\gamma M_s^2 - (\gamma-1)}{(\gamma+1)} \quad \rightarrow \quad \frac{2\gamma}{\gamma+1}M_s^2 \tag{2.6}$$

$$\frac{T_2}{T_1} = \frac{(2\gamma M_s^2 - (\gamma-1))\,((\gamma-1)M_s^2+2)}{(\gamma+1)^2 M_s^2} \quad \rightarrow \quad \frac{2\gamma(\gamma-1)}{(\gamma+1)^2}M_s^2 \tag{2.7}$$

where r is the compression ratio of the shock (defined as the speeds ratio) and where the formula on the right are obtained in the limit of strong shocks ($M_s \gg 1$). We note that the velocity jump and density compression are limited: for a usual polytropic index $\gamma = 5/3$ strong shocks have a compression ratio of $r = 4$ (but the downstream pressure and temperature can grow without limits).

To end this short presentation we would like to note that physically the shock is of course not a perfect mathematical discontinuity: the upstream to downstream state transition occurs through particle collisions over a few mean free paths. But in astrophysical conditions shocks are actually non-collisional: plasma particles don't actually collide on each other (their mean free path is far too high) but interact through collective electromagnetic effects (that are not yet fully understood). The shock width is then of the order of a few Larmor radii of the particles.

2.1.1.3 Spherical Geometry

In spherical geometry a point-source explosion such as a supernova yields a particular structure composed of three waves (see figure 2.2 and simulations of the appendix):
- the **forward shock**, which progresses in the upstream undisturbed medium (and accelerates it);
- the **contact discontinuity**, which separates matter from the supernova (ejecta) and matter from the interstellar medium;
- the **reverse shock**, which propagates back in the ejecta (and slow them down).

From the supernova explosion to the dilution in the interstellar medium a supernova remnant evolves through four distinct phases (see Chevalier (1977) and Truelove and McKee (1999)). The key physical parameters are the supernova energy $E_{\rm sn}$ (typically 10^{51} erg), the ejecta mass $M_{\rm ej}$ (typically a few solar masses $M_\odot = 2 \times 10^{30}$ kg) and the interstellar medium (ISM) density $n_{\rm ism}$ (typically 1 particle per cm^3, but with possible variations of a few order of magnitudes above or below).

Free expansion phase. For the first hundred of years the SNR evolution is driven by the ejecta: its radius evolves as

$$R_{\rm snr}(t) = v_s t \tag{2.8}$$

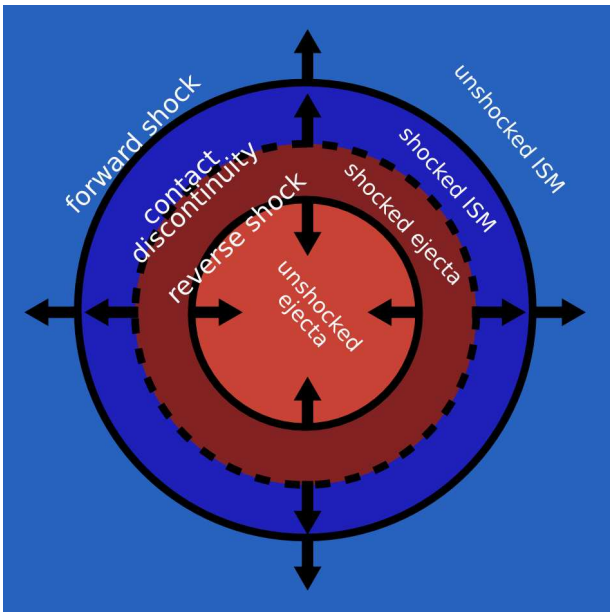

Figure 2.2: Waves structure for a spherical shock.
The ejecta are in red and the interstellar medium is in blue. Material in dark colors have been shocked, material in light colors are still undisturbed.

where the constant expansion speed v_s is obtained from energy conservation, identifying the kinetic energy of the ejecta to the mechanical energy released by the supernova:

$$E_{\rm sn} = \frac{1}{2} M_{\rm ej} v_s^2 \,. \tag{2.9}$$

The ejecta being supersonic, a shock wave precedes them in the ISM. The ejecta push the shocked ISM accumulated between the contact discontinuity and the forward shock.

Sedov-Taylor phase. The ejecta expand freely until they have swept-up a mass of ISM roughly equal to their own mass. This occurs after a time

$$t_{\rm ST} \simeq 210\,{\rm yr} \left(\frac{E_{\rm sn}}{10^{51}\,{\rm erg}}\right)^{-1/2} \left(\frac{M_{\rm ej}}{1\,M_\odot}\right)^{5/6} \left(\frac{n_{\rm ism}}{1\,{\rm cm}^3}\right)^{-1/3} \tag{2.10}$$

corresponding to a radius and velocity

$$R_{\rm ST} \simeq 2.8\,{\rm pc} \left(\frac{M_{\rm ej}}{1\,M_\odot}\right)^{1/3} \left(\frac{n_{\rm ism}}{1\,{\rm cm}^3}\right)^{-1/3} \tag{2.11}$$

$$v_{\rm ST} \simeq 6500\,{\rm km/s} \left(\frac{E_{\rm sn}}{10^{51}\,{\rm erg}}\right)^{1/2} \left(\frac{M_{\rm ej}}{1\,M_\odot}\right)^{-1/2} . \tag{2.12}$$

After that the SNR evolution is dominated by the swept-up shell of shocked ISM, so that energy conservation now reads

$$E_{\rm sn} = \frac{1}{2} \left(\frac{4}{3}\pi R_s^3\, \rho_{\rm ism}\right) v_s^2 \tag{2.13}$$

which yields

$$R_{\rm snr}(t) \propto \left(\frac{E_{\rm sn}}{\rho_{\rm ism}}\right)^{1/5} t^{2/5} \,. \tag{2.14}$$

As the ejecta can't expand freely any longer a reverse shock develops from the contact discontinuity towards the interior of the remnant, heating and decelerating the ejecta. This shock rebounds at the SNR center, and progressively disappears. The contact discontinuity itself breaks as it gets instable. The SNR is then a hot expanding bubble.

Pressure-driven phase. The first two phases are non radiative, meaning that the cooling time of the (very hot) gas is so long that radiative energy losses are negligible regarding the SNR dynamics. But after 10 000 years or so the swept-up ISM starts cooling, quickly collapsing to form a thin and cold outer shell. The transition occurs more precisely after a time

$$t_{\rm PD} \simeq 29\,000\,{\rm yr} \left(\frac{E_{\rm sn}}{10^{51}\,{\rm erg}}\right)^{4/7} \left(\frac{n_{\rm ism}}{1\,{\rm cm}^3}\right)^{-9/17} \tag{2.15}$$

corresponding to a radius

$$R_{\rm PD} \simeq 18\,{\rm pc} \left(\frac{E_{\rm sn}}{10^{51}\,{\rm erg}}\right)^{5/17} \left(\frac{n_{\rm ism}}{1\,{\rm cm}^3}\right)^{-7/17} \,. \tag{2.16}$$

The hot interior then pushes the shell like a snowplow: the SNR expansion is sustained by its own pressure $P_{\rm snr}$ so that

$$\frac{d}{dt}\left(M_{\rm snr} v_s\right) = 4\pi R_{\rm snr}^2 P_{\rm snr} \tag{2.17}$$

from which one derives

$$R_{\rm snr}(t) \propto t^{2/7} \,. \tag{2.18}$$

Momentum-driven phase. The SNR pressure eventually matches the ISM pressure, so that the shell no longer undergoes any force and moves inertially:

$$\frac{d}{dt}\left(M_{\rm snr} v_{\rm snr}\right) = 0 \tag{2.19}$$

from which one derives

$$R_{\rm snr}(t) \propto t^{1/4} \,. \tag{2.20}$$

The remnant eventually merges with the ISM when its expansion speed decreases to the local sound speed.

Note that according to Lagage and Cesarsky (1983) cosmic-ray acceleration is mostly efficient in the early phases of the SNR evolution (as the subsequent remnant expansion leads to high energy losses), with maximum energies propably achieved at the beginning of the Sedov-Taylor phase[3]. Note also that in this global picture we have not yet considered any effects of the cosmic-ray population accelerated by the shock (see sections 2.3 and 2.5.2).

[3]However detailed studies of cosmic-ray acceleration by late stage SNR are still missing.

2.1.2 Magnetic Field Waves

The magnetic field has a crucial role in the DSA process. Scattering off magnetic waves couples the individual high-energy particles to macroscopic structures (such as a SNR). Thus although cosmic-rays are labelled as non-thermal as they are not in equilibrium with the other particles of the plasma, they are involved in a thermalization process with the shock wave as a whole. It is then no surprise that they can get accelerated to extremely high energies.

2.1.2.1 Effects of Waves on Particles

The random walk of cosmic-rays through our Galaxy (1.3.2.1) is provided by the irregularities of the Galactic magnetic field. In the same way magnetic turbulence in the vicinity of SNR shocks scatters high energy particles (see the review of Skilling (1975a) or the lecture of Achterberg (1998)). This is a collective process in the sense that cosmic rays are not scattered by individual particles of the ISM but by waves supported by the plasma *as a whole*.

We recall that plasmas host two main kind of waves, Alfven waves which rely on the magnetic tension and magnetosonic waves which rely on the magnetic pressure and kinetic pressure. The most important for us here are the Alfven waves, that is non compressive transverse $\mathbf{B}$ perturbations travelling at a speed

$$v_A = \frac{B}{\sqrt{\mu_0 \rho}} \simeq 2.2\,\mathrm{km/s} \left(\frac{B}{1\,\mu\mathrm{G}}\right) \left(\frac{n}{1\,\mathrm{cm}^3}\right)^{-1/2}. \tag{2.21}$$

As is well known charged particles are forced to rotate around magnetic field lines, with a gyration radius called their Larmor radius and given by

$$r_L = \frac{m v_\perp}{qB} \tag{2.22}$$

where $v_\perp$ is the speed in the plane perpendicular to the field lines. For relativistic particles this can be written

$$r_L = \frac{p}{qB} = \frac{E/c}{qB} \simeq (1.1\,\mathrm{pc})\ Z \left(\frac{E}{1\,\mathrm{PeV}}\right) \left(\frac{B}{1\,\mu\mathrm{G}}\right)^{-1}. \tag{2.23}$$

On the opposite particles are free along the magnetic field lines, so that their trajectory in a homogeneous and constant magnetic field is a spiral characterized by r_L and the angle α between the particle velocity and magnetic field lines (called the pitch angle).

What happens if the magnetic field lines are deformed by waves of wavelength λ? It depends on the ratio r_L/λ. If $r_L \ll \lambda$ the particle remains attached to its field line, simply following its slow curvature. If $r_L \gg \lambda$ the particle doesn't feel the waves perturbations, simply following the mean magnetic field. The case of interest is $r_L \sim \lambda$: in that case the particle travels along the field line together with the perturbation, which allows an efficient

interaction. This is the *resonance* condition, which can more generally be written

$$\omega - k v_{\parallel} = n\,\Omega \tag{2.24}$$

where ω, k are the wave pulsation and vector, Ω, $v_{\parallel}$ are the particle rotation frequency (around $\mathbf{B}$) and speed (along $\mathbf{B}$) and n is an integer. The case $r_L = \lambda$ corresponds to $n = 0$. One shows that if that condition holds the pitch angle of the particle varies proportionally to the wave amplitude δB. Taking into account the finite correlation time of the resonance (because of the superposition of different waves of different wavelengths) one simply gets

$$\frac{\delta\alpha}{2\pi} \simeq \frac{\delta B}{B}\sin\varphi \tag{2.25}$$

where φ is the phase of the wave. This formula gives the change in pitch-angle per resonant interaction with a single wave. Different waves are incoherent so that φ is random and thus in average $< \delta\alpha >= 0$. However $< (\delta\alpha)^2 > \neq 0$ so that the pitch angle performs a random walk. One can evaluate the time in which a particle reverses its direction, yielding a mean free path

$$l_{\rm mfp} \simeq r_L \left(\frac{\delta B}{B}\right)^{-2}_{\lambda\sim r_L} \tag{2.26}$$

where the $\lambda \sim r_L$ subscript recalls that the waves to be considered are the ones of resonant wavelength.

The random walk of particles leads to a space diffusion of the cosmic-rays population, which can be described through a diffusion coefficient

$$D = \frac{1}{3} l_{\rm mfp} v \tag{2.27}$$

(so that the macroscopic diffusive flux of particles is $-D\overrightarrow{\nabla} n_{\rm cr}$). The problem is now to get a quantitative estimate of $l_{\rm mfp}$. In the quasilinear theory, that is for small field fluctuations ($\delta B/B \ll 1$), this quantity can be formally derived for a given waves power spectrum $W(k)$ defined so that

$$\frac{\delta B^2}{4\pi} = \int_k W(k)\,dk\,. \tag{2.28}$$

If $\delta B \sim B$ the situation is much more complicated and one mostly relies on numerical simulations.

A special case of interest is the "Bohm limit" reached when $l_{\rm mfp} \sim r_L$, that is when particles are scattered by the waves within one gyro-period, meaning that the turbulence causing their scattering is random on the scale r_L (that is $\delta B \sim B$ in equation (2.26)). This constitutes a lower limit on the (parallel) diffusion coefficient[4]. This case has been widely favored in the literature (see eg Kang

[4]And on the DSA acceleration time-scale as we shall see in section 2.2.

and Jones (1991) and Duffy (1992) in the context of numerical simulations). In that case $D \propto pv$ so that

$$D_{\mathrm{Bohm}}(p) \propto \frac{p^2}{\sqrt{1+p^2}} \rightarrow \begin{cases} p^2 & p \ll 1 \\ p & p \gg 1 \end{cases} \tag{2.29}$$

where the cosmic-ray momenta p are expressed in $m_p c$ units. For relativistic particles equation (2.29) can be expressed as

$$D_{\mathrm{Bohm}}(E) = \frac{1}{3} r_L(E)\, c \simeq \left(3 \times 10^{22}\ \mathrm{cm}^2/\mathrm{s}\right) Z \left(\frac{E}{1\,\mathrm{GeV}}\right) \left(\frac{B}{1\,\mu\mathrm{G}}\right)^{-1} \tag{2.30}$$

2.1.2.2 Effect of Particles on Waves

The diffusion process described above, and thus the presence of magnetic turbulence, is mandatory for the DSA process to work. But as was noted early (Skilling 1975b) the cosmic-rays can generate themselves the waves on which they shall diffuse. They can indeed trigger various instabilities upstream of the shock, most notably the "streaming instability", producing magnetic turbulence that is then advected downstream. It is thus possible to compute the diffusion coefficient $D(x,p,t)$ self-consistently from the cosmic-rays distribution itself, by solving the wave transport equation which in its simplest form reads

$$\frac{\partial W}{\partial t} + \tilde{u}\frac{\partial W}{\partial x} = \Gamma_g - \Gamma_d \tag{2.31}$$

where $W(k,x,t)$ is the waves power spectrum defined by equation (2.28), $\tilde{u}$ is the speed of the waves in the shock rest frame (this is simply the fluid speed u in the case of super-Alfvenic shocks), Γ_g is the growth rate of the waves (which can be expressed as a function of the cosmic-rays distribution function) and Γ_d is their damping rate. This aspect has already been addressed by Jones (1994) but using a simplified model for cosmic-rays transport, namely the "two-fluid" model in which cosmic-rays are described as a fluid (see section 2.3.3). Jones and Kang (2006) are now investigating MHD simulations, while Amato and Blasi (2006) use a semi-analytical approach and Vladimirov et al. (2006) use a Monte-Carlo model. We haven't addressed ourselves this problem in the limited framework of the present thesis, but clearly it would be a quite natural and surely interesting development of our work.

2.1.2.3 Magnetic Field Amplification

We would like to end this short presentation of the magnetic field role by discussing its value. The typical interstellar magnetic field is of the order of a few μG. But both observational and theoretical evidence have accumulated lately showing that the magnetic field at SNR shocks is probably considerably amplified. Using radio observations of the synchrotron radiation of electrons in the Tycho and Kepler SNRs Reynolds and Ellison (1992) have obtained a

best fit of the spectrum with values of B of the order of the mG. Exploiting the abscence of a radio precursor (expected because of non-linear effects, see more in sections 2.3.2 and 2.5.2.1) Achterberg et al. (1994) have derived a magnetic turbulence at least 60 times higher than previously supposed. Addressing through direct simulations the problem of the magnetic waves growth induced by cosmic-rays instabilities (see section 2.1.2.2) Lucek and Bell (2000), Bell and Lucek (2001), Bell (2004) have found that the power in magnetic fluctuations can rise two orders of magnitude above the pre-existent magnetic field. Conducting a detailed analysis of the sharp X filaments observed recently in a few young SNRs thanks to the high resolution of Chandra and XMM-Newton, Parizot et al. (2006) have derived values of B close the shock between 100 and 500 μG [5]. The value of the magnetic field is of primary importance as it controls the maximum energy achievable by cosmic-rays in SNRs (see the discussion of section 1.3.1.2 and the recent works of Blasi et al. (2007) and Ellison and Vladimirov (2008)).

2.2 Linear Theory

In this section we will show how diffusive shock acceleration (DSA) can actually accelerate particles at a shock front (see the lectures of Kirk (1994), Achterberg (1998), Parizot (2004) for more details). Note that in all this section we work in the *test-particle* regime, that is we consider that the cosmic-rays accelerated by the shock don't back-react on its dynamics (we will see in section 2.3 that this assumption doesn't hold and then investigate *non-linear* models). The basic idea of DSA is that highly energetic particles crossing the velocity discontinuity gain an energy proportional to their current energy, and that they can cross the shock a great many times thanks to their scattering off magnetic waves which isotropizes them on both side of the shock.

First, following the first idea of Fermi, we will compute the energy gained by a particle through a "collision" with a magnetic structure. Then, averaging over a sequence of random or regular collisions, we will obtain the net energy gain of the two Fermi processes, and show how such processes naturally build power-law spectra. Finally, we will see how a magnetized shock naturally provides a regular (and thus efficient) Fermi acceleration, and compute by different approaches the remarkable resulting power-law index.

2.2.1 Energy Gain in a Collision

In his first model Fermi proposed that cosmic-rays were accelerated through encounters with moving magnetized clouds[6]. When entering a cloud of con-

[5] They have also obtained values of the diffusion coefficient, between 1 and 10 times the Bohm limit.

[6] Modern scattering centers are the magnetic field waves we have introduced in section 2.1.2 and we shall put at work in section 2.2.3.

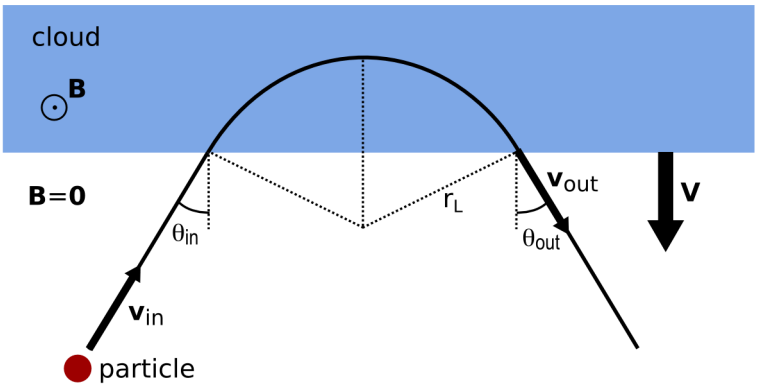

Figure 2.3: Sketch of the collision of a charged particle with a magnetized cloud.

stant and homogeneous **B** a charged particle begins gyrating around **B** until it escapes the cloud. If **B** is strong enough the particle might be deflected back to its original direction, so that it appears to "rebound" on the cloud (see figure 2.3). What is the energy exchange during one such encounter? Even if the scattering itself is elastic (meaning that the particle energy doesn't vary when moving around **B** inside the cloud) the energy of the particle measured in the Galactic rest frame (with respect to which the clouds are moving) will change, because of the velocity difference between the particle and cloud.

2.2.1.1 Change of Frame

The most straightforward way to see it is to perform frame transformations. Let $E_{\rm in}$ and $\mathbf{p}_{\rm in}$ be the energy and impulsion of the particle in the Galactic frame, in which the cloud travels at speed $\mathbf{V}$. In the cloud frame the energy $E'_{\rm in}$ and impulsion $\mathbf{p}'_{\rm in}$ are given by a Lorentz transform:

$$\begin{cases} E'_{\rm in} = \gamma \left(E_{\rm in} - V\, p_{\rm in\parallel} \right) \\ p'_{\rm in\parallel} = \gamma \left(p_{\rm in\parallel} - \frac{V}{c^2} E_{\rm in} \right) \end{cases} \tag{2.32}$$

where $\gamma(V)$ is the Lorentz factor of the cloud and $p_\parallel$ denotes the component of $\mathbf{p}$ along $\mathbf{V}$. Lets consider now an elastic reflection inside the cloud, so that (still in the cloud frame)

$$\begin{cases} E'_{\rm out} = E'_{\rm in} \\ p'_{\rm out\parallel} = -p'_{\rm in\parallel} \end{cases} \tag{2.33}$$

To go back into the Galactic frame we have to perform a second Lorentz transform (with opposite velocity):

$$\begin{cases} E_{\rm out} = \gamma \left(E'_{\rm out} + V\, p'_{\rm out\parallel} \right) \\ p_{\rm out\parallel} = \gamma \left(p'_{\rm out\parallel} + \frac{V}{c^2} E'_{\rm out} \right) \end{cases} \tag{2.34}$$

Combining equations (2.32), (2.33) and (2.34) one obtains the energy change $\Delta E = E_{\text{out}} - E_{\text{in}}$ as

$$\frac{\Delta E}{E} = 2\gamma^2 \frac{(\mathbf{V} - \mathbf{v}) \cdot \mathbf{V}}{c^2} \tag{2.35}$$

where $\mathbf{v}$ is the particle's velocity and we recall that $\mathbf{V}$ is the cloud's velocity. To the first order in V/c equation (2.35) reduces to

$$\frac{\Delta E}{E} = -2\frac{\mathbf{v} \cdot \mathbf{V}}{c^2}\,. \tag{2.36}$$

We observe that the change in energy depends on the geometry of the encounter: for head-on collisions ($\mathbf{v} \cdot \mathbf{V} < 0$) the particle gains energy ($\Delta E > 0$), for overtaking collisions ($\mathbf{v} \cdot \mathbf{V} > 0$) the particle loses energy ($\Delta E < 0$).

2.2.1.2 Electric Field Work

The change of frame approach of the last paragraph gives quite quickly the energy gain (or loss) of the particle but it hides where the energy actually comes from (or goes to). As we explained in 1.3.1.2 the particle is in fact accelerated by the electromagnetic field. To show that we will consider now for the sake of simplicity that the velocities of the particle $\mathbf{v}$ and of the cloud $\mathbf{V}$ lie in a plane perpendicular to the (constant and homogeneous) magnetic field $\mathbf{B}'$ of the cloud as shown in figure 2.3. In that case the particle enters the cloud with some direction θ (with respect to the cloud's velocity) then describes an arc of circle around $\mathbf{B}'$ (of radius r_L) until it crosses the cloud surface back, travelling a distance $2\,r_L\,\cos\theta$ inside the cloud (approximating locally the cloud frontier by a planar surface perpendicular to $\mathbf{V}$). During that time the particle feels the electric field $\mathbf{E} = -\mathbf{V} \times \mathbf{B}'$ induced by the magnetic field of the cloud (as seen from the Galactic frame). The energy gain of the particle is nothing but the work of the Lorentz force $\mathbf{F} = q\mathbf{E}$ integrated over the path of the particle inside the cloud:

$$\Delta E = \int \mathbf{F} \cdot \mathbf{dl} = qVB \int dl = qVB \times 2\frac{p}{qB}\cos\theta = 2E\frac{vV\cos\theta}{c^2} \tag{2.37}$$

(where we have used $p = Ev/c^2$). This is the same result as equation (2.36). Note how the magnetic field value B (as actually all the details of the interaction) disappears in the final result: the only parameters are the respective velocities of the particle and cloud (scattering center).

2.2.2 Fermi Processes

We have seen in the last section that through a collision with a magnetic cloud a particle changes its energy, and that it can both gain or lose energy (see equation (2.36)). What is the net result of many such encounters? We will show now that it's (statistically) always a net acceleration, but at a speed which depends on whether the scattering centers move in a random or regular fashion

(leading to two distinct Fermi acceleration processes, the original *stochastic* one and the more recent *regular* one).

If one takes into account the actual direction of entry $\theta_{\rm in} = (\widehat{\mathbf{v}_{\rm in}, \mathbf{V}})$ and of exit $\theta_{\rm out} = (\widehat{\mathbf{v}_{\rm out}, \mathbf{V}})$ of the particle equation (2.35) becomes

$$\frac{\Delta E}{E} = \frac{\beta\left(\cos\theta'_{\rm out} - \cos\theta_{\rm in}\right) + \beta^2\left(1 - \cos\theta'_{\rm out}\cos\theta_{\rm in}\right)}{1-\beta} \tag{2.38}$$

where $\beta = V/c$ is the cloud speed (and as before primed quantities are measured in the cloud frame). To find the *mean* change in energy of a particle as it encounters many different clouds we have to average equation (2.38) over the angles of entry and exit.

2.2.2.1 Stochastic Acceleration

Lets consider first the original idea of Fermi of randomly moving clouds. In that case the probability of collision between a particle and a given cloud is proportional to their relative velocity $v - V\cos\theta_{in}$, from which we derive

$$< \cos\theta_{\rm in} >= -\frac{1}{3}\frac{V}{v} \simeq -\frac{1}{3}\beta\,. \tag{2.39}$$

where in the last equality we have considered relativistic particles ($v \simeq c$). Assuming that the exit angle is random we can also write

$$< \cos\theta'_{\rm out} >= 0\,. \tag{2.40}$$

Then averaging equation (2.38) we obtain:

$$< \frac{\Delta E}{E} >= \frac{4}{3}\frac{\beta^2}{1-\beta^2} \simeq \frac{4}{3}\beta^2\,. \tag{2.41}$$

We note that $< \Delta E >> 0$: particles are accelerated. This is due to the fact that head-on collisions (where particles gain energy) are more frequent than overtaking collisions (where particles lose energy) because particles are themselves in motion (and thus on average see the clouds coming to them). Equation (2.41) however gives only the *mean* energy gain: some individual particles will gain more, others will gain less or even lose some. This is why this mechanism is called *stochastic Fermi acceleration*. It is also called *second-order Fermi acceleration* (or simply Fermi II) because as seen from equation (2.41) the mean relative energy gain rises as β^2. As β is small this means that the acceleration is actually fairly slow: Fermi himself realized that this process wasn't probably efficient enough to produce the bulk of Galactic cosmic-rays.

2.2.2.2 Regular Acceleration

What happens now if we consider some special geometry where only face-on collisions occur? In that case the distribution of the particles upstream of the cloud is isotropic, so that

$$< \cos\theta_{\rm in} >= -\frac{2}{3}\,. \tag{2.42}$$

The same holds symmetrically for the exit angle of the particles, so that

$$< \cos\theta'_{\rm out} >= +\frac{2}{3}\,. \tag{2.43}$$

Then averaging equation (2.38) we obtain now a mean energy gain

$$< \frac{\Delta E}{E} >= \frac{\frac{4}{3}\beta + \frac{13}{9}\beta^2}{1-\beta^2} \simeq \frac{4}{3}\beta\,. \tag{2.44}$$

We have again $< \Delta E >> 0$, but now ΔE is proportional to β (hence the name *first-order Fermi acceleration* – or simply Fermi I): the acceleration is usually much faster than in the previous case, as particles now gain energy in each encounter (hence the name *regular Fermi acceleration*). We will see in section 2.2.3 how this mechanism is at work at SNR shocks.

2.2.2.3 Building Power-Laws

Before studying the DSA mechanism per se we would like to show how the Fermi mechanisms can produce power-law spectra in energy (as commonly observed).

From a general point of view an acceleration mechanism can be characterized by its acceleration time $\tau_{\rm acc}$ (defined so that particles are accelerated at a rate $\partial E/\partial t = E/\tau_{\rm acc}$) and its escape time (defined so that particles escape the accelerator at a rate $\partial N/\partial t = N/\tau_{\rm esc}$). Neglecting other kind of losses the density of particles $N(E,t)$ obeys a simple transport equation (in the energy space):

$$\frac{\partial N}{\partial t} + \frac{\partial}{\partial E}\left(\left(\frac{\partial E}{\partial t}\right)_{\rm acc} N\right) = Q_{\rm inj} - \left(\frac{\partial N}{\partial t}\right)_{\rm esc} \tag{2.45}$$

where $Q_{\rm inj}$ is a source term. If one considers mono-energetic injection of particles at E_0, that is $Q_{\rm inj}(E) \propto \delta(E-E_0)$ where δ is the Dirac distribution, then above E_0 the steady-state ($\partial/\partial t = 0$) energy density of the particles is given by the equilibrium between acceleration and escape:

$$\frac{\partial}{\partial E}\left(\frac{E}{\tau_{\rm acc}(E)} N(E)\right) = -\frac{N(E)}{\tau_{\rm esc}(E)}\,. \tag{2.46}$$

As seen from equations (2.41) and (2.44) the main property of Fermi processes is that the energy gain is proportional to the current energy at each encounter.

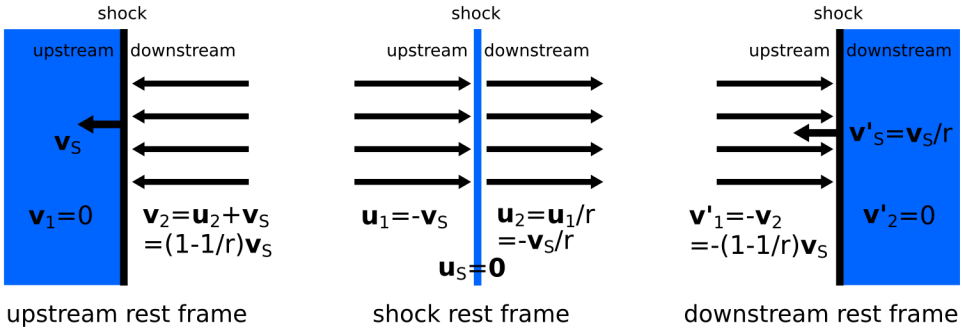

Figure 2.4: Sketch of a shock as seen from the three natural frames. Velocities are shown in the upstream rest frame (left), in the shock rest frame (center), and in the downstream rest frame (right).

If the typical time between two encounters is $t_{\rm cyc}$ the mean energy gain per unit time equals

$$\left(\frac{\partial E}{\partial t}\right)_{\rm Fermi} = \frac{<\Delta E>}{t_{\rm cyc}} = \frac{E}{\tau_{\rm acc}} \tag{2.47}$$

where $\tau_{\rm acc} = 3\,t_{\rm cyc}/4\,\beta$ for Fermi I and $3\,t_{\rm cyc}/4\,\beta^2$ for Fermi II is independent of the energy. If the escape time $\tau_{\rm esc}$ is also independent of the energy then equation (2.46) simplifies to

$$\frac{\partial N}{\partial E} = -\frac{N}{E}\left(1+\frac{\tau_{\rm acc}}{\tau_{\rm esc}}\right) . \tag{2.48}$$

The solution is naturally a power-law

$$N(E) \propto E^{-s} \quad \text{with} \quad s = 1+\frac{\tau_{\rm acc}}{\tau_{\rm esc}} . \tag{2.49}$$

2.2.3 Shock Acceleration

As seen from figure 2.4 a shock wave, being a converging flow, provides a configuration in which only face-on encounters occur: both the upstream and the downstream medium see the opposite side arriving against them – and at the same speed

$$\Delta V = \frac{r-1}{r} v_s \quad \left(= \frac{3}{4}\, v_s \text{ if } r = 4\right) \tag{2.50}$$

where v_s is the speed of the shock (with respect to the unperturbed upstream medium). Here comes the central hypothesis under the DSA mechanism: because of their diffusion due to the magnetic turbulence the cosmic-rays are isotropized on each side of the shock, that is, their mean velocity relative to the local flow is null both upstream and downstream. Thus, they experience a regular Fermi acceleration, the clouds of section 2.2.2 being replaced by a

reflecting wall moving at velocity ΔV. Adapting equation (2.44) one finds a mean energy gain

$$< \frac{\Delta E}{E} >= \frac{4}{3}\frac{\Delta V}{c} \ (= \beta_s \text{ if } r = 4) \ . \tag{2.51}$$

The energy ΔE is gained over each cycle of the form upstream $\rightarrow$ downstream $\rightarrow$ upstream (that is two successive crossings of the shock, that is one complete reflection on the opposite medium). Thanks to their scattering off the magnetic field which give them random velocities (and as their speed is much higher than the shock speed) the cosmic-rays can cross the shock many times before being eventually advected downstream of the shock. The computation of the actual cycle time and escape probability will be done in the next sub-sections using two different approaches (following the fate of individual particles or the evolution of their global distribution function). We note already that they both depend on the particle energy, so that neither $\tau_{\rm acc}$ nor $\tau_{\rm esc}$ (as defined in 2.2.2.3) is independent of the energy as we had assumed previously. However it turns out that the ratio $\tau_{\rm acc}/\tau_{\rm esc}$ is independent of E, so that the power-law given by equation (2.49) still holds. Not only the logarithmic slope s is constant, but the beauty of the DSA mechanism is that it depends on a single simple parameter, namely the shock compression ratio r, which in the limit of strong shocks is always $r = 4$ (see section 2.1.1.2) – regardless of the details of the diffusion of particles. To end this section we shall now demonstrate this well-known result

$$N(E) \propto E^{-s} \quad \text{with} \quad s = \frac{r+2}{r-1} \ (= 2 \text{ if } r = 4) \ . \tag{2.52}$$

We find it more convenient to work with the particle distribution function in momentum $f(p)$, defined so that the number density of cosmic-rays is

$$n_{\rm cr}(\mathbf{x}, t) = \int_p f(\mathbf{x}, p, t)\, 4\pi p^2 dp. \tag{2.53}$$

In that case equation (2.52) becomes

$$f(p) \propto p^{-s} \quad \text{with} \quad s = \frac{3\,r}{r-1} \ (= 4 \text{ if } r = 4) \ . \tag{2.54}$$

2.2.3.1 Microscopic Approach

Individual particles gain energy through the repetition of acceleration cycles of the form upstream $\rightarrow$ downstream $\rightarrow$ upstream. Assuming isotropy of particles velocities both upstream and downstream (thanks to their diffusion), one computes the energy gain of a particle during such a cycle to be

$$< \Delta p >= 2 \times \frac{2}{3}\frac{u_1 - u_2}{v} p \tag{2.55}$$

where u_1 and u_2 are the speed of the upstream and downstream flows respectively (in the shock frame) and v is the particle speed (this corresponds to equation (2.36)). We have to evaluate now how many crossings a particle can do. Upstream the shock will always catch up with the particles, downstream particles may be advected too far away from the shock to complete the cycle. The flux of particles escaping downstream is $n\,u_2$ whereas the flux of particle entering the downstream region from upstream is $n\,v/4$ (assuming isotropy one half of the particles are moving this way, with an average projected velocity of one half v), therefore the probability of never returning to the shock is

$$P_{\rm esc} = \frac{4\,u_2}{v} \tag{2.56}$$

which by assumption is small (that is, almost all the particles cross the shock many times). With equations (2.55) and (2.56) one can compute the particle spectrum evolution after many cycles. Lets consider that all particles are advected in from upstream with the same momentum p_0. After n cycles (that is $2\,n$ crossings) the typical momentum of a particle is

$$p_n = \prod_{i=1}^{n} \left(1 + \frac{4}{3}\frac{u_1 - u_2}{v_i}\right) p_0\,. \tag{2.57}$$

The probability of a particle reaching this momentum is

$$P_n = \prod_{i=1}^{n} \left(1 - \frac{4u_2}{v_i}\right)\,. \tag{2.58}$$

Eliminating v_i between equations (2.57) and (2.58) one gets

$$P_n = \left(\frac{p_n}{p_0}\right)^{-\frac{3\,u_2}{u_1-u_2}}\,. \tag{2.59}$$

The downstream number density of particles accelerated from p_0 up to p_n or more is then simply

$$n_2\,(\geq p_n) = P_n \times n_2\,(p_0) = \left(\frac{p_n}{p_0}\right)^{-\frac{3\,u_2}{u_1-u_2}} n_{2,0} \tag{2.60}$$

where $n_{2,0} = (u_1/u_2)\,n_{1,0}$ is the initial downstream density produced by compression of the upstream density $n_{1,0}$. Thus the downstream distribution function is

$$f_2(p) = -\frac{1}{4\pi p^2}\frac{\partial n_2(\geq p)}{\partial p} = s\,\frac{n_{1,0}}{4\pi p_0^3}\left(\frac{p}{p_0}\right)^{-s} \quad \text{with} \quad s = \frac{3\,u_1}{u_1 - u_2} = \frac{3\,r}{r-1}\,. \tag{2.61}$$

Note that we have obtained the *energy* distribution of the particles without giving any details of their scattering off the magnetic waves: the only assumption is that scattering maintains an isotropic distribution on both sides of the shock. However we need to address particles diffusion in more details to study the *time* evolution of the spectrum (see section 2.2.3.3).

2.2.3.2 Macroscopic Approach

One can obtain equation (2.61) directly by solving the transport equation of the cosmic-rays. The conservation of the number of particles in the phase space ($\mathbf{x}$, p) reads

$$\frac{\partial f}{\partial t} + \frac{\partial \mathbf{F}_\mathbf{x}(f)}{\partial \mathbf{x}} + \frac{\partial \mathbf{F}_p(f)}{\partial p} = 0\,. \tag{2.62}$$

The diffusive approximation allows to write the space flux $F_\mathbf{x}$ as

$$\mathbf{F}_\mathbf{x} = \mathbf{u}\, f - D\,\frac{\partial f}{\partial \mathbf{x}} \tag{2.63}$$

where $\mathbf{u} = \partial\mathbf{x}/\partial t$ is the flow velocity and $D(\mathbf{x}, p)$ is the particles diffusion coefficient (see section 2.1.2.1). The momentum flux $\mathbf{F}_p = (\partial p/\partial t) \times f$ is due to the adiabatic change in energy of the particles, given by

$$\frac{\partial p}{\partial t} = -\frac{1}{3}\frac{\partial \mathbf{u}}{\partial \mathbf{x}}\,p\,. \tag{2.64}$$

Equation (2.64) is equivalent to equation (2.55). It corresponds to the usual $-P\,dV$ term of thermodynamics, the cosmic-rays pressure P being powered by their impulsion p (see equation (2.80)) and the volume variation dV being given by the velocity divergence $\partial\mathbf{u}/\partial\mathbf{x}$ (which is thus the engine of the acceleration process: particles get accelerated as a shock is a converging flow). Developping derivatives in equation (2.62) one finally gets

$$\frac{\partial f}{\partial t} + \mathbf{u}\frac{\partial f}{\partial \mathbf{x}} = \frac{\partial}{\partial \mathbf{x}}\left(D\frac{\partial f}{\partial \mathbf{x}}\right) + \frac{1}{3}\frac{\partial \mathbf{u}}{\partial \mathbf{x}} p \frac{\partial f}{\partial p}\,. \tag{2.65}$$

We will now solve equation (2.65) for a 1D shock, that is a velocity discontinuity defined by (see figure 2.1)

$$u(x) = \begin{cases} u_1 & x < 0 \text{ (upstream)} \\ u_2 & x > 0 \text{ (downstream)}\,. \end{cases} \tag{2.66}$$

According to equation (2.65) the steady-state ($\partial/\partial t = 0$) distribution of the particles in the upstream and downstream regions ($\partial u/\partial x = 0$) is given by

$$u\frac{\partial f}{\partial x} = \frac{\partial}{\partial x}\left(D\frac{\partial f}{\partial x}\right) \tag{2.67}$$

(where u equals u_1 or u_2), the general solution of which is

$$f(x,p) = A(p) + B(p)\,\exp\left(\int_0^x \frac{u}{D(x',p)}dx'\right)\,. \tag{2.68}$$

We need four more independent relations to determine the unknown functions A_1, A_2, B_1, B_2. Two come from boundary conditions far from the shock, by

imposing the far upstream distribution to be some given f_1 and by imposing the far downstream distribution to remain finite[7]. Two come from jump conditions at the shock[8], namely the continuity of the particle density

$$[f]_{x=0^-}^{x=0^+} = 0 \tag{2.69}$$

and the continuity of the particle "streaming"

$$\left[D\frac{\partial f}{\partial x}\right]_{x=0^-}^{x=0^+} + \frac{1}{3}\,[u]_{x=0^-}^{x=0^+}\, p\frac{\partial f}{\partial p} = 0\,. \tag{2.70}$$

Combining all these relations one finds the downstream distribution function to be the solution of

$$(r-1)\frac{\partial f_2}{\partial p} = 3\,r\,(f_1 - f_2) \tag{2.71}$$

where $r = u_1/u_2$ is the shock compression ratio (note that the diffusion coefficient has disappeared). Setting $s = 3\,r/(r-1)$ the solution is found to be

$$f_2(p) = sp^{-s}\int_0^p p'^{s-1} f_1(p')dp'\,. \tag{2.72}$$

If the upstream spectrum is a mono-energetic distribution $f_1(p) = f_{1,0}\,\delta(p-p_0)$ the downstream spectrum is a power-law distribution

$$f_2(p) = s\,\frac{f_{1,0}}{p_0}\left(\frac{p}{p_0}\right)^{-s} \quad \text{with} \quad s = \frac{3\,r}{r-1} \tag{2.73}$$

which is the same as equation (2.61) (given that $n_{1,0} = 4\pi p_0^2\, f_{1,0}$).

2.2.3.3 Acceleration Timescale and Maximum Energy

To end this presentation of the linear DSA theory we would like to discuss the acceleration time-scales in connection with the maximum momentum issue. We find it easier to use here the microscopic approach of section 2.2.3.1[9]. We found the mean momentum gain per cycle to be given by equation (2.55), to get the acceleration rate we need to evaluate the cycle duration. Upstream of the shock the balance between advection (to the shock) and diffusion (away from the shock) leads to an exponential decay of the cosmic-rays density:

$$n_1(x) = n_1(0)\,\exp\left(-\frac{|x|}{x_1}\right) \quad \text{with} \quad x_1 = \frac{D_1}{u_1}\,. \tag{2.74}$$

[7]This implies $B_2 = 0$ so that the steady-state solution is constant downstream.

[8]These two conditions can be obtained from equation (2.65), using the "weak solutions" technique to deal with the discontinuity.

[9]The macroscopic approach of section 2.2.3.2 can also be used to get the same results looking for time-dependent solutions of equation (2.65) thanks to Laplace transforms.

The typical upstream column density is thus $N_1 \simeq n_1(0)\, x_1$. As we have already seen the flux of particles crossing the shock is $F_{1\to 2} = n_1(0)\, v/4$ (because of isotropy). The mean residence time upstream is therefore $< t_1 >= 4\, D_1/v\, u_1$. Downstream the particle escape if $|u_2|\, t > \sqrt{D_2 t}$, thus in a time D_2/u_2^2. Multiplying by the probability of escape (given by equation (2.56)) we get the mean residence time downstream as $< t_2 >= 4\, D_2/v\, u_2$. Thus the mean duration of a cycle is

$$< t_{1\to 2\to 1} >=< t_1 > + < t_2 >= \frac{4}{v}\left(\frac{D_1}{u_1} + \frac{D_2}{u_2}\right) . \tag{2.75}$$

Given equation (2.55) this implies an acceleration time-scale

$$\begin{aligned} t_{\rm acc}(p) = \frac{p\Delta t}{\Delta p} &= \frac{3}{u_1 - u_2}\left(\frac{D_1(p)}{u_1} + \frac{D_2(p)}{u_2}\right) \\ &= \frac{3}{v_s^2}\frac{r}{r-1}\left(D_1 + r\, D_2\right) . \end{aligned} \tag{2.76}$$

If we assume that D is constant in space then $t_{\rm acc}(p) = (6r/(r-1))\, D_1/v_s^2 = 20\, D_1/v_s^2$ for $r = 4$. If we mimic the compression of the magnetic field at the shock as $D(x) \propto \rho_1/\rho(x)$ then $t_{\rm acc}(p) = (3r(r+1)/(r-1))\, D_1/v_s^2 = 8\, D_1/v_s^2$ for $r = 4$. The time it takes to accelerate a particle from a momentum p_0 to a momentum p is given by:

$$t_{\rm acc}\left(p_0 \to p\right) = \int_{p_0}^{p} t_{\rm acc}(p')\frac{dp'}{p'} . \tag{2.77}$$

If D has a simple power-law dependence[10] on p: $D(p) \propto p^\alpha$ then we get

$$t_{\rm acc}\left(p_0 \to p\right) = t_{\rm acc}\left(p_0\right) \begin{cases} \frac{1}{\alpha}\left(\left(\frac{p}{p_0}\right)^\alpha - 1\right) & \alpha \neq 0 \\ \ln\left(\frac{p}{p_0}\right) & \alpha = 0 . \end{cases} \tag{2.78}$$

The spectrum defined by equation (2.61) or (2.73) thus extends from p_0 to a maximum momentum $p_{\rm max}$ given by

$$\ln\left(p_{\rm max}\right)(t) = \ln\left(p_0\right) + \begin{cases} \frac{1}{\alpha}\ln\left(1 + \alpha\frac{t}{t_{\rm acc}\left(p_0\right)}\right) & \alpha \neq 0 \\ \frac{t}{t_{\rm acc}\left(p_0\right)} & \alpha = 0 . \end{cases} \tag{2.79}$$

Note that this is actually an upper limit on the maximum energy achievable by cosmic-rays, which will be limited by various other processes such as losses or escape.

[10]Note that the Bohm coefficient given by equation (2.29) reduces to such a power-law in the non-relativistic ($\alpha = 2$) and ultra-relativistic ($\alpha = 1$) limits.

2.3 Non-Linear Effects

All the theory presented before in section 2.2 assumes the *test-particle* regime: cosmic-rays are supposed to be passively accelerated, with no feedback on the acceleration process. However, even before linear DSA theory was fully established, Parker (1958) noted that cosmic-rays modify the medium in which they propagate, as being relativistic they tend to lower the overall adiabatic index of the flow. Wentzel (1971) and Axford et al. (1978) were the first to take into account the cosmic-rays pressure (2.3.1) in the shock dynamics in their study of the DSA process. In the 1980s the non-linear DSA theory was developed through various analytical approaches (2.3.3). From the 1990s numerical simulations have been extensively used to investigate this complex problem (2.3.4). We will only summarize the main approaches here (see the reviews of Jones and Ellison (1991) and Malkov and Drury (2001) and references therein for more details), trying to give a simple and physical understanding of the cosmic-rays feedback on the acceleration process (2.3.2).

2.3.1 Cosmic-Rays Pressure

Cosmic-rays are bound to the underlying flow through their scattering off the magnetic waves present in it. Therefore the thermal fluid can "feel" the cosmic-rays pressure, defined by

$$P_{\rm cr} = \int_p \frac{p\,v}{3}\, f(p)\, 4\pi p^2 dp = \frac{4\pi}{3} m_p c^2 \int_p \frac{p^4}{\sqrt{1+p^2}}\, f(p)\, dp \tag{2.80}$$

where the distribution function $f(p)$ is defined by equation (2.53) (and where in the right expression momenta are expressed in $m_p c$ units). As the cosmic-rays distribution is not uniform upstream (see equation (2.74)), the upstream thermal fluid undergoes a force $\mathbf{F} = -\nabla P_{\rm cr}$ induced by the cosmic-rays pressure gradient.

Lets model the interstellar medium as a non-relativistic and inviscid fluid. It is then described by the Euler equations, which simply state the conservation of the mass density ρ, momentum ρu and total energy density e:

$$\frac{\partial \rho}{\partial t} + \nabla \cdot (\rho \mathbf{u}) = 0 \tag{2.81}$$

$$\frac{\partial \rho \mathbf{u}}{\partial t} + \nabla \cdot (\rho \mathbf{u}\mathbf{u} + P\mathbf{I}) = \mathbf{0} \tag{2.82}$$

$$\frac{\partial e}{\partial t} + \nabla \cdot ((e+P)\,\mathbf{u}) = 0 \tag{2.83}$$

We recall that to close this system we need an independent relation between the fluid pressure P and the other variables. With the usual polytropic equation of state (2.2) the total energy is given by

$$e = \frac{P}{\gamma - 1} + \frac{1}{2}\rho u^2 \tag{2.84}$$

where γ is the adiabatic index of the thermal fluid (without relativistic particles). To take into account the cosmic-rays in the fluid dynamics we need to add the force $\mathbf{F}$ in the momentum equation (2.82) and its work $\mathbf{F} \cdot \mathbf{v}$ in the energy equation (2.83), so that hydrodynamical system now reads

$$\frac{\partial \rho}{\partial t} + \nabla \cdot (\rho \mathbf{u}) = 0 \tag{2.85}$$

$$\frac{\partial \rho \mathbf{u}}{\partial t} + \nabla \cdot (\rho \mathbf{u}\mathbf{u} + \mathrm{P}\mathbf{I}) = -\nabla \cdot (P_{\mathrm{cr}}\mathbf{I}) \tag{2.86}$$

$$\frac{\partial e}{\partial t} + \nabla \cdot ((e + P)\,\mathbf{u}) = -(u + v_A)\,\nabla \cdot (P_{\mathrm{cr}}\mathbf{I}) \tag{2.87}$$

Note that in equation (2.87) we use $v = u + v_A$ where u is the fluid speed and v_A is the Alfven speed (defined by equation (2.21)) as the cosmic-rays interact with the fluid through the magnetic waves, which are themselves in motion with respect to the fluid.

2.3.2 General Picture

We will now try to understand how the cosmic-rays pressure modifies the shock dynamics, and thus the acceleration process itself (see eg the simple model of Berezhko and Ellison (1999)).

2.3.2.1 Modified Shocks

The first effect of the cosmic-rays pressure gradient is to pre-accelerate the upstream fluid (as seen in the upstream rest frame). Indeed, as the cosmic-rays travel at a much higher speed (close to c) than the fluid sound speed, and as they are constantly scattered on both sides of the shock, they somehow "warn" the upstream fluid (through their pressure P_{cr}) that something is going on (a shock wave is coming). As cosmic-rays of different energies explore different distances upstream of the shock (typically proportionally to their energy, see x_1 in equation (2.74) with D given by equation (2.30)), the sharp velocity discontinuity of the shock (see figure 2.1) is progressively replaced (as cosmic-rays get accelerated) by a smooth and extended upstream velocity ramp, called the *precursor*, preceding a smaller velocity jump, called the *sub-shock* (see figure 2.5, in blue). The same picture holds for all the other hydrodynamical profiles (density, pressure, temperature).

One needs to distinguish now the sub-shock compression ratio $r_{\mathrm{sub}} = u_1/u_2$ and the overall compression ratio $r_{\mathrm{tot}} = u_0/u_2$, where u_0 is the far upstream (constant) speed, u_1 is the upstream speed just before the sub-shock, and u_2 is the (constant) downstream speed. r_{sub} is lower than the fiducial value given by equation (2.5), that is lower than 4 even for a strong (high Mach number) shock. This is due to the presence of the precursor as explained above. On the other hand r_{tot} can be much greater than 4 (which is the limit for unmodified shocks). This is due to the fact that the incoming fluid gets more compressible

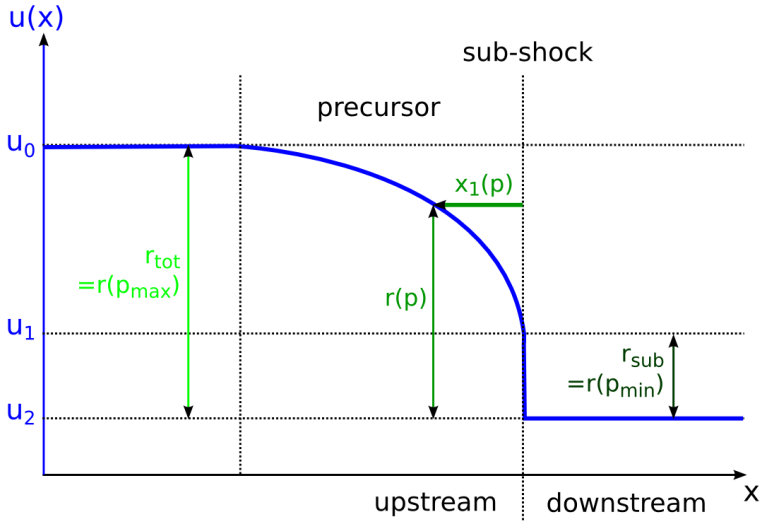

Figure 2.5: Sketch of the non-linear shock modification (in the shock frame).

as it loses energy, given to cosmic-rays that eventually escape the system (see Berezhko and Ellison 1999)[11].

2.3.2.2 Modified Spectra

As cosmic-rays modify the very structure of the shock that accelerates them, they also modify the way they are accelerated. This modifies their energy distribution, which in turns modifies the shock again, and so on. Thus because of cosmic-rays back-reaction DSA is a fully non-linear process.

Here again the key point is that cosmic-rays of increasing energy explore increasing distances upstream of the shock. Thus as seen from figure 2.5 (in green) cosmic-rays of increasing energies will "see" increasing velocity jumps. This is of primary importance as the velocity jump is the engine of the acceleration as we have seen in 2.2.3. Particles don't feel the same velocity jump given by equation (2.50): they feel an energy-dependent jump. Thus in equation (2.55) the upstream fluid speed u_1 has to be replaced by the speed of the fluid $u_{\rm cr}(p)$ at the position up to which a particle of momentum p can go. Adapting the approach of 2.2.3.1 one then finds a spectrum logarithmic slope

$$s(p) = -\frac{\partial \ln f(p)}{\partial \ln p} = \frac{3\,u_{\rm cr}(p)}{u_{\rm cr}(p) - u_2} + \frac{{\rm d}\,\ln u_{\rm cr}(p)}{{\rm d}\,\ln p} \qquad (2.88)$$

For un-modified shocks $u_{\rm cr}(p) = u_1 = u_0 = ct\ \forall p$ so that one recovers the constant slope $s_{\rm test} = 3\,u_1/(u_1 - u_2)$ of equation (2.54). For modified shocks the slope is now energy-dependent, so that the spectrum is no longer a power-law

[11] The same phenomenon ($r > 4$) occurs for radiative shocks too (also because of energy losses).

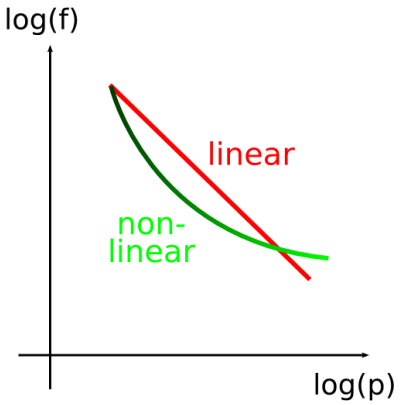

Figure 2.6: Sketch of the non-linear spectrum modification.

but gets concave, as illustrated on figure 2.6. Particles of low energy ($p \ll m_p c$) only samples the sub-shock, feeling a compression $\simeq r_{\rm sub}$ and producing a slope $s_{\rm max} \simeq 3\,u_1/(u_1 - u_2)$ larger than $s_{\rm test}$ (that is, a steeper spectrum). Particles of high energy ($p \gg m_p c$) sample the whole shock structure, feeling a compression $\simeq r_{\rm tot}$ and producing a slope $s_{\rm min} \simeq 3\,u_0/(u_0 - u_2)$ smaller than $s_{\rm test}$ (that is, a flatter spectrum). Particles of intermediate energies explore all the compressions between $r_{\rm sub}$ and $r_{\rm tot}$, producing a wide range of spectral indexes from $s_{\rm min}$ to $s_{\rm max}$.

To end this presentation of the cosmic-rays back-reaction effects we would like to note that one of the historically most attractive features of DSA was its ability to produce naturally power-law spectra. But as shown here the true spectrum, taking properly into account non-linear effects, just cannot be a perfect power-law.

2.3.3 Analytical Attempts

Finding the actual shock profile and cosmic-rays spectrum requires solving the coupled set formed by the hydrodynamical equations (2.85), (2.86), (2.87) and the kinetic equation (2.65). This is highly non-trivial and can be done only in a limited number of cases.

This problem has been first investigated in the framework of the so-called *two-fluid* model (eg Drury and Völk 1981). The idea is to replace the kinetic transport equation of the cosmic-rays (2.65) by a fluid-like equation based on their macroscopic properties, namely their pressure defined by equation (2.80) and their internal energy density defined by

$$e_{\rm cr} = \int_p K(p)\, f(p)\, 4\pi p^2 dp = 4\pi m_p c^2 \int_p \left(\sqrt{1+p^2} - 1\right)\, f(p)\, p^2 dp \qquad (2.89)$$

where $K(p) = E(p) - m_p c^2$ is the kinetic energy of a single particle of momentum p (and where in the right expression momenta are expressed in $m_p c$ units).

Taking the moments of the transport equation one gets a "hydrodynamical" equation for cosmic-rays:

$$\frac{\partial e_{\rm cr}}{\partial t} + \frac{\partial u e_{\rm cr}}{\partial x} = \frac{\partial}{\partial x}\bar{D}\frac{\partial e_{\rm cr}}{\partial x} - P_{\rm cr}\frac{\partial u}{\partial x} \tag{2.90}$$

where $\bar{D}$ is a mean diffusion coefficient, averaged over all the momenta. This greatly simplifies the problem, but a clear shortcoming of the method is the need to prescribe $\bar{D}$ (as well as the cosmic-rays "adiabatic index" $\gamma_{\rm cr}$ relating $P_{\rm cr}$ and $e_{\rm cr}$): this is rather delicate as many features of non-linear DSA rely precisely on the fact that particles of different energies experience different situations.

The two-fluid approach allows to study the shock structure, but of course not directly the cosmic-rays spectrum. For that matter Drury et al. (1982) used the kinetic description, finding a complete analytical solution only in the very special case where the flow velocities and particles diffusion coefficient are related by

$$D\frac{\partial u}{\partial x} = \beta\,(u - u_1)\,(u - u_2) \tag{2.91}$$

where β is a constant. Again this requires that D is independent of p. Malkov and Drury (2001) presented a solution for a p-dependent D, but it's only an asymptotic solution in the strongly non-linear case. Blandford (1980) used a different approach, regarding the cosmic-rays back-reaction as a small perturbation and expanding the shock profile and particles spectrum in powers of the ratio $P_{\rm cr}/\rho u$. This presents the obvious limitation of only working when the shock is an inefficient accelerator – which is probably rarely the case. Using the method of *integral equations*, Malkov (1997a, 1997b) has been able to find approximate non-linear solutions in more general cases.

In his study of the injection mechanism Eichler (1979) introduced the idea of considering the speed of the fluid as a function of the cosmic-rays momentum (as $u_{\rm cr}(p)$ in 2.3.2.2). This allows to catch the non-linear modifications well when D is a growing function of p (as expected). The same approach has recently allowed Blasi (2002) to develop a tractable semi-analytical model of non-linear DSA. His first model was exact for $D(p) \propto p$, it has been extended by Amato and Blasi (2005) to arbitrary $D(x, p)$.

2.3.4 Numerical Simulations

As the full non-linear DSA problem is mathematically almost intractable, numerical simulations have been extensively used to investigate it (see eg the short review of Jones (2001)). As for theoretical approaches the numerical approaches can be divided into two conceptual groups: one kind follows individual particles, the other works directly with the particles distribution.

Particle methods generally make no formal distinction between thermal and supra-thermal populations. The most exact ones are hybrid plasma simulations, in which the equations of motion of the ions are solved explicitly

in a defined electromagnetic field (the electrons, whose individual motions are much quicker, are treated as a light charged fluid). This simulation are computationally very expensive, so that they are limited to short space- and time-scales: they are impractical to study the acceleration of cosmic-rays at entire SNRs shocks and up to the maximum energies. However *particle-in-cell* (PIC) codes have gained more interest lately (see eg Dieckmann et al. (2000)). Another kind of particle method has been developed by Ellison and Eichler (1984), namely Monte-Carlo simulations. In this approach a scaterring law is prescribed for ions (again electrons are difficult to track at low energies – but they behave just like ions once they reach their energies), and a large set of numerical experiments for individual particles is conducted, until one can establish the statistical properties of the cosmic-rays. This greatly speeds up the calculations over full plasma simulations. However this method is still quite expensive if one wants to investigate time-dependent and non-linear situations.

The alternative methods work with the cosmic-rays distribution function $f(p)$ as defined by equation (2.53). In that case one generally separates the thermal population, supposed to behave like a fluid (that is described by equations (2.85), (2.86), (2.87)), and the supra-thermal population, supposed to have a diffusive propagation (that is described by the Fokker-Planck equation (2.65) or equivalents). This approach has been implemented both within the simplified two-fluid model (eg Kang and Jones (1990) and Jones and Kang (1990)) and using the full kinetic description (eg Bell (1987), Falle and Giddings (1987), Kang and Jones (1991)). The later is much more precise but also much more computationally expensive, first because one deals with two dimensions (space and momentum), secondly because one has to resolve a huge range of space- and time-scales induced by the momentum-dependent diffusion coefficient. This is the reason why the first simulations of this kind were limited to low dependence of D on p and/or to low maximum energies. This limitations have been progressively removed through the use of various techniques: change of variable adapted to the diffusion coefficient (Berezhko et al. 1994), adaptive mesh refinement (Duffy 1992, Kang et al. 2001), finite-volumes momentum grid (Jun and Jones 1999). We will discuss all this problems in more details in part II, devoted to numerical simulations, where we present our own code based on this kinetic approach.

To end this short review we note that the cosmic-rays diffusion-convection equation is formally equivalent to a stochastic differential equation (SDE). Kruells and Achterberg (1994) and Marcowith and Kirk (1999) have shown that it allows to solve the kinetic equation through a Monte-Carlo method. At the moment this approach is probably the only one to be really tractable in 2D and 3D. However it doesn't seem to be very efficient for the study of non-linear acceleration (because of the high statistics required to reconstruct the cosmic-rays pressure everywhere at every time).

2.4 Injection

The key assumption of the theory of DSA presented in section 2.2 is that accelerated particles diffuse in space (at a macroscopic level) or have isotropically distributed velocities (at a microscopic level). To be more precise, all the work of 2.2.3 is valid for particles having a speed v such that $V/v \ll 1$ where V is the plasma speed (given by equation (2.50)). That is, the theory presented before only applies to particles of sufficient energy. However, these accelerated particles are thought to come from the thermal flow itself (and thus have initially a speed of typically V). Studies of the Earth bow shock and Monte-Carlo simulations have indeed shown that shock acceleration doesn't need seed particles[12]: cosmic-rays are nothing but interstellar material swept-up by shock waves[13] (which is consistent with their observed composition presented in section 1.2.2). Actually micro-physics studies of collisionless shock waves suggest that the acceleration of some of the incident particles is a natural and unavoidable part of the shock formation process itself. The problem is then to explain how some particles of the thermal pool get energized enough so that they obey to the DSA process. The mechanism feeding the accelerator from the flow is referred to as the *injection* process. This is a difficult and not yet solved problem. We won't go into much details here (see Jones and Ellison (1991) and Malkov and Drury (2001) for more): our goal is simply to get the basic ideas required to design the numerical simulations presented in part II.

2.4.1 Theory

The basic idea under the injection process is that some of the particles incident on the shock, after crossing downstream and getting heated, can cross the shock backwards to the downstream medium. The resulting beam excites waves that scatter the particles. The initial physical ingredients are thus the same as in DSA, but these middly suprathermal particles have an anisotropic distribution so that a more refined treatment of the transport is required. This problem has been recently addressed by Malkov and collaborators (see Malkov and Völk (1995) and Malkov (1998)). His model, known as the *thermal leakage* model, allows to fill the (artificial) gap between the flow and the cosmic-rays, providing a smooth connection between the downstream Maxwellian distribution (which is believed to form even if the shock is collisionless) and the highly energetic particles power-law distribution (which is handled by the DSA formalism).

Note that one of the parameters that control the injection mechanism is probably the magnetic field orientation at the shock (see section 2.1.1.1). The thermal leakage mechanism described above is supposed to be at work at quasi-parallel shocks. It is yet uncertain whether injection is more or less efficient

[12]But clearly pre-existing energetic particles will also automatically enter the acceleration process, as we shall see in chapters 3 and 8.

[13]Note that for cosmic-ray modified shocks (as presented in 2.5.2.1) what we call here the *shock* is the velocity discontinuity, that is the *sub*-shock.

at quasi-perpendicular shocks.

To end this very brief review of the theoretical efforts for a better understanding of injection, we would like to note that the recent developments mostly explain injection of protons. Electrons require specific injection mechanisms, as there gyration radii are roughly two orders of magnitude lower than the gyration radii of the protons (and of the wavelength of the waves the protons trigger). Energizing electrons so that they can enter the DSA process, although feasible, is far less obvious than for protons. This is really an embarrassing situation, as only accelerated electrons have been firmly identified at SNRs shocks (see section 2.5). Evidence of accelerated protons is still rare, although we firmly believe that they are efficiently accelerated at SNRs shocks (but as is well known electrons have a much higher radiative efficiency than protons).

2.4.2 Parametrization

Although DSA, as described in sections 2.2 and 2.3, only works for particles of energy already higher than the typical energy of the particles in the thermal flow, one doesn't necessarily always need a precise description of the injection process to study shock acceleration. A convenient and frequent approach (the one we develop in part II) is to consider separately the fluid and the cosmic-rays and to simply parametrize injection from the former to the latter[14].

The simplest way to do it is to postulate that some fraction η of the particles crossing the shock become cosmic-rays at some momentum $p_{\rm inj}$ (see eg Falle and Giddings (1987) and Kang and Jones (1991)). The injection momentum can be fixed to some value above the thermal one, or defined by

$$p_{\rm inj} = \xi \, p_{\rm th,2} \tag{2.92}$$

where $p_{\rm th,2} = \sqrt{2\, m_p \, k_B \, T_2}$ is the mean downstream momentum of the thermal flow (or alternatively by $v_{\rm inj} = \xi' \, c_{s,2}$ where $c_{s,2} = \sqrt{\gamma \, k_B \, T_2 / m_p}$ is the downstream sound speed). ξ is expected to be in the range $2 - 4$, as cosmic-rays must have a gyration radius high enough so that they can cross the shock and see it as a velocity discontinuity ($\xi'/\xi = \sqrt{2/\gamma} \simeq 1.1$ for $\gamma = 5/3$).

More recently Gieseler et al. (2000) have adapted Malkov's *thermal leakage* model presented in 2.4.1 to get a self-consistent[15] injection prescription in their numerical simulations. Technically they introduce a "transparency function" which connects the thermal and supra-thermal distributions. They have then only one remaining parameter, namely the "wave amplitude" ϵ, which is rather well constrained (at least for strong shocks).

[14] Monte-Carlo simulations however can treat the thermal and non-thermal particles consistently.

[15] Note that this type of injection is actually rather "self-adjusted" than "self-consistent", as it responds to the shock modifications, but still relies on a free parameter.

Using the same *thermal leakage* approach Blasi et al. (2005) have proposed a simpler recipe for self-consistent[15] injection. For a given value of ξ (so that $p_{\rm inj}$ is given by equation (2.92)) they compute the injection rate as

$$\eta(\xi) = \frac{4}{3\sqrt{\pi}} \, (r-1) \, \xi^3 \exp\left(-\xi^2\right) \tag{2.93}$$

where r is the shock compression ratio. There is also only one remaining parameter, ξ, which is also well constrained (but we note that η has a strong dependence on it[16]). Note that as η is a function of r it is also a function of time in the case of modified shocks (see section 2.3): the $r-1$ factor acts as an injection regulator when the shock gets smoothed by cosmic-rays back-reaction.

2.5 Observational Support

To end this chapter we will discuss the various observational evidence supporting the DSA scenario (see the reviews of Drury et al. (2001), Ballet (2004), Marcowith (2007a) and references therein). We will make use of all the information provided by multi-wavelength studies (as shown for Cas A on figure 2.7). We will give particular attention to non-linear effects.

2.5.1 Particle Acceleration

In this sub-section we will summarize the SNRs observations in each wavelength domain, showing clear evidence for particle acceleration. We summarize in table 2.1 the main relevant parameters for six young SNRs, including the four well known historical SNs. Detailed broad-band emission models have been developed in the last decade. Most of them use a simplified prescription for particle acceleration, which however accounts now for cosmic-rays feedback (Baring et al. 1999, Ellison et al. 2000, Ellison and Cassam-Chenaï 2005, Ellison et al. 2007). Others try to couple explicitly the shock hydrodynamics and particle diffusion, which is more precise but more expensive (eg Berezhko et al. 2002).

Note that cosmic-rays are also expected to produce a neutrino emission (collisions between cosmic-rays protons and interstellar protons produce charged pions which decay in neutrinos and anti-neutrinos), but the expected fluxes are very low and only marginally detectable by experiments such as ANTARES or even the planned Km3NeT (Kappes et al. 2007).

[16] See the discussion of simulations results in sections 6.3.2.2 and 8.2.3.2.

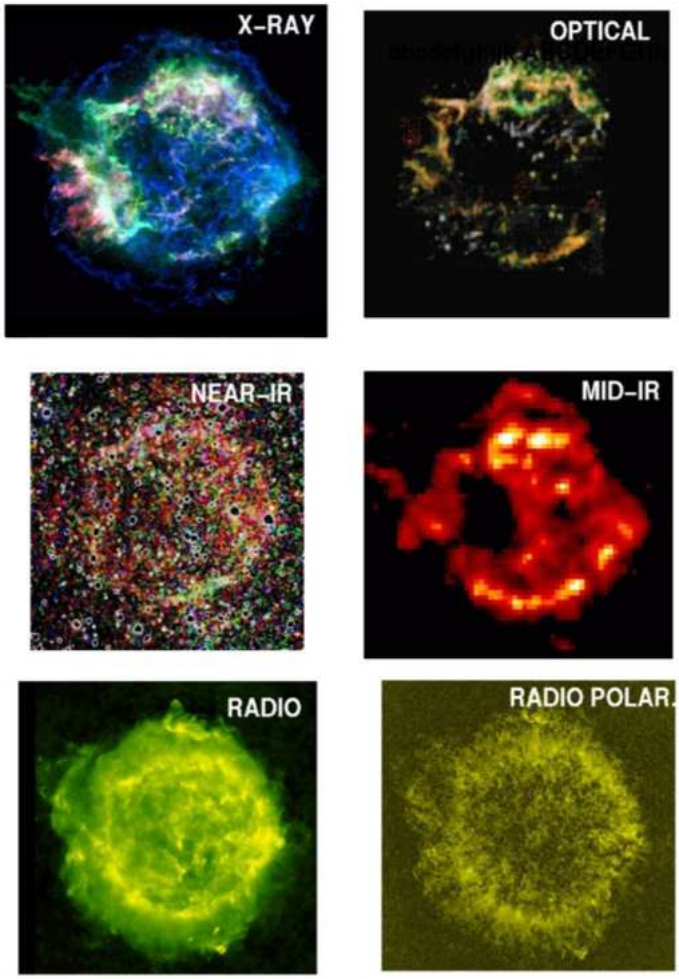

Figure 2.7: Multi-wavelength observations of the SNR Cassiopae A. X-rays (Chandra): Fe (red) and S (green) lines, 4-6 keV continuum (blue) – optical (HST) – infrared (2Mass and ISO) – radio (VLA): 6 cm emission and polarization (from Rudnick 2001)

2.5.1.1 Radio Emission

The radio emission of SNRs is entirely due to the synchrotron emission of accelerated electrons. An electron of energy E radiates around frequency

$$\nu_{\rm sync} = 1.6\,{\rm MHz}\,\left(\frac{E}{1\,{\rm GeV}}\right)^2\left(\frac{B}{1\,\mu{\rm G}}\right)\,\sin\theta \tag{2.94}$$

where θ is the pitch-angle. In standard interstellar magnetic fields of a few μG, the radio emission observed around 1 GHz is due to electrons of a few GeV.

A power-law distribution of the electrons $N(E) \propto E^{-s}$ yields a power-law

name	d	t	v_s	α	ν_c	γ
Cassiopae A	3.4 kpc	321 yr ?	5200 km/s	0.77	1.2 keV	yes ?
Kepler	4.8 kpc	401 yr	5400 km/s	0.64	0.9 keV	-
Tycho	2.3 kpc	431 yr	4600 km/s	0.61	0.3 keV	-
SN 1006	2.2 kpc	1001 yr	3000 km/s	0.60	3.0 keV	yes ?
G347.3-0.5	1.3 kpc	1621 yr ?	4000 km/s	-	2.6 keV	-
RCW86	2.8 kpc	1823 yr ?	1700 km/s	0.60	0.9 keV	yes

Table 2.1: Summary of the observations of six young SNRs (which all exhibit X-rays filaments).
The first three parameters describe the SNR itself: distance d, age t, shock speed v_s. The other three parameters describe the emission induced by accelerated particles: radio spectral index α, X-rays synchrotron cut-off ν_c, γ-rays detection. (compiled by Marcowith 2007a)

synchrotron spectrum

$$F_{\rm sync} \propto \nu^{-\alpha} \quad \text{with} \quad \alpha = \frac{s-1}{2} \leftrightarrow s = 2\,\alpha + 1\,. \tag{2.95}$$

We indeed observe this power-law emission, with spectral slopes α ranging from 0.4 to 0.7 – with variations both from place to place within one SNR and from one SNR to another (see table 2.1) – corresponding to cosmic-rays slopes s from 1.8 to 2.4, in general agreement with the predictions of DSA ($s = 2.0$ for a single linear shock).

Moreover emission is clearly limb-brightened, which shows that high-energy electrons are produced around the shock front. Thus radio observations provide the most obvious sign that particle acceleration is indeed going on at SNRs shocks.

Note also that polarization is detected at a much lower level (5%) than the theoretical level in an ordered magnetic field (70%): this gives evidence that the magnetic field is highly turbulent, as required for the DSA mechanism to work (to scatter particles).

2.5.1.2 Optical And Ultraviolet Emission

SNR emission in the optical domain and around is largely dominated by thermal emission. Observations thus don't give direct information on cosmic-ray acceleration, however they provide useful diagnostics of the shock structure and evolution, and thus can help indirectly to constrain how DSA is working.

In the early (non-radiative) phases of SNR evolution (see section 2.1.1.3), faint Balmer lines [Hα], [Hβ] are emitted at the blast wave (Chevalier and Raymond 1978). They are produced through collisional excitation of neutral particles. As neutral atoms don't "see" the shock (as the "collision" is actually made through collective electromagnetic effects) they are still cold downstream

and thus give rise to narrow lines. However some neutrals are heated through charge exchange with the hot protons, and thus give rise to broad lines. Thus the width of the narrow and broad components gives directly respectively the pre-shock and post-shock protons kinetic temperature. The ratio of the flux between the two components also depends on the electron temperature (and other parameters such as the shock velocity). It is found, as expected, that electrons are not in equilibrium with protons downstream of the shock (they have a lower temperature) – all the more so since the shock speed is high.

Forbidden lines such as [OII], [OIII], [NII], [SII] are emitted at the shock wave at later (radiative) SNR stages. They are not of direct use for the study of cosmic-ray acceleration – but for the fact that they mark the presence of shocks. However these lines are observed in the early phases too, from the ejecta within the remnant, revealing *fast moving knots* that might result from the interaction with energetic particles accelerated at the shock front and propagating towards the SNR interior (Bykov 2002).

2.5.1.3 X Emission

Most of the X-ray emission of SNRs is thermal, due to the shock heated gas (at a temperature of several million degrees). It is dominated by atomic lines of heavy elements (from O to Fe) and is particularly strong in young SNRs (because of metal-rich ejecta). Again this is not directly related to particle acceleration but provides powerful diagnostics of the shock (thanks to the high performances of the new generation of satellite telescopes such as XMM-Newton and Chandra): spectroscopy gives the electron temperature and imagery gives the waves geometry (on the top left image of figure 2.7 one clearly distinguishes the ejecta frontier from the forward shock).

Above the thermal emission, a non-thermal tail is observed in many SNRs just behind the forward shock[17] (up to above 1 keV, see table 2.1). This is commonly interpreted as the tail of the synchrotron emission seen in radio, produced by electrons of energies from 10 to 100 TeV (such suprathermal electrons may also produce a bremsstrahlung emission provided the nuclei density is high enough). This high-energy observations thus confirm particle acceleration, but puts the ability of SNRs to produce cosmic-rays up to the knee (a few PeV) into question.

2.5.1.4 Gamma Emission

High-energy electrons emitting synchrotron X-rays also emit γ-rays by inverse Compton scattering on the photon field (dominated, in most cases, by the cosmic microwave background). When both the X-rays and γ-rays emission are observed, their ratio provides an estimate of the total magnetic field within

[17]Note that a distinct X-ray emission is also observed at the interface between the ejecta and the shocked ISM. Its nature is still uncertain, it could involve particle acceleration by fast ejecta at the contact discontinuity.

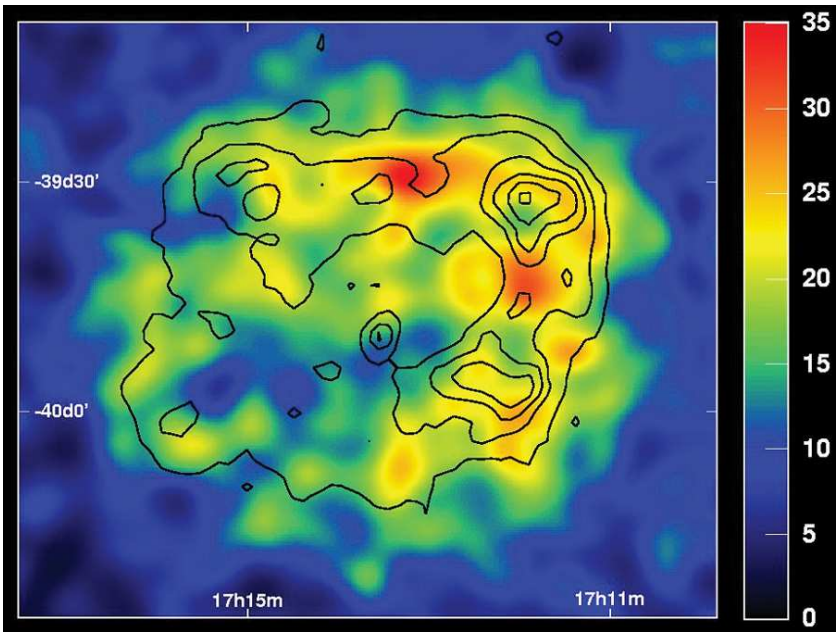

Figure 2.8: TeV map of the SNR RXJ1713.7-3946 obtained with HESS. Black countours show X-ray emission (1-3 keV) obtained with ASCA. (from Aharonian et al. (2004))

the SNR. Cosmic-rays protons may also radiate in γ-rays, as collisions with the interstellar protons produce neutral pions π^0 which decay into two γ rays. This emission starts at 70 MeV and presents a distinctive bump around 1 GeV. It will dominate over inverse Compton emission by electrons when the ISM density is high enough.

γ-rays detection of SNRs has long been awaited, as a clear detection of pionisation emission would give unambiguous proof of accelerated nuclei in SNRs (see eg Drury et al. (1994) and Berezhko and Völk (2000)). The development of ground-based TeV detectors in the last few years has finally opened this new window on cosmic-rays observations at SNRs shocks. After a few γ-rays *detections*, the HESS experiment has recently produced the first γ-rays *images* of SNRs (RXJ1713.7-3946, shown on figure 2.8, and RXJ0852.0-4622, known as Vela Junior)[18]. However it is still uncertain whether the emission is of leptonic or hadronic origin (or both): more observations are required, including at intermediate energies (around the GeV)[19].

[18]Note that RXJ1713.7-3946 had already been detected by CANGAROO, but that HESS doesn't confirm the detection of SN 1006 by CANGAROO.

[19]New experiments such as GLAST and HESS 2 will help filling the current gap between the MeV and TeV ranges.

2.5.2 Non-Linear Effects

We will now show more specifically how the observations can probe the non-linear modifications presented in section 2.3. Although there are no firm proofs yet, evidence is growing in favor of efficient particle acceleration at SNR shocks – so that one must take cosmic-rays feedback into account in the modelling of SNRs evolution and emission.

2.5.2.1 Modified Shocks

A distinctive feature of non-linear acceleration is the presence of an extended precursor upstream of the shock. The radio images, though, are sharp edged, with no evidence of such a precursor[20]. In the optical domain the [Hα] narrow lines (see section 2.5.1.2) seem too wide with respect to the ambient ISM temperature, which suggests that the flow is indeed pre-accelerated before the shock. However the Doppler shift of the lines then expected is not observed. In the X-rays domain the situation is unclear. Thus there is no convincing evidence of a precursor yet.

As emphasized by Decourchelle et al. (2000) another important feature of modified shocks is the lower downstream temperature (as a part of the energy of the incoming flow is channelled into cosmic-rays). For unmodified shocks the jump relations (see section 2.1.1.2) imply the following relation between the mean post-shock temperature T_2 and the shock speed v_s:

$$T_2 = \frac{3}{16}\frac{\bar{m}}{k_B}\, v_s^2 \tag{2.96}$$

(where $\bar{m}$ is the mean particle mass accounting for the nuclei composition). As we have seen in section 2.5.1.3 X-rays observations provide both the shock velocity and the downstream electron temperature. Thanks to Chandra observations Hughes et al. (2000) have obtained a downstream temperature in 1E 0102.2-7219 almost 25 times lower than given by equation (2.96). However as we have seen in section 2.5.1.2 the electrons are most likely not in equilibrium with the protons (which dominate the shock dynamics), which complicates the computation of the actual proportion of energy gone in accelerated particles.

As noted by Decourchelle et al. (2000) the different repartition of the upstream energy induced by efficient acceleration also alters the waves geometry: the distance between the contact discontinuity and the forward shock gets smaller as the shock gets modified. Thanks again to precise Chandra observations Warren et al. (2005) have shown that Tycho's remnant morphology can't be explained by purely hydrodynamical model, giving evidence of efficient ion acceleration.

[20]Note that this puts an upper limit on the diffusion coefficient of electrons radiating at these energies (around 1 GHz), that is a lower limit on the turbulent magnetic field. This suggests high magnetic field amplification (see section 2.1.2.3).

2.5.2.2 Modified Spectra

Regarding cosmic-rays themselves, the main feature of non-linear acceleration is the concavity of their spectrum.

Observed radio indexes α larger than 0.5 (see section 2.5.1.1) imply cosmic-rays slopes s larger than 2 at low energies. Reynolds and Ellison (1992) have shown that this can naturally be explained by their non-linear acceleration model in the case of Tycho and Kepler remnants (note that such a hard slope can also be produced by linear acceleration at a weak shock ($r < 4$), but this is excluded in these two young SNRs). Radio indexes below 0.5, also observed, could be due to shock compression ratios above 4 (because of energy losses, due either to efficient thermal radiation or to efficient particle acceleration) or simply to confusion with thermal radio emission.

To get a clearer answer one needs to determine the cosmic-rays spectrum slope on a broader range in energy. Jones et al. (2003) have been able for the first time to distinguish the synchrotron emission of a SNR (Cas A) in the infrared domain (at a few μm), where the thermal component (due to dust) dominates. They obtain an index 8% lower in the [6 cm - 2 μm] range than in the [20 cm - 6 cm] range, which is compatible with the curvature produced by shock modification. Combining radio data from MOST and X data from Chandra, Allen et al. (2006) have obtained the same result in SN 1006: the electron spectrum seems to flatten with increasing energy. At 1 GeV (radio-emitting momenta) the power-law index is about 2.2, at 10 TeV (X-ray-emitting momenta) the index is about 2.0. This result is qualitatively consistent with expectations of non-linear DSA, and thus implies that cosmic-rays are dynamically important instead of being *test-particles*.

References

Achterberg, A. (1998). Cosmic Ray Physics - Sources of energetic particles in the universe. Nova Autumn School.

Achterberg, A., Blandford, R. D., and Reynolds, S. P. (1994). Evidence for enhanced MHD turbulence outside sharp-rimmed supernova remnants. A&A, 281:220–230.

Aharonian, F. A., Akhperjanian, A. G., Aye, K.-M., Bazer-Bachi, A. R., Beilicke, M., Benbow, W., Berge, D., Berghaus, P., Bernlöhr, K., Bolz, O., Boisson, C., Borgmeier, C., Breitling, F., Brown, A. M., Bussons Gordo, J., Chadwick, P. M., Chitnis, V. R., Chounet, L.-M., Cornils, R., Costamante, L., Degrange, B., Djannati-Ataï, A., Drury, L. O., Ergin, T., Espigat, P., Feinstein, F., Fleury, P., Fontaine, G., Funk, S., Gallant, Y. A., Giebels, B., Gillessen, S., Goret, P., Guy, J., Hadjichristidis, C., Hauser, M., Heinzelmann, G., Henri, G., Hermann, G., Hinton, J. A., Hofmann, W., Holleran, M., Horns, D., de Jager, O. C., Jung, I., Khélifi, B., Komin, N., Konopelko,

A., Latham, I. J., Le Gallou, R., Lemoine, M., Lemière, A., Leroy, N., Lohse, T., Marcowith, A., Masterson, C., McComb, T. J. L., de Naurois, M., Nolan, S. J., Noutsos, A., Orford, K. J., Osborne, J. L., Ouchrif, M., Panter, M., Pelletier, G., Pita, S., Pohl, M., Pühlhofer, G., Punch, M., Raubenheimer, B. C., Raue, M., Raux, J., Rayner, S. M., Redondo, I., Reimer, A., Reimer, O., Ripken, J., Rivoal, M., Rob, L., Rolland, L., Rowell, G., Sahakian, V., Saugé, L., Schlenker, S., Schlickeiser, R., Schuster, C., Schwanke, U., Siewert, M., Sol, H., Steenkamp, R., Stegmann, C., Tavernet, J.-P., Théoret, C. G., Tluczykont, M., van der Walt, D. J., Vasileiadis, G., Vincent, P., Visser, B., Völk, H. J., and Wagner, S. J. (2004). High-energy particle acceleration in the shell of a supernova remnant. *Nature*, 432:75–77.

Allen, G. E., Houck, J. C., and Sturner, S. J. (2006). Evidence of a Curved Cosmic-Ray Electron Spectrum in the Supernova Remnant SN 1006. In *Bulletin of the American Astronomical Society*, volume 38 of *Bulletin of the American Astronomical Society*, page 330.

Amato, E. and Blasi, P. (2005). A general solution to non-linear particle acceleration at non-relativistic shock waves. MNRAS, 364:L76–L80.

Amato, E. and Blasi, P. (2006). Non-linear particle acceleration at non-relativistic shock waves in the presence of self-generated turbulence. MNRAS, 371:1251–1258.

Axford, W. I., Leer, E., and Skadron, G. (1978). The acceleration of cosmic rays by shock waves. In *International Cosmic Ray Conference*, pages 132–137.

Ballet, J. (2004). Cosmic-ray acceleration in supernova remnants. In Parizot, E., Marcowith, A., Tatischeff, V., Pelletier, G., and Salati, P., editors, *Physique et astrophysique du rayonnement cosmique (Ecole CNRS de Goutelas XXVI)*, pages 1–6.

Baring, M. G., Ellison, D. C., Reynolds, S. P., Grenier, I. A., and Goret, P. (1999). Radio to Gamma-Ray Emission from Shell-Type Supernova Remnants: Predictions from Nonlinear Shock Acceleration Models. ApJ, 513:311–338.

Bell, A. R. (1978a). The acceleration of cosmic rays in shock fronts. I. MNRAS, 182:147–156.

Bell, A. R. (1978b). The acceleration of cosmic rays in shock fronts. II. MNRAS, 182:443–455.

Bell, A. R. (1987). The non-linear self-regulation of cosmic ray acceleration at shocks. MNRAS, 225:615–626.

Bell, A. R. (2004). Turbulent amplification of magnetic field and diffusive shock acceleration of cosmic rays. MNRAS, 353:550–558.

Bell, A. R. and Lucek, S. G. (2001). Cosmic ray acceleration to very high energy through the non-linear amplification by cosmic rays of the seed magnetic field. MNRAS, 321:433–438.

Berezhko, E. G. and Ellison, D. C. (1999). A Simple Model of Nonlinear Diffusive Shock Acceleration. ApJ, 526:385–399.

Berezhko, E. G., Ksenofontov, L. T., and Völk, H. J. (2002). Emission of SN 1006 produced by accelerated cosmic rays. A&A, 395:943–953.

Berezhko, E. G. and Völk, H. J. (2000). Kinetic theory of cosmic ray and gamma-ray production in supernova remnants expanding into wind bubbles. A&A, 357:283–300.

Berezhko, E. G., Yelshin, V. K., and Ksenofontov, L. T. (1994). Numerical investigation of cosmic ray acceleration in supernova remnants. *Astroparticle Physics*, 2(2):215–227.

Blandford, R. D. (1980). On the mediation of a shock front by Fermi-accelerated cosmic rays. ApJ, 238:410–416.

Blandford, R. D. and Ostriker, J. P. (1978). Particle acceleration by astrophysical shocks. ApJ, 221:L29–L32.

Blasi, P. (2002). A semi-analytical approach to non-linear shock acceleration. *Astroparticle Physics*, 16:429–439.

Blasi, P., Amato, E., and Caprioli, D. (2007). The maximum momentum of particles accelerated at cosmic ray modified shocks. MNRAS, 375:1471–1478.

Blasi, P., Gabici, S., and Vannoni, G. (2005). On the role of injection in kinetic approaches to non-linear particle acceleration at non-relativistic shock waves. MNRAS, 361:907–918.

Bykov, A. M. (2002). X-ray line emission from supernova ejecta fragments. A&A, 390:327–335.

Chevalier, R. A. (1977). The interaction of supernovae with the interstellar medium. ARA&A, 15:175–196.

Chevalier, R. A. and Raymond, J. C. (1978). Optical emission from a fast shock wave - The remnants of Tycho's supernova and SN 1006. ApJ, 225:L27–L30.

Decourchelle, A., Ellison, D. C., and Ballet, J. (2000). Thermal X-Ray Emission and Cosmic-Ray Production in Young Supernova Remnants. ApJ, 543:L57–L60.

Dieckmann, M. E., Chapman, S. C., McClements, K. G., Dendy, R. O., and Drury, L. O. (2000). Electron acceleration due to high frequency instabilities at supernova remnant shocks. A&A, 356:377–388.

Drury, L. O. (1983). An Introduction To The Theory Of Diffusive Shock Acceleration Of Energetic Particles In Tenuous Plasmas. *Reports on Progress in Physics*, 46(8):973–1027.

Drury, L. O., Aharonian, F. A., and Völk, H. J. (1994). The gamma-ray visibility of supernova remnants. A test of cosmic ray origin. A&A, 287:959–971.

Drury, L. O., Axford, W. I., and Summers, D. (1982). Particle acceleration in modified shocks. MNRAS, 198:833–841.

Drury, L. O., Ellison, D. E., Aharonian, F. A., Berezhko, E., Bykov, A., Decourchelle, A., Diehl, R., Meynet, G., Parizot, E., Raymond, J., Reynolds, S., and Spangler, S. (2001). Test of galactic cosmic-ray source models - Working Group Report. *Space Science Reviews*, 99:329–352.

Drury, L. O. and Völk, J. H. (1981). Hydromagnetic shock structure in the presence of cosmic rays. ApJ, 248:344–351.

Duffy, P. (1992). The self-consistent acceleration of cosmic rays in modified shocks with Bohm-type diffusion. A&A, 262:281–294.

Eichler, D. (1979). Particle acceleration in collisionless shocks - Regulated injection and high efficiency. ApJ, 229:419–423.

Ellison, D. C., Berezhko, E. G., and Baring, M. G. (2000). Nonlinear Shock Acceleration and Photon Emission in Supernova Remnants. ApJ, 540:292–307.

Ellison, D. C. and Cassam-Chenaï, G. (2005). Radio and X-Ray Profiles in Supernova Remnants Undergoing Efficient Cosmic-Ray Production. ApJ, 632:920–931.

Ellison, D. C. and Eichler, D. (1984). Monte Carlo shock-like solutions to the Boltzmann equation with collective scattering. ApJ, 286:691–701.

Ellison, D. C., Moebius, E., and Paschmann, G. (1990). Particle injection and acceleration at earth's bow shock - Comparison of upstream and downstream events. ApJ, 352:376–394.

Ellison, D. C., Patnaude, D. J., Slane, P., Blasi, P., and Gabici, S. (2007). Particle Acceleration in Supernova Remnants and the Production of Thermal and Nonthermal Radiation. ApJ, 661:879–891.

Ellison, D. C. and Vladimirov, A. (2008). Magnetic Field Amplification and Rapid Time Variations in SNR RX J1713.7-3946. ApJ, 673:L47–L50.

Falle, S. A. E. G. and Giddings, J. R. (1987). Time-dependent cosmic ray modified shocks. MNRAS, 225:399–423.

Fermi, E. (1949). On the Origin of the Cosmic Radiation. *Physical Review*, 75(8):1169–1174.

Fermi, E. (1954). Galactic Magnetic Fields and the Origin of Cosmic Radiation. ApJ, 119:1–6.

Gieseler, U. D. J., Jones, T. W., and Kang, H. (2000). Time dependent cosmic-ray shock acceleration with self-consistent injection. A&A, 364:911–922.

Hughes, J. P., Rakowski, C. E., and Decourchelle, A. (2000). Electron Heating and Cosmic Rays at a Supernova Shock from Chandra X-Ray Observations of 1E 0102.2-7219. ApJ, 543:L61–L65.

Jones, F. C. and Ellison, D. C. (1991). The plasma physics of shock acceleration. *Space Science Reviews*, 58:259–346.

Jones, T. J., Rudnick, L., DeLaney, T., and Bowden, J. (2003). The Identification of Infrared Synchrotron Radiation from Cassiopeia A. ApJ, 587:227–234.

Jones, T. W. (1994). Time-dependent simulation of cosmic-ray shocks, including Alfven transport. ApJS, 90:969–973.

Jones, T. W. (2001). Numerical Simulation of Cosmic-Ray Acceleration. *Journal of Korean Astronomical Society*, 34:231–235.

Jones, T. W. and Kang, H. (1990). Time-dependent evolution of cosmic-ray-mediated shocks in the two-fluid model. ApJ, 363:499–514.

Jones, T. W. and Kang, H. (2006). Time Evolution of Cosmic-Ray Modified MHD Shocks. *Cosmic Particle Acceleration, 26th meeting of the IAU, Joint Discussion 1, 16-17 August, 2006, Prague, Czech Republic, JD01, #41*, 1.

Jun, B.-I. and Jones, T. W. (1999). Radio Emission from a Young Supernova Remnant Interacting with an Interstellar Cloud: Magnetohydrodynamic Simulation with Relativistic Electrons. ApJ, 511:774–791.

Kang, H. and Jones, T. W. (1990). Diffusive cosmic-ray acceleration - Two-fluid models with in situ injection. ApJ, 353:149–158.

Kang, H. and Jones, T. W. (1991). Numerical studies of diffusive particle acceleration in supernova remnants. MNRAS, 249:439–451.

Kang, H., Jones, T. W., LeVeque, R. J., and Shyue, K. M. (2001). Time Evolution of Cosmic-Ray Modified Plane Shocks. ApJ, 550:737–751.

Kappes, A., Hinton, J., Stegmann, C., and Aharonian, F. A. (2007). Potential Neutrino Signals from Galactic Gamma-Ray Sources. ApJ, 656:870–878.

Kirk, J. G. (1994). Particle Acceleration. In *Saas-Fee Advanced Course 24*, page 225.

Kruells, W. M. and Achterberg, A. (1994). Computation of cosmic-ray acceleration by Ito's stochastic differential equations. A&A, 286:314–327.

Krymskii, G. F. (1977). A regular mechanism for the acceleration of charged particles on the front of a shock wave. *Akademiia Nauk SSSR Doklady*, 234:1306–1308.

Lagage, P. O. and Cesarsky, C. J. (1983). The maximum energy of cosmic rays accelerated by supernova shocks. A&A, 125:249–257.

Lucek, S. G. and Bell, A. R. (2000). Non-linear amplification of a magnetic field driven by cosmic ray streaming. MNRAS, 314:65–74.

Malkov, M. A. (1997a). Analytic Solution for Nonlinear Shock Acceleration in the Bohm Limit. ApJ, 485:638–654.

Malkov, M. A. (1997b). Bifurcation, Efficiency, and the Role of Injection in Shock Acceleration with the Bohm Diffusion. ApJ, 491:584–595.

Malkov, M. A. (1998). Ion leakage from quasiparallel collisionless shocks: Implications for injection and shock dissipation. Phys. Rev. E, 58:4911–4928.

Malkov, M. A. and Drury, L. O. (2001). Nonlinear theory of diffusive acceleration of particles by shock waves. *Reports on Progress in Physics*, 64(4):429.

Malkov, M. A. and Völk, H. J. (1995). Theory of ion injection at shocks. A&A, 300:605–626.

Marcowith, A. (2007a). Les supernovae comme sources des rayons cosmiques I. Les supernovae isolées [brouillon]. Ecole de Gif sur les rayons cosmiques de haute énergie.

Marcowith, A. and Kirk, J. G. (1999). Computation of diffusive shock acceleration using stochastic differential equations. A&A, 347:391–400.

Parizot, E. (2004). Accélération des particules : les mécanismes de Fermi. In Parizot, E., Marcowith, A., Tatischeff, V., Pelletier, G., and Salati, P., editors, *Physique et astrophysique du rayonnement cosmique (Ecole CNRS de Goutelas XXVI)*, pages 87–143.

Parizot, E., Marcowith, A., Ballet, J., and Gallant, Y. A. (2006). Observational constraints on energetic particle diffusion in young supernovae remnants: amplified magnetic field and maximum energy. A&A, 453:387–395.

Parker, E. N. (1958). Suprathermal Particle Generation in the Solar Corona. ApJ, 128:677–685.

Reynolds, S. P. and Ellison, D. C. (1992). Electron acceleration in Tycho's and Kepler's supernova remnants - Spectral evidence of Fermi shock acceleration. ApJ, 399:L75–L78.

Rudnick, L. (2001). Cas A-A Y2K status report. In Holt, S. S. and Hwang, U., editors, *Young Supernova Remnants*, volume 565 of *American Institute of Physics Conference Series*, pages 247–256.

Skilling, J. (1975a). Cosmic ray streaming. I - Effect of Alfven waves on particles. MNRAS, 172:557–566.

Skilling, J. (1975b). Cosmic ray streaming. II - Effect of particles on Alfven waves. MNRAS, 173:245–254.

Truelove, J. K. and McKee, C. F. (1999). Evolution of Nonradiative Supernova Remnants. ApJS, 120:299–326.

Vladimirov, A., Ellison, D. C., and Bykov, A. (2006). Nonlinear Diffusive Shock Acceleration with Magnetic Field Amplification. ApJ, 652:1246–1258.

Warren, J. S., Hughes, J. P., Badenes, C., Ghavamian, P., McKee, C. F., Moffett, D., Plucinsky, P. P., Rakowski, C., Reynoso, E., and Slane, P. (2005). Cosmic-Ray Acceleration at the Forward Shock in Tycho's Supernova Remnant: Evidence from Chandra X-Ray Observations. ApJ, 634:376–389.

Wentzel, D. G. (1971). High-Speed Interstellar Gas Dynamics: Shocks Moderated by Cosmic Rays. ApJ, 170:53–63.

Chapter 3

Multiple Shocks

In many astrophysical contexts cosmic-rays are likely to experience many successive shocks: in chaotic stellar winds (White 1985), in rotating accreting flows (Spruit 1988), in radio sources with multiple hot spots (Pope et al. 1996), in the Galactic center (Melrose and Crouch 1997), in the OB associations inside superbubbles (Klepach et al. 2000, Parizot et al. 2004, part III of this thesis), in the early cosmological flows (Kang and Jones 2005) and in galaxy clusters (Brunetti and Lazarian 2007). Many efforts have been made to better understand multiple diffusive shock acceleration, but on quite particular cases, and clearly not to the same extent as single diffusive shock acceleration. We review here the major aspects specific to this mechanism.

3.1 Inter-Shocks Physics

A new important point to consider when simulating multiple shocks is the fate of the cosmic-rays *between* two successive shocks. In this section we adopt a *leaky-box* treatment such as the one used in section 2.2.2.3, that is we consider quantities spatially averaged over the acceleration region, which thus depend on the particle energy only.

3.1.1 Adiabatic Decompression

First the shocked fluid will decompress to recover its initial state, and the cosmic-rays being bound to it through scattering will experience adiabatic decompression (see eg Melrose and Pope 1993): when the shocked fluid density is decreased by a factor r the cosmic-rays momenta are decreased by a factor

$$R = r^{1/3} \geq 1 \tag{3.1}$$

as the phase-space volume $\propto p^3/\rho$ is conserved. The inclusion of this decompression is essential in the correct treatment of multiple DSA as we shall see in section 3.2.1.1.

3.1.2 Escape

Apart from these energy losses due to decompression the cosmic-rays might simply escape the system before the next shock occurs. This can be expressed as

$$\left(\frac{\partial f}{\partial t}\right)_{\rm esc} = -\frac{f}{\tau_{\rm esc}(p)} \tag{3.2}$$

where $\tau_{\rm esc}(p)$ is the typical escape time of the particles of momentum p. Cosmic-rays can be confined in a medium thanks to their diffusion (see sections 2.1.2.1 and 1.3.2.1), whose typical length scale grows with the cosmic-rays energy, so that the cosmic-rays spectrum will be depleted from its highest energy part. In a given physical situation, given the typical time between two shocks and the diffusion experienced by cosmic-rays during that time (not necessarily of Bohm type) we can estimate the maximum momentum $p_{\rm cut}$ of the remaining cosmic-rays when the next shock arrives (the case of superbubbles will be detailed in sections 7.3.2 and 8.2.1 of part III).

3.1.3 Second-Order Acceleration

Second order Fermi acceleration mechanism, usually neglected at the shocks themselves, might become an important process between the shocks (particularly at low energies). This process comes from the fact that the scattering centers (the waves) are not fixed in the fluid as assumed in section 2.2.3, but have a motion relative to the background (at the Alfven speed v_A given by (2.21)). This gives rise to a diffusion in momentum (see eg Achterberg 1998):

$$\left(\frac{\partial f}{\partial t}\right)_{\rm II} = \frac{1}{p^2}\frac{\partial}{\partial p}\left(p^2 D_p \frac{\partial f}{\partial p}\right) \tag{3.3}$$

where D_p is the momentum diffusion coefficient, linked to the space diffusion coefficient D by

$$D_p(p,t) \simeq \frac{v_A^2}{D(p,t)}\, p^2. \tag{3.4}$$

Again we note that in the inter-shocks region D is not necessarily the same as at the shock front.

3.1.4 Radiation Losses

Finally accelerated particles suffer energy losses as they radiate. This is not a concern for protons that we will consider in part II, but this must be taken into account for electrons[1]. Formally this can be expressed as:

$$\left(\frac{\partial f}{\partial t}\right)_{\rm rad} = \frac{1}{p^2}\frac{\partial}{\partial p}\left(p^2 < \dot{p} > f\right) \tag{3.5}$$

where $< \dot{p} > (p)$ is the momentum loss rate for a particle of momentum p.

[1]So that electrons would require a separate treatment if we were to add them in our code.

3.2 Acceleration by a Sequence of Shocks

3.2.1 Linear Regime

From a theoretical point of view, multiple DSA is well understood in the linear regime, as we can simply add the effect of a single shock. Being of astrophysical interest it has been investigated analytically since the early developments of the DSA theory (see eg Eichler 1980, Blandford and Ostriker 1980). The main result of multiple DSA is that the cosmic-rays spectrum flattens progressively to a universal asymptotic power-law of index $s = 3$ (regardless of the shocks compression ratios). This can be understood from equation (2.49) which shows that the slope is controlled by the acceleration and escape timescales. The case of an infinity of successive identical shocks is formally equivalent to the case of a single shock from which escape is impossible, that is $\tau_{\rm esc} = \infty$, which indeed gives $N(E) \propto E^{-1}$ that is $f(p) \propto p^{-3}$. We will now study the evolution of the spectrum in more details, using two different equivalent approaches.

3.2.1.1 Iterative Treatment

First we will compute step-by-step the resulting spectrum after a sequence of identical shocks, including adiabatic decompression between each pair of shocks (as in Melrose and Pope 1993 and Pope and Melrose 1994), but assuming there are no other types of losses (for that matter see Schneider 1993).

Lets assume that cosmic-rays are injected at each shock with a mono-energetic distribution

$$\phi_{\rm inj} = k\,\delta\left(p - p_{\rm inj}\right)\ . \tag{3.6}$$

According to equation (2.72) of section 2.2.3.2 the distribution downstream of the first shock is given by

$$f_1(p) = s_1 p^{-s_1} \int_0^p p'^{s_1-1} \phi_{\rm inj}(p') dp' \tag{3.7}$$

where $s_1 = 3r/(r-1)$ is the canonical slope for a single shock. Using (3.6) we get

$$f_1(p) = \frac{k\,s_1}{p_{\rm inj}} \left(\frac{p}{p_{\rm inj}}\right)^{-s_1} H\left(p - p_{\rm inj}\right) \tag{3.8}$$

where H is the Heaviside function. As explained in 3.1.1 the fluid decompression then cools the particles: p changes to $p' = p/R$. According to Liouville's theorem the distribution function after decompression $f_1'(p')$ is equal to the distribution function before decompression $f_1(p)$, so that we get

$$f_1'(p) = f_1(R\,p) \tag{3.9}$$

that is

$$f_1'(p) = \frac{k\,s_1}{p_{\rm inj}} \left(\frac{R\,p}{p_{\rm inj}}\right)^{-s_1} H\left(p - \frac{p_{\rm inj}}{R}\right)\ . \tag{3.10}$$

Assuming there are no other losses, the input distribution for the second shock is $f_1' + \phi_{\text{inj}}$, so that again according to equation (2.72) the distribution downstream of the second shock is given by

$$f_2(p) = s_1 p^{-s_1} \int_0^p p'^{s_1-1} \left(f_1'(p') + \phi_{\text{inj}}(p')\right) dp' \,. \tag{3.11}$$

Using (3.10) and (3.6) we get

$$f_2(p) = \frac{k\, s_1^2}{p_{\text{inj}}} \left(\frac{R\, p}{p_{\text{inj}}}\right)^{-s_1} \ln\left(\frac{R\, p}{p_{\text{inj}}}\right) H\left(p - \frac{p_{\text{inj}}}{R}\right) + f_1(p) \tag{3.12}$$

and after decompression

$$f_2'(p) = \frac{k\, s_1^2}{p_{\text{inj}}} \left(\frac{R^2\, p}{p_{\text{inj}}}\right)^{-s_1} \ln\left(\frac{R^2\, p}{p_{\text{inj}}}\right) H\left(p - \frac{p_{\text{inj}}}{R^2}\right) + f_1'(p) \,. \tag{3.13}$$

The first term, hereafter noted $f_{(2)}'$, represents particles injected at the first shock, accelerated by the first shock and re-accelerated by the second shock. The second term f_1' represents particles injected at the second shock, which form the same spectrum as just after the first shock. In the same way after the third shock we obtain

$$f_3(p) = \frac{k\, s_1^3}{p_{\text{inj}}} \left(\frac{R^2\, p}{p_{\text{inj}}}\right)^{-s_1} \frac{1}{2} \left(\ln\left(\frac{R^2\, p}{p_{\text{inj}}}\right)\right)^2 H\left(p - \frac{p_{\text{inj}}}{R^2}\right) + f_2(p) \tag{3.14}$$

$$f_3'(p) = \frac{k\, s_1^3}{p_{\text{inj}}} \left(\frac{R^3\, p}{p_{\text{inj}}}\right)^{-s_1} \frac{1}{2} \left(\ln\left(\frac{R^3\, p}{p_{\text{inj}}}\right)\right)^2 H\left(p - \frac{p_{\text{inj}}}{R^3}\right) + f_2'(p) \,. \tag{3.15}$$

More generally the contribution from the injection at the first shock to the distribution downstream of the i-th shock (after decompression) is

$$f_{(i)}'(p) = \frac{k\, s_1^i}{p_{\text{inj}}} \left(\frac{R^i\, p}{p_{\text{inj}}}\right)^{-s_1} \frac{1}{(i-1)!} \left(\ln\left(\frac{R^i\, p}{p_{\text{inj}}}\right)\right)^{i-1} H\left(p - \frac{p_{\text{inj}}}{R^i}\right) \,. \tag{3.16}$$

The functions $f_{(i)}'(p)$ are plotted on figure 3.1 for $i = 1 \ldots 10$ (for strong shocks of $r = 4$). This shows the effects of adiabatic decompression (a constant shift towards lower energies) and of re-acceleration (a more and more concave shape at low energies, a more and more hard slope at high energies). The slope (above p_{inj}) can be analytically expressed as

$$s_{(i)}(p) = -\frac{\partial \ln f_{(i)}'(p)}{\partial \ln p} = s_1 - \frac{i-1}{\ln \frac{R\, p}{p_{\text{inj}}}} \,. \tag{3.17}$$

Since all the shocks are equivalent $f_{(i)}'$ is also the contribution from the injection at the $(n-i+1)$-th shock to the distribution downstream of the n-th

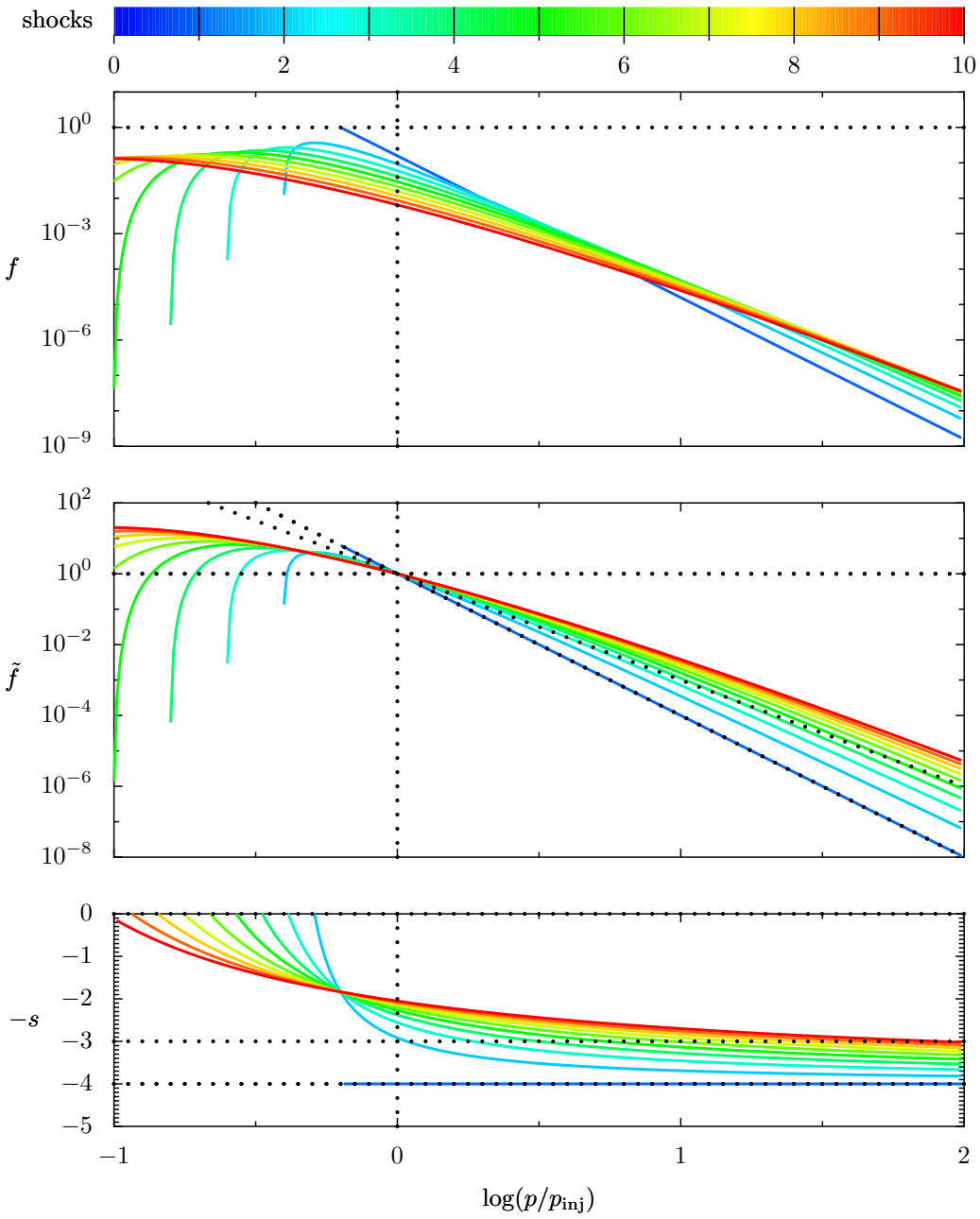

Figure 3.1: Spectra resulting from the injection at the first shock and acceleration by ten successive shocks ($r = 4$).
The spectra are shown downstream of the last shock, after decompression. This corresponds to equation (3.16). The top plot shows the distribution function f, the middle plot shows the normalized distribution function $\tilde{f}$ (so that $\tilde{f}_{(i)}(p_{\mathrm{inj}}) = 1\ \forall i$), the bottom plot shows its logarithmic slope $-s = -\partial \ln f / \partial \ln p$.

shock. The total distribution downstream of the n-th shock is the sum of the contributions from the injection at all the n shocks:

$$f'_n(p) = \sum_{i=1}^{n} f'_{(i)}(p) \; . \tag{3.18}$$

As far as we know there is no simple analytical expression of $f'_n(p)$ (and a fortiori of its slope). However one can show that in the limit of an infinity of shocks (3.18) reduces to a simple power-law (for $p > p_{\rm inj}$):

$$f'_\infty(p) \propto \left(\frac{p}{p_{\rm inj}}\right)^{-3} \; . \tag{3.19}$$

The functions $f'_n(p)$ are plotted on figure 3.2 for $n = 1 \ldots 50$ (for strong shocks of $r = 4$). This shows the actual spectra produced by multiple shocks. For instance the spectrum after the 10-th shock corresponds to the sum of all the 10 spectra of figure 3.1. We clearly see that the spectrum hardens to the limit of a power-law of slope $s = 3$. In between the spectrum is never a simple power-law, as the asymptotic convergence to $s = 3$ is all the more slow since the momentum is high. The way the slope goes to 3 at different momenta is shown on the top of figure 3.3. The bottom of figure 3.3 shows the same result but for weak shocks of $r = 3$. We observe the same convergence to $s = 3$. The convergence at any given momentum is slower than in the case $r = 4$, simply because we start from a steeper spectrum of slope $s_1 = 4.5$ instead of $s_1 = 4$. Thus a hard spectrum can be the result of acceleration by either a few strong shocks either many weak shocks. The $s = 3$ result still holds for a sequence of shocks of random ratios, but at low energies around p_{inj} where the normalization wobbles (as it is proportional to s and thus r as seen from equation (2.73)). The case of two alternating compression ratios r_1, r_2 is shown in some details in Pope and Melrose (1994). They find that the paired shocks evolution can be well represented by a sequence of identical shocks of mean ratio $\bar{r} = (r_1 + r_2)/2$.

We would like now to show the effect of adiabatic decompression. In all the plots shown so far we have considered that the fluid fully decompresses, so that R is given by (3.1) with r being the actual shock compression ratio ($R \simeq 1.59$ for $r = 4$). What happens if the decompression is not exact, that is $R = r'^{1/3}$ with $r' \neq r$? Figures 3.4 shows the result for a systematic under-decompression $r' = 3 < r = 4$ ($R \simeq 1.44$). We see that as cosmic-rays keep more energy they have harder spectra, of slopes smaller than 3 - and which are never constant. Figure 3.5 shows the limit case of no decompression at all between the shocks, that is $r' = 1 = R$ (with still $r = 4$ here). We see that the particles then pile-up from injection momentum, producing a constant spectrum (of zero slope). Figures 3.6 and 3.7 show the case (quite theoretical) of over-decompressions

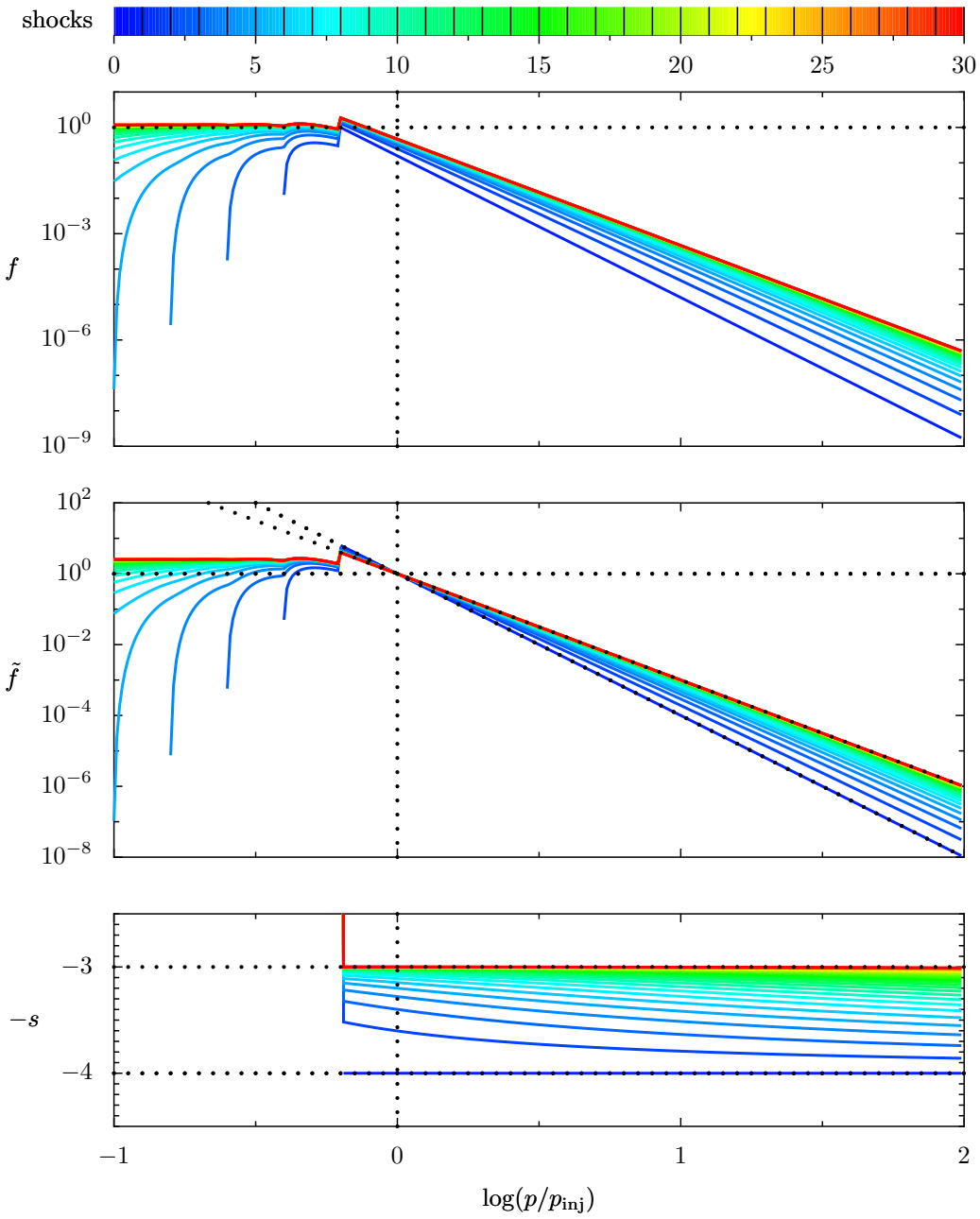

Figure 3.2: Spectra resulting from acceleration by multiple shocks, with injection at each shock ($r = 4$).
The spectra are shown downstream of the last shock, after decompression. This corresponds to equation (3.18). The top plot shows the normalized distribution function f, the middle plot shows the normalized distribution function $\tilde{f}$ (so that $\tilde{f}_{(i)}(p_{\mathrm{inj}}) = 1\ \forall i$), the bottom plot shows its logarithmic slope $-s = -\partial \ln f / \partial \ln p$.

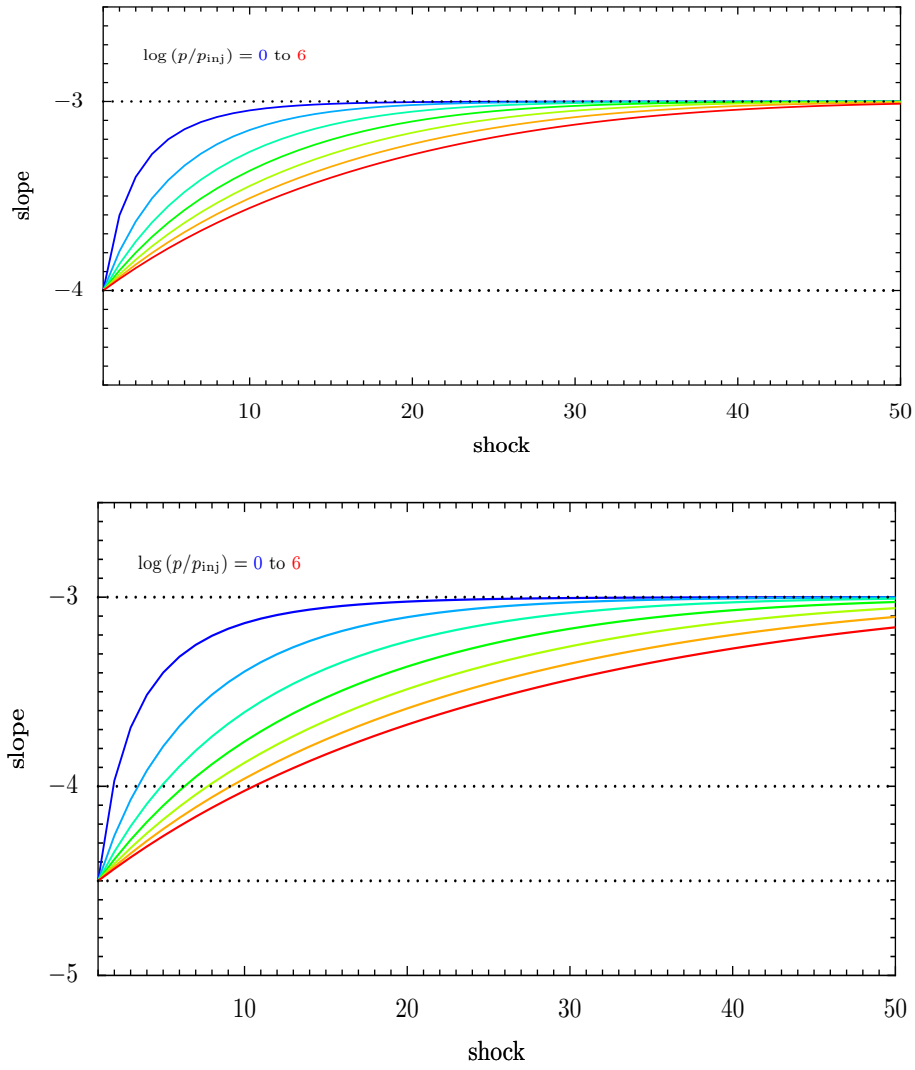

Figure 3.3: Slope evolution under acceleration by multiple shocks. The spectrum slope s is shown as a function of the number of successive shocks for 7 different momenta. The top plot corresponds to a strong shock of $r = 4$ (this plot consists in vertical slices in the bottom of figure 3.2), the bottom plot corresponds to a weaker shock of $r = 3$.

with respectively $r' = 5$ ($R \simeq 1.71$) and $r' = 10$ ($R \simeq 2.15$). We see that in that case the spectra still converge to a perfect power-law, but a steeper one (of slope $s > 3$). Thus a sequence of (linear) shocks of ratio r will produce the well-known $s = 3$ spectrum if and only if the cosmic-rays are decompressed by the corresponding $r^{1/3}$ factor between each shock.

3.2.1.2 Global Treatment

We will now outline the approach developed by Achterberg (1990)[2], which relies on the use of *Green functions*. One defines the single-shock Green function $G(p|p_0)$ so that

$$f_{i,\mathrm{down}}(p) = \int_0^\infty dp_0 \; G(p|p_0) \; (f_{i,\mathrm{up}}(p_0) + \phi_{\mathrm{inj}}(p_0)) \tag{3.20}$$

where $f_{i,\mathrm{up}} + \phi_{\mathrm{inj}}$ is the input distribution (advected and injected cosmic-rays) for shock i and $f_{i,\mathrm{down}}$ is the resulting downstream distribution just after this shock. $G(p|p_{\mathrm{inj}})$ can be thought as the *response function* of the shock-accelerated downstream distribution to a fluctuation in the upstream distribution at momentum p_0. It is the *impulsive response* of DSA in the sense that $f_{i,\mathrm{down}}(p) = G(p|p_0)$ when $f_{i,\mathrm{up}}(p) = 0$ and $\phi_{\mathrm{inj}}(p) = \delta(p - p_0)$. According to equation (2.72) of section 2.2.3.2 it is given by

$$G(p|p_0) = \frac{s_1}{p_0} \left(\frac{p}{p_0}\right)^{-s_1} H\,(p - p_0) \tag{3.21}$$

where $s_1 = 3r/(r-1)$ is the canonical slope for a single shock.

In the same way one can describe the evolution of particles between two shocks through the use of a *transmission function* $T(p|p')$ defined so that

$$f_{i+1,\mathrm{up}}(p) = \int_0^\infty dp' \; T(p|p') \; f_{i,\mathrm{down}}(p') \tag{3.22}$$

where $f_{i,\mathrm{down}}$ is the distribution produced by shock i (given by equation (3.20)) and $f_{i+1,\mathrm{up}}$ is the input distribution for the shock $i+1$ (after propagation of particles between shocks i and $i+1$). For instance adiabatic decompression of factor R can be simply written

$$T(p|p') = \delta(p' - R\,p)\,. \tag{3.23}$$

Combining equations (3.20) and (3.22) we get

$$f_{i,\mathrm{down}}(p) = \int_0^\infty dp_0 \; G(p|p_0) \; \left(\int_0^\infty dp' \; T(p|p') \; f_{i-1,\mathrm{down}}(p') + \phi_{\mathrm{inj}}(p_0) \right)\,. \tag{3.24}$$

For a system of identical shocks one can then define the *renormalized Green function* $G_r(p|p_0)$ so that

$$f_{\mathrm{down}}(p) = \int_0^\infty dp_0 \; G_r(p|p_0) \; \phi_{\mathrm{inj}}(p_0)\,. \tag{3.25}$$

$G_r(p|p_0)$ appears as the response function of the distribution downstream of an infinite sequence of shocks to a fluctuation in the source of cosmic-rays.

[2]Note that we work here with the differential distribution function $f(p)$ while Achterberg works with the integral distribution function $F(p) = 4\pi p^2 dp$.

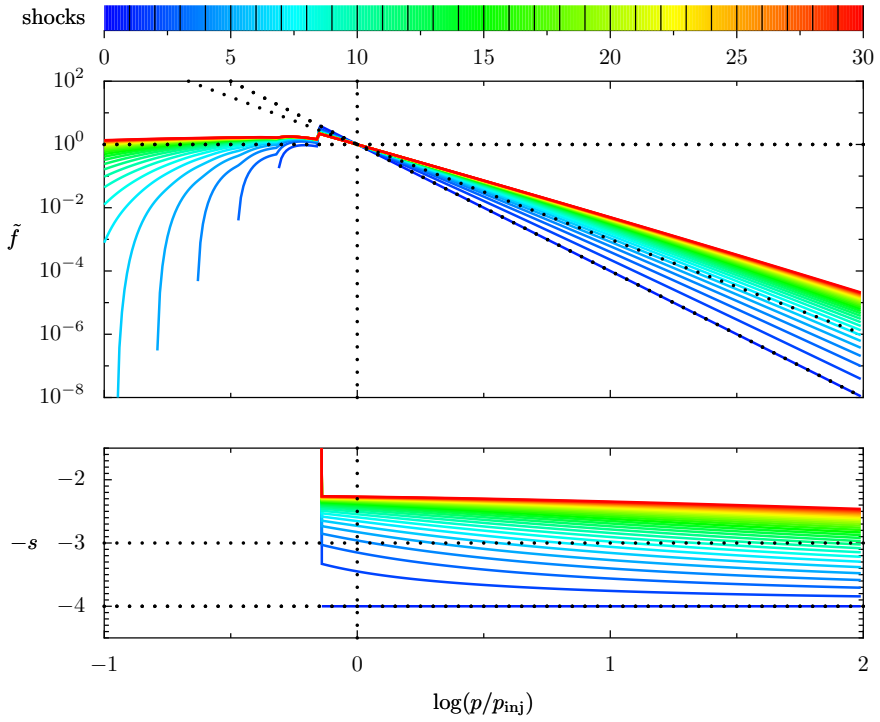

Figure 3.4: Spectra produced by multiple shocks ($r = 4$, $r' = 3$).

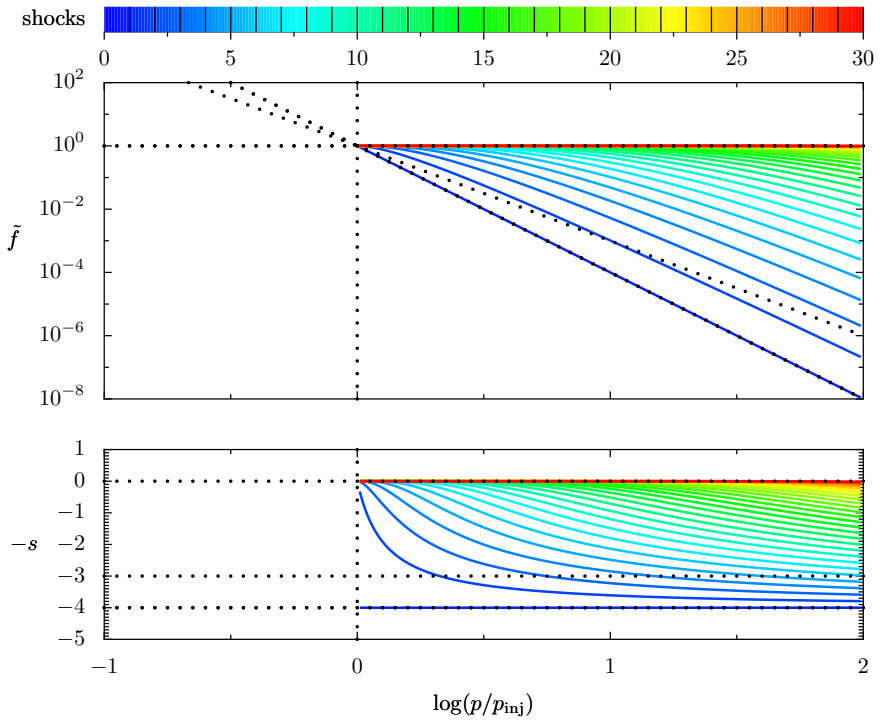

Figure 3.5: Spectra produced by multiple shocks ($r = 4$, $r' = 1$).

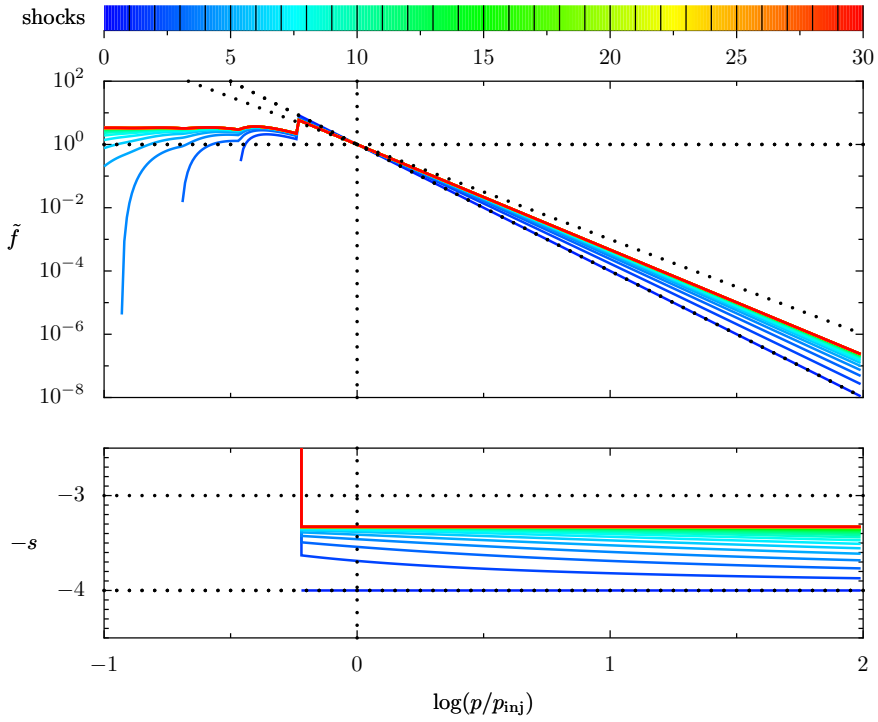

Figure 3.6: Spectra produced by multiple shocks ($r = 4$, $r' = 5$).

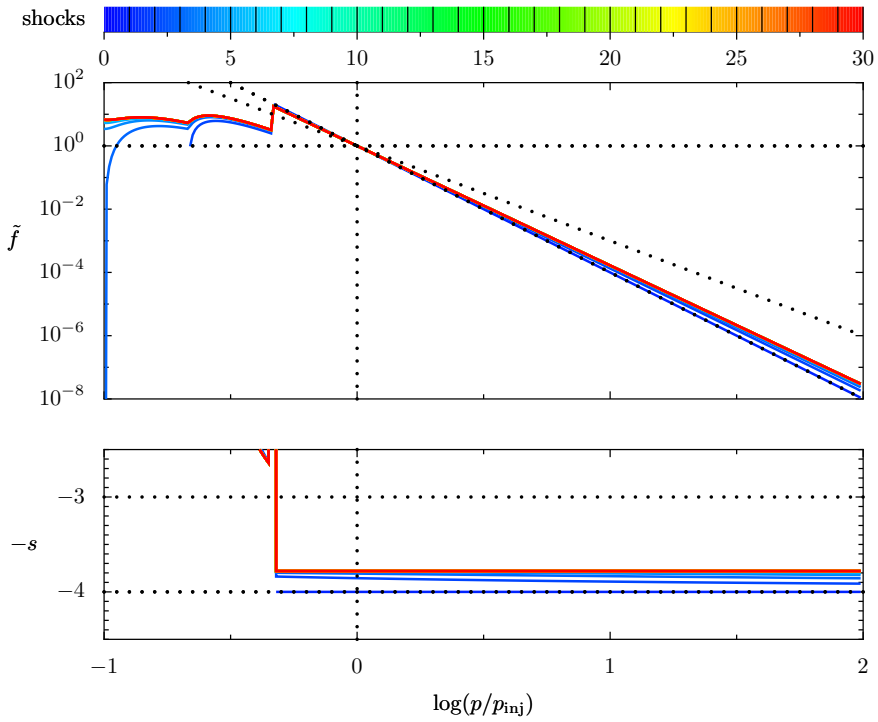

Figure 3.7: Spectra produced by multiple shocks ($r = 4$, $r' = 10$).

According to (3.24) it is formally the solution of the following equation:

$$G_r(p|p_0) = \; G(p|p_0) + \int_0^\infty dp'' G(p|p'') \int_0^\infty dp' \; T(p''|p') \; G_r(p'|p_0) \; . \qquad (3.26)$$

The two terms in this expression correspond respectively to acceleration by a single shock and by multiple shocks. Equation (3.26) does not in general have a simple analytical solution. In the special case where the transmission function has the form

$$T(p|p') = \frac{1}{p'} U(\frac{p}{p'}) \qquad (3.27)$$

it can be reduced to an algebraic equation through the use of the *Mellin transform*, defined by

$$\tilde{G}(\xi) = \int_0^\infty dx \; G(x) \; x^{\xi - 1} \; . \qquad (3.28)$$

Solving the equation and inverting the Mellin transform one can then express $G_r(p|p_0)$ as a sum of power-laws:

$$G_r(p|p_0) = \; \frac{s_1}{p_0} \sum_m \left| \frac{dN}{d\xi}(\xi_m) \right|^{-1} \left(\frac{p}{p_0} \right)^{-(2+\xi_m)} \qquad (3.29)$$

where the ξ_m are the roots of

$$N(\xi) = \frac{(r-1)(1-\xi) - 3(1 - \tilde{U}(\xi))}{r-1} \qquad (3.30)$$

where $\tilde{U}(\xi)$ is the Mellin transform of $U(x)$ defined by equation (3.27) (the positive roots of N give the solution for $p > p_0$, the negative roots of N give the solution for $p < p_0$).

Lets consider now that particles only suffer adiabatic decompression between two shocks (Achterberg also considers Fermi II acceleration presented in 3.1.3). This process satisfies equation 3.27 with

$$U(x) = \delta(1 - R \, x) \; , \qquad (3.31)$$

the Mellin transform of which is simply

$$\tilde{U}(\xi) = R^{1-\xi} = r^{(1-\xi)/3} \; . \qquad (3.32)$$

The roots of $N(\xi)$ are then $\xi = -2$ and $\xi = +1$, producing a flat spectrum $G_r(p|p_0) = ct$ for $p < p_0$ and a hard spectrum $G_r(p|p_0) \propto p^{-3}$ for $p > p_0$, in agreement with our previous calculations for mono-chromatic injection as plotted on figure 3.2.

3.2.2 Non-Linear Regime

All calculations of section 3.2.1 implicitly assume that the cosmic-rays back-reaction is negligible. As explained in section 2.3 of chapter 2 this is likely not to hold, changing the overall picture in a sizeable way. Actually non-linear effects are likely to be all the more important since cosmic-rays experience acceleration by many shocks.

While there is a well-defined analytic framework for the linear multiple DSA, there is no such thing in the non-linear regime. However Bykov (2001) has developed a non-linear model of the acceleration by chaotic large scales fluid motions inside superbubbles (see more in section 8.2.2.2 of part III), and Blasi (2004) has proposed a simple semi-analytical model including "seed" particles (its main conclusion is that the presence of upstream cosmic-rays can dominate over the injection of fresh cosmic-rays at the shock front). Both models don't explicitly deal with the time evolution of the spectra nor with the precise geometry of the shocks.

From a numerical point of view, as we have already seen the fully non-linear regime is quite well studied now, but in the single shock model: although feasible, multiple DSA has received extremely reduced attention so far. Gieseler and Jones (2000) have studied acceleration at multiple oblique shocks, but in the test-particle regime (they found the cosmic-rays spectrum to harden substantially). Tammi and Dempsey (2007) have begun to investigate acceleration at multiple relativistic shocks, but again in the linear regime. Kang and Jones (2005) have investigated the effect of an upstream cosmic-rays pressure in the non-linear regime, but for single shocks (they conclude that it doesn't affect strong shocks much but may enhance the efficiency of weak ones).

Our aim with the code presented in this thesis is to be able to study cosmic-ray acceleration by multiple shocks in details, in the full *time-dependent* and *non-linear* regime.

References

Achterberg, A. (1990). Particle acceleration by an ensemble of shocks. A&A, 231:251–258.

Achterberg, A. (1998). Cosmic Ray Physics - Sources of energetic particles in the universe. Nova Autumn School.

Blandford, R. D. and Ostriker, J. P. (1980). Supernova shock acceleration of cosmic rays in the Galaxy. ApJ, 237:793–808.

Blasi, P. (2004). Nonlinear shock acceleration in the presence of seed particles. *Astroparticle Physics*, 21:45–57.

Brunetti, G. and Lazarian, A. (2007). Compressible turbulence in galaxy clusters: physics and stochastic particle re-acceleration. MNRAS, 378:245–275.

Bykov, A. M. (2001). Particle Acceleration and Nonthermal Phenomena in Superbubbles. *Space Science Reviews*, 99:317–326.

Eichler, D. (1980). Basic inconsistencies in models of interstellar cosmic-ray acceleration. ApJ, 237:809–813.

Gieseler, U. D. J. and Jones, T. W. (2000). First order Fermi acceleration at multiple oblique shocks. A&A, 357:1133–1136.

Kang, H. and Jones, T. W. (2005). Efficiency of Nonlinear Particle Acceleration at Cosmic Structure Shocks. ApJ, 620:44–58.

Klepach, E. G., Ptuskin, V. S., and Zirakashvili, V. N. (2000). Cosmic ray acceleration by multiple spherical shocks. *Astroparticle Physics*, 13:161–172.

Melrose, D. B. and Crouch, A. (1997). Effect of synchtrotron losses on multiple diffusive shock acceleration. *Publications of the Astronomical Society of Australia*, 14:251–257.

Melrose, D. B. and Pope, M. H. (1993). Diffusive Shock Acceleration by Multiple Shocks. *Proceedings of the Astronomical Society of Australia*, 10:222–224.

Parizot, E., Marcowith, A., van der Swaluw, E., Bykov, A. M., and Tatischeff, V. (2004). Superbubbles and energetic particles in the Galaxy. I. Collective effects of particle acceleration. A&A, 424:747–760.

Pope, M. H., Ball, L., and Melrose, D. B. (1996). Shock acceleration in hotspots. *Publications of the Astronomical Society of Australia*, 13:132–139.

Pope, M. H. and Melrose, D. B. (1994). Diffusive shock acceleration by multiple shock fronts with differing properties. *Proceedings of the Astronomical Society of Australia*, 11:175–179.

Schneider, P. (1993). Diffusive particle acceleration by an ensemble of shock waves. A&A, 278:315–327.

Spruit, H. C. (1988). Particle acceleration in a flow accreting through shock waves. A&A, 194:319–327.

Tammi, J. and Dempsey, P. (2007). Particle acceleration by multiple parallel shocks. In *ICRC'07 proceedings (pre-conference edition)*.

White, R. L. (1985). Synchrotron emission from chaotic stellar winds. ApJ, 289:698–708.

Part II

Numerical Simulations

As emphasized in chapter 2 of part I the non-linear interaction between cosmic-rays and the interstellar medium makes the real diffusive shock acceleration mechanism a very delicate problem. This is the very reason why we resort here, as most people working on that subject, to the use of direct numerical simulations. We have developed a new code[3], named Marcos for *Machine à Accélérer les Rayons COSmiques*[4], but relying on well-known techniques. The code and its first results have been presented in a dedicated paper and at two conferences at the SF2A[5] and the ICRC[6] (see references below). Our approach consists of coupling the thermal (described by standard hydrodynamics) and non-thermal (described by a more general kinetic theory) populations (chapter 4). As seen in chapter 1 nature accelerates cosmic-rays over an impressive range of energies, corresponding to impressive ranges of space- and time-scales. This is a major difficulty for all numerical simulations, which have to deal with their finite ressources. To alleviate this problem we resort to the technique of adaptive mesh refinement (AMR, chapter 5). Then, to be able to explore the question of multiple shocks, detailed in chapter 3, we also make use of the parallelization technique (chapter 6). We are now well equipped to address the situation of our primary environment of interest, the superbubbles (part III).

- Ferrand, G., Downes, T.P., and Marcowith, A. (2008). Simulations de l'accélération non-linéaire par chocs multiples. To appear in SF2A '07 proceedings.
- Ferrand, G., Downes, T.P., and Marcowith, A. (2008). Simulations of time-dependent non-linear multiple diffusive shock acceleration. To appear in ICRC '07 proceedings.
- Ferrand, G., Downes, T.P., and Marcowith, A. (2008). MARCOS, a numerical tool for the simulation of time-dependent non-linear diffusive shock acceleration. MNRAS, 383, 41-56.

[3]The code consists of roughly 7000 lines of C, written almost entirely from scratch, plus more than 1000 lines of Python for the graphical post-processing.

[4]The French for *Cosmic-ray accelerating machine.*

[5]Société Française d'Astronomie et d'Astrophysique, the French association of professional astronomers and astrophysicists.

[6]International Cosmic-Ray Conference, a big meeting covering all the fields of cosmic-ray physics every two years.

Chapter 4

Accelerating Particles: Coupling Hydrodynamic and Kinetic Theories

In our approach the thermal (fluid being shocked) and non-thermal (cosmic-rays) particles, although intimately coupled, are handled as two different populations (see section 2.3.4). The fluid, described by its moments ρ, u, P, obeys the Euler equations, while the cosmic-rays, described by their distribution function $f(x,p)$, follow a more general transport equation.

4.1 Fluid Dynamics

The hydrodynamics are described by the (non-relativistic) Euler equations (2.81), (2.82), (2.83) which can be written in the general form:

$$\frac{\partial \mathbf{X}}{\partial t} + \nabla \cdot \mathbf{F}(\mathbf{X}) = \mathbf{0} \tag{4.1}$$

where (from now on in 1D slab geometry, see appendix A for the spherical case) the conservative variables are

$$\mathbf{X} = \begin{pmatrix} \rho \\ \rho u \\ e \end{pmatrix} \tag{4.2}$$

and their flux

$$\mathbf{F}(\mathbf{X}) = \begin{pmatrix} \rho u \\ \rho u^2 + P \\ (e+P)u \end{pmatrix}. \tag{4.3}$$

To close this system we consider the usual polytropic equation of state (2.2) of adiabatic index γ so that the total energy is given by (2.84).

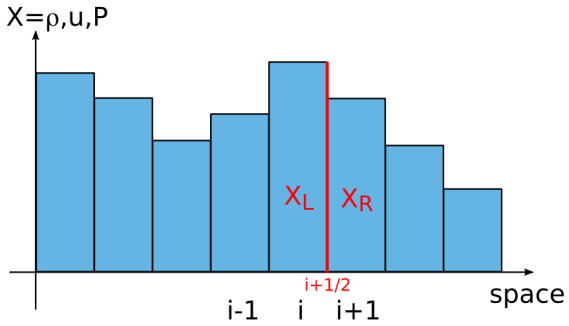

Figure 4.1: Sketch of the finite-volumes approach (with constant values).

4.1.1 Finite-Volumes Scheme

Our hydrodynamic scheme is adapted from the one used in Downes and Ray (1998). It uses an Eulerian finite-volume approach: the space axis x is split into cells indexed by i (see figure 4.1). This allows us to take advantage of the conservative (hyperbolic) form (4.1) of the Euler system (see eg **?**). In this approach the functions $X(x)$ (where X denotes any of the three components of $\mathbf{X}$) are replaced by piece-wise approximations X_i. The simplest approximation (which is first order in space) consists in taking for X_i the cell averaged value of X:

$$\bar{X}_i = \frac{1}{V_i} \int_{V_i} X(x)\, dV \tag{4.4}$$

where V_i is the volume of cell i.

To update the X values from time n to time $n+1$ (that is by a time-step δt) we then readily discretize equation (4.1) as

$$\frac{V_i X_i^{n+1} - V_i X_i^n}{\delta t} = +S_{i-\frac{1}{2}} F_{i-\frac{1}{2}}^{n+\frac{1}{2}} - S_{i+\frac{1}{2}} F_{i+\frac{1}{2}}^{n+\frac{1}{2}} \tag{4.5}$$

where $S_{i-1/2}$ ($S_{i+1/2}$) is the surface at the left (right) of cell i and $F_{i-1/2}^{n+1/2}$ ($F_{i+1/2}^{n+1/2}$) is the flux of X through this surface during the time-step δt, that is the cells values are updated according to their fluxes at the cells interfaces. As $F_{i+1/2}^{n+1/2} = F_{(i+1)-1/2}^{n+1/2}$ this scheme has the interesting property that (but for boundary effects) the X quantities are numerically conserved, which is critical for computing the correct velocity of the shock discontinuity.

4.1.1.1 Evaluation of the Fluxes

The problem is now to evaluate the fluxes $F_{i\pm1/2}^{n+1/2}$. We use here the approach developed by Godunov (1959): the fluxes are computed using the values of X at the interfaces computed by a *Riemann solver*. Using approximation (4.4) each cells interface indeed defines what is known as a *Riemann problem* (see

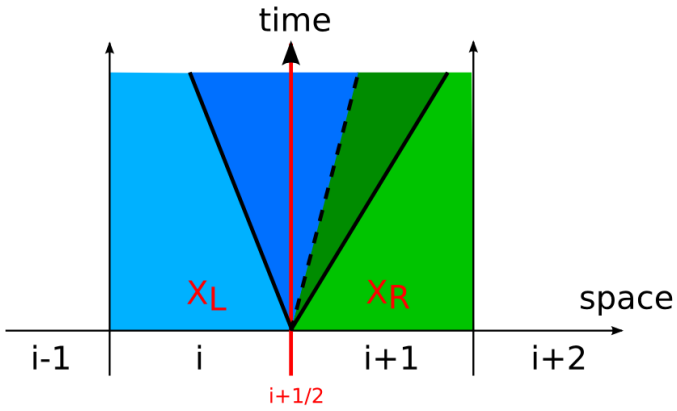

Figure 4.2: Sketch of the Riemann problem at cells interfaces.

figures 4.1 and 4.2), that is two constant states ($\mathbf{X_L}$ at the left and $\mathbf{X_R}$ at the right) separated by a discontinuity at $x' = 0$ at $t' = 0$. The outcome of such an initial condition is a set of three waves: a contact discontinuity (dashed), which separates fluids that were previously on the left (in blue) and on the right (in green) – it is a jump in the density profile, but not in the velocity and pressure ones – and two waves (plain) which propagate into the left and right media and modify them (both can be either a shock wave either a rarefaction wave). Solving the Riemann problem first requires to discuss the position of the waves. It may be that both left and right waves are on the same side (that is $x' > 0$ or $x' < 0$), in which case the interface is simply in the left or right state. In the general case the interface is in the modified state between the two left and right waves. It is possible to work out analytically an implicit equation giving the pressure in this modified state, from which one can derive the other variables (to find this pressure we use an exact iterative solver with a linear approximation in smooth regions). We then compute the interface fluxes as

$$\mathbf{F}_{i+1/2}^{n+1/2} = F\left(\mathbf{X}^*\left(\mathbf{X_L} = \mathbf{X}_i^n; \mathbf{X_R} = \mathbf{X}_{i+1}^n\right)\right) \tag{4.6}$$

where $\mathbf{X}^*$ is the computed interface state ($x' = 0$, $t' = 0^+$).

As stated before this leads to a first order scheme in both space and time. To obtain a higher order scheme we have to use higher order extrapolations. The code can be made second order in space using a linear reconstruction in each cell (see figure 4.3):

$$X_i(x) = \bar{X}_i + \sigma_i(x - c_i) \tag{4.7}$$

where c_i is the center of cell i (defined so that $\bar{X}_i$ is the average value of X_i) and σ_i is the slope of the reconstructed profile X_i, which can be evaluated from the variations of $\bar{X}$ around cell i:

$$\sigma_i = \mathrm{av}\left(\frac{\bar{X}_i - \bar{X}_{i-1}}{c_i - c_{i-1}}, \frac{\bar{X}_{i+1} - \bar{X}_i}{c_{i+1} - c_i}\right) \tag{4.8}$$

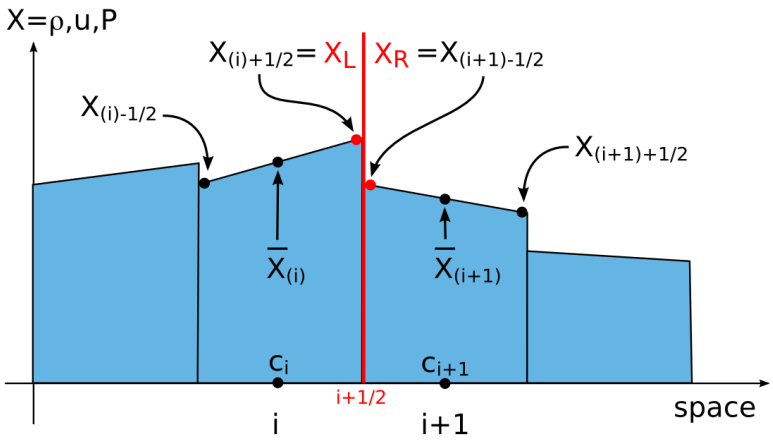

Figure 4.3: Sketch of the finite-volumes approach (with slopes reconstructions).

where av() is some averaging function (see equation (4.10) just below). We then give to the Riemann solver the values of X evaluated just at the interface:

$$\mathbf{F}_{i+1/2}^{n+1/2} = \mathbf{F}\left(\mathbf{X}^*\left(\mathbf{X_L} = \mathbf{X}_{(i)+1/2}^n; \mathbf{X_R} = \mathbf{X}_{(i+1)-1/2}^n\right)\right). \tag{4.9}$$

This technique known as *slopes reconstruction* one has a draw-back: if the slopes σ_i get too high the scheme might become unstable (and produce oscillations). To prevent that we need to use (empirical) *slope limiters* (see eg **?**) such as

$$\mathrm{av}(a,b) \quad = \begin{cases} \begin{cases} \frac{2ab}{a+b} & \text{(VanLeer)} \\ \begin{cases} a \text{ if } |a|<|b| \\ b \text{ if } |b|<|a| \end{cases} & \text{(minmod)} \\ \frac{a^2b+b^2a}{a^2+b^2} & \text{(Falle)} \end{cases} & ab > 0 \\ 0 & & ab < 0 \end{cases} \tag{4.10}$$

which have been proposed respectively by van Leer (1977), Roe (1986), Falle (1991). Note that all these functions satisfy $\mathrm{av}(a,a) = a$ and for $a \neq b$ gives more weight to the slope of lowest absolute value – and revert to the piece-wise constant approach ($\sigma = 0$) when the flow is not monotonic ($ab < 0$).

Up to now we have assumed that the interface fluxes (computed at $t = 0^+$) are constant for the whole time-step δt. To get a better estimate of the fluxes variations one can first evaluate the state $\mathbf{X}^{n+1/2}$ after half the time-step and use this intermediary state to work out the fluxes actually used to compute $\mathbf{X}^n$:

$$\mathbf{F}_{i+1/2}^{n+1/2} = \mathbf{F}\left(\mathbf{X}^*\left(\mathbf{X_L} = \mathbf{X}_{(i)+1/2}^{n+1/2}; \mathbf{X_R} = \mathbf{X}_{(i+1)-1/2}^{n+1/2}\right)\right). \tag{4.11}$$

This technique, known as the *leap-frog* scheme, makes the code second order in time (as we use now linear time reconstructions of the fluxes instead of constant ones).

Finally we note that the Godunov scheme works with the *conservative* variables ρ, ρu, e, whereas the Riemann solver works with the *primitive* variables ρ, u, P. The pressure is computed as the difference between the total and kinetic energy of the fluid: $P = (\gamma - 1)(e - 0.5\rho u^2)$ so that in strong shocks where $0.5\rho u^2 \gg P$ and $e \sim 0.5\rho u^2$ its evaluation might become rather imprecise. Actually such a scheme can produce some fake "negative pressures" which have to be corrected to some fixed convenient $P_{\min}$ (see eg **?**). To prevent that problem Kang et al. (2002) decided to add another equation specifically for the pressure, the equation of conservation of the "modified entropy" $S = P/\rho^{\gamma-1}$ (note that this equation is not valid at the shock, so that they need to combine it appropriately with the usual energy equation). They show that this technique provides more accuracy to their code in the precursor region of modified shocks, however we keep here the Euler scheme.

4.1.1.2 Time-Step Computation

We recall that our scheme, as all discrete explicit schemes, is subject to the *Courant condition*

$$\delta t_{\mathrm{adv},x} < \frac{\delta x}{u_{\max}} \tag{4.12}$$

where $u_{\max} = (|u| + c_{\mathrm{s}})_{\max}$ is the maximum physical signal speed at the time considered (for modified shocks the cosmic-rays pressure is taken into account in the expression (2.3) of the sound speed). Physically equation (4.12) simply states that the numerical time-step has to be small enough so that information from one interface doesn't reach the next interface (in which case different Riemann problems would be mixed and the previous discussion would not hold). In other words all the information required to solve the fluid evolution in cell i during δt has to be contained within the cells effectively used by the code to do the computations at that step. Numerically condition (4.12) is parametrized by the *Courant number*

$$C = \frac{u_{\max}\,\delta t}{\delta x} \in]0, 1[\,. \tag{4.13}$$

4.1.2 Shock Setup and Boundary Conditions

The shock wave is generated by a supersonic piston: a piston of constant Mach number $M_{\mathrm{p}} = u_{\mathrm{p}}/c_{s,\mathrm{upst}}$ generates a shock of constant Mach number $M_{\mathrm{S}} = u_{\mathrm{S}}/c_{s,\mathrm{upst}}$ given by (eg Landau and Lifshitz (1959))

$$M_{\mathrm{S}} = \frac{\gamma+1}{4} M_{\mathrm{p}} + \sqrt{1 + \left(\frac{\gamma+1}{4} M_{\mathrm{p}}\right)^2}. \tag{4.14}$$

Equation (4.14) can be inverted as :

$$M_{\mathrm{p}} = \left(1 - \frac{(\gamma-1)M_{\mathrm{S}}^2 + 2}{(\gamma+1)M_{\mathrm{S}}^2}\right) M_{\mathrm{S}}. \tag{4.15}$$

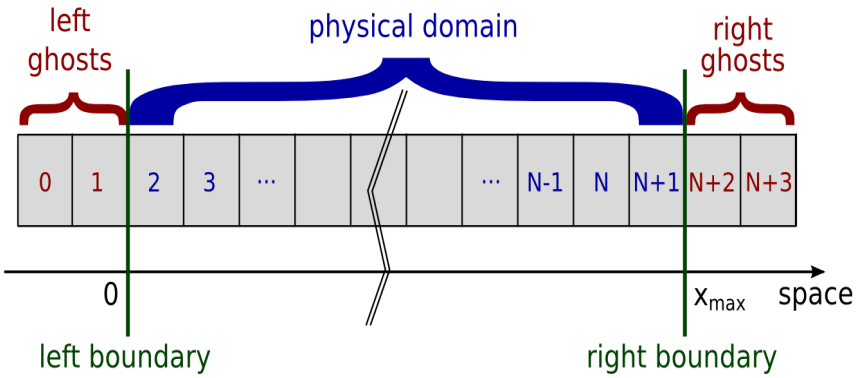

Figure 4.4: Sketch of the computational domain.

The piston motion is imposed through the left boundary conditions (so that the shock is travelling to the right). We recall that in finite volume codes boundary conditions are enforced thanks to *ghost cells* at the border of the actual physical domain (see figure 4.4), cells that are used for computational purpose only (and are not shown in the plots of all the results presented). As our hydrodynamical scheme is second order in space we need two ghosts cells at both the left and the right boundary. The right boundary condition is usually chosen to be gradient zero:

$$\begin{cases} \rho_{N+3} = \rho_{N+2} = \rho_{N+1} \\ u_{N+3} = u_{N+2} = u_{N+1} \\ P_{N+3} = P_{N+2} = P_{N+1} \end{cases} . \tag{4.16}$$

Regarding the left boundary condition we make use of two different initializations of the piston:

moving piston: if one enforces the correct jump conditions at the left boundary:

$$\begin{cases} \rho_0 = \rho_1 = r\,\rho_{\text{upst}} \\ u_0 = u_1 = u_p \\ P_0 = P_1 = P_{\text{upst}} \left(1 + \frac{\gamma(\gamma+1)u_p^2}{4c_{\text{upst}}^2} + \gamma \frac{u_p}{c_{\text{upst}}} \sqrt{1 + \frac{(\gamma+1)^2 u_p^2}{16 c_{\text{upst}}^2}} \right) \end{cases} \tag{4.17}$$

then the piston is emerging of it, travelling to the right at speed u_p, with the shock ahead of it, at speed given by equation (4.14).

fixed piston: as a piston is basically a moving wall, a simple way to initialize it is to work in the piston frame (in which the upstream medium is

given a velocity of $-u_{\rm p}$) using a "reflecting" left boundary condition:

$$\begin{cases} \rho_0 = \rho_3 \\ u_0 = -u_3 \\ P_0 = P_3 \end{cases} \qquad \begin{cases} \rho_1 = \rho_2 \\ u_1 = -u_2 \\ P_1 = P_2 \end{cases} . \tag{4.18}$$

A great advantage of this method is that, as we only simulate the *relative* motion of the shock (at speed $u_s - u_p$), we can use much smaller grids. But this method has a drawback too: in the piston frame the flow between the piston and the shock is quasi-stationnary, which is more difficult for the Godunov scheme to handle properly (see eg **?**) – particularly when adding the transport of cosmic-rays.

All the simulations presented to validate our code in chapters 4, 5, 6 make use of the "fixed piston" initialization. In the simulations of chapter 8 we found the need to use the "moving piston" initialization (in these cases the diffusion length of highly energetic particles is of the same order as the total distance travelled by the shock so that the space grid has to be big anyway).

4.2 Particles

Cosmic-rays are described with the kinetic approach of section 2.2.3.2, through their isotropic distribution function $f(x, p, t)$ defined so that their density is

$$n(x,t) = \int_p f(x,p,t) 4\pi p^2 dp. \tag{4.19}$$

f obeys the Fokker-Plank equation (2.65), here written in the conservative form:

$$\frac{\partial f}{\partial t} + \frac{\partial u f}{\partial x} = \frac{\partial}{\partial x}\left(D\frac{\partial f}{\partial x}\right) + \frac{1}{3p^2}\frac{\partial p^3 f}{\partial p}\frac{\partial u}{\partial x}. \tag{4.20}$$

The second l.h.s. term represents convection : cosmic-rays are advected in space as they are bound to the fluid by scattering off the magnetic waves present in it. Here again we neglect the movements of the scattering centres (the waves) with respect to the fluid ($v_A \ll u$), so that we don't consider diffusion in momentum (known as Fermi II acceleration). We consider only Fermi I acceleration, made possible through the combined effect of space diffusion (conveniently described by the diffusion coefficient $D(x,p)$, see section 2.1.2.1 and chapter 5) and momentum advection (powered by the velocity divergence of the flow $\partial u/\partial x$, see section 2.2.3).

4.2.1 Transport Scheme

From now on we consider that cosmic-rays are protons (of mass m_p), and we express cosmic-rays momenta in $m_p c$ units (and their velocities in c units, their energy and pressure in $m_p c^2$ units).

Following Falle and Giddings (1987) we work with $g = p^4 f$ and $y = \ln(p)$ for numerical convenience. We then rewrite equation (4.20) as

$$\frac{\partial g}{\partial t} + \frac{\partial ug}{\partial x} = \frac{\partial}{\partial x}\left(D\frac{\partial g}{\partial x}\right) - u_y \frac{\partial g}{\partial y} + u_y g \tag{4.21}$$

where $u_y = -\frac{1}{3}\frac{\partial u}{\partial x}$ appears as a y-advection velocity (note also the new source term $u_y g$). The momentum variable y is linearly discretized with step δy, so that in each space cell (indexed by i) we have the full piece-wise spectrum of the particles (indexed by j). Our kinetic scheme follows the one presented by Falle and Giddings (1987), but for the fact that we use here a Eulerian code (instead of a Lagrangian one) so that we have to deal with space advection. In fact the particle transport is done in two steps, using the operator splitting technique. Space transport (l.h.s of equation (4.21)) is embedded into the hydrodynamic Godunov module: during each hydrodynamic step cosmic-rays are transported with the fluid as a passive tracer, so that the flux of particles of energy j at the interface $i + 1/2$ between states X_i and X_{i+1} is

$$F_{i+1/2}(g_j) = \begin{cases} \frac{g_{i,j}}{\rho_i} F_{i+1/2}(\rho) & F_{i+1/2}(\rho) > 0 \\ \frac{g_{i+1,j}}{\rho_{i+1}} F_{i+1/2}(\rho) & F_{i+1/2}(\rho) < 0 \end{cases} . \tag{4.22}$$

Then diffusive acceleration (r.h.s. of equation (4.21)) is solved using a separate finite-difference module. Ignoring the space transport terms, equation (4.21) is discretized as

$$\begin{aligned} \frac{g_{i,j}^{n+1} - g_{i,j}^{n}}{\delta t} &= \omega^n \frac{D_{i+\frac{1}{2}}(g_{i+1,j}^{n} - g_{i,j}^{n}) - D_{i-\frac{1}{2}}(g_{i,j}^{n} - g_{i-1,j}^{n})}{\delta x^2} \\ &+ \omega^{n+1} \frac{D_{i+\frac{1}{2}}(g_{i+1,j}^{n+1} - g_{i,j}^{n+1}) - D_{i-\frac{1}{2}}(g_{i,j}^{n+1} - g_{i-1,j}^{n+1})}{\delta x^2} \\ &- {u_{y_i}}^n \frac{g_{i,j^+}^{n} - g_{i,j^-}^{n}}{\delta y} + {u_{y_i}}^n g_{i,j}^{n} \end{aligned} \tag{4.23}$$

where we have allowed for a space-dependent diffusion coefficient, to be evaluated at the cells interfaces $i \pm 1/2$, and where ω^n are coefficients which define the particular numerical scheme (see below).

Y-advection (last two r.h.s terms) is discretized using an upwind scheme, so that $j^+ = j$ and $j^- = j - 1$ when $u_y > 0$. This leads to a Courant condition

$$\delta t_{\mathrm{adv},y} < \frac{\delta y}{u_{y_{\max}}} \tag{4.24}$$

usually slightly more restrictive than the hydrodynamic condition (4.24): in that case we just sub-cycle DSA according to the hydrodynamic time-step $\delta t_{\mathrm{adv},x}$.

The Courant condition for the diffusive terms with a fully explicit scheme now reads

$$\delta t_{\mathrm{diff},x} < \frac{\delta x^2}{2D_{\max}} \tag{4.25}$$

which is much more restrictive than the advection condition, because of its quadratic dependence on the space resolution, and because D is an increasing function of p (see section 2.1.2.1) so that exploring acceleration to higher maximum momenta requires lowering $\delta t_{\mathrm{diff},x}$. To overcome this limitation we use implicit schemes which are not limited by the Courant condition (but at the cost of more involved computations, and with the risk of loosing accuracy control). As seen from equation (4.23) our scheme can be explicit ($\omega^n = 1, \omega^{n+1} = 0$), implicit ($\omega^n = 0, \omega^{n+1} = 1$), or both, the special case $\omega^n = 1/2, \omega^{n+1} = 1/2$ being known as the *Crank-Nicholson* scheme. This scheme is of particular interest as it is the only one to be second order in both space and time. However it has some drawbacks too, as it may give unphysical negative values for large values of δt (Park and Petrosian 1996). In that respect the fully implicit scheme is more robust (but it is less accurate). Using an implicit scheme we now have to solve (for each momentum bin j) a linear system of the form

$$a_i X_i = b_i X_{i+1} + c_i X_{i-1} + d_i \tag{4.26}$$

where $X_i = g_i^{n+1}$ is the new value of g in cell i and the coefficients a_i, b_i, c_i can be obtained from equation (4.23). This system being tridiagonal it can easily be solved (using Thomas algorithm).

We have also investigated the *Super-Time-Stepping* technique (STS) which allows explicit schemes to overcome the Courant condition (see eg Alexiades et al. (1996) for an introduction). The basic idea of the method is to require stability not after each time-step δt_{exp} (as given by the Courant condition) but only after some longer "super-time-step" δT. δT will still be split into N_{sts} computational sub-steps τ_k, but the key point is that it is possible to split δT in much less than $N_{\mathrm{exp}} = \delta T / \delta t_{\mathrm{exp}}$ sub-steps. With the optimal choice of sub-steps, given by

$$\tau_k = \delta t_{\mathrm{exp}} \left((-1+\nu) \cos\left(\frac{2k-1}{N_{\mathrm{sts}}} \frac{\pi}{2} \right) + 1 + \nu \right)^{-1} \qquad k = 1 \ldots N_{\mathrm{sts}}, \tag{4.27}$$

we get $N_{\mathrm{sts}} = \sqrt{N_{\mathrm{exp}}}$ as $\nu \to 0$, so that we divide the order of magnitude of the required number of iterations by a factor 2. Note that ν is a free parameter which has to be carefully set-up by hand to some non-zero but small value: if $\nu = 0$ the scheme gets unstable, but if ν is too big N_{sts} rapidly rises and the STS is no longer efficient. We have successfully implemented this method in our code by requesting that the explicit diffusion scheme runs over super-time-steps $\delta T = \delta t_{\mathrm{adv}}$, that is to match the relevant advection time-step. However this technique didn't prove as time-saving as implicit schemes (but it might become more interesting in 3D geometry, where implicit schemes can be really cumbersome to implement).

4.2.2 Boundary Conditions

Regarding space diffusion, boundary conditions can be either *no flux* (reflecting boundaries) or *no particle* (absorbent boundaries). Regarding space advection cosmic-rays, being handled by the Godunov scheme, share the boundary conditions of the fluid density (section 4.1.2). In order to contain all the shock precursor in the simulation box, we always make sure that the distance between the shock and the right boundary is many times the diffusion length of particles of highest momenta, so that the actual numerical condition at $x_{\max}$ for cosmic-rays is actually not very important here. But we have to stress that we then don't explicitly deal yet with *escape* of particles upstream of the shock, although it is a key ingredient of the acceleration process at high energies. Indeed the momentum of particles grows according to equation (2.79) in the first stage of acceleration but at some point it will be limited by other processes. In particular the highest energy particles will escape the accelerator, because of the finite extent of the shock[1] and/or insufficient scaterring far upstream. To model this effect Ellison and co-workers (1990, 1993) included a "free escape boundary" in their Monte-Carlo simulations, simply removing any upstream particle reaching a specified distance x_{FEB}. In order to make detailled comparisons with these works Kang and Jones (1995) included this feature in their two-fluid code (by setting $P_{\mathrm{cr}} = 0$ upstream of x_{FEB}) and in their kinetic code (by setting $f = 0$ upstream of x_{FEB} for all momenta reaching this boundary). We could quite easily mimic geometrical effects in our code in the same way, but we haven't addressed this issue yet[2]. However we have to stress that in all the simulations presented in this thesis the maximum momentum achieved by particles is much lower than what is expected to be the maximum momentum produced by supernovae remnants, so that escape is not a crucial issue so far: we are investigating only early and intermediate stages of the shock evolution and particle acceleration. According to Berezhko (1996) geometric effects become important only above $\log(p_{\max}) = 3$, which is the maximum value we have investigated. In the future we plan to increase this value to $\log(p_{\max}) = 6$ or more, with a more precise treatment of the fate of the highest energy particles.

For particles we also need to define boundary conditions in momentum. We simply impose that $g(p < p_{\min}) = 0$ and $g(p > p_{\max}) = 0$. Note that the actual numerical condition at $p_{\max}$ is actually unimportant as (i) particles are advected from p_{inj} towards $p_{\max}$, so that no information propagates from this upper boundary, and (ii) we always stop simulations by the time particles reach $p_{\max}$, so that actually all cosmic-rays always remain within the momentum grid.

[1] It is because of this size limit that (isolated) supernovae remnants can't accelerate particles to energies much higher than the knee.

[2] Note that other effects may compete to set the actual maximum momentum of cosmic-rays, such as the magnetic field fate.

4.2.3 Injection Mechanism

Because of our approach consisting in dealing separately with the fluid and the cosmic-rays, we need to describe the injection of cosmic-rays from the fluid (see section 2.4). We simply parametrize it by the two quantities η (injection fraction) and $p_{\rm inj}$ (injection momentum) as defined in section 2.4.2. We recall that this two parameters can be reduced to a single one, ξ (the ratio of the gyro-radii of the cosmic-rays at injection energy and of the fluid at mean energy), thanks to equations (2.92) and (2.93). In that case both $p_{\rm inj}$ and η are time-dependent, providing a consistent description of the way injection is self-regulated in the case of modified shocks.

We thus add a source term to the r.h.s of equation (4.20):

$$Q_{\rm inj}(x,p,t) = \eta\left(\xi(t)\right)\frac{\partial F(x_{\rm S},t)}{\partial x}G(x-x_{\rm S})\delta(p-p_{\rm inj}) \tag{4.28}$$

where $x_{\rm S}$ is the shock location, $F(x_{\rm S}) = (\rho u)_{\rm S}/m_p$ is the particles flux through the shock (evaluated in the shock frame), $G(x) = \frac{1}{\sqrt{2\pi\epsilon}}\exp\left(-\frac{x^2}{2\epsilon^2}\right)$ is a Gaussian distribution which slightly spreads the injection around the shock location (as diffusion schemes behave badly with too sharp initials profiles, and as anyway the numerical width of the hydrodynamical shock is always of a few cells), and δ is the Dirac distribution. Moreover we have to take account of the fact that these particles are extracted from the thermal population. As usual we neglect the inertia of the fresh cosmic-rays, but we remove their energy from the fluid: we add a corresponding sink term to the fluid energy equation:

$$S(x,t) = \eta\left(\xi(t)\right)\frac{\partial F(x_{\rm S},t)}{\partial x}G(x-x_{\rm S})\frac{m_p u_{\rm inj}^2}{2}. \tag{4.29}$$

4.2.4 Cosmic-Rays Back-Reaction

To take the cosmic-rays pressure into account in the fluid dynamics (see equations (2.85), (2.86), (2.87) in section 2.3.1) we simply add the source term

$$\mathbf{Q}\left(\mathbf{X}\right) = \begin{pmatrix} 0 \\ -\nabla P_{\rm cr} \\ -u\nabla P_{\rm cr} \end{pmatrix} \tag{4.30}$$

on the r.h.s. of equation (4.1) (note that we neglect here the speed of the waves v_A with respect to the flow speed)[3]. Numerically $P_{\rm cr}$ is evaluated as

$${P_{\rm cr}}_i^n = \frac{4\pi}{3}\delta y\sum_j \frac{p_{i,j}}{\sqrt{1+p_{i,j}^2}}g_{i,j}^n. \tag{4.31}$$

[3]Note that this assumption can be a crude approximation for low Mach number shocks, and this limitation should be removed in the near future. However most supernovae shocks travelling in the interstellar medium are superalfvenic. In superbubbles the situation is unclear as the magnetic field is unknown (see section 7.3.1).

and its space gradient is computed using centred differences.

The particle back-reaction is done at each hydrodynamical step. If the hydrodynamical and kinetic time-scales are too different we may miss the actual cosmic-rays back-reaction. To prevent the cosmic-rays decoupling from the fluid we make sure that within each hydrodynamical time-step the relative variation of the fluid energy $\Delta e/e$ due to the cosmic-rays back-reaction is never higher than 10%.

4.3 Test 1: a Modified Shock

To test our code we start with the second test case from the pioneers of the kinetic approach Falle and Giddings (1987) (hereafter FG).

4.3.1 Test Design

The upstream medium is initially of constant density $\rho_1^0 = 1$ and pressure $P_1^0 = 1$. The piston Mach number is $M_\mathrm{p} = 3.5$, so that $M_\mathrm{S} = 4.87$, $u_\mathrm{S} = 4.52$ in the upstream rest frame, and $r = 3.55$.

There are no cosmic-rays upstream initially ($P_\mathrm{cr}^0 = 0$). Particles are injected at a constant rate $\eta = 0.0225$ at a variable momentum defined by $\xi' = 2$. The piston beta ($\beta = u_p/c$) is adjusted so that initially $p_\mathrm{inj}^0 = 10^{-1}$ as done in FG. The momentum grid extends from $\log(p_\mathrm{min}) = -3$ to $\log(p_\mathrm{max}) = +4$, with a resolution (not critical here) $\delta y = 0.23$ (that is 10 bins per decade). The diffusion coefficient is a power-law with a weak momentum dependence: $D(p) \propto p^{0.25}$. Its normalisation is adjusted so that the simulation unit time is the acceleration time-scale at injection $t_\mathrm{acc}(p_\mathrm{inj})$ (see equation (2.76)) as implicitly done in FG.

The simulation is run to $t_\mathrm{end} = 40$ as in FG to show convergence of the coupled fluid/cosmic-rays system (in the linear case we then expect cosmic-rays to be accelerated to $\log(p_\mathrm{max}) = 3.2 < 4$). The space box size equals the distance travelled by the shock during that time (at constant velocity $u_\mathrm{S} = 1.77$ with respect to the piston located at $x = 0$) plus 10 times the diffusion length of the highest energy cosmic-rays[4] that is $x_\mathrm{max} = 250$. The space resolution is set to $\delta x = 2.9 \times 10^{-2}$ to achieve numerical convergence[5]. The hydrodynamical Courant number is set to 0.8, the kinetic scheme is sub-cycled by another factor of 2.

4.3.2 Test Results

The results of the simulation are presented in figures 4.5 to 4.9.

[4]Corresponding to $\Lambda = 10$ as defined by equation (5.4)

[5]Corresponding to $\lambda = 0.050$ at p_min (and $\lambda = 0.037$ at p_inj^0) as defined by equation (5.3)

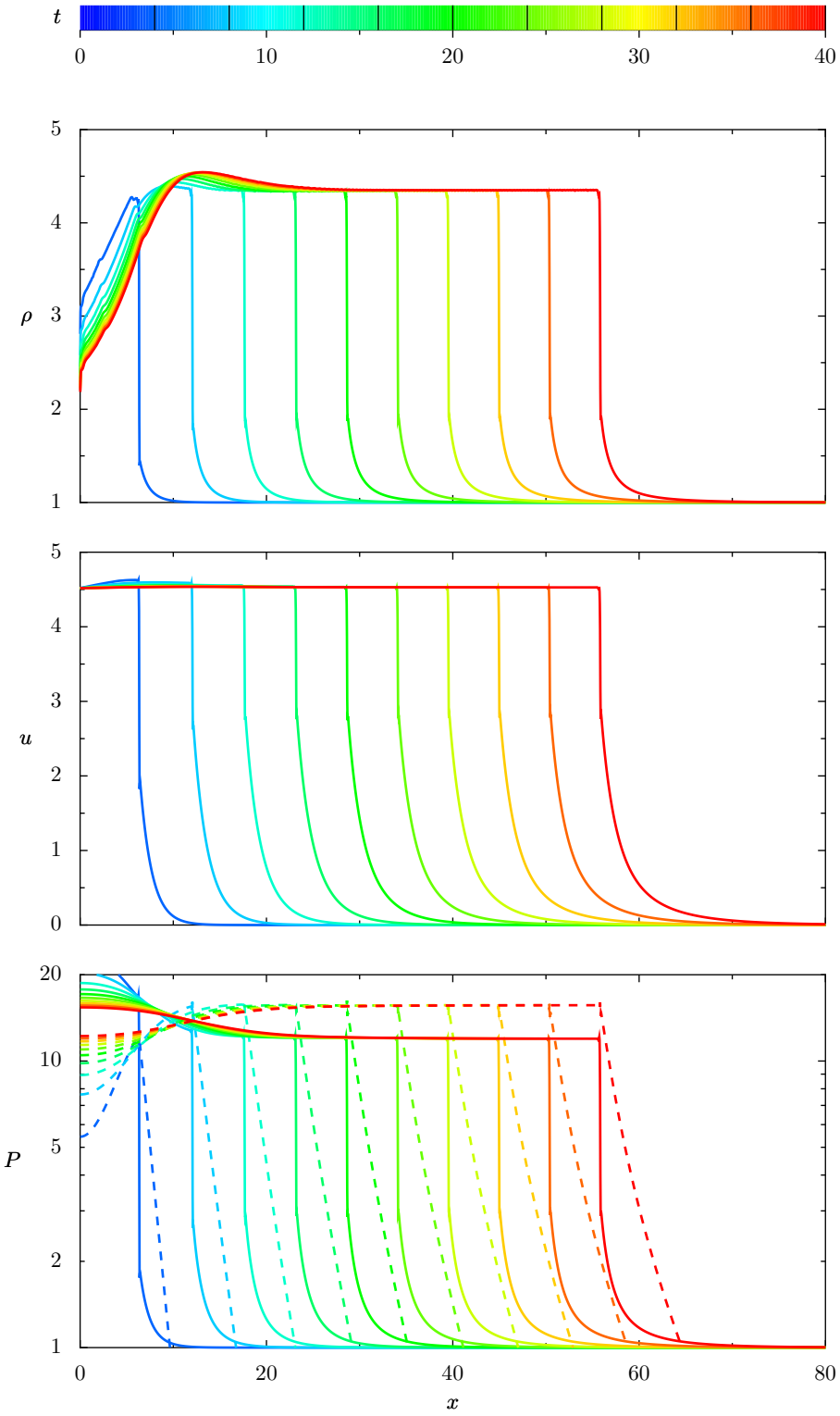

Figure 4.5: Time evolution of the hydrodynamical profiles for a modified shock (with $D(p) \propto p^{0.25}$).
See section 4.3.1 for simulation details). Plotted are the fluid density ρ, velocity u and pressure P (the cosmic-rays pressure $P_{\rm cr}$ is added dashed).

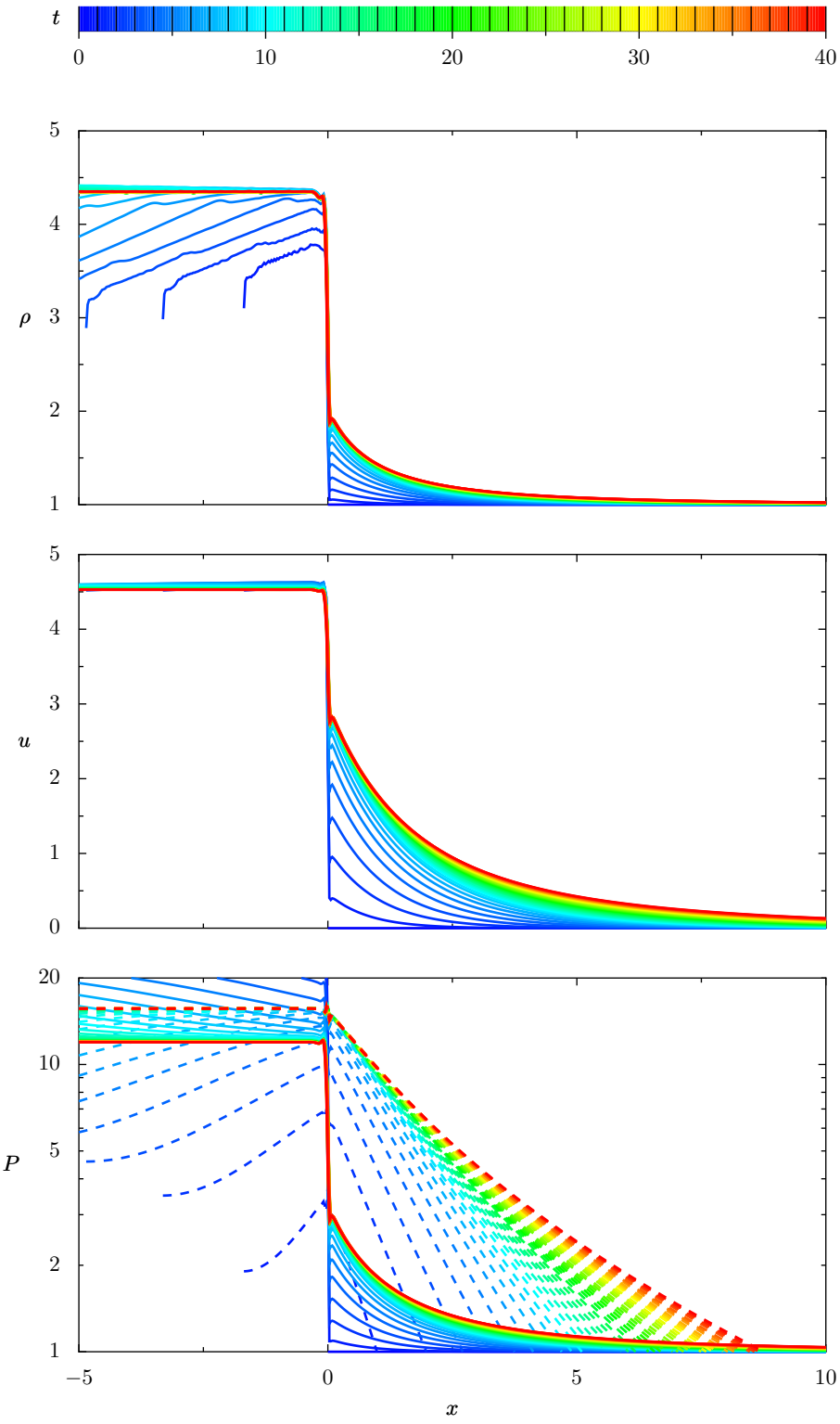

Figure 4.6: Same as figure 4.5, but in the shock frame instead of the upstream rest frame.

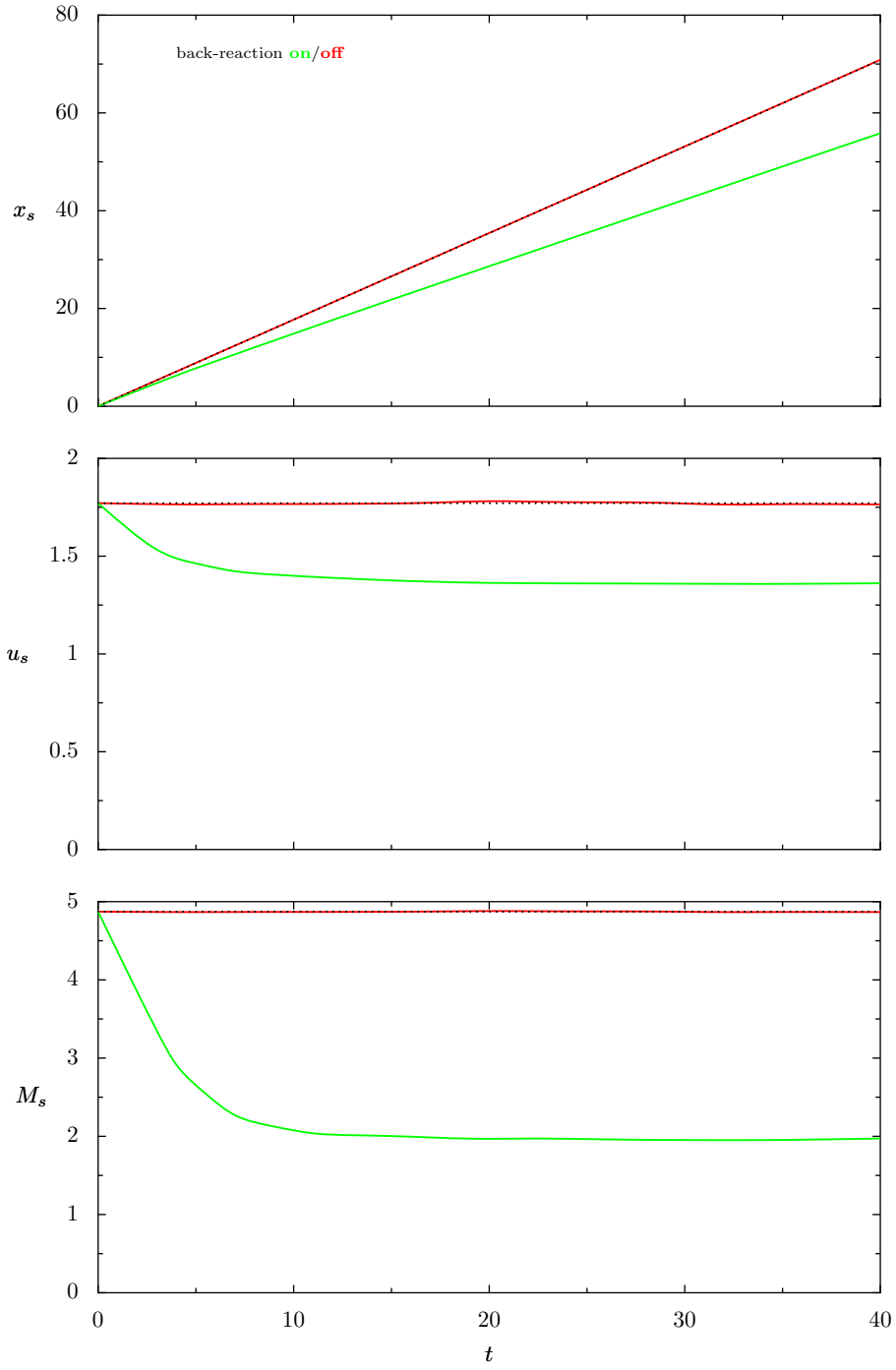

Figure 4.7: Evolution of the strongly modified shock (in green) of figure 4.5. The shock position x_s, velocity u_s and Mach number M_s are plotted versus time. In red are added the results when cosmic-rays back-reaction is turned off, which follow the theoretical evolution (dotted).

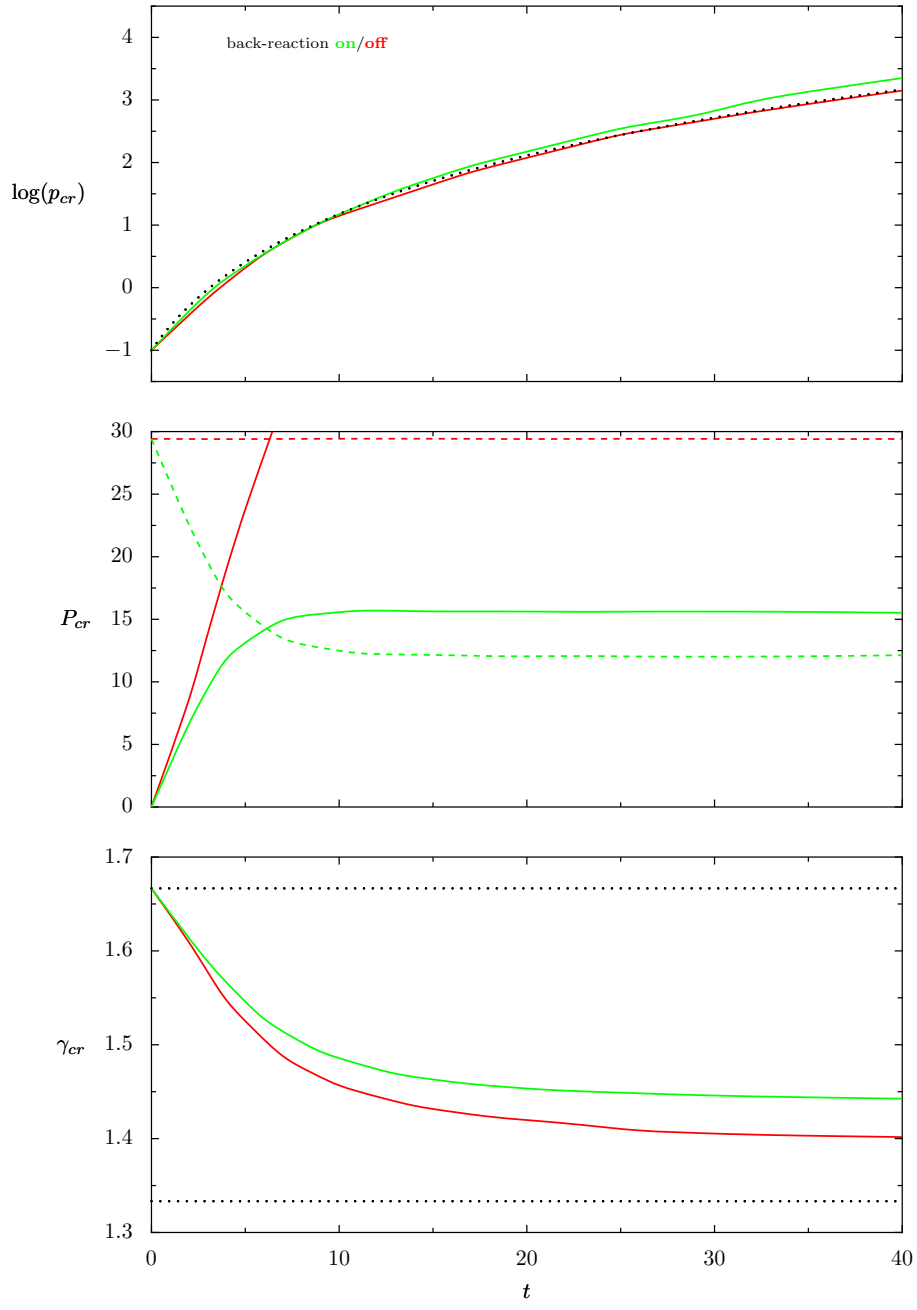

Figure 4.8: Evolution of some key cosmic-rays parameters for the modified shock (in green) of figure 4.5.
Plotted versus time are the maximum momentum $p_{\rm cr}$ (its theoretical linear evolution is added dotted, see equation (2.79)), pressure $P_{\rm cr}$ (the fluid pressure is added dashed) and adiabatic index $\gamma_{\rm cr}$ (the non-relativistic (5/3) and ultra-relativistic (4/3) values are added dotted). In red are added the results when cosmic-rays back-reaction is turned off.

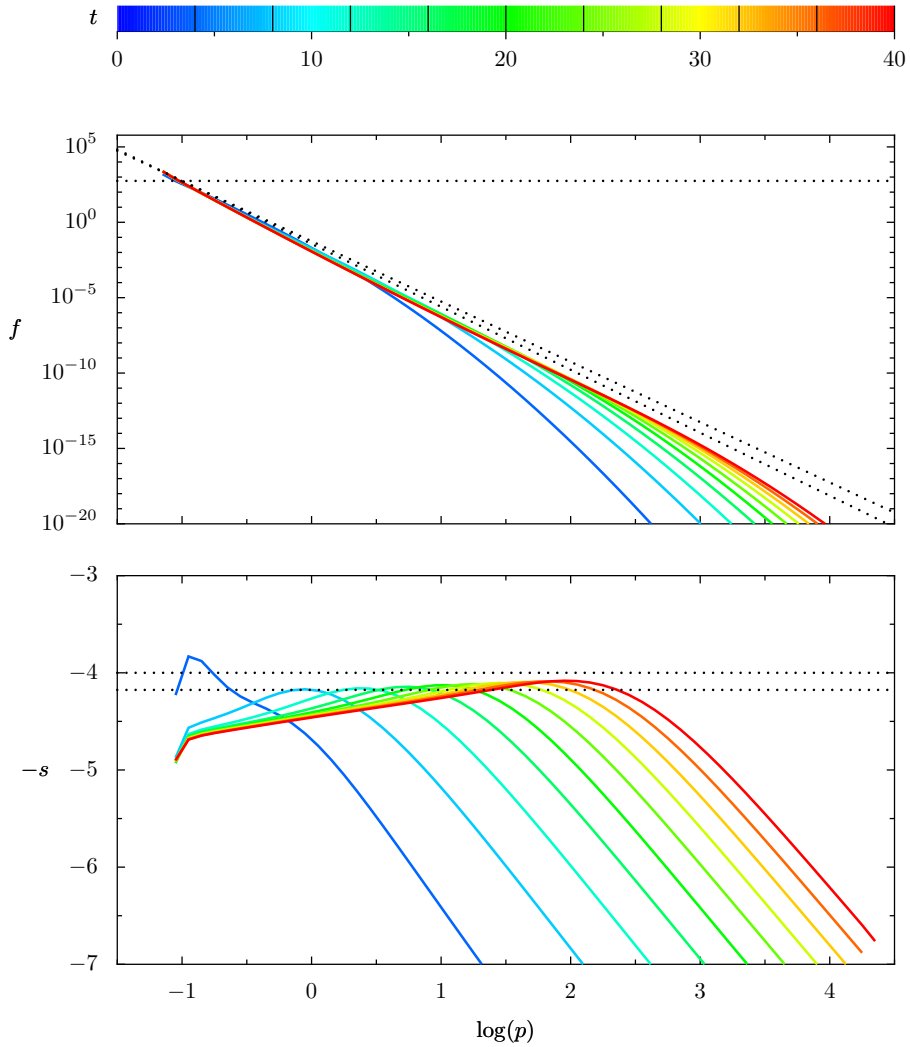

Figure 4.9: Time evolution of the cosmic-rays spectrum just downstream of the modified shock of figure 4.5.
The spectrum $f(p)$ is shown on top. On this plot the horizontal dotted line marks the theoretical spectrum normalization f_0 at injection (in the linear case) and the two other dotted lines are power-law spectra of slopes $s = 4$ and $s_1 = 4.18$ = the theoretical linear slope (for this shock compression ratio $r = 3.55$) and of same normalization f_0 at injection. These two remarkable slope values are also marked dotted on the bottom plot, which shows the spectrum logarithmic slope $-s = \partial \log(f)/\partial \log(p)$.

Figure 4.5 shows the hydrodynamical profiles for various times. The shock is visible as a discontinuity traveling to the right (the piston is fixed at $x = 0$, but the velocities are plotted in the far upstream rest frame). As expected (see section 2.3.2) it is smoothed by the presence of a precursor, visible in all profiles, caused by the presence of cosmic-rays upstream of the shock – their pressure, added dashed on the bottom plot, exceeds the fluid one. We see that after a quick initial adjustment the shock structure reaches a quasi-stationary state, as observed by FG.

Figure 4.6 shows the same profiles in the shock frame. We see how the precursor grows over time and how the shock structure converges to a quasi-equilibrium state (note that the time discretization is linear).

Figure 4.7 shows the time evolution of the shock (in green). We see that after the quick initial adjustment the shock velocity is again almost constant, but slower than in the linear case (added in red).

Figure 4.8 shows the time evolution of the cosmic-rays population (again with back-reaction switched on/off in green/red). In both cases the cosmic-rays maximum momentum agrees well with the dotted theoretical linear prediction (the determination of p_{cr} is less reliable in the non-linear case, the differences seen are not conclusive). Note again that in our present simulations its value is only age-limited, whereas in real astrophysical environments it would be also size-limited. The cosmic-rays pressure quickly converges thanks to the regulation effect of the back-reaction (as both the sub-shock mass flux and downstream temperature are reduced) whereas it grows linearly in time in the linear regime. The cosmic-rays adiabatic index is computed as $\gamma_{\mathrm{cr}} = 1 + P_{\mathrm{cr}}/e_{\mathrm{cr}}$ where P_{cr} is the "cosmic-rays fluid" pressure given by equation (2.80) and e_{cr} is the "cosmic-rays fluid" internal energy density given by equation (2.89). As expected γ_{cr} starts at the same value as the adiabatic index of a non-relativistic fluid $\gamma = 5/3$ (as cosmic-rays are injected from the thermal pool) and goes down as cosmic-rays are accelerated to high energies (tending to the adiabatic index $\gamma = 4/3$ of a relativistic fluid). We note that γ is lowered more and more slowly in time, but that it never reaches convergence as P_{cr}.

The latter quantities are global (macroscopic) properties of the cosmic-rays (seen as a fluid). But our code is a kinetic one, with a full cosmic-rays spectrum in p in each x cell, from which P_{cr} and γ_{cr} are derived. Figure 4.9 shows the cosmic-rays spectrum (and its slope) just downstream of the shock at some given times. We see how DSA progressively builds the cosmic-rays distribution. Note that the time discretization is linear as in figure 4.5, so we see that it takes more and more time to accelerate particles to higher energies: this is because of the diffusion coefficient dependence on p (see equation (2.76)). Initially the cosmic-rays are injected at $\log(p^0_{\mathrm{inj}}) = -1$, with a normalization which agrees with the theoretical one in the linear case (see equation (2.61)). But soon afterwards p_{inj} drifts slightly towards lower energies as the downstream temperature is reduced (see the bottom plot of figure 4.5). The cosmic-rays spectra extend over 20 orders of magnitude, they seem to approach a power-

law form but the plot of their local slope clearly shows that they are actually concave: they are softer at low energies and harder at high energies than the theoretical linear slope $s_1 = 4.18$. This is another well-known feature of the acceleration by cosmic-rays-modified shocks (see section 2.3.2), due again to the energy dependence of the diffusion coefficient, which implies that cosmic-rays of different energies explore different regions around the shock and thus "see" different compression ratios (because of the precursor they create in the fluid, see figure 4.5).

Finally we would like to comment on the fact that, at the end of the simulation, the shock structure reaches a quasi-converged state, although particles are still accelerated and don't escape the system. First we note that only a very small fraction of particles reach very high energies, whereas, at low energies, injection is reduced as the subshock weakens. And even more important is the fact that as particles are accelerated to higher and higher energies they travel farther and farther away from the shock and on longer and longer time-scales (because of their momentum-dependent diffusivity). Thus, although energy is not escaping the whole computed system, it is considerably diluted around the (sub-)shock – allowing for large overall compression (see eg Kang et al. 2002).

4.3.3 Comparison with Previous Study

Results presented here can be compared to FG second test (section 4.2, especially their figure 7). Most notably the fluid and cosmic-rays pressure have exactly the same time evolution, with a convergence at the same values within a few percents. The shock Mach number and cosmic-rays adiabatic index also agree well. We have also succesfully reproduced their two other test cases of weakly modified and very strongly modified shocks (not shown here). This is to our knowledge the first direct comparison to the results of FG, and this success cross-validates the two codes. It proves that our code can handle well a modified shock produced by the tight coupling of fluid hydrodynamics and cosmic-rays diffusive acceleration.

Finally we note that in the intermediate case we have chosen to design our tests the shock Mach number isn't very high, whereas non-linear effects are important for high Mach number shocks as expected in young supernova remnants, but technically our code can deal with any relevant value of the Mach number. For instance in section 8.2.3.2 we present the results of numerical simulations of strong shocks of $M_S = 50$ propagating in a superbubble-like environment.

References

Alexiades, V., Amiez, G., and Gremaud, P. A. (1996). Super-time-stepping acceleration of explicit schemes for parabolic problems. *Communications in Numerical Methods in Engineering*, 12(1):31–42.

Berezhko, E. G. (1996). Maximum energy of cosmic rays accelerated by supernova shocks. *Astroparticle Physics*, 5:367–378.

Downes, T. P. and Ray, T. P. (1998). Numerical simulations of the Kelvin-Helmholtz instability in radiatively cooled jets. A&A, 331:1130–1142.

Ellison, D. C., Giacalone, J., Burgess, D., and Schwartz, S. J. (1993). Simulations of particle acceleration in parallel shocks: Direct comparison between Monte Carlo and one-dimensional hybrid codes. J. Geophys. Res., 98:21085.

Ellison, D. C., Moebius, E., and Paschmann, G. (1990). Particle injection and acceleration at earth's bow shock - Comparison of upstream and downstream events. ApJ, 352:376–394.

Falle, S. A. E. G. (1991). Self-similar jets. MNRAS, 250:581–596.

Falle, S. A. E. G. and Giddings, J. R. (1987). Time-dependent cosmic ray modified shocks. MNRAS, 225:399–423.

Godunov, S. K. (1959). Finite difference method for numerical computation of discontinous solution of the equations of fluid dynamics. *Mat. Sb.*, 47(271).

Kang, H. and Jones, T. W. (1995). Diffusive Shock Acceleration Simulations: Comparison with Particle Methods and Bow Shock Measurements. ApJ, 447:944–961.

Kang, H., Jones, T. W., and Gieseler, U. D. J. (2002). Numerical Studies of Cosmic-Ray Injection and Acceleration. ApJ, 579:337–358.

Landau, L. D. and Lifshitz, E. M. (1959). *Course of theoretical physics - Fluid mechanics*. Pergamon Press.

Park, B. T. and Petrosian, V. (1996). Fokker-Planck Equations of Stochastic Acceleration: A Study of Numerical Methods. ApJS, 103:255–267.

Roe, P. L. (1986). Characteristic-based schemes for the Euler equations. *Annual Review of Fluid Mechanics*, 18:337–365.

van Leer, B. (1977). Towards the ultimate conservative difference scheme. IV. A new approach to numerical convection. *Journal of Computational Physics*, 23(3):276–299.

Chapter 5

Resolving Diffusion Scales: Adaptive Mesh Refinement

We have seen in the previous chapter how the energy dependence of the diffusion coefficient drives the main features of modified shocks. This is also the reason why realistic kinetic simulations of DSA are numerically a challenging problem: the difficulty is the potentially huge range of space and time scales which must be resolved. We now investigate this important issue in more details, showing how *adaptive mesh refinement* can help alleviate this problem.

5.1 Principle

The fluid Euler equations don't introduce any scales, but the cosmic-rays transport equation does, through the momentum-dependent coefficient D (see section 2.1.2.1). This is a difficulty for the kind of code we use, in which space is discretized in cells of finite size, so that we have to consider more involved space discretizations than the regular one used in chapter 4.

5.1.1 The Problem: Diffusion Scales

Whatever the precise description used for D, the key point is that it is thought to be a growing function of p. As the cosmic-rays momenta span many orders of magnitude, from say $p = 10^{-2}$ to $p = 10^6$ or even $p = 10^9$ for galactic cosmic-rays (in $m_p c$ units), this introduces a wide range of scales. The relevant time scale is the diffusive acceleration time-scale (see equation (2.76)):

$$t_{\mathrm{acc}}(p) \propto \frac{D(p)}{u_{\mathrm{S}}^2}. \tag{5.1}$$

The relevant space scale is the diffusion length of the cosmic-rays upstream of the shock (see equation (2.74)):

$$x_{\mathrm{upst}}(p) = \frac{D(p)}{u_{\mathrm{S}}}. \tag{5.2}$$

The space scales range from the microscopic scale where the cosmic-rays decouple from the fluid (of the order of a few thermal gyration lengths) to macroscopic scales (of the order of the supernova remnant radius for high energy cosmic-rays, which then escape, thus limiting the $p_{\max}$ the remnant can achieve).

From a numerical perspective the space resolution δx of the grid is dictated by the diffusion of the lowest energy cosmic-rays (we must ensure $\delta x \ll D(p_{\min})/u_S$ to catch their dynamics well) whereas the size of the grid is dictated by the diffusion of the highest energy cosmic-rays (we must ensure $x_{\max} \gg D(p_{\max})/u_S$ not to lose them artificially). The ratio $D(p_{\max})/D(p_{\min})$, and thus the number of cells $x_{\max}/\delta x$, may exceed ten orders of magnitude if $D(p) \propto p$, which is extremely demanding in terms of memory requirements and computing time. This is the reason why the first simulations were made with low p dependence of D ($D(p) \propto p^{0.25}$ in Falle and Giddings (1987) and in Kang and Jones (1991)), before exploring the Bohm regime (Duffy 1992) – which was achieved by using more involved numerical techniques.

5.1.2 The Answer: Adaptive Mesh Refinement

Fortunately we need very high resolution (δx small) only around the shock, as this resolution is required by the lowest energy particles only, which don't diffuse far away from the shock (see figure 2.5). More generally cosmic-rays of a given energy require a certain space resolution on a certain space extended around the shock (the key parameter being $x_{\text{upst}}(p)$). Hence the idea, pioneered by Duffy (1992) and developed by Kang et al. (2001), to implement techniques of Adaptive Mesh Refinement (AMR) to allow the numerical resolution δx to vary according to the needs of the cosmic-rays that are likely to be found at a given location at a given time. This allows correct handling of the transport of cosmic-rays whereas considerably lowering the numerical requirements[1].

5.2 Scheme

5.2.1 Grids Design

We adopt here the technique of nested grids[2] (Berger and Oliger 1984): N subgrids of increasing resolution are added to the base-grid around the shock (see figure 5.1). The resolution of the grid at level k (base grid being level 0) is $\delta r_k = \delta r_0/R^i$ where R is the arbitrary refinement factor, taken as usual to be $R = 2$.

[1] See also Berezhko et al. (1994) for a different approach based on a change of variable.

[2] We haven't used tree-based AMR as this technique is much more complicated to implement and as its main advantage is its versatility but the situation we have to deal with is well defined.

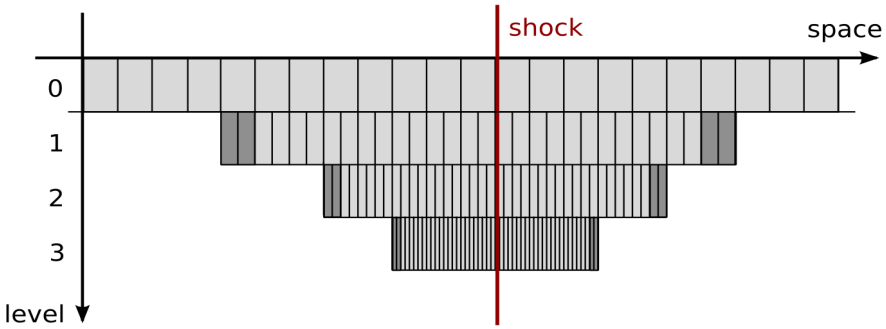

Figure 5.1: Sketch of the AMR grids hierarchy.
The ghosts cells, used to apply nested boundary conditions, are shown darker.

The grid hierarchy is automatically designed by the code according to the cosmic-rays diffusion properties as follows. The resolution at the last sub-level N is adapted to the lowest energy cosmic-rays, of momentum $p_{\rm min} = p_N$:

$$(\delta x)_N = \lambda \times x_{\rm upst}(p_{\rm N}) \tag{5.3}$$

where $\lambda \ll 1$ (Kang and Jones (1991) suggest $\lambda = 0.05$, and this is indeed what test 1 of section 4.3 required for full convergence). The resolution of the $N-1$ sub-level will necessarily be $\delta x_{N-1} = R \times \delta x_N$. This resolution will be good enough for all particles of momentum above some p_{N-1} so that $\delta x_{N-1} = \lambda \times x_{\rm upst}(p_{N-1})$. Then the sub-grid N should take care of all cosmic-rays of momenta from $p_N = p_{\rm min}$ to p_{N-1}, in particular it must contain them as they diffuse from the shock, so we set its half-size Δx as

$$(\Delta x)_N = \Lambda \times x_{\rm upst}(p_{N-1}) \tag{5.4}$$

with $\Lambda > 1$. The sub-grid N is now fully defined by its size Δx and resolution δx, the process is then iterated to the level $N-1$, the resolution of which is imposed by the resolution at level N and the size of which is imposed by the resolution at level $N-2$, and so on. The total number of sub-grids is adjusted semi-empirically to maximize the AMR efficiency.

From now on the grids design will be conveniently described by the two parameters λ and Λ defined by relations (5.3) and (5.4). We use the same Λ for all sub-grids, and we extend its definition to a base grid where Δx now refers to the distance $x_{\rm max} - u_{\rm S} \times t_{\rm end}$ between the position of the shock at the end of the simulation and the position of the right physical boundary (so that in all cases Δx is the minimum distance upstream of the shock).

```
advance(grid, dt):
  | transport_hydro(grid, dt)
  | transport_dsa(grid, dt)
  | track_shock(grid)
  | if (grid = LAST) inject(grid)
  | for (i = 1 to R)
  |   | advance(grid->child, dt/R)
  | get_finer(grid, grid->child)
  | correct_fluxes(grid, grid->child)
```

Figure 5.2: The AMR recursive algorithm.
The functions doing the actual physical computations are in bold (they implement the schemes presented in chapter 4), the rest deals with grids refinement (as explained in section 5.2.2, with the last two functions detailed on figure 5.3).

5.2.2 AMR Algorithm

5.2.2.1 Grids Motion

The grid hierarchy is set up around the shock position at start-up and moves with it over time (so that initially it emerges out of the left boundary). For the shock tracking to remain efficient with any number of grids levels we allow each sub-grid to move independently both in space and time. However a sub-grid can move only by $R = 2$ of its cells to keep the simple 1 to 2 correspondence of the AMR refinement scheme (and only at the end of a complete refinement step). The shock is located as the cell with the maximum absolute divergence of velocity. We thus keep shock tracking simpler than Kang et al. (2001), who use the waves speed given by the Riemann solver to locate the shock position *within a single cell* and then sub-divide this cell at this position so that the shock is always exactly coincident with an interface, which allows them to keep it as a perfect discontinuity – with the cost of completely redefining the sub-grids hierarchy at each time-step so that it matches the current arbitrary shock position.

5.2.2.2 Grids Update

At each hydrodynamical time-step $\delta t_{\mathrm{adv,x}}$ (as given by equation (4.12) where δx is the base grid resolution) the whole hierarchy is updated, from the base grid to the last sub-grid. We recall that the refinement is both a refinement in space (the resolution is divided by R at each level) and a refinement in time (because of the Courant condition (4.12)), so that the sub-grid at level $n = 1 \dots N$ actually makes R^n steps of length $\delta t_{\mathrm{adv},x}/R^n$ each. The nested-grids algorithm is a recursive one (see figure 5.2): at each level (from top to bottom) we update the quantities on the whole grid, we run the same process at the sub-level, and then we replace the grid coarse quantities by the sub-grid

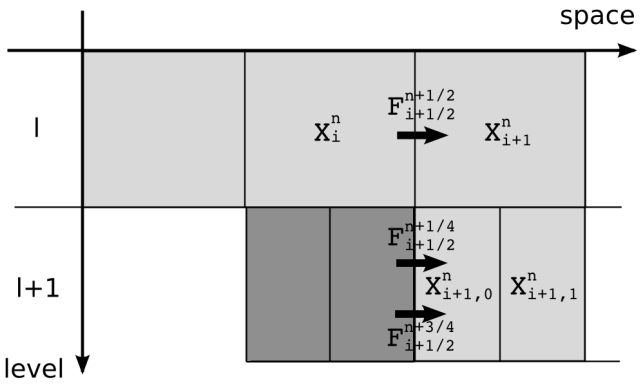


```
get_finer(grid):
  for (i overlapped by grid->child)
    X_i^n ← ( X_{i,0}^n + X_{i,1}^n )/2

correct_fluxes(grid):
  for (i at the border of grid->child)
    X_i^n ( F_{i+1/2}^{n+1/2} .dt) ← X_i^n ( F_{i+1/2}^{n+1/4} .dt/2 + F_{i+1/2}^{n+3/4} .dt/2)
```

Figure 5.3: The AMR correction process between two grids levels.

finer quantities. For that matter we simply take the mean of the sub-cells: if a cell i of level n is split into R cells i, ι at level $n+1$ its quantities X are updated as

$$\tilde{X}_i = \frac{1}{R} \sum_{\iota=1}^{R} X_{i,\iota} \,. \tag{5.5}$$

Thus the information propagates from the deepest levels to the top ones. Note that updating a grid with its child values not only means replacing the quantities of overlapping cells, but also correcting the values of the first non-refined cells at the border of the sub-grid (see figure 5.3): indeed these values have been previously computed using interface fluxes determined from the coarse quantities of some not yet refined cells, and the sub-grid has now computed better estimates of these fluxes. More precisely the quantities X in the cell i of level n being the first non-refined cell at the left of level $n+1$ have to be updated as

$$\tilde{X}_i = X_i + \frac{\delta t}{\delta x} \left(-F_{i+1/2}^{\text{adv}} \left(\delta t \right) + \frac{1}{R} \sum_{\iota=1}^{R} \tilde{F}_{i+1/2}^{\text{adv}} \left(\frac{\delta t}{R} \right) \right) \tag{5.6}$$

where the interface flux $F_{i+1/2}^{\text{adv}}$ over δt had been obtained on level n itself and the interface fluxes $\tilde{F}_{i+1/2}^{\text{adv}}$ over R sub-steps $\delta t / R$ of δt have been obtained on level $n+1$. This enforces matching of the fluxes at the boundaries of different

levels and therefore preserves the important property of the hydrodynamical scheme of respecting the conservation equations (see section 4.1.1).

To set up the refinement the child grid must be given appropriate boundary conditions to match its parent profiles (only once it is fully nested, as long as it intersects the left base-grid boundary it is given the same physical boundary conditions). Regarding the hydrodynamics we note that the advection fluxes are controlled directly by the hydrodynamic quantities, so that we simply fill the child's ghost cells with the corresponding values of its parent, that is with the same notations as above

$$X_{i,\iota} = X_i \quad \forall \iota = 1 \dots R \tag{5.7}$$

where i is the cell of level n covering the R ghost cells i, ι of level $n+1$. Regarding the kinetic part we note that diffusion fluxes are controlled by the *gradient* of the quantities, so that the previous approach wouldn't hold as the space resolution is grid-dependent. Our approach is to enforce matching of the diffusion flux between the child and parent level: we impose the border flux on the child grid to be

$$\tilde{F}^{\text{diff}}_{i+1/2}\left(\delta t/R\right) = F^{\text{diff}}_{i+1/2}\left(\delta t\right) \tag{5.8}$$

where again i is the cell of level n covering the ghosts cells of level $n+1$, and $F^{\text{diff}}_{i+1/2}$ is the flux already measured at level n. At the beginning of each sub-step $\delta t/R$ the values of the quantities X in the last ghost cell $\iota = R$ are adjusted so that their gradient at the interface satisfies equation (5.8). Note that this mechanism works whatever the diffusion coefficient scheme (be it explicit or implicit), but that the Crank-Nicholson scheme gets more sensitive because of such nested boundary conditions (it requires more sub-cycling).

Finally we note that the hydrodynamic and kinetic operators operate conjointly at each level, as refining them separately would artificially decouple their effects. Note also that injection is done at bottom level only (and at the end of a complete refinement step) and propagates to all the upper levels as they are updated.

5.3 Test 2: Bohm Scaling

Here we extend test 1 using a more realistic diffusion model.

5.3.1 Test Design

The physical parameters are the same as in section 4.3.1, but for the fact that we now use the relativistic[3] Bohm scaling for the diffusion coefficient, that is $D(p) \propto p$ (see section 2.1.2.1). Numerically we then enter a new world, because of the requirements induced by equations (5.1) (longer run) and (5.2) (higher resolution). Simulation of test 1 runs within 2 hours at high resolution on a desktop-class processor. Now with the same $p_{\max}$ it wouldn't be even possible to allocate the grid in memory. We thus apply the AMR technique to lower the numerical requirements. We use here $\lambda = 0.3$ at $\log(p_{\min}) = -1.5$ (that is $\lambda = 0.1$ at $\log(p^0_{\text{inj}}) = -1$); and $\Lambda = 6$ for each sub-grid (as we have observed that for $\Lambda \geq 6$ the sub-grids nested boundary conditions for diffusion are indifferent for all the cosmic-rays up to the momentum a sub-grid has to deal with) and $\Lambda = 10$ for the base grid. We use a better momentum resolution than in test 1: $\delta_y = 0.1$ (that is 23 bins per decade). We have run different simulations with different maximum momenta $\log(p_{\max})$ ranging from 0 to 3 by steps of 0.5. We have run each simulation up to the time required for cosmic-rays to reach this maximum momentum (derived from equation (2.79)), ranging accordingly from 10 to 10000 (the unit time is as for test 1 the acceleration time-scale at injection $t_{\text{acc}}(p_{\text{inj}})$ given by equation (2.76)). We set the Courant number to 0.5 and we sub-cycle the DSA scheme a few times (all the more so since we are at a deep level). The number N of sub-grids ranges from 1 to 7 as $\log(p_{\max})$ rises from 0 to 3.

5.3.2 Physical Results

Figures 5.4 to 5.8 show the results in the case $\log(p_{\max}) = 1$, $t_{\text{end}} = 100$, $N = 3$ (note that on figure 5.5 one sees how the grid hierarchy follows the shock). The global picture remains the same as in test 1: quick convergence to a quasi-steady state where the fluid and cosmic-rays pressures are of the same order (here the cosmic-rays pressure hasn't reached the fluid one). The effects of the dependence of D on p, which were already visible in test 1, are now enhanced: the shock precursor is more extended (figure 5.5), the cosmic-rays are more slowly accelerated towards high energies (figure 5.8, where we recall that the time discretization is linear).

Figures 5.9 and 5.10 show the shock evolution in the case $\log(p_{\max}) = 3$, $t_{\text{end}} = 10\,000$, $N = 7$. We see that the shock structure still evolves in a self-similar fashion. The time evolution of cosmic-rays is shown on figure 5.11 (in the case $\log(p_{\max}) = 2$, $t_{\text{end}} = 1\,000$, $N = 5$ and in the case $\log(p_{\max}) = 3$, $t_{\text{end}} = 10\,000$, $N = 7$). We note that the cosmic-rays parameters connect smoothly between the three simulations. We observe that the downstream cosmic-ray pressure is still rising, but on longer and longer time-scales.

[3]Using the exact Bohm scaling, that is $D(p) \propto p^2$ at injection energies, considerably increases the numerical cost of the simulation without changing much the physical results, see eg Kang and Jones (2006).

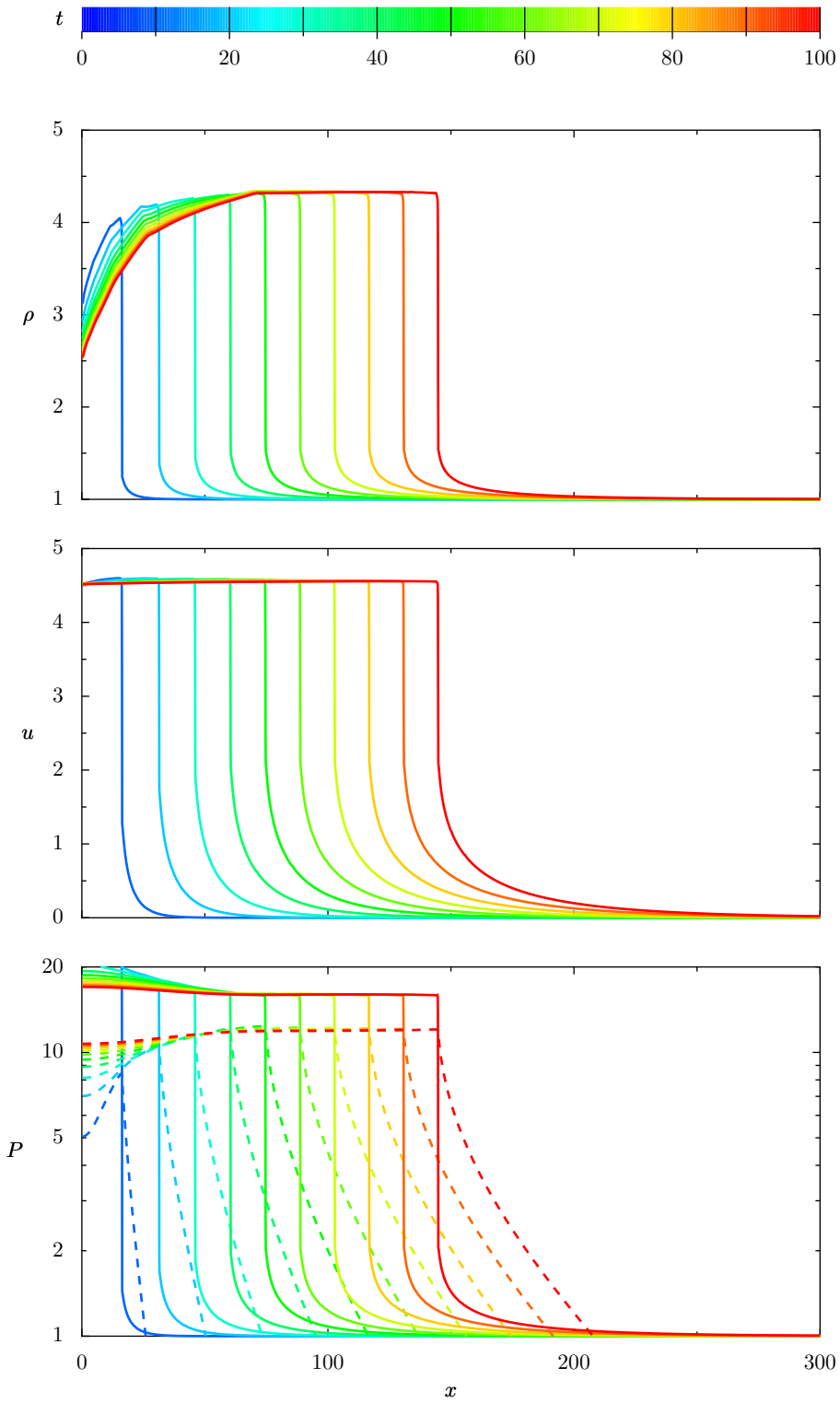

Figure 5.4: Time evolution of the hydrodynamical profiles for a modified shock (with $D(p) \propto p$ and $p_{\max} = 10$).
See sections 5.3.1 for simulation details. Plotted are the fluid density ρ, velocity u and pressure P (the cosmic-rays pressure P_{cr} is added dashed).

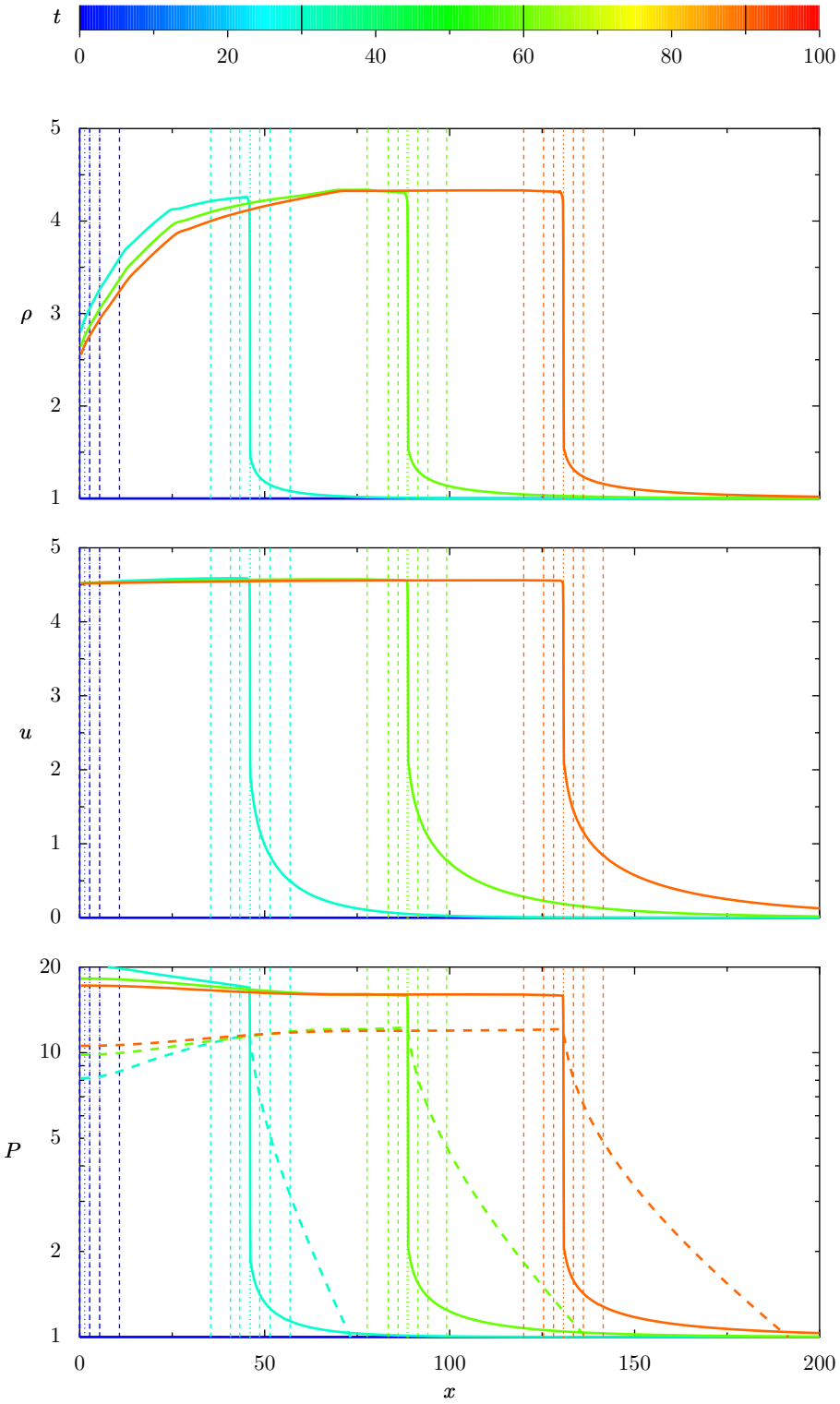

Figure 5.5: Same as figure 5.4, with the AMR grids hierarchy over-plotted at each output time.
Dotted lines mark the center of the grids (which follow the shock), dashed lines mark the boundaries of the 3 nested sub-grids.

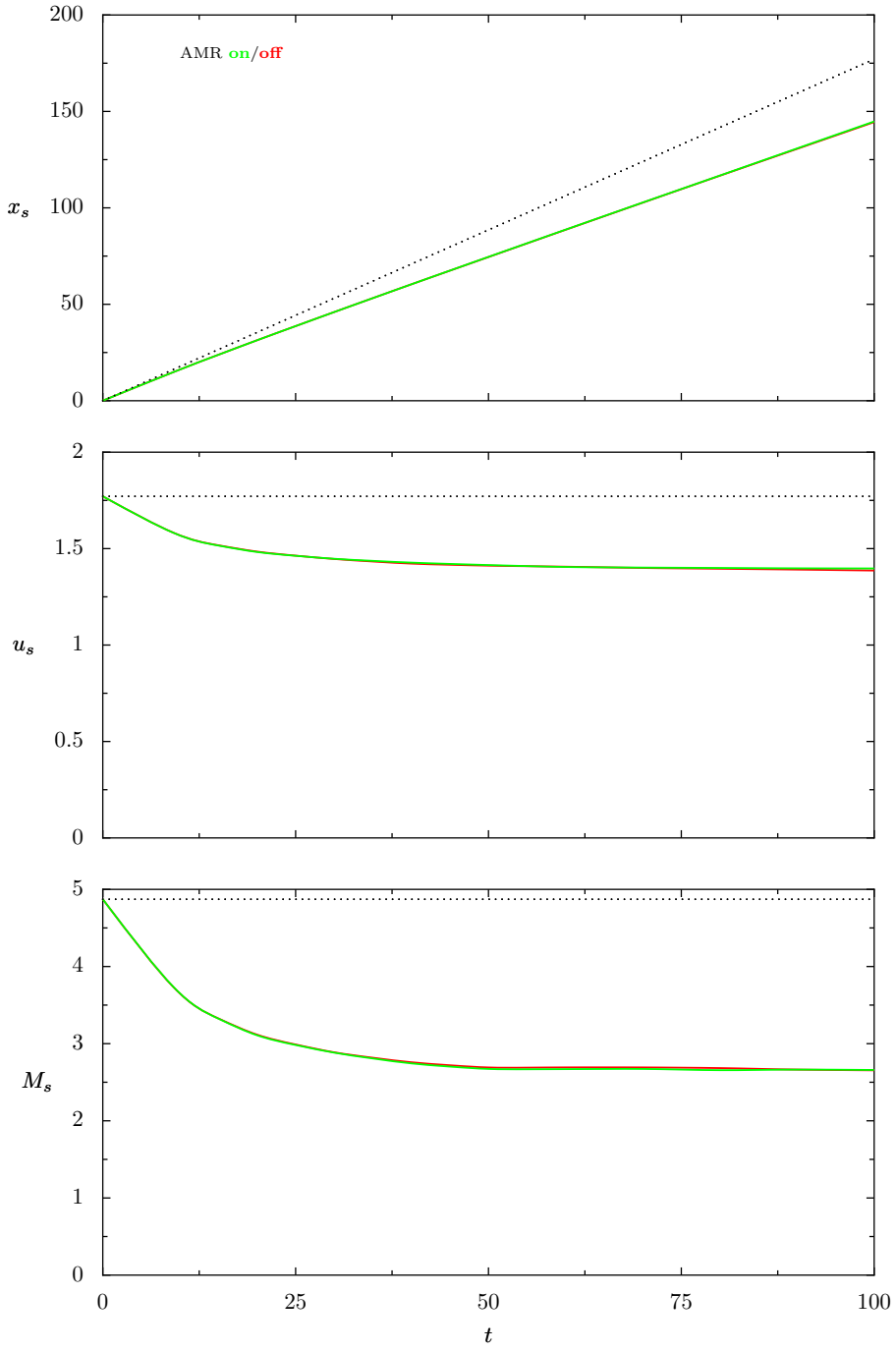

Figure 5.6: Evolution of the strongly modified shock of figure 5.4. The shock position x_s, velocity u_s and Mach number M_s are plotted versus time. The theoretical evolution in the non-modified case is added as the dotted line. Results obtained with($N = 3$) and without using AMR are shown in green and red respectively.

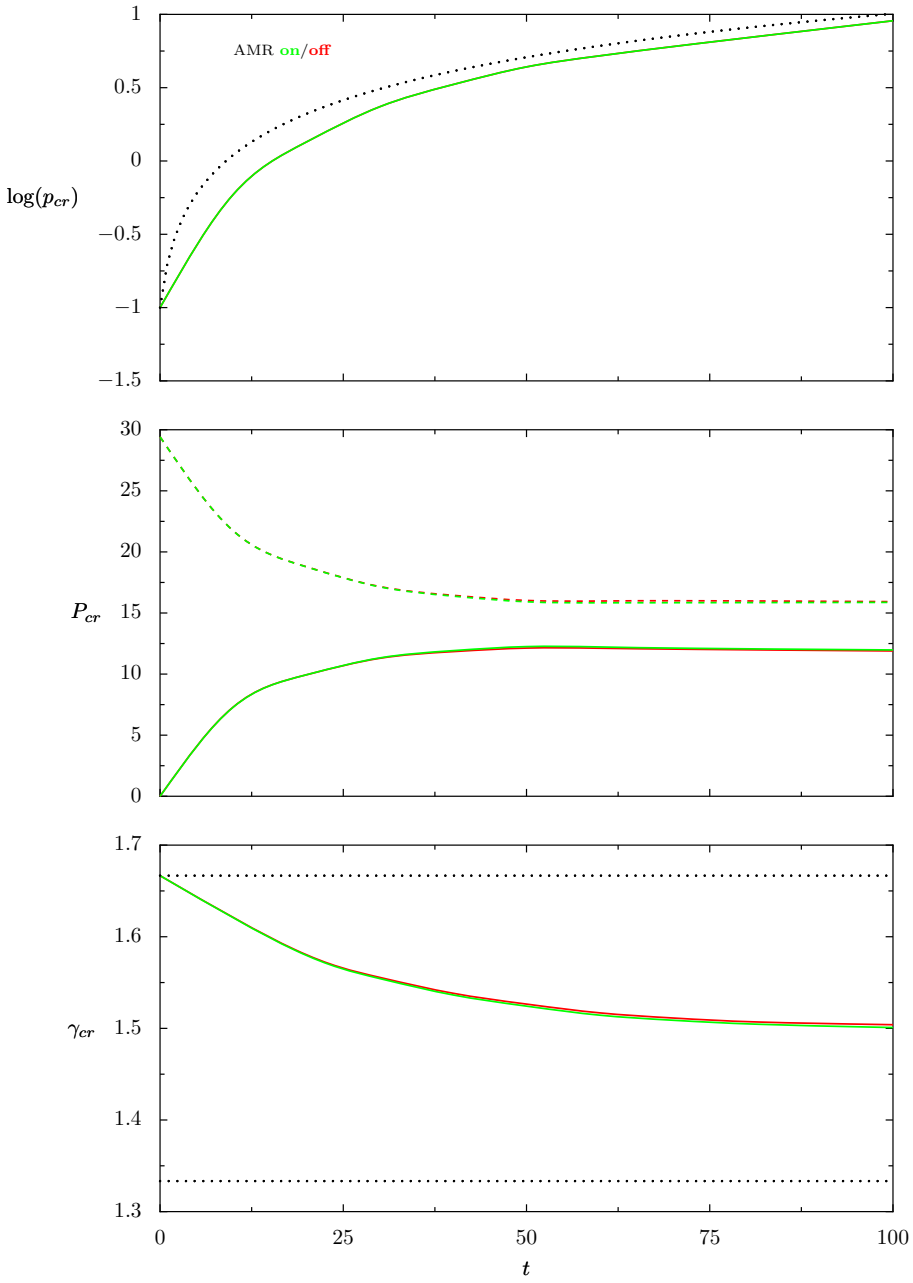

Figure 5.7: Evolution of some key cosmic-rays parameters for the modified shock of figure 5.4.
Plotted versus time are the maximum momentum $p_{\rm cr}$ (its theoretical linear evolution is added dotted, see equation (2.79)), pressure $P_{\rm cr}$ (the fluid pressure is added dashed) and adiabatic index $\gamma_{\rm cr}$ (the non-relativistic (5/3) and ultra-relativistic (4/3) values are added dotted). Results obtained with ($N = 3$) and without using AMR are shown in green and red respectively.

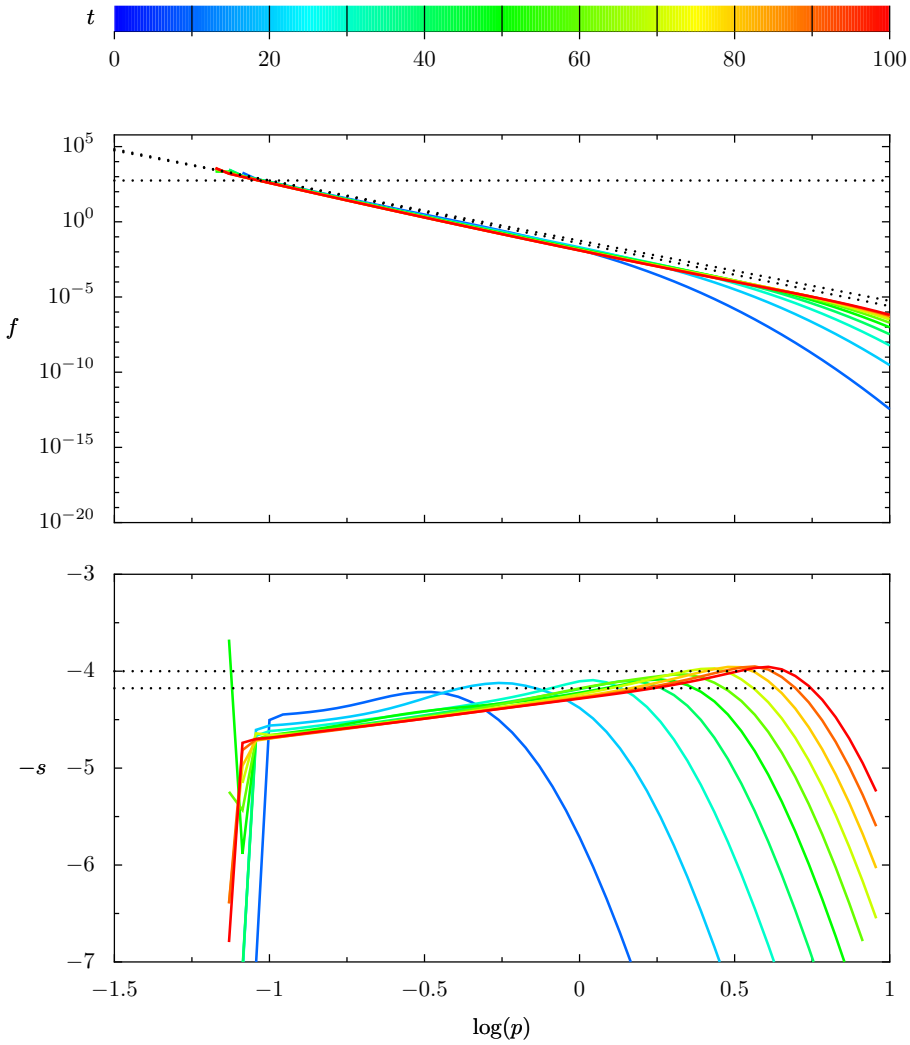

Figure 5.8: Time evolution of the cosmic-rays spectrum just downstream of the modified shock of figure 5.4.
The spectrum $f(p)$ is shown on top. On this plot the horizontal dotted line marks the theoretical spectrum normalization f_0 at injection (in the linear case) and the two other dotted lines are power-law spectra of slopes $s = 4$ and $s_1 = 4.18 =$ the theoretical linear slope (for this shock compression ratio $r = 3.55$) and of same normalization f_0 at injection. These two remarkable slope values are also marked dotted on the bottom plot, which shows the spectrum logarithmic slope $-s = \partial \log(f)/\partial \log(p)$.

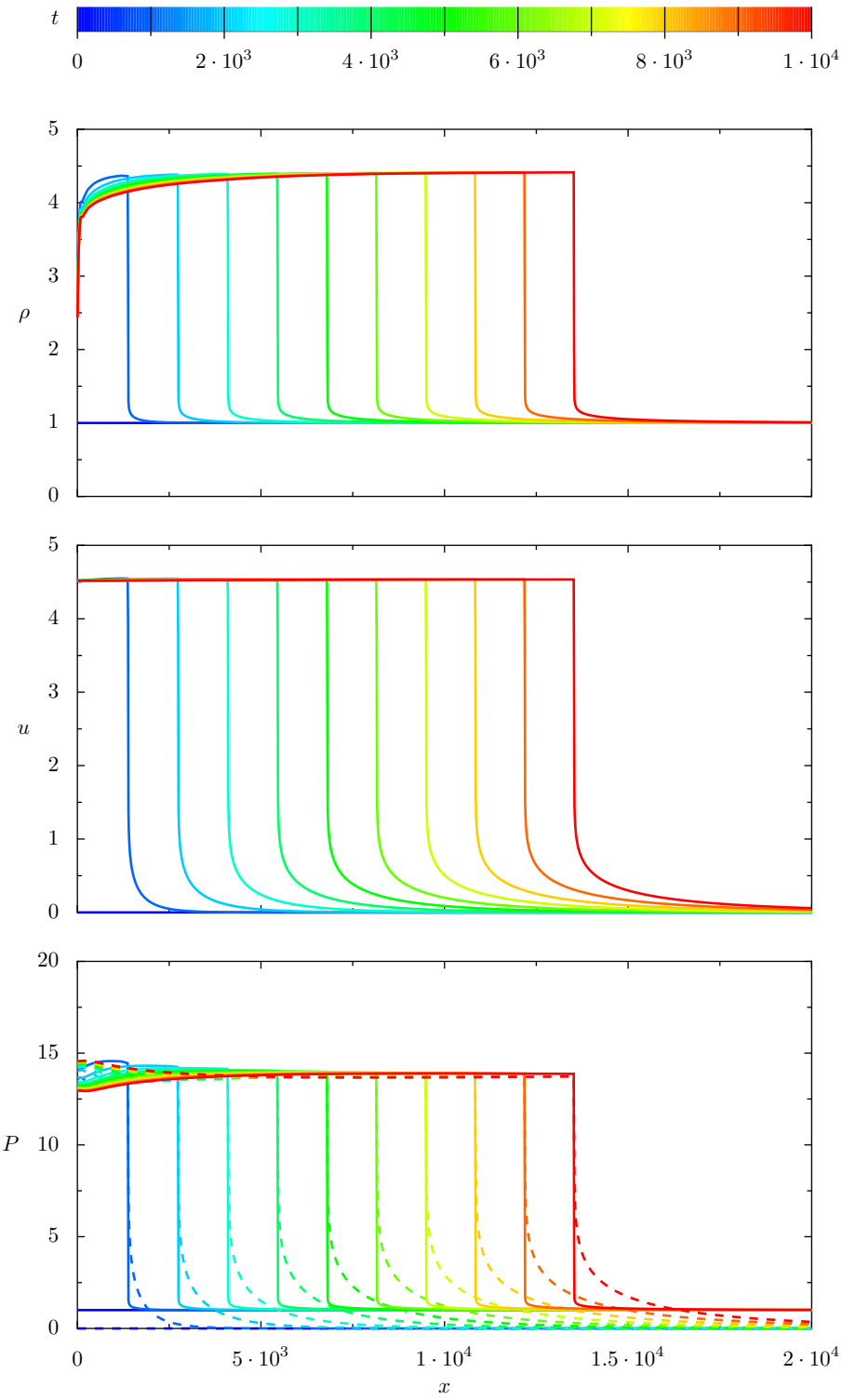

Figure 5.9: Time evolution of the hydrodynamical profiles for a modified shock (with $D(p) \propto p$ and $p_{\max} = 10^3$).
See sections 5.3.1 for simulation details. Plotted are the fluid density ρ, velocity u and pressure P (the cosmic-rays pressure $P_{\rm cr}$ is added dashed).

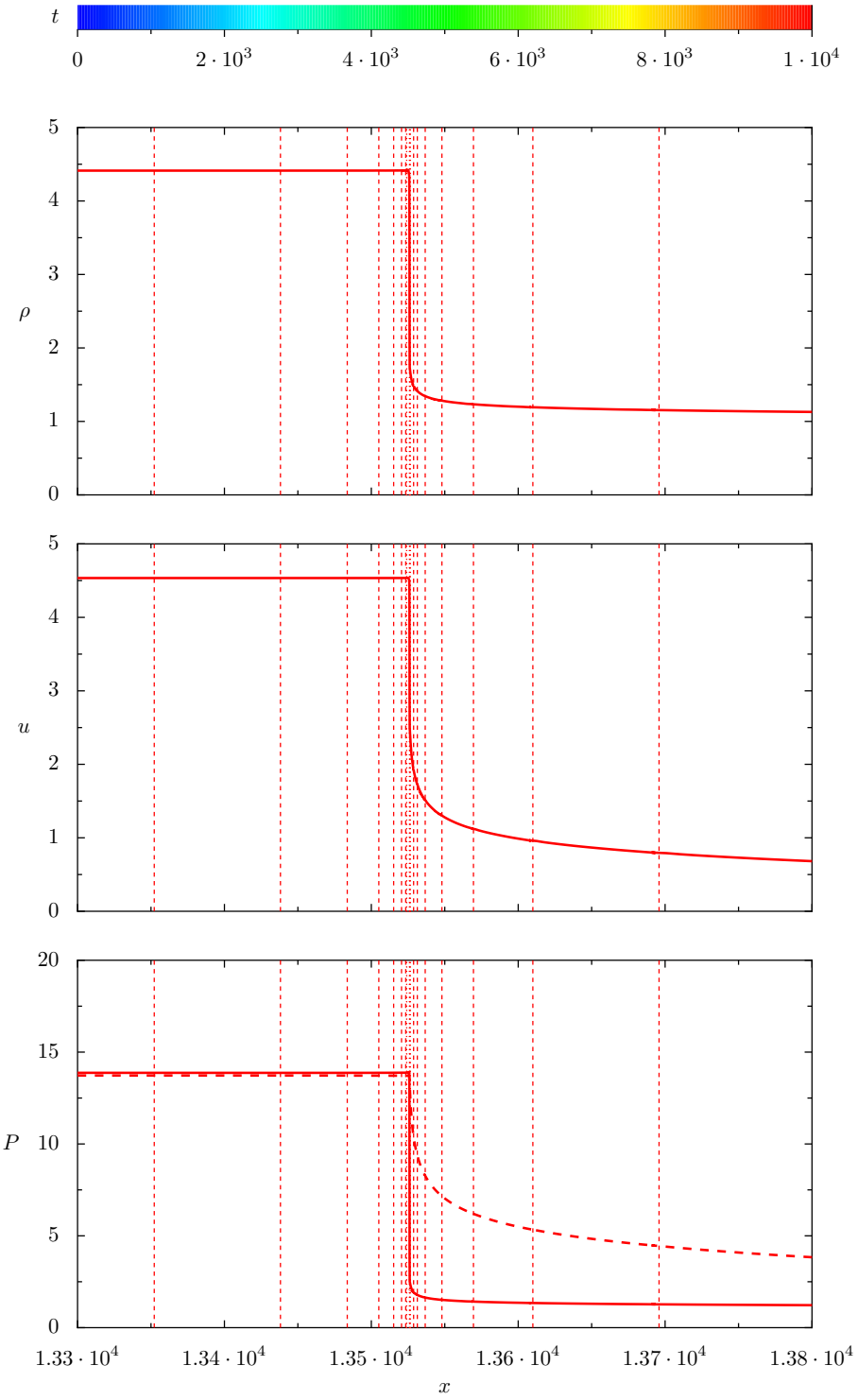

Figure 5.10: Same as figure 5.9 for $t = 10^4$, with the AMR grids hierarchy over-plotted.
Dotted lines mark the center of the grids (which follow the shock), dashed lines mark the boundaries of the 7 nested sub-grids.

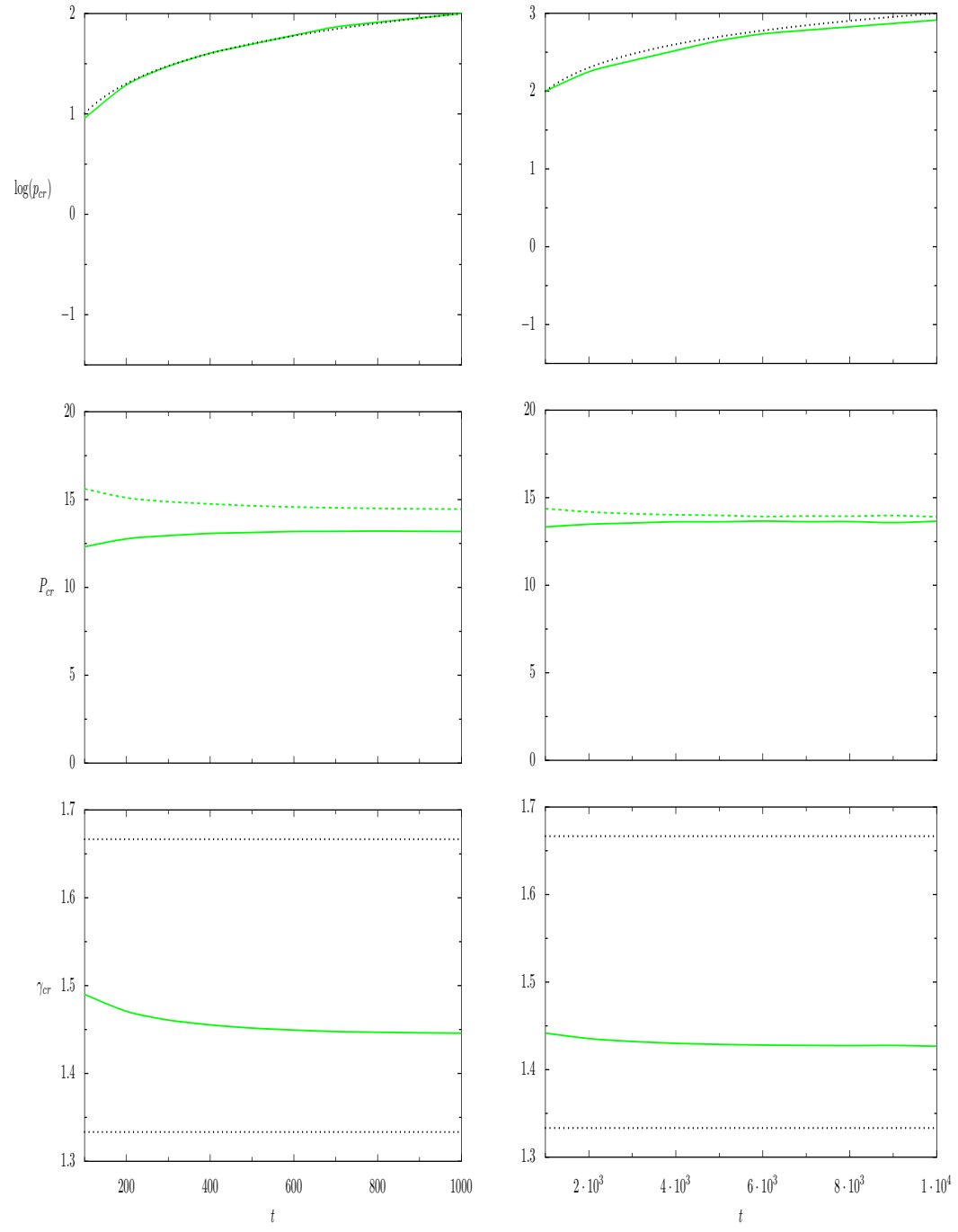

Figure 5.11: Evolution of cosmic-rays parameters for the modified shock of figure 5.4 for $t = 10^2 - 10^3$ ($p_{\max} = 10^2$) and $t = 10^3 - 10^4$ ($p_{\max} = 10^3$). Plotted versus time are the maximum momentum $p_{\rm cr}$ (its theoretical linear evolution is added dotted, see equation (2.79)), pressure $P_{\rm cr}$ (the fluid pressure is added dashed) and adiabatic index $\gamma_{\rm cr}$ (the non-relativistic (5/3) and ultra-relativistic (4/3) values are added dotted). Results obtained with AMR (with respectively 5 and 7 sub-grids).

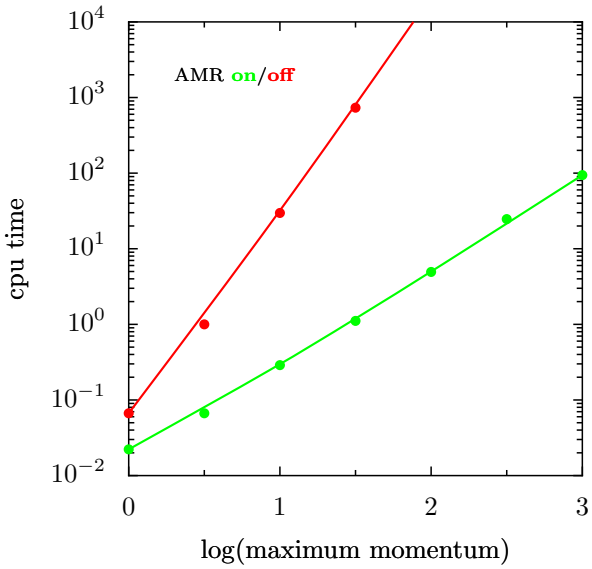

Figure 5.12: Computing time as a function of the maximum momentum $p_{\max}$ for a Bohm-like diffusion ($D(p) \propto p$).
The time unit on this plot is arbitrary, on an Itanium II processor the simulation to $\log(p_{\max}) = 1$ lasted 13.4 H with AMR off and 8 mn with AMR on. The cosmic-rays are injected at $\log(p_{\text{inj}}) = -1$ at $t = 0$, the minimum momentum is set to $\log(p_{\min}) = -1.5$. The two sets of measures have been done with (green) and without (red) activating the automatic AMR scheme (see section 5.3.1 for details). Physical results for $\log(p_{\max}) = 1$ are shown on figures 5.5 to 5.8, with comparisons of results with and without AMR on figures 5.6 and 5.7.

5.3.3 AMR Efficiency

On figures 5.6 and 5.7 the red curves show the results without activating AMR (in the case $\log(p_{\max}) = 1$), that is with a single grid having the same size as the base grid (given by $\Lambda = 10$) and the same resolution as the deepest grid (given by $\lambda = 0.3$). The results can hardly be distinguished, which proves that AMR doesn't compromise the physical accuracy. And we show now that on the other hand it considerably lowers the numerical cost. Simulations described previously have been made (up to $\log(p_{\max}) = 1.5$) without using AMR too. The computing time of each simulation with (green) and without (red) AMR is shown on figure 5.12. In the case $\log(p_{\max}) = 1$ presented in section 5.3.2 the speed-up is of roughly two orders of magnitude; and it grows steadily as $p_{\max}$ grows – up to $\log(p_{\max}) = 2$ above which the code would simply be of no use without AMR. We note that both curves are power-laws, with an index 2.4 times lower when AMR is activated. Thus the AMR technique is both very efficient and absolutely mandatory to address such difficult problems.

As shown on figure 5.12, using AMR we have simulated Bohm-like diffusion ($D(p) \propto p$) until $\log(p_{\max}) = 3$. This compares well with simulations made by Kang and Jones and collaborators. When they introduced this technique (Kang et al. 2001) the final simulation used $\log(p_{\max}) = 4$ but AMR tests were done with $\log(p_{\max}) = 2$. And until the middle of this thesis all their parametric studies of large scale shocks were made setting $\log(p_{\max})$ between 2 and 3 (eg Kang and Jones 2002, Kang and Jones 2004). Recently they have been able to rise $\log(p_{\max})$ to more than 6, but that was only at the cost of considerably lowering the resolution, either in momentum either in space. In 2005 they presented their "coarse-grained finite momentum volumes" scheme which lowers the momentum dimension cost (see the note in section 6.2.2). In 2006 they introduced a new AMR scheme where the grid is comoving with the shock in order to be able to address spherical geometry too, and found out that the code was working well even with unusually low resolutions in space (that is with λ defined by equation (5.3) of the order of unity, or even higher than unity). They attributed this nice side-effect to the fact that, the shock remaining at the same location in the comoving grid, "the compression rate is applied consistently to the cosmic-rays distribution at the subshock", which "results in much more accurate and efficient low energy cosmic-ray acceleration and faster numerical convergence on coarser grid spacings, compared to the simulations in a fixed Eulerian grid". At the end of this thesis Kang and Jones (2007) ported this comoving scheme back to the slab geometry version of their code, and confirmed that simulations are running correctly with space resolution orders of magnitudes smaller than before, which allows to reach maximum momenta orders of magnitude higher than before. However we note that in the simulation presented with $\log(p_{\max}) \simeq 7$ the cells on the deepest grid are roughly 800 times bigger than the diffusion length of injected particles, so that even if the code reaches numerical convergence as stated, we believe that it automatically misses the real dynamics of low-energy particles (up to roughly the relativistic regime). Now that our tool is functionnal, we plan to investigate ourselves this interesting but delicate issue.

References

Berezhko, E. G., Yelshin, V. K., and Ksenofontov, L. T. (1994). Numerical investigation of cosmic ray acceleration in supernova remnants. *Astroparticle Physics*, 2(2):215–227.

Berger, M. J. and Oliger, J. (1984). Adaptive Mesh Refinement For Hyperbolic Partial-Differential Equations. *Journal of Computational Physics*, 53(3):484–512.

Duffy, P. (1992). The self-consistent acceleration of cosmic rays in modified shocks with Bohm-type diffusion. A&A, 262:281–294.

Falle, S. A. E. G. and Giddings, J. R. (1987). Time-dependent cosmic ray modified shocks. MNRAS, 225:399–423.

Jones, T. W. and Kang, H. (2005). An efficient numerical scheme for simulating particle acceleration in evolving cosmic-ray modified shocks. *Astroparticle Physics*, 24:75–91.

Kang, H. and Jones, T. W. (1991). Numerical studies of diffusive particle acceleration in supernova remnants. MNRAS, 249:439–451.

Kang, H. and Jones, T. W. (2002). Acceleration of Cosmic Rays at Large Scale Cosmic Shocks in the Universe. *Journal of Korean Astronomical Society*, 35:159–174.

Kang, H. and Jones, T. W. (2004). Cosmic Ray Acceleration at Cosmological Shocks. *Journal of Korean Astronomical Society*, 37:405–412.

Kang, H. and Jones, T. W. (2006). Numerical studies of diffusive shock acceleration at spherical shocks. *Astroparticle Physics*, 25:246–258.

Kang, H. and Jones, T. W. (2007). Self-similar evolution of cosmic-ray-modified quasi-parallel plane shocks. *Astroparticle Physics*, 28:232–246.

Kang, H., Jones, T. W., LeVeque, R. J., and Shyue, K. M. (2001). Time Evolution of Cosmic-Ray Modified Plane Shocks. ApJ, 550:737–751.

Chapter 6

Running Multiple Shocks: Parallelization

In this chapter we extend our studies of time-dependent non-linear DSA to the effects of multiple (ie successive) shocks (as introduced in chapter 3). We recall that we have now to consider the fate of the cosmic-rays *between* two shocks. However we don't achieve that through direct simulations but through simple prescriptions. Regarding the shock simulations themselves, even using the numerical trick of AMR (as introduced in chapter 5) the computing time of realistic DSA simulations can still be very high. This quickly becomes an unacceptable limitation if one wants to investigate the effects of multiple, successive shocks, which lead us to save even more on computational time by *parallelizing* our code. Making use of all these developments we present the first simulations of linear and non-linear acceleration by multiple shocks.

6.1 Inter-Shocks Treatment

Our code is fully automated to run a sequence of shocks. Assuming that the fluid has enough time to decompress between two shocks, the same initial hydrodynamical conditions are used for each shock. The shock Mach number (and thus velocity and compression ratio) can however vary from shock to shock. At the end of each shock we take the downstream cosmic-rays spectrum, modify it to take into account the inter-shock physics of section 3.1, and pre-inject it in each space cell before launching the next shock. Although this mechanism seems simple we have to elucidate a few points.

6.1.1 Downstream Spectrum

First the very idea of a "downstream spectrum" supposes that we have reached some converged state downstream of the shock. According to Kang and Jones (2005) such a quasi-stationnary state is obtained once the cosmic-rays are accelerated up to the relativistic regime ($p > m_p c$), which agrees with our own

observations[1]. In the following we consider that the time each shock is run is long enough so that each single shock can fully relax regarding particle acceleration (up to the maximum momentum we consider), so that the downstream cosmic-rays pressure is well defined.

6.1.2 Adiabatic Decompression

To mimic adiabatic decompression the cosmic-rays spectrum $\ln(f)$ is shifted in $y = \ln(p)$ by

$$\Delta y(r) = \frac{1}{3}\ln(r) \tag{6.1}$$

towards lower energies. Lost values of f below $y_{\min}$ are simply discarded. We have checked by lowering the value of $y_{\min}$ that they don't influence the overall subsequent spectrum evolution. Missing values of f between $y_{\max} - \Delta y$ and $y_{\max}$ are filled by linearly extrapolating the slope from the end of f. This treatment gives the best accuracy at high energies in the linear regime.

As emphasised in chapter 3 to obtain correct results we need to resolve precisely this decompression shift and thus to use a high resolution in momentum: $\delta y \ll \Delta y$. We have found that in order to obtain exactly $s = 3$ in the linear regime, the shift $\Delta y/\delta y$ must in fact be an exact number of bins, and must be as high as roughly 10. But Δy depends on r, and we want to be able to run multiple simulations with variable r, and in non-linear simulations r will be constantly modified (see section 2.3.2) so that we will never know its final value beforehand. To solve this problem we proceed as follows. We use the same momentum resolution δy to run all shocks, fixed so that $\delta y < \Delta y(r_{\min})/J$ where J is a chosen integer $\gg 1$ and $r_{\min}$ is the lowest allowed compression ratio (note that in the case of modified shocks the relevant ratio for decompression is the total one, which will always be greater than the ratio imposed initially, so that $r_{\min}$ is well defined). At the end of each shock we measure the actual value r of the compression ratio, re-bin the numerical spectrum f with new resolution $\delta y' = \Delta y(r)/J$, shift this under-sampled f by $\Delta y(r)$ that is by exactly J bins, and then re-bin f back to the nominal resolution δy.

[1]To get a more precise estimate the simple analytical model of Berezhko and Ellison (1999) might be helpful. According to them there is a critical momentum

$$\frac{p_{\rm crit}}{m_p c} \simeq \left(0.43\sqrt{10}M_S^{3/4}\eta\frac{p_{\rm inj}}{m_p c}\left(\frac{c}{u_S}\right)^2\right)^{-4}$$

which marks the transition (when reached by the accelerated cosmic-rays) from an almost unmodified shock to a strongly modified one (which then doesn't evolve much). But the -4 power in the above formula gives extremely strong dependencies of $p_{\rm crit}$ on the shock and cosmic-rays parameters, so that this formula actually didn't prove to be very useful. Here we note that even if the functional dependencies obtained by Berezhko and Ellison (1999) derive from general arguments their precise expression strongly depends on the way they choose to represent the concave cosmic-rays spectrum in their simple non-linear model.

6.1.3 Escape

Regarding escape we simply give to the code a cut-off momentum p_{cut} above which the cosmic-rays spectrum f is set to zero[2].

6.2 Parallelization

Even using AMR running multiple realistic shocks simulations can easily be very demanding in computing time, limiting drastically the possibility to do parameter studies and thus fully explore the DSA mechanism. In order to get full access to the power of super-computers, which are actually nowadays clusters of processors, we have parallelized our code. We have considered the paradigm which consists of splitting the grid over many processors, each processor running the same code but on its own data. Of course this involves some communications between the processors[3], most notably to enforce the continuity of the physical profiles at all the boundaries between processors. As seen on figure 6.1 the computational domains of neighbouring processors actually slightly overlap: on each processor the grid has ghosts cells located at the same physical position as the closest cells of the physical domain of its neighbours. At the beginning of each time-step these ghosts are filled with the values previously computed by the neighbouring processors, so that each processor has for boundary conditions what would indeed be observed at these positions using a single grid. Note that therefore the splitting of the grid is truly transparent to the user: whereas AMR saves power by downsizing the problem to an optimized design, parallelization is a purely technical tool that can't compromise the physical results of the code.

6.2.1 In Space

The first idea to parallelize our code might be to split the space grid amongst the processors. Although we were able to do so, we encountered two major problems which make this approach of little help to investigate particle acceleration.

The first problem regarding parallelization in space is cosmic-rays diffusion. Implicit schemes, that we are eager to use because of their speed, are quite difficult to parallelize because of the coupling between all space cells they introduce (recall that they give the full solution everywhere at once at each time step by inverting a matrix). They can still be parallelized using iterative techniques, but we didn't considered this possibility. Explicit schemes on the

[2]This feature is not used in the test of section 6.3, but see the discussion of section 8.2.1 in the case of superbubbles.

[3]For which we use the MPI library, which is a de facto standard (see for instance the tutorials on the website of IDRIS, the national supercomputing center of CNRS, the French national agency for research).

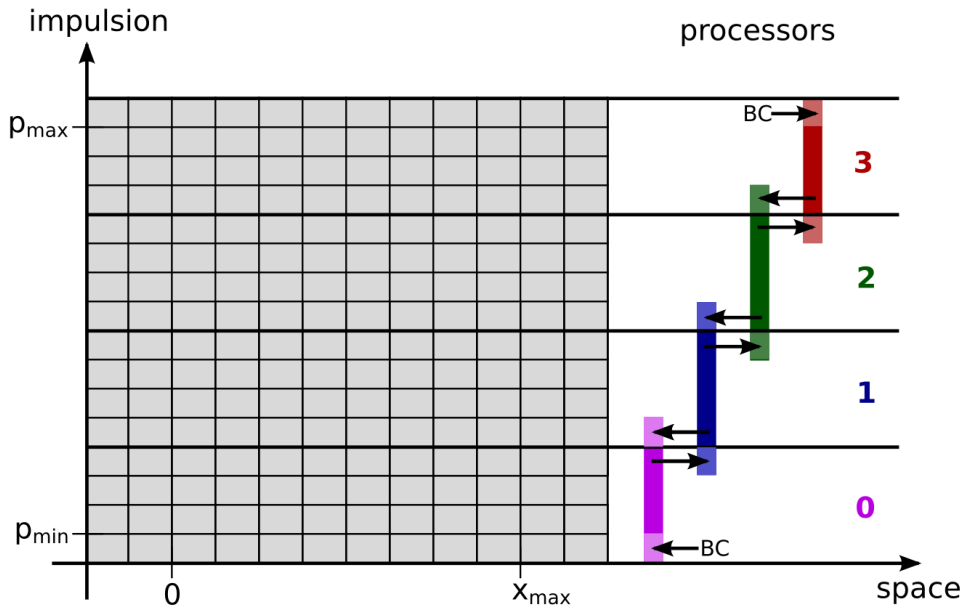

Figure 6.1: Sketch of the parallelization of the grid in momentum. The momentum bins are splitted here over four processors (in four different colors, with the ghost cells in lighter color). Double arrows indicate communications between processors required for boundaries matching (at real boundaries physical boundary conditions are used).

other hand are straightforward to parallelize. But for diffusion as we discussed in section 4.2.1 they are usually so much slower than the implicit schemes that, even massively parallelized, they are usually of no practical use. However, explicit schemes can be accelerated: it is possible to make them run faster than required by the usual Courant condition, thanks to the super-time-stepping method (STS, see section 4.2.1). We won't discuss more the performances of this technique of parallelizing accelerated explicit schemes, as space parallelization is anyway inefficient with AMR as shown just below, however we note that the STS method might become of interest again if we are to go to higher space dimensions, in which case implicit schemes can really be very cumbersome to parallelize and even to implement.

The biggest problem regarding parallelization in space is AMR. The problem is to split all the grids in a way that balances the load of all the processors well, otherwise the computing time of all the available processors won't be used efficiently (when communications are required lightly loaded processors will have to wait for heavily loaded ones, thus wasting some computing power). We have investigated the idea of doing the grid splitting at top-level only. Clearly with the grids hierarchy structure shown on figure 5.1 a regular cut will always be ill-balanced. But we have realised that even if we would

allow for a non-regular and dynamic cut, realistic DSA problems are so intrinsically ill-balanced that the effective number of processors used (defined by the processors effective working time) would hardly reach 2 or 3, whatever the number of actual processors being used. One could also suggest to split each level independently, but the sub-grids are actually rather small (typically a few tens of cells), which would limit the number of processors over which they can be shared. Moreover such a level-dependent split would require more complicated and frequent communications between the processors. Whatever the approach, we believe one can't get an efficient parallelization in the space dimension conjointly with AMR – a technique we want to keep as it already provides huge savings of memory and time.

6.2.2 In Momentum

If space parallelization seems to be a dead-end we should now have a new look at the other dimension, namely the momentum one[4]. Indeed we recall that even if the code is 1D in space the inclusion of the full spectrum of particles in each cell makes it actually 2D. And it turns out that parallelization in momentum is straightforward to implement (as nothing happens in momentum but a global advection to higher energies, whereas in space we have to deal with special features such as the shock front) and perfect load-balances can always be obtained (provided we slightly adjust the resolution δy so that the number of momentum bins is an exact multiple of the number of processors).

However parallelization in momentum suffers from two limitations. First, contrary to the space approach, not *all* the code is parallelized but only the parts dealing with cosmic-rays, and the maximal efficiency of the parallelization of a code is always limited by the non-parallelized (sequential) portion of the code (regardless of the number of processors used). However the kinetic part of the code, which fully benefits from the $p-$parallelization, can easily dominate over the hydrodynamics part, and the hydrodynamics part also benefits from $p-$parallelization, as the cosmic-rays advection is embedded into it (and cosmic-rays advection can dominate over the fluid advection too). So it is quite easy for difficult realistic problems to reach very high ratios of the parallelized over un-parallelized fractions of the code (more than 90%). Secondly, this ratio determines only the *maximum* acceleration achievable through paral-

[4]Note that Jones and Kang (2005) use an interesting "coarse-grained finite momentum volumes" technique which lowers the constraints imposed by the p dimension. The basic idea under this approach (first introduced by Jun and Jones (1999) and Jones et al. (1999)) is simply to lower the numerical resolution δy in momentum, but prescribing a power-law spectrum shape to each part of the discretized spectrum in order to keep reasonable accuracy. The numerical spectrum is then no longer a piece-wise constant function but a piece-wise linear function. This technique allows reasonably good estimates of the modified shock evolution with unusually low momentum resolutions (which can be as low as 2-3 bins per decade). However we believe that the adiabatic decompression between multiple shocks wouldn't be handled properly by such low resolutions, as it is typically of only $1/5$ of decade and has to be well sampled to get precise results in the linear regime (see section 6.1.2).

lelization. In practice the effective efficiency of parallelization is limited by the over-cost induced by inter-processors communications (mostly to share boundary conditions), which rises with the number of processors, leading eventually to a saturation of the efficiency. We managed however to achieve good parallelization scaling (see section 6.3.3) – thanks to some numerical optimisations.

Finally we recall that $p-$parallelization lets us free to use whatever numerical methods we want in the space dimension, notably the fast Crank-Nicholson diffusion scheme as well as the efficient AMR technique.

6.3 Test 3: Multiple Shocks

Here we present the evolution of test 2 when multiple shocks are run. To the best of our knowledge, these are the first direct numerical simulations of time-dependent non-linear multiple DSA.

6.3.1 Test Design

We start from the design of section 5.3.1, with the same hydrodynamical initial conditions for each shock, but an evolving cosmic-rays population, as explained in section 6.1. We recall that particles are injected at $\log(p_{\text{inj}}) = -1$. We want here to study acceleration up to $\log(p) = 1$[5]. When multiple shocks are run with cosmic-rays now present everywhere upstream the code faces harder numerical precision issues at high energies. To fix that first we set a bigger maximum momentum $\log(p_{\max}) = 1.5$ and we set bigger sub-grids ($\Lambda = 15$ as defined by equation (5.4)). We use the same space resolution as before: $\lambda = 0.3$ at $\log(p_{\min}) = -1.5$ that is $\lambda = 0.1$ at $\log(p^0_{\text{inj}}) = -1$ (as defined by equation (5.3)). We use a better momentum resolution: $\delta_y = 0.036$ corresponding to exactly 64 bins per decade (which, over 3 decades in p, allows perfect load balancing when running the code in parallel on clusters of processors that are powers of 2 up to 64). This nominal resolution is adjusted at the end of each shock to be exactly 10 bins per decompression shift (as explained in section 6.1.2). We consider here that $p_{\text{cut}} > p_{\max}$ so that cosmic-rays don't escape between two shocks (section 3.1.2).

[5]This a rather low maximum momentum, but
(i) numerically, even using advanced techniques such as AMR and parallelization the time cost of such simulations is still high (and automatically increases very fast with $p_{\max}$ as $D \propto p$), so that we were not able to adress directly the issue of the maximum momentum in the limited time of this thesis;
(ii) physically, it seems to be a reasonable and already interesting start, as it is sufficient to assess the known linear results, and as particles of energies higher than roughly 10 GeV won't probably experience acceleration by many shocks inside superbubbles (see section 8.2.1).

6.3.2 Physical Results

6.3.2.1 Linear Regime

Figures 6.2 and 6.3 show the evolution of test 2 when 30 such shocks are successively launched with cosmic-rays back-reaction turned off. In this linear case the cosmic-rays pressure grows forever, so that we end each shock at the time $t_{\rm end} = 300$ corresponding to $\log(p_{\rm max}) = 1.5$.

Figure 6.2 shows the evolution of the cosmic-rays spectra just downstream of the last shock. The spectra are all normalized at the injection momentum to emphasize the slope evolution (the actual normalization rises by a factor of roughly two). We clearly see the convergence of the spectrum from an initial power-law of slope $s = 3r/(r-1)$ (the well-known linear solution for a single shock) to a final power-law of slope $s = 3$ (the well-known limit in the case of multiple shocks, see section 3.2.1).

The way the spectrum hardens at different momenta is shown on figure 6.3, where we plot the slope as a function of the number N of shocks. Dashed is added the theoretical slope computed (with centered finite differences) from the analytical expression (3.18) of the spectrum produced after N shocks. Our code reproduces the expected behavior within roughly 1% for the three momenta (close to the maximum momentum it is less precise). This validation of our code in the linear regime gives us confidence to explore the unknown non-linear regime.

6.3.2.2 Non-Linear Regime

On figure 6.4 we now allow the cosmic-rays to back-react on the shock. Each shock is run until the downstream cosmic-rays pressure has converged, before doing decompression and launching the next one. We recall that one of the consequences of cosmic-rays back-reaction is that $p_{\rm inj}$ varies in time (as the downstream state changes). However we still use here a fixed injection fraction η, but we run different simulations with different values of η as this parameter is quite poorly constrained. To get an overall picture we use a broad range of values of η, around the value $\eta_0 = 0.0225$ used since test 1 to match Falle and Giddings (1987) parameters. For $\eta \geq 10^{-1}$ (a value which seems physically unreasonably high) the very first shock gets fully "smoothed" by cosmic-rays back-reaction before $P_{\rm cr}$ has converged. Following Falle and Giddings we consider a shock to be smoothed as soon as the Mach number of the sub-shock drops below $M_{S,{\rm cut}} = 1.3$ – and then stop the simulation for this shock. Note that in reallity shock smoothing would stop the injection of fresh cosmic-rays, but not the acceleration of already produced ones – and their back-reaction on the shock structure. Therefore the actual fate of the shock when it gets smoothed would require a more careful analysis[6]. We postpone

[6]Falle and Giddings (1987) have already investigated cosmic-rays-dominated "self-sustaining" shock without injection of fresh particles.

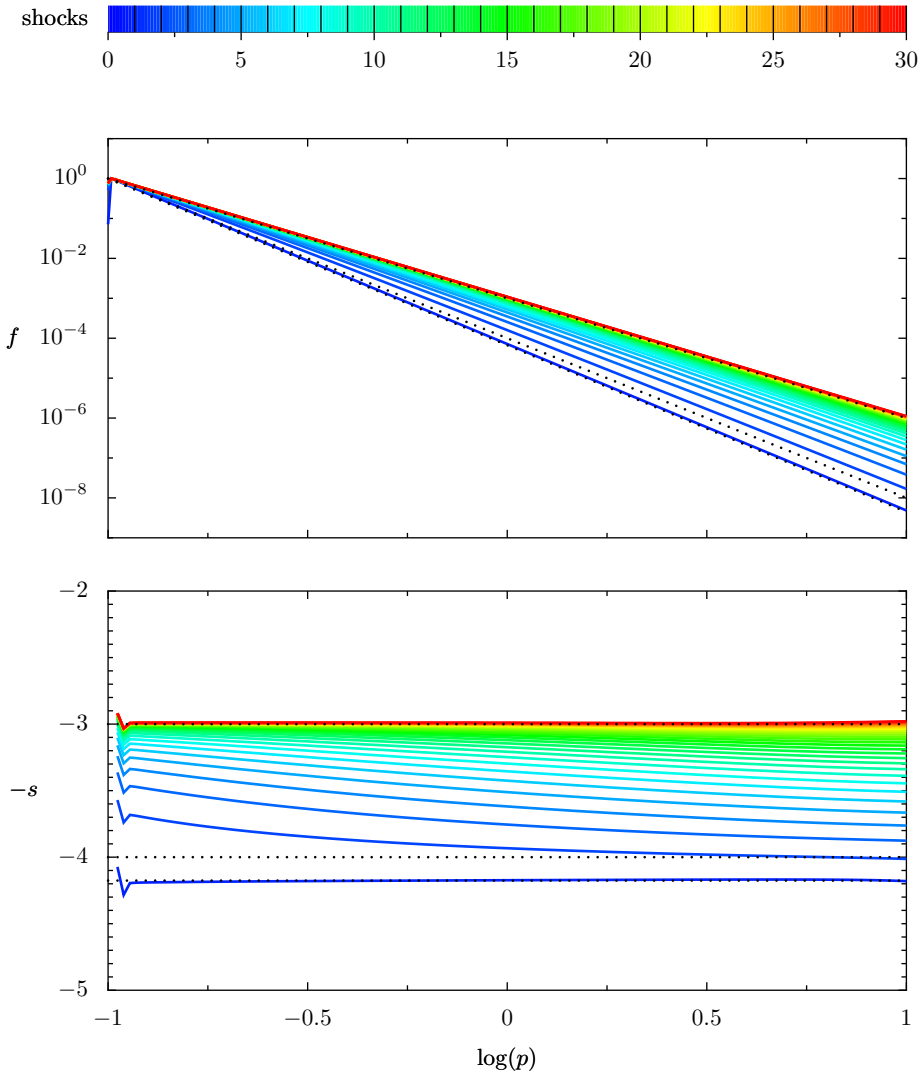

Figure 6.2: Time evolution of the final downstream cosmic-rays spectra for a sequence of successive linear shocks.
See sections 6.3.1 and 6.3.2.1 for details. Each colored line shows the cosmic-rays distribution just at the end of a shock. The spectra $f(p)$ are shown on top (all normalized so that $f(p_{\mathrm{inj}}) = 1$), where we have added (dotted) the three power-laws of slope $s = 3$ and $s = 4$ and $s_1 = 4.18$ the theoretical linear slope for the compression ratio $r = 3.55$ of the shocks. These three remarkable slope values are also marked (dotted) on the bottom plot, which shows the spectra logarithmic slopes $-s = \partial \log(f)/\partial \log(p)$. The evolution of the slope from s_1 to 3 with the number of shocks is shown on figure 6.3 for three different momenta.

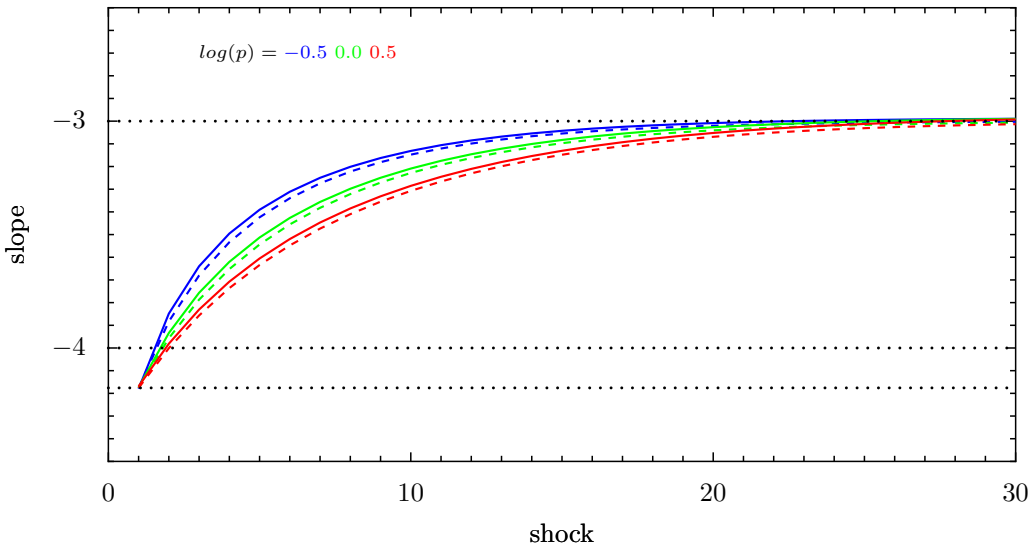

Figure 6.3: Evolution of the final cosmic-rays spectrum slope at three different momenta for a sequence of successive linear shocks.
This figure consists in three vertical cuts in the bottom plot of figure 6.2 at $\log(p) = -0.5, 0.0, +0.5$. in the bottom plot of figure 11). The theoretical results (from equations (3.18) and (3.16)) are added dashed. The three remarkable slopes $s = 3$, $s = 4$ and s_1 are marked dotted.

this important issue to a future work, we are simply interested here in the time it takes until shocks get smoothed by cosmic-rays, as an estimate of the back-reaction strength. As η is lowered to around 10^{-2} the first shock can run until a quasi-steady state is reached (as in test 1 of section 4.3), but the cumulative effect of *successive* shocks is such that one shock eventually gets smoothed too. As η is lowered to around 10^{-3} the number of shocks N before smoothing occurs raises exponentially: below roughly $\eta_c = 1.5 \times 10^{-3}$ it seems that virtually any number of shocks could run (although all this shocks are still modified ones). We have limited here the maximum number of shocks to 30, as this seems reasonable for both numerical reasons (given the evolution of the red curve it would take extremely long times to fully explore the very low injection fractions), and physical reasons (considering a few tens of successive strong shocks makes sense in environments such as superbubbles).

At the last shock N we measure the range of spectra slopes s (between the injection momentum and the momentum of hardest slope, at which its final decay starts). We observe two evolutions as η decreases. First the spectra globally harden as η is lowered, which is expected as more shocks can run. Note that as we limit ourselves to $N = 30$ the slopes below η_c can't be directly compared with the slopes above η_c: below η_c the slopes would get closer to the $s = 3$ limit if one would allow for a higher number of shocks. Anyway we see that in the non-linear regime the building of the $s = 3$ spectrum within 30 shocks (as on figures 6.2 and 6.3) requires an injection fraction lower than

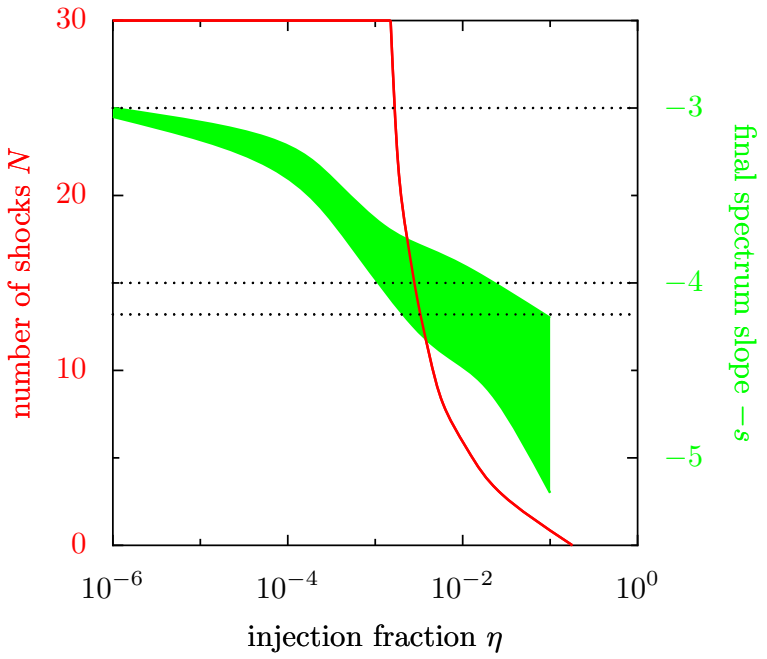

Figure 6.4: Evolution of the number of shocks N (up to 30) that reach a quasi-steady state before complete smoothing and of the range of final cosmic-rays spectra slopes $-s$ as a function of the injection fraction η in the non-linear case.
See sections 6.3.1 and 6.3.2.2 for details.

$\eta = 10^{-6}$. Second the range of slopes gets constantly narrower, especially below η_c (that is when when cosmic-rays no longer limit the number of shocks). Thus this simulations suggest the existence of two regimes of multiple DSA with respect to the injection ratio η: there seems to be some critical η_c (here of roughly 1.5×10^{-3}) above which cosmic-rays dictate the fate of the shocks (producing soft and irregular spectra) and below which cosmic-rays are almost transparent to the successive shocks (producing harder and more regular spectra). We have observed the same global picture with other simulations (not shown here) involving a constant diffusion coefficient D.

We note that the self-consistent injection fraction proposed by Blasi et al. (2005) (equation (2.93)) is here initially $\eta_B \simeq 10^{-1}$, thus in the regime where cosmic-rays dominate from the very first shock. This self-consistent η_B is time-dependent and is lowered as the shock gets modified, but we have observed that the first shock still gets fully smoothed before a quasi-steady state has been reached. Such a very high back-reaction might be surprising for a thermal leakage mechanism. It comes from our particular choice (to match FG param-

eters) of the ratio of the velocity of injected cosmic-rays to the downstream sound speed $\xi' = 2$, as η_B has a very strong dependence on this free parameter (recall that $\xi' = 1.1\xi$). $\xi' = 2$ is a realistic but rather low value, we could suggest as well $\xi' = 3$, in which case η_B is initially 270 times lower, that is $\eta_B \simeq 3.7 \times 10^{-4}$, that is in the regime where cosmic-rays are transparent to the successive shocks. Thus this points out that Blasi's model, although providing a self-consistent injection fraction, still requires some initial tuning.

Finally we note that the actual fate of such cosmic-ray-dominated shocks might depend on geometry effects too. For the sake of (both numerical and physical) simplicity we have considered here a piston-driven shock in slab geometry, this work shall now be extended to a supernova-like shock in spherical symmetrical geometry (see appendix). We also recall that all this results were obtained with a numerical momentum box limited to $\log(p_{max}) = 1.5$. Thus their validity depends on the assumption that cosmic-rays accelerated to higher energies: (i) don't have a major impact on the final shock structure (and thus on the spectrum shape at lower energies); (ii) have enough time to escape from the system between two shocks. Another more fundamental assumption on which we rely (as all other studies of that kind) is that the inertia of the cosmic-rays is negligible. Although reasonable for single DSA this might be questionable for multiple DSA because of the cumulative effect of shocks. However we note that the higher the injection fraction, the lower the number of shocks that we actually run. And we have checked that the ratio ρ_{cr}/ρ remains always below 10% in all our non-linear simulations.

In conclusion our simulations show that multiple diffusive shock acceleration, in the non-linear regime, can produce low energy spectra either softer (because of non-linear effects) either harder (because of repeated acceleration effects) than in the (ideal) linear regime. If particles can be accelerated by a great number of shocks, their spectra might become much harder than what is believed to be the source spectrum for cosmic-rays. However we note that the actual spectrum of cosmic-rays depends on many parameters of the model, and in particular one has to better evaluate the number of successive shocks and the level of injection in a particular environment (see more regarding superbubbles in section 8.2). And multiple shock acceleration has already been invoked in explaining some hard radio synchrotron spectra in extra-galactic jets by Ferrari and Melrose (1997a, 1997b).

6.3.3 Parallelization Efficiency

Figure 6.5 shows the gain brought by parallelization. The right plot corresponds to the simulations of test 3, the left plot corresponds to a slightly different simulation design where the cosmic-rays over fluid cost ratio is purposely reduced. We obtain good scalings up to a few tens of processors. Thus parallelization allows us to study the acceleration by multiple shocks within the time previously required to study acceleration by a single shock.

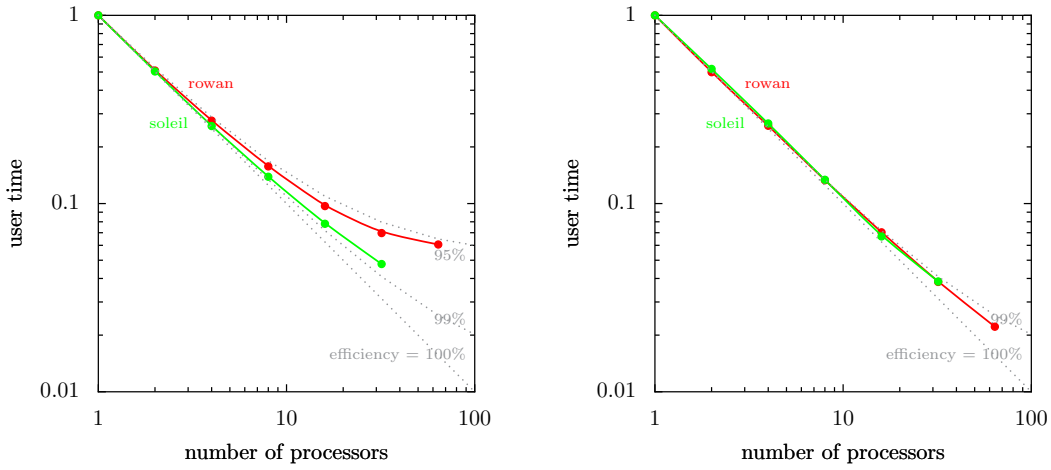

Figure 6.5: User computing time as a function of the number of processors for simulations of the kind of section 6.3.1.
Measures have been made on two machines, the *soleil* super-computer of the French *Calmip* collaboration (a cluster of 120 Itanium II processors with shared memory) and the *rowan* super-computer of the Irish *Cosmogrid* collaboration (a cluster of 256 Xeon processors with Gigabit Ethernet). Tests have been made up to the maximum number of processors available on this middle-class machines (32 on *soleil* and 64 on *rowan*). The computing times have been normalized to emphasize the parallelization scaling with the number of processors. The dotted lines show the theoretical scaling for a perfect parallelization (that is with no induced over-cost) of 95%, 99% and 100% of the code.

In the simulations of section 6.3.1 (right plot) the DSA operator represents a bit more than 90% of the computations time, and as the hydrodynamic operator also advects cosmic-rays the fraction of the code actually benefiting from parallelization is more than 99.5%. On the slightly less cosmic-rays-dominated simulation (left plot) the scaling is slightly less good on the distributed memory machine than on the shared memory machine, which shows that our code is bound by communications[7]. Anyway the slightly less good scaling observed with 64 processors is no surprise given that in that case each processor deals with only 3 momenta cells (on both plots), which makes a high surface/volume (that is communications/computations) ratio. We note here that a good point of parallelization in momentum is that it's all the more useful since one wants to investigate high energies. Indeed the higher $p_{\max}$, the bigger the momentum grid, and the more processors one can use with a same given efficiency.

[7]Note that *rowan* has been used here with its standard Gigabit Ethernet network, the experimental Infiniband network gives better scaling.

References

Berezhko, E. G. and Ellison, D. C. (1999). A Simple Model of Nonlinear Diffusive Shock Acceleration. ApJ, 526:385–399.

Blasi, P., Gabici, S., and Vannoni, G. (2005). On the role of injection in kinetic approaches to non-linear particle acceleration at non-relativistic shock waves. MNRAS, 361:907–918.

Falle, S. A. E. G. and Giddings, J. R. (1987). Time-dependent cosmic ray modified shocks. MNRAS, 225:399–423.

Ferrari, A. and Melrose, D. B. (1997a). Particle acceleration and energy spectra in extragalactic jets. *Memorie della Societa Astronomica Italiana*, 68:171–174.

Ferrari, A. and Melrose, D. B. (1997b). Particle acceleration and energy spectra in extragalactic radiosources. *Vistas in Astronomy*, 41:259–263.

Jones, T. W. and Kang, H. (2005). An efficient numerical scheme for simulating particle acceleration in evolving cosmic-ray modified shocks. *Astroparticle Physics*, 24:75–91.

Jones, T. W., Ryu, D., and Engel, A. (1999). Simulating Electron Transport and Synchrotron Emission in Radio Galaxies: Shock Acceleration and Synchrotron Aging in Axisymmetric Flows. ApJ, 512:105–124.

Jun, B.-I. and Jones, T. W. (1999). Radio Emission from a Young Supernova Remnant Interacting with an Interstellar Cloud: Magnetohydrodynamic Simulation with Relativistic Electrons. ApJ, 511:774–791.

Kang, H. and Jones, T. W. (2005). Efficiency of Nonlinear Particle Acceleration at Cosmic Structure Shocks. ApJ, 620:44–58.

Part III

Superbubbles

If cosmic-rays are accelerated by supernova shocks (as presented in part I), then the sources of cosmic-rays are in the material where supernovae explode and their blast waves pass through. Although most observed supernovae are isolated ones, the great majority of them explode into groups of massive stars called *OB associations*. The winds and explosions of these massive stars form vast expanding structures of hot and tenuous gas, known as *superbubbles* (chapter 7). It is here, in a complex medium quite different from the standard interstellar one, that most supernovae explode – with a high correlation in space and time. This has major implications on the phenomenology of cosmic-rays (chapter 8), mostly because of the particular composition of superbubbles, and also because of the possibility of acceleration by multiple shocks (that we begin to investigate here with the tool presented in part II). Non-thermal radiation is now clearly observed from superbubbles (chapter 9), proving that high energy phenomena are indeed commonly occurring in these environments.

Chapter 7

The Superbubbles Environment

Most supernovae explode into superbubbles, big (a few 100 pc) hot ($T \simeq 10^6$ K) and tenuous ($n \simeq 10^{-2}$ cm^{-3}) bubbles powered by the winds of their massive progenitors then by the explosions themselves. In this chapter we review the specificities of this environment with respect to the standard interstellar medium (ISM). We first present the superbubbles objects in more details, then discuss how the two ingredients of diffusive shock acceleration, namely the shock waves and the magnetic waves, are affected (see also the review of Parizot et al. (2004) and the lecture of Marcowith (2007b)).

7.1 Superbubbles Origin and Structure

Superbubbles are closely related to OB associations, clusters of massive stars that have powerful winds and end their lives in supernovae explosions.

7.1.1 Massive Stars Clusters

Most supernovae (80%-90%) are core-collapsed ones (types II, Ib, Ic)[1] , corresponding to the death of stars of mass $> 8\,M_\odot$ (see Woosley et al. (2002) for a review of the final phases and explosion). These stars, of spectral type O and B, have a high surface temperature (a few 10^4 K). In their late stages they evolve to red supergiants ($M > 40\,M_\odot$) or blue luminous variables ($M < 40\,M_\odot$). As all stars they are born in clusters in giant molecular clouds (eg Elmegreen and Scalo 2004). They have modest initial dispersion velocities $v \leq 3$ km/s (de Zeeuw et al. 1999)[2], and a short life expectancy (see figure 7.1). Indeed stars burn their material all the more fast since they are massive: our Sun will live for 10^{10} years, a $8\,M_\odot$ star (the threshold for supernova production) lives a few 10^7 years, a $100\,M_\odot$ star lives only a few 10^6 years (eg Schaller et al. 1992). Thus, although they are not gravitationally bound, most massive stars actually spend all their life in groups, called OB associations. It is estimated

[1] The remainder are thermonuclear explosions of accreting white dwarfs (type Ia).

[2] Although a few *runaway stars* of $v > 30$ km/s exist.

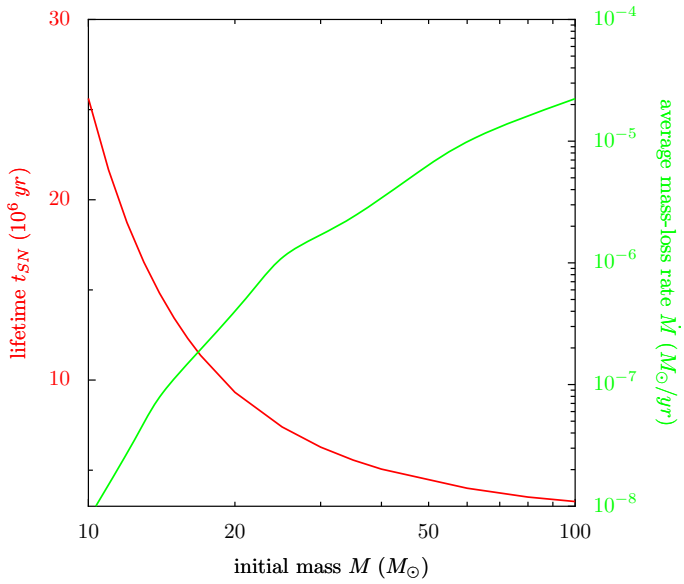

Figure 7.1: Lifetime and average mass-loss rate of massive stars. (data from Limongi and Chieffi (2006))

that at least the majority (>60%, Garmany 1994) and up to the quasi-totality (>90%, Higdon et al. 1998) of OB stars belong to such associations (see more in section 7.2.1).

The number $N_{\rm OB}$ of OB stars in a single OB association ranges from a few tens to a few hundreds. All this stars are confined within regions of radius $r_{\rm OB}$ ∼35 pc (Garmany 1994, Bresolin et al. 1999, Pietrzyński et al. 2001). For evenly distributed stars the mean distance between two closest neighbours can be evaluated as

$$d_{\star,\rm OB} = \frac{\frac{4}{3}\pi r_{\rm OB}^3}{N_{\rm OB}} \simeq 12\,{\rm pc}\,\left(\frac{r_{\rm OB}}{35\,{\rm pc}}\right)\left(\frac{N_{\rm OB}}{100}\right)^{-1/3}\,. \qquad (7.1)$$

And one has observed OB associations structured in subgroups (eg de Geus et al. 1989, Brown et al. 1994), in which $d_{\star,\rm OB}$ might be much smaller than the above average value. For instance Walborn et al. (1999) have found in the Doradus complex subgroups containing more than 10 OB stars within a few pc. Moreover, we recall that a majority of stars are grouped in systems of two stars or more.

7.1.2 Stellar Winds

An important feature of massive stars is the continuous ejection of matter through strong winds during their whole life (see figure 7.1). While the Sun blows a wind of a about 300 km/s, loosing roughly $10^{-14}\,M_\odot$ per year, B stars blow winds of about 500 km/s, loosing of the order of 10^{-12} to $10^{-7}\,M_\odot$ per year, and O stars blow winds of a few 1000 km/s, loosing of the order of

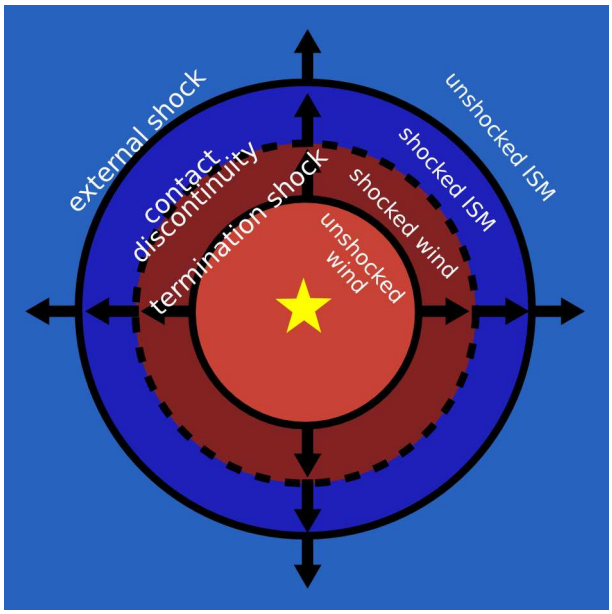

Figure 7.2: Structure of a wind-blown stellar bubble.
The wind is in red and the interstellar medium is in blue. Material in dark colors have been shocked, materials in light colors are still undisturbed.

10^{-7} to $10^{-5}\,M_\odot$ per year (see eg Schaller et al. (1992), Maeder and Meynet (2003) and companion papers). In their very last phases the most massive stars (of typically $M > 20\,M_\odot$) become so-called Wolf-Rayet stars, characterized by extremely powerful winds, with a mass-loss rate one order of magnitude higher than standard O stars, up to $10^{-4}\,M_\odot$ per year. The wind luminosity is defined as

$$L_w = \frac{1}{2}\dot{M}_w V_w^2 \simeq 3 \times 10^{36}\ \mathrm{erg/s} \left(\frac{\dot{M}_w}{10^{-5} M_\odot/\mathrm{yr}}\right) \left(\frac{V_w}{10^3\ \mathrm{km/s}}\right)^2 . \qquad (7.2)$$

The wind velocity V_w and mass-loss rate $\dot{M}_w$ are not constant during stellar evolution, but the total wind energy (integrated over the star's lifetime) amounts typically to 10^{51} erg, that is the same amount as the supernova kinetic energy release.

The powerful winds of massive stars are directly connected with their high luminosity (see Lamers and Cassinelli (1999) for a comprehensive introduction to winds physics). The photons of the star, especially in the UV range, are absorbed and re-emitted by the circumstellar material. As incident photons all come from the star, and outgoing photons are re-emitted isotropically, the net effect is an acceleration of the atoms away from the star. In this way the wind generates a hot low-density bubble around the star.

The structure and evolution of such a stellar bubble is presented in Castor et al. (1975) and Weaver et al. (1977). The bubble structure is shown on figure 7.2. Note the similarity with figure 2.2 showing the structure of a super-

nova remnant (but for the fact that here all three waves are going outwards, as the wind energy injection is continuous). Two shocks are present, the inner *termination shock*, which marks the end of the free expansion of the wind around the star, and the outer *external shock*, which marks the end of the bubble progressing into the circumstellar medium. A third wave is present, a discontinuity contact separating the wind and the ambient medium. The bubble evolves in three distinct phases. During the first phase the radiative losses are negligible so that the evolution is adiabatic. During this phase the wind expands rapidly in the ambient medium, with a termination shock at

$$r_{\rm term}(t) \simeq 2\,{\rm pc}\,\left(\frac{\dot{M}_w}{10^{-5}\,M_\odot/{\rm yr}}\right)^{\frac{3}{10}}\left(\frac{V_w}{10^3\,{\rm km/s}}\right)^{\frac{1}{10}}\left(\frac{n_{\rm ext}}{10^2\,{\rm cm^{-3}}}\right)^{-\frac{3}{10}}\left(\frac{t}{10^6\,{\rm yr}}\right)^{\frac{2}{5}} \tag{7.3}$$

where $n_{\rm ext}$ is the external mass density (assumed here to be uniform, with a typical value of $100\,{\rm cm^{-3}}$ in the parent molecular cloud). When the bubble age becomes of the order of the cooling time radiative losses induce a collapse of the matter. This occurs first in the shocked ambient medium, after just a few thousands of years. Thus during the second phase the expanding wind is pushing a colder thin shell of swept-up material, with an external shock at

$$r_{\rm ext}(t) \;\simeq\; 13\,{\rm pc}\,\left(\frac{L_w}{3\times10^{36}\,{\rm erg/s}}\right)^{\frac{1}{5}}\left(\frac{n_{\rm ext}}{100\,{\rm cm^{-3}}}\right)^{-\frac{1}{5}}\left(\frac{t}{10^6\,{\rm yr}}\right)^{\frac{3}{5}}\;. \tag{7.4}$$

The shell temperature is of the order of 10^4 K, the shocked wind temperature is given by

$$T(r,t) \simeq 3{\times}10^6{\rm K}\left(\frac{L_w}{3\times10^{36}\,{\rm erg/s}}\right)^{\frac{8}{35}}\left(\frac{n_{\rm ext}}{10^2\,{\rm cm^{-3}}}\right)^{\frac{2}{35}}\left(\frac{t}{10^6\,{\rm yr}}\right)^{-\frac{6}{35}}\left(1-\frac{r}{r_{{\rm ext}(t)}}\right)^{\frac{2}{5}}. \tag{7.5}$$

This phase is the longest and the most observed (thanks to the X emission of the shocked wind and the H_α emission of the ionised shell). It is only after a few millions of years that radiative losses become important in the shocked wind too and the bubble enters the third phase.

7.1.3 Superbubbles

In an OB association the external shock radius of a single stellar bubble $r_{\rm ext}$ given by equation (7.4) is of the same order as the mean distance between two stars $d_{\star,{\rm OB}}$ given by equation (7.1). Therefore the individual wind bubbles actually collide and merge within the first million year of activity. The result is a large collective bubble expanding around the whole OB association, powered by the sum of the mechanical luminosities of the individual stars of the cluster, and soon after by the energy releases of the successive supernovae, called a superbubble (see figure 7.3).

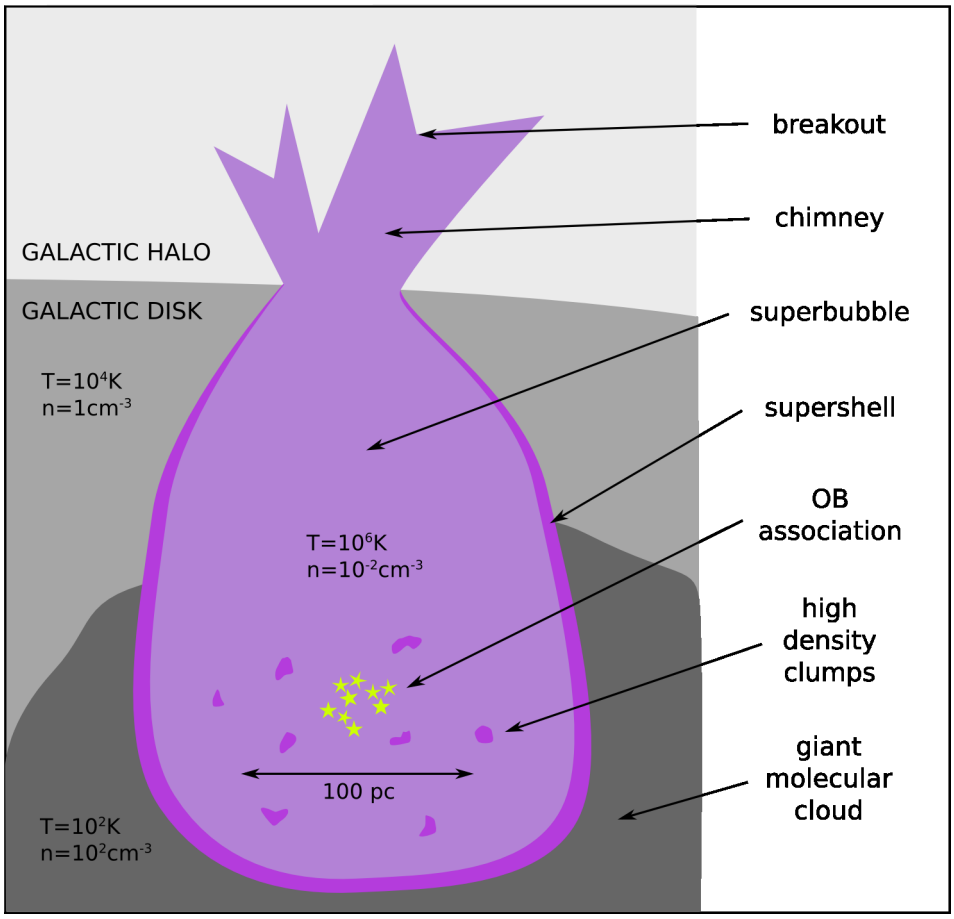

Figure 7.3: Sketch of a superbubble.

7.1.3.1 The Basics

Adapting the single stellar wind theory of Weaver et al. (1977) presented in section 7.1.2 to the case of superbubbles Mac Low and McCray (1988) established the basic properties of these objects.

The energy release in the superbubble is not continuous but experiences peaks when a star enters the Wolf-Rayet stage or explodes as a supernova. However in sufficiently evolved superbubbles the variations in the driving power are smoothed out in the superbubble interior, which acts as a buffer, well before reaching the external supershell (see more in section 7.2.2). Therefore to study the superbubbles dynamics one can as a first approximation consider an average constant power $L_{\rm OB}$[3], typically of the order of 10^{38} erg/s (that's for instance ∼30 winds of the kind of equation (7.2) or one supernova of 10^{51} erg every $\sim 3 \times 10^5$ yr). According to equation (7.4) such a luminosity powers a

[3]See Koo and McKee (1992b) and Shull and Saken (1995) for the effects of a time-dependent luminosity.

bubble of size

$$r_{\rm SB} \simeq 270\,{\rm pc}\,\left(\frac{L_{\rm OB}}{10^{38}\,{\rm erg/s}}\right)^{\frac{1}{5}}\left(\frac{n_{\rm ISM}}{1\,{\rm cm^{-3}}}\right)^{-\frac{1}{5}}\left(\frac{t}{10^7\,{\rm yr}}\right)^{\frac{3}{5}}. \quad (7.6)$$

One can also derive the density and temperature inside the superbubble:

$$n_{\rm SB} \simeq 4\times10^{-3}\,{\rm cm^{-3}}\,\left(\frac{L_{\rm OB}}{10^{38}\,{\rm erg/s}}\right)^{\frac{6}{35}}\left(\frac{n_{\rm ISM}}{1\,{\rm cm^{-3}}}\right)^{\frac{19}{35}}\left(\frac{t}{10^7\,{\rm yr}}\right)^{-\frac{22}{35}} f(x)^{-1} \quad (7.7)$$

$$T_{\rm SB} \simeq 3.5\times10^{6}\,{\rm K}\,\left(\frac{L_{\rm OB}}{10^{38}\,{\rm erg/s}}\right)^{\frac{8}{35}}\left(\frac{n_{\rm ISM}}{1\,{\rm cm^{-3}}}\right)^{\frac{19}{35}}\left(\frac{t}{10^7\,{\rm yr}}\right)^{-\frac{6}{35}} f(x) \quad (7.8)$$

with $f(x) = (1-x)^{2/5}$ where $x = r/r_{\rm SB}$ is the relative distance to the superbubble center. Note that the internal pressure $P_{\rm SB} = \mu n_{\rm SB} k_B T_{\rm SB}$ is independent of $f(x)$: it has no pronounced spacial gradients as the sound crossing time is lower than the superbubble dynamical time. Assuming a multiplicity $\mu = 2.3$ (corresponding to a fully ionized medium of solar abundances) one gets

$$P_{\rm SB} \simeq 4.3\times10^{-12}\,{\rm erg.cm^{-3}}\,\left(\frac{L_{\rm OB}}{10^{38}\,{\rm erg/s}}\right)^{\frac{2}{5}}\left(\frac{n_{\rm ISM}}{1\,{\rm cm^{-3}}}\right)^{\frac{3}{5}}\left(\frac{t}{10^7\,{\rm yr}}\right)^{-\frac{4}{5}}. \quad (7.9)$$

7.1.3.2 A Complex Medium

The above formulae (7.7), (7.8), (7.9) give an average description of a superbubble, but as argued by Parizot et al. (2004) the superbubble interior is likely to have a complex structure.

First it is likely to be a clumpy medium. Indeed giant molecular clouds (GMCs) are not homogeneous: their average density if of the order of 10^2 cm^{-3} but they contain high density clumps of densities ranging from 10^3 to 10^6 cm^{-3}, and clumps of too high density can't be swept up by the stars' winds. Parizot et al. (2004) give the following rough estimate of the density above which a clump remains inside the superbubble:

$$n_{\rm cl} = 1.5\times10^{3}\ \ {\rm cm^{-3}}\,\left(\frac{r_{\rm cl}}{0.1\,{\rm pc}}\right)^{-1}\left(\frac{n_{\rm GMC}}{10^2\,{\rm cm^{-3}}}\right)\left(\frac{d_{\star,\rm OB}}{12\,{\rm pc}}\right) \quad (7.10)$$

where $r_{\rm cl}$ is the clump radius, expected to be between 0.01 and 1 pc.

Secondly the superbubble's supershell corresponds to the merging of the *external* winds shocks, but what about the winds *internal* termination shocks? Their radius is obtained by equating the ram pressure of the wind $P_w = \rho_w V_w^2 = \dot{M}_w V_w/4\pi r^2 = L_w/2\pi V_w r^2$ with the thermal pressure in the superbubble interior $P_{\rm SB}$ given by equation (7.9), which gives

$$r_{\rm term,SB} = 13\,{\rm pc}\ \ \left(\frac{L_w}{3\times10^{36}\,{\rm erg/s}}\right)^{\frac{1}{2}}\left(\frac{V_w}{10^3\,{\rm km/s}}\right)^{-\frac{1}{2}}\left(\frac{L_{\rm OB}}{10^{38}\,{\rm erg/s}}\right)^{-\frac{1}{5}}\left(\frac{n_{\rm ISM}}{1\,{\rm cm^{-3}}}\right)^{-\frac{3}{10}}\left(\frac{t}{10^7\,{\rm yr}}\right)^{\frac{2}{5}}. \quad (7.11)$$

This is again of the same order as the average distance between stars $d_{\star,\mathrm{OB}}$ (equation (7.1)), therefore direct wind-wind interactions should occur in OB associations inside superbubbles: the winds of two neighbouring stars can actually terminate each other. The interaction region is expected to be of much higher pressure than the typical pressure of the superbubble interior and to be highly instable, leading probably to strong hydrodynamical turbulence.

7.1.3.3 A Complex Environment

The theory of superbubbles evolution has been developed in great details during the last 20 years, mostly by the means of numerical simulations. As the size of a superbubble is close to the Galactic disk height (∼500 pc), such objects have to be considered in the Galactic context. Various authors (eg Tomisaka and Ikeuchi 1986, Mac Low et al. 1989, Norman and Ikeuchi 1989, Koo and McKee 1992a) have considered the fate of superbubbles breaking out of the Galactic plane, forming "chimneys" directly connected to the Galactic halo (a phenomenon first observed by Normandeau et al. (1996)). Tomisaka (1990,1998) and Ferrière et al. (1991) studied the effect of the Galactic magnetic field on the confinement of superbubbles in the Galactic plane. Korpi et al. (1999) combined various other effects such as the non-uniformity of the interstellar medium, the Galactic differential rotation, the gravitational potential. They observed that after a few tens of millions of years the superbubble shape can become very irregular. Silich and Franco (1999) and Breitschwerdt et al. (2000) concentrated their efforts on the the morphology and evolution of realistic superbubbles.

7.2 Supernovae in Superbubbles

We investigate now how the special environment of superbubbles affects the development of supernova remnants (see the outline of their evolution in section 2.1.1.3). This is of primary importance as the great majority of supernovae explode in this kind of environment, as we shall show first.

7.2.1 The Supernovae - Superbubbles Connection

The connection between supernovae and superbubbles is natural as both are powered by OB stars. Garmany (1994) suggested that at least 60% of all OB stars, and therefore of all core-collapse supernovae, belong to OB associations, and therefore to superbubbles. Higdon and Lingenfelter (2005) showed that this fraction is likely much higher. Their argument is as follows. The size-frequency distribution of young stellar clusters in the Galaxy appears observationally to follow a universal power-law

$$\frac{dN_{\mathrm{sc}}(N_\star)}{dN_\star} = 6.1 \times \frac{1.7 \times 10^6}{N_\star^2} \tag{7.12}$$

where $dN_{\rm sc}(N_\star)$ denotes the number of clusters having a number of stars (of any type) between $N_\star$ and $N_\star + dN_\star$. $N_\star$ appears to range between $N_{\star\rm min} = 190$ and $N_{\star\rm max} = 1.7 \times 10^6$. Dividing equation (7.12) by the typical lifetime of an OB association ~ 3.7 Myr one gets the birth rate of clusters of $N_\star$ stars. As already stated the $N_\star$ stars can be of any type, we are only interested here in the number $N_\star^{\rm SN} = f_{\rm SN} \times N_\star$ of stars producing a core-collapse supernova, that is of stars of mass $> 8\ M_\odot$. According to the modified Kroupa (2002) initial mass function (IMF), which gives the mass distribution of newly-born stars as a multi-power-law, their fraction is $f_{\rm SN} = 1.1 \times 10^{-3}$ (so that clusters of less than 900 stars have low probability of creating any supernova). One can then express the birthrate of supernovae belonging to a cluster of $N_\star$ stars as

$$\frac{d^2 N_\star^{\rm SN}(N_\star)}{dN_\star dt} = f_{\rm SN} N_\star \times \frac{d^2 N_{\rm sc}(N_\star)}{dN_\star dt} = \frac{3.085}{N_\star}\,{\rm kyr}^{-1}\,. \tag{7.13}$$

Summing over $N_\star$ yields the total birthrate of supernovae in the Galaxy:

$$\frac{dN_\star^{\rm SN}}{dt} = \int_{N_{\star\rm min}}^{N_{\star\rm max}} dN_\star \frac{d^2 N_\star^{\rm SN}(N_\star)}{dN_\star dt} = \frac{2.81}{100\ {\rm yr}} \tag{7.14}$$

which is consistent with other estimates (eg van den Bergh and McClure 1994). Summing for $N_\star > N_\star^{\rm SN}$ and normalizing by the total rate (7.14) yields the cumulative probability for the clustered occurrence of $N_\star^{\rm SN}$ supernovae or more:

$$P\left(N_\star^{\rm SN}\right) = \frac{\int_{N_\star^{\rm SN}}^{N_{\star\rm max}} dN_\star \frac{d^2 N_\star^{\rm SN}(N_\star)}{dN_\star dt}}{\int_{N_{\star\rm min}}^{N_{\star\rm max}} dN_\star \frac{d^2 N_\star^{\rm SN}(N_\star)}{dN_\star dt}} = 0.828 - 0.11 \ln N_\star^{\rm SN}\,. \tag{7.15}$$

The question is now, how many massive stars are required so that their association produces a superbubble? Higdon and Lingenfelter confirm the finding of previous authors that simulations of superbubbles powered by discrete supernovae explosions converge to the same results as simulations powered by a continuous wind release (of equivalent energy) as soon as $N_\star^{\rm SN} \geq 5$. This means that only 5 supernovae are required to produce a "mature" superbubble (not to say about the action of the winds of their progenitors). Therefore according to equation (7.15) at least 65% of all core-collapse supernovae occur in superbubbles as described in section 7.1.3.1. However Higdon and Lingenfelter show that this number is considerably enhanced when one considers temporal and spatial correlations within OB associations. Temporal correlations come from the hierarchical formation of clusters subgroups. They increase the above value up to 80%. Spatial correlations come from the facts that the star formation rate seems proportional to the parent cloud mass and that the clouds mass-frequency distribution is a flat power-law so that a few clouds contain most of the total mass. They increase the above value to 90%. When both effects are taken into account the fraction of supernovae occurring inside superbubbles is found to be 92±2%. Higdon and Lingenfelter also recall that the fraction of

OB stars that are runaway stars (and might escape their association) is small, only ∼5%. They also show that algorithms commonly used to find clustered stars may easily miss up to one third of them (which are then falsely said to be "field stars").

We hope to have convinced the reader that the primary site of supernovae explosions are superbubbles, so that the knowledge of the way supernova remnants develop in these environments is mandatory to get a proper understanding of the acceleration of Galactic cosmic-rays[4].

7.2.2 Remnant Length- and Time-Scales

Core-collapse supernovae all release a few $M_\odot$ of ejecta having $\sim 10^{51}$ erg of kinetic energy. But as emphasized by Parizot et al. (2004) the evolution of the supernova remnant (see section 2.1.1.3) depends on the ambient medium properties. The interstellar medium has a typical density $n_{\rm ISM} \sim 1$ cm^{-3} and a typical temperature $T \sim 10^4$ K (regulated by the stars luminosity). This fiducial values will be used in the following as our "standard" ISM. In a typical superbubble after ten millions years of evolution (see section 7.1.3.1) the density is 250 times lower, $n_{SB} \sim 4 \times 10^{-3}$ cm^{-3}, and the temperature is 350 times higher, $T_{\rm SB} \sim 3.5 \times 10^6$ K. Note that the pressure $P \propto nT$ is however of the same order $\sim 3 - 4 \times 10^{-12}$ erg.cm^{-3}.

Because of the low ambient density the remnant expands freely for a longer time: it enters the Sedov-Taylor phase ∼6 times later, that is after more than one thousand of years rather than after a few hundreds of years (equation (2.10)), with a radius ∼6 times bigger (equation (2.11)). For the same reason this self-similar phase lasts almost 20 times more, that is for hundreds of thousands of years instead of tens of thousands of years (equation (2.15)) – with a final radius 10 times bigger (equation (2.16)). Thus the early adiabatic phases last for a much longer time in a superbubble than in the standard interstellar medium.

And because of the high ambient temperature the subsequent radiative phases probably never happen: the sound speed $c_s \propto \sqrt{T}$ is so high that the blast waves becomes subsonic before being radiative. Using $\overline{m} = 1.4 m_p$ and $\gamma = 5/3$ in equation (2.3) one gets

$$c_s \simeq 100\,\mathrm{km/s} \left(\frac{T}{10^6\,\mathrm{K}}\right)^{\frac{1}{2}} \tag{7.16}$$

that is $c_{s,\rm SB} \sim 200$ km/s, 20 times higher than $c_{s,\rm ISM} \sim 10$ km/s. Using the time dependence of $T_{\rm SB}$ given by equation (7.8) – assuming $L_{\rm SB} = 10^{38}$ erg/s

[4]Note that Montmerle (1979), because of the observed coincidences between SNRs and OB associations (which he therefore called "SNOBs"), already had the intuition that superbubbles were a major source of cosmic-rays.

and $n_{\rm ISM} = 1\,{\rm cm}^{-3}$ – one gets more precisely

$$c_s \simeq 200\,{\rm km/s}\,\left(\frac{t_{\rm SB}}{10^7\,{\rm yr}}\right)^{-\frac{3}{35}}\,. \tag{7.17}$$

From equation (2.14), and using the time dependence of $n_{\rm SB}$ given by equation (7.7), one can express the shell radius and velocity in the Sedov-Taylor phase as

$$r_{\rm SNR} = 38\,{\rm pc}\,\left(\frac{t_{\rm SNR}}{10^4\,{\rm yr}}\right)^{\frac{2}{5}}\left(\frac{t_{\rm SB}}{10^7\,{\rm yr}}\right)^{\frac{22}{175}} \tag{7.18}$$

$$v_{\rm SNR} = 1470\,{\rm km/s}\,\left(\frac{t_{\rm SNR}}{10^4\,{\rm yr}}\right)^{-\frac{3}{5}}\left(\frac{t_{\rm SB}}{10^7\,{\rm yr}}\right)^{\frac{22}{175}} \tag{7.19}$$

where the normalizations are obtained from equations (2.10), (2.11), (2.12) assuming $M_{\rm ej} = 10\,M_\odot$ and $E_{\rm sn} = 10^{51}$ erg. Comparing equations (7.17) and (7.19) one sees that the shock reaches the sonic point ($v_{\rm SNR} = c_s$) after a time

$$t_{\rm sub} \simeq 3.1\times10^5\,{\rm yr}\,\left(\frac{t_{\rm SB}}{10^7\,yr}\right)^{\frac{37}{105}}\,. \tag{7.20}$$

From equation (2.15), and using the time dependence of $n_{\rm SB}$ given by equation (7.7), one can express the onset time of the radiative phase as

$$t_{\rm rad} \simeq 5.4\times10^5\,{\rm yr}\,\left(\frac{t_{\rm SB}}{10^7\,{\rm yr}}\right)^{\frac{198}{595}}\,. \tag{7.21}$$

We have

$$\frac{t_{\rm sub}}{t_{\rm rad}} \simeq 0.6\,\left(\frac{t_{\rm SB}}{10^7\,{\rm yr}}\right)^{\frac{1}{51}}\,. \tag{7.22}$$

so that no matter how old the superbubble is $t_{\rm sub} < t_{\rm rad}$: the supernova remnant becomes subsonic before being radiative. Lets check now that this occurs inside the superbubble. Replacing $t_{\rm sub}$ from equation (7.20) into equation (7.18) the remnant has reached a radius

$$r_{\rm sub} \simeq 150\,{\rm pc}\,\left(\frac{t_{\rm SB}}{10^7\,{\rm yr}}\right)^{\frac{4}{15}}\,, \tag{7.23}$$

to be compared with the superbubble size given by equation (7.6):

$$r_{\rm SB} \simeq 270\,{\rm pc}\,\left(\frac{t_{\rm SB}}{10^7\,{\rm yr}}\right)^{\frac{4}{15}}\,. \tag{7.24}$$

We have

$$\frac{r_{\rm sub}}{r_{\rm SB}} \simeq 0.56\,\left(\frac{t_{\rm SB}}{10^7\,{\rm yr}}\right)^{-\frac{1}{3}} \tag{7.25}$$

so that but if the superbubble is very young $r_{\rm sub} < r_{\rm rad}$: the supernova remnant becomes subsonic (and gets diluted) well inside the superbubble (but if the supernova explodes very close to its border). Thus the supernova's ram (kinetic) energy ultimately aliments the superbubble's internal (thermal) energy. This justifies the hypothesis made in section 7.1.3.1 that discrete energy releases in the superbubble are smoothed out and that one can assume a continuous driving power for the superbubble as a whole. Finally we would like to note that in the discussion above we have retained one superbubble parameter only, its age $t_{\rm SB}$, as it is the most relevant: dependencies in the luminosity $L_{\rm SB}$ and in the ISM density $n_{\rm ISM}$ are very weak.

The main results of this section (absence of radiative phase, mixing of the remnant with the superbubble interior) are confirmed by the few simulations adressing the evolution of supernova remnants in bubbles (Tenorio-Tagle et al. 1991) and superbubbles (Tang and Wang 2005).

7.2.3 Shock Characteristics

We now focus our attention on the shock discontinuity itself, still comparing the superbubble environment to the average interstellar medium.

The shock speed v_s is initially the same, as during the free expansion phase it depends only on the ejecta's mass $M_{\rm ej}$ and energy $E_{\rm sn}$ (see section 2.1.1.3). In the Sedov-Taylor phase it is $\sim$3 times higher due to the low ambient density. The shock speed is thus of the same order of magnitude, but its Mach number $M_s = v_s/c_s$ is one order of magnitude lower as the sound speed is one order of magnitude higher. From equation (7.16) we have

$$M_s = 500 \left(\frac{u_s}{5000\,\mathrm{km/s}}\right)\left(\frac{T}{10^4\,\mathrm{K}}\right)^{-\frac{1}{2}} \tag{7.26}$$

so that for a typical supernova shock of speed $v_s \sim 5000\,$km/s we have $M_{s,\rm SB} \sim 50$ in a superbubble and $M_{s,\rm ISM} \sim 500$ in a more standard ISM.

The strength of the shock determines its compression ratio r according to equation (2.5), that is assuming $\gamma = 5/3$:

$$r(M_s) = \frac{4\,M_s^2}{M_s^2 + 3}\,. \tag{7.27}$$

We recall that r controls (in the linear regime at least) the slope s of the cosmic-rays distribution according to equation (2.73). Figure 7.4 shows r and s as a function of M_s. We see that a $M_s = 50$ shock is already a "strong shock" as defined in section 2.1.1.2, as $r > 3.99$ as soon as $M_s > 35$ (and $s < 4.01$ as soon as $r > 3.97$). More precisely for $M_s = 50$: $r \simeq 3.9952$, $s \simeq 4.0016$ and for $M_s = 500$: $r \simeq 3.999952$, $s \simeq 4.000016$. As the shock slows down to $v_s \sim 1000\,$km/s we have $M_s = 10$ and $r \simeq 3.88$, $s \simeq 4.04$. Thus shocks in superbubbles are *marginally* strong shocks.

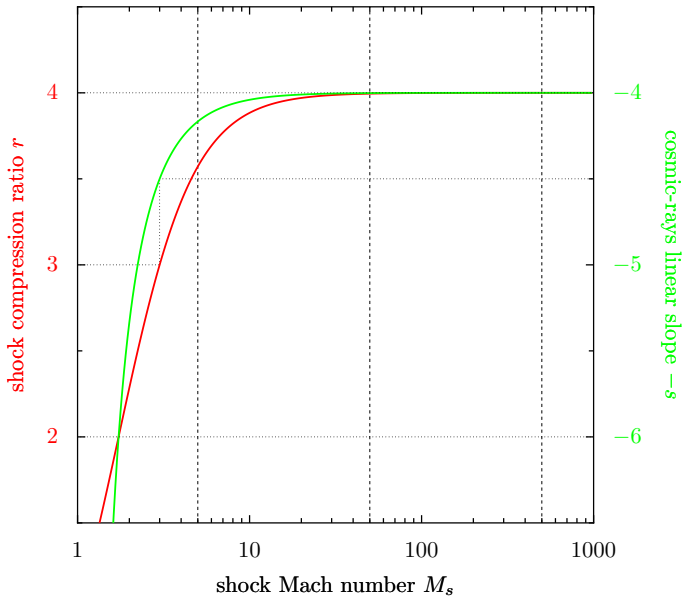

Figure 7.4: Shock compression ratio and cosmic-rays slope as a function of the Mach number.
Three remarkable pairs (r,s) are shown dotted: (2,6), (3,4.5), (4,4). Three Mach numbers are highlighted dashed: 5: typical secondary shock in a superbubble, 50: typical primary shock in a superbubble, 500: typical shock in a standard interstellar medium.

But as they evolve in a complex clumpy environment (see section 7.1.3.2), Parizot et al. (2004) expect that the few strong supernova shocks will produce many more weak secondary shocks, through reflections on the dense clumps embedded into the superbubble. For these shocks we expect $1 < M_s < 10$. For $M_s = 5$ we have $r \simeq 3.57$, $s \simeq 4.17$. The existence of many weak shocks will probably enhance the hydrodynamical turbulence inside the superbubble – adding to the effect of the direct wind-wind interactions (see section 7.1.3.2). In turn Bykov (1982) has shown that a shock front propagating into a turbulent medium gets distorted. The shock front isn't destroyed, but some of its kinetic energy is transferred to the turbulence. In conclusion all these effects put into question the assumption of spherical symmetry for supernova shocks inside superbubbles.

Finally we note that all this simple discussion doesn't take into account the back-reaction of cosmic-rays (see section 2.3), although we believe cosmic-rays play an important role in superbubbles (see chapter 8).

7.2.4 Supernovae Rate

To end this section we discuss the typical time between two supernovae $\Delta t_{\rm SN}$ in a superbubble (see the implications on cosmic-ray acceleration in section 8.2). Clearly $\Delta t_{\rm SN}$ depends on the OB association stars number and mass distri-

bution, and it varies during the superbubble life. Using a standard Salpeter IMF Cerviño et al. (2000) have simulated the supernova rate in a stellar cluster of total mass $M_{\rm OB}$ (in solar masses). Supernova activity starts suddenly after 4×10^6 yr (the lifetime of the most massive stars), with a high rate $8 \times 10^{-9}\,{\rm yr}^{-1} M_{\rm OB}^{-1}$ for a very short time $\simeq 10^5$ yr. Then the supernova rate slowly decreases from $2 \times 10^{-9} {\rm yr}^{-1} M_{\rm OB}^{-1}$ to $5 \times 10^{-10} {\rm yr}^{-1} M_{\rm OB}^{-1}$ over $\simeq 30 \times 10^7$ yr (up to the lifetime of the most massive stars, where supernova activity brutally stops). Thus the mean time between two supernovae in a superbubble is

$$\Delta t_{\rm SN} \sim 10^6 \text{ yr } \left(\frac{M_{\rm OB}}{10^3\ M_\odot} \right)^{-1} \tag{7.28}$$

$\Delta t_{\rm SN}$ is inversely proportional to the initial mass $M_{\rm OB}$ of the cluster powering the superbubble, which ranges typically from 10^3 to $10^6\ M_\odot$, so that $\Delta t_{\rm SN}$ ranges from $\sim 10^6$ yr in small clusters to $\sim 10^3$ yr in big clusters (this is indeed the value infered in a superbubble inside M82 by Weiss et al. (1999)). As the typical lifetime of a supernova remnant is $\sim 3 \times 10^5$ yr (see equation (7.20)), we expect that in most superbubbles there is at least one and probably many such remnants at any time.

7.3 Magnetic Field in Superbubbles

To end this chapter we briefly discuss the magnetic field inside superbubbles, as it is a crucial ingredient in diffusive shock acceleration (see sections 1.3.1.2 and 2.1.2), and as it determines the fate of accelerated particles between two acceleration episodes.

7.3.1 Magnetic Field Strength

Magnetic field can be probed through Zeeman effect and Faraday rotation measurements. Direct measurements in superbubbles are difficult and rather scarce. In his review of cosmic magnetic fields Vallée (2004) reports values of the order of 10 μG in the hot ISM phase, that is a few times higher than in the standard ISM where B is typically of a few μG.

From a theoretical perspective many people expect quite high magnetic fields inside superbubbles. Parizot et al. (2004) argue that turbulence generation trough direct wind-wind interactions and shock-clumps interactions (section 7.1.3.2) and shocks distortions (section 7.2.3) should be accompanied by MHD wave generation – all the more efficiently that the medium is already ionized and magnetized. They believe that the aforementioned mechanisms degrade an important fraction of the supernova energy, which cascades to small scales and produce a magnetized turbulence[5]. A few recent numerical simulations give support to this scenario (eg Velázquez et al. 2003, Breitschwerdt and

[5]Note that this calls into question the neglect of second-order Fermi acceleration inside superbubbles, especially between shocks (section 3.1.3).

de Avillez 2007). And we recall that the supernovae die within the superbubble and before being radiative (section 7.2.2), so that all their kinetic energy not put into cosmic-rays ultimately feeds the thermal and/or magnetic pressure in the superbubble. Assuming equipartition of all the mechanical energy released by massive stars between thermal pressure $P_{\rm SB}$ (equation (7.9)) and magnetic pressure $P_B \propto B^2$, Parizot et al. (2004) obtain $B_{\rm SB} \simeq 10$ μG. Equating the magnetic energy density to the total energy density in the superbubble $\epsilon \simeq L_{\rm SB} \times t_{\rm SB}/(4/3)\pi r_{\rm SB}^3$ they get $B_{\rm SB} \simeq 20$ μG. Bykov and Toptygin (1988, 2001) investigated magnetic field amplification upstream of shocks propagating in a hot and partially ionized medium such as the one expected in superbubbles. They found that the magnetic field can easily reach 10-30 μG.

However a few authors (eg Ferrière et al. 1991) believe that the magnetic field inside superbubbles should be greatly reduced, as being frozen in the fluid it is swept-up outwards by the winds and explosions and accumulates in the supershell. Thus the actual situation within superbubbles is still rather uncertain.

7.3.2 Turbulence and Cosmic-Ray Diffusion

As the supernovae die inside the superbubble (section 7.2.2) the cosmic-rays produced by the shock are released inside the superbubble. They will then be advected by the superbubble expansion and diffuse on the magnetic turbulence, until they eventually reach the supershell and escape the superbubble. The transport of cosmic-rays in the superbubble is intimately connected with the nature of the turbulence in these objects – which, unfortunately, is poorly known. Following Parizot et al. (2004) lets consider a power-law spectrum (see section 2.1.2.1)

$$W(k) \propto \eta_T \, (k \, \lambda_{\rm max})^{\beta} \tag{7.29}$$

where $\eta_T = \langle \delta B^2 \rangle \, / \, (\langle \delta B^2 \rangle + B^2)$ is the level of turbulence, probably close to 1 (see previous section), $\lambda_{\rm max}$ is the external scale of the turbulence, probably of the order of the distance between stars that is $\sim$10 pc (see equation (7.1)) and β is the turbulence index, 5/3 for a Kolmogorov cascade (a value supported by observations of the electrons density in Perseus OB2 by Minter and Spangler (1996) and in Cygnus OB1 by Spangler and Cordes (1998)). According to Casse et al. (2002) the (parallel) diffusion coefficient of a particle of energy E is then given by

$$D(E) \;=\; \frac{1}{3\eta_T} \lambda_{\rm max} c \left(\frac{r_L(E)}{2\pi \lambda_{\rm max}} \right)^{2-\beta} \tag{7.30}$$

where r_L is the Larmor radius (equation (2.23)), that is assuming $\beta = 5/3$:

$$D(E) \;=\; \frac{6.5 \times 10^{26}}{\eta_T} {\rm cm}^2/{\rm s} \left(\frac{E}{1\,{\rm GeV}} \right)^{\frac{1}{3}} \left(\frac{B}{10\,\mu{\rm G}} \right)^{-\frac{1}{3}} \left(\frac{\lambda_{\rm max}}{10\,{\rm pc}} \right)^{\frac{2}{3}} . \tag{7.31}$$

Finally we note that we could also consider diffusion on hydrodynamical turbulence (see sections 7.1.3.2 and 7.2.3), which can be decribed by a diffusion coefficient (independent of the particle energy)

$$D_{\rm hydro} = L \times u_{\rm rms} \simeq 3 \times 10^{26} {\rm cm}^2/{\rm s} \left(\frac{L}{10\,{\rm pc}}\right)\left(\frac{u_{\rm rms}}{100\,{\rm km/s}}\right) \qquad (7.32)$$

where L is the average distance between two turbulent sources (taken here to be of the order of the distance between stars) and $u_{\rm rms} = \sqrt{< u^2 >}$ is the average turbulent speed. $D_{\rm hydro}$ might be of the same order of magnitude as $D(E)$ up to about $E = 1$ GeV, but at very high energies diffusion caused by magnetic turbulence dominates the spreading of the cosmic-rays population.

References

Breitschwerdt, D. and de Avillez, M. A. (2007). Dynamical evolution of a supernova driven turbulent interstellar medium. volume 237 of *IAU Symposium*, pages 57–64.

Breitschwerdt, D., Freyberg, M. J., and Egger, R. (2000). Origin of H I clouds in the Local Bubble. I. A hydromagnetic Rayleigh-Taylor instability caused by the interaction between the Loop I and the Local Bubble. A&A, 361:303–320.

Bresolin, F., Kennicutt, Jr., R. C., and Garnett, D. R. (1999). The Ionizing Stars of Extragalactic H II Regions. ApJ, 510:104–124.

Brown, A. G. A., de Geus, E. J., and de Zeeuw, P. T. (1994). The Orion OB1 association. I. Stellar content. A&A, 289:101–120.

Bykov, A. M. (1982). Interstellar Turbulence and Shock Waves. *Soviet Astronomy Letters*, 8:320–322.

Bykov, A. M. and Toptygin, I. N. (1988). Generation of cosmic rays by supernovae in the inhomogeneous interstellar medium. *Akademiia Nauk SSSR Izvestiia Seriia Fizicheskaia*, 52:2290–2292.

Bykov, A. M. and Toptygin, I. N. (2001). A Model of Particle Acceleration to High Energies by Multiple Supernova Explosions in OB Associations. *Astronomy Letters*, 27:625–633.

Casse, F., Lemoine, M., and Pelletier, G. (2002). Transport of cosmic rays in chaotic magnetic fields. Phys. Rev. D, 65(2):023002 1–15.

Castor, J., McCray, R., and Weaver, R. (1975). Interstellar bubbles. ApJ, 200:L107–L110.

Cerviño, M., Knödlseder, J., Schaerer, D., von Ballmoos, P., and Meynet, G. (2000). Gamma-ray line emission from OB associations and young open clusters. I. Evolutionary synthesis models. A&A, 363:970–983.

de Geus, E. J., de Zeeuw, P. T., and Lub, J. (1989). Physical parameters of stars in the Scorpio-Centaurus OB association. A&A, 216:44–61.

de Zeeuw, P. T., Hoogerwerf, R., de Bruijne, J. H. J., Brown, A. G. A., and Blaauw, A. (1999). A HIPPARCOS Census of the Nearby OB Associations. AJ, 117:354–399.

Elmegreen, B. G. and Scalo, J. (2004). Interstellar Turbulence I: Observations and Processes. ARA&A, 42:211–273.

Ferrière, K. M., Mac Low, M.-M., and Zweibel, E. G. (1991). Expansion of a superbubble in a uniform magnetic field. ApJ, 375:239–253.

Garmany, C. D. (1994). OB associations: Massive stars in context. PASP, 106:25–37.

Higdon, J. C. and Lingenfelter, R. E. (2005). OB Associations, Supernova-generated Superbubbles, and the Source of Cosmic Rays. ApJ, 628:738–749.

Higdon, J. C., Lingenfelter, R. E., and Ramaty, R. (1998). Cosmic-Ray Acceleration from Supernova Ejecta in Superbubbles. ApJ, 509:L33–L36.

Koo, B.-C. and McKee, C. F. (1992a). Dynamics of wind bubbles and superbubbles. I. Slow winds and fast winds. ApJ, 388:93–126.

Koo, B.-C. and McKee, C. F. (1992b). Dynamics of Wind Bubbles and Superbubbles. II. Analytic Theory. ApJ, 388:103–126.

Korpi, M. J., Brandenburg, A., Shukurov, A., and Tuominen, I. (1999). Evolution of a superbubble in a turbulent, multi-phased and magnetized ISM. A&A, 350:230–239.

Kroupa, P. (2002). The Initial Mass Function of Stars: Evidence for Uniformity in Variable Systems. *Science*, 295:82–91.

Lamers, H. J. G. L. M. and Cassinelli, J. P. (1999). *Introduction to Stellar Winds*. Cambridge University Press, June 1999.

Limongi, M. and Chieffi, A. (2006). The Nucleosynthesis of 26Al and 60Fe in Solar Metallicity Stars Extending in Mass from 11 to 120 Solar Masses: The Hydrostatic and Explosive Contributions. ApJ, 647:483–500.

Mac Low, M.-M. and McCray, R. (1988). Superbubbles in disk galaxies. ApJ, 324:776–785.

Mac Low, M.-M., McCray, R., and Norman, M. L. (1989). Superbubble blowout dynamics. ApJ, 337:141–154.

Maeder, A. and Meynet, G. (2003). Stellar evolution with rotation and magnetic fields. I. The relative importance of rotational and magnetic effects. A&A, 411:543–552.

Marcowith, A. (2007b). Les supernovae comme sources des rayons cosmiques II. Les régions de formation d'étoiles massives et les superbulles [brouillon]. Ecole de Gif sur les rayons cosmiques de haute énergie.

Minter, A. H. and Spangler, S. R. (1996). Observation of Turbulent Fluctuations in the Interstellar Plasma Density and Magnetic Field on Spatial Scales of 0.01 to 100 Parsecs. ApJ, 458:194–214.

Montmerle, T. (1979). On gamma-ray sources, supernova remnants, OB associations, and the origin of cosmic rays. ApJ, 231:95–110.

Norman, C. A. and Ikeuchi, S. (1989). The disk-halo interaction - Superbubbles and the structure of the interstellar medium. ApJ, 345:372–383.

Normandeau, M., Taylor, A. P., and Dewdney, P. E. (1996). A galactic chimney in the Perseus arm of the Milky Way. *Nature*, 380(6576):687–689.

Parizot, E., Marcowith, A., van der Swaluw, E., Bykov, A. M., and Tatischeff, V. (2004). Superbubbles and energetic particles in the Galaxy. I. Collective effects of particle acceleration. A&A, 424:747–760.

Pietrzyński, G., Gieren, W., Fouqué, P., and Pont, F. (2001). A Catalog of OB Associations in the spiral galaxy NGC 300. A&A, 371:497–506.

Schaller, G., Schaerer, D., Meynet, G., and Maeder, A. (1992). New grids of stellar models from 0.8 to 120 solar masses at Z = 0.020 and Z = 0.001. A&AS, 96:269–331.

Shull, J. M. and Saken, J. M. (1995). Noncoeval star formation, starbursts, and the growth of supershells in OB associations. ApJ, 444:663–671.

Silich, S. and Franco, J. (1999). Superbubble Evolution Including the Star-forming Clouds: Is It Possible to Reconcile Large Magellanic Cloud Observations with Model Predictions? ApJ, 522:863–869.

Spangler, S. R. and Cordes, J. M. (1998). VLBI Measurements of Plasma Turbulence Associated with the Cygnus OB1 Association. ApJ, 505:766–783.

Tang, S. and Wang, Q. D. (2005). Supernova Blast Waves in Low-Density Hot Media: A Mechanism for Spatially Distributed Heating. ApJ, 628:205–209.

Tenorio-Tagle, G., Rozyczka, M., Franco, J., and Bodenheimer, P. (1991). On the evolution of supernova remnants. II - Two-dimensional calculations of explosions inside pre-existing wind-driven bubbles. MNRAS, 251:318–329.

Tomisaka, K. (1990). Blowout of superbubble in Galactic magnetic field. ApJ, 361:L5–L8.

Tomisaka, K. (1998). Superbubbles in magnetized interstellar media: blowout or confinement? MNRAS, 298:797–810.

Tomisaka, K. and Ikeuchi, S. (1986). Evolution of superbubble driven by sequential supernova explosions in a plane-stratified gas distribution. *Publications of the Astronomical Society of Japan*, 38:697–715.

Vallée, J. P. (2004). Cosmic magnetic fields - as observed in the Universe, in galactic dynamos, and in the Milky Way. *New Astronomy Review*, 48:763–841.

van den Bergh, S. and McClure, R. D. (1994). Rediscussion of extragalactic supernova rates derived from Evans's 1980-1988 observations. ApJ, 425:205–209.

Velázquez, P. F., Koenigsberger, G., and Raga, A. C. (2003). A Supernova Remnant Collision with a Stellar Wind. ApJ, 584:284–292.

Walborn, N. R., Drissen, L., Parker, J. W., Saha, A., MacKenty, J. W., and White, R. L. (1999). HST/FOS Spatially Resolved Spectral Classification of Compact OB Groups in the Large Magellanic Cloud. AJ, 118:1684–1699.

Weaver, R., McCray, R., Castor, J., Shapiro, P., and Moore, R. (1977). Interstellar bubbles. II - Structure and evolution. ApJ, 218:377–395.

Weiss, A., Walter, F., Neininger, N., and Klein, U. (1999). Evidence for an Expanding Molecular Superbubble in M 82. In *Bulletin of the American Astronomical Society*, volume 31, page 949.

Woosley, S. E., Heger, A., and Weaver, T. A. (2002). The evolution and explosion of massive stars. *Reviews of Modern Physics*, 74:1015–1071.

Chapter 8

Cosmic-Ray Production in Superbubbles

In this chapter we discuss how the fact that most supernovae explode inside superbubbles affects the phenomenology of the cosmic-rays they produce. We distinguish two aspects. First we review the impact on the composition of the cosmic radiation, which was not our main concern in this thesis, but which is an important and well established matter (see eg Parizot 2005). Secondly we investigate the possibility of repeated acceleration by multiple (successive) shocks, which is still an open question and was the first motivation of this thesis.

8.1 Effects of the Environment

Cosmic-ray composition is an essential clue to their origin, and superbubble models predict different composition biases than models of isolated supernova remnants developping in a standard ISM. A distinctive difference is that superbubbles are the place where most of the freshly synthesized heavy nuclei are released by supernovae explosions (Bykov, 1999).

8.1.1 Light Elements Nucleosynthesis

Around the middle of the XXth century it has been realized that almost all elements in the Universe are produced through two mechanisms, namely primordial nucleosynthesis and stellar nucleosynthesis. The early "big bang" have produced elements up to A=4 (Hydrogen and Helium); since then the inner fusion and outer explosion of stars have produced elements above A=12 (Carbon). Light elements in between: ^{6}Li, ^{7}Li, ^{9}Be, ^{10}Be, ^{11}Be (commonly referred to collectively as "LiBeB") are too unlikely to be synthesized in the primordial conditions and too weak to survive into stars. Their current relative abundances $\mathrm{Li/H} = (1-2)\times10^{-9}$, $\mathrm{Be/H} = (1-3)\times10^{-11}$, $\mathrm{B/H} = (2-8)\times10^{-10}$ are therefore very low – however they are non-zero. As LiBeB is too difficult to

build from lighter elements, it must be produced by breaking heavier elements (such as C, N, O): this is the *spallation* mechanism, pointed out by Reeves et al (1970, 1973). The energetic particles responsible for triggering such reactions were quickly identified as being cosmic-rays, as spallation is indeed required to explain their own composition (see section 1.2.2), and as the global energy budget to explain the observed current LiBeB ratio is correct.

But observations of old stars have shown that their [LiBeB/Fe] ratio is roughly independent of their metallicity[1] [Fe/H], so that LiBeB concentration is roughly proportional to Iron one. Therefore, although being a *secondary* element (produced through spallation of pre-existing nuclei), LiBeB exhibits a *primary* element behaviour[2]. Casse et al. (1995), Vangioni-Flam et al. (1996) understood that the solution of this paradox is that LiBeB is actually produced through *inverse* spallation, that is cosmic-rays heavy ions colliding on ambient H or He atoms at rest, rather than through direct spallation (energetic H or He nuclei colliding with heavy elements at rest). But cosmic-rays are thought to be injected from the ambient interstellar medium (see section 2.4), in which the heavy elements (CNO) abundances is low, especially in the early stages of the Galaxy when the aforementioned stars where observed. Parizot and Drury (1999a, 1999b) have shown that because of that cosmic-rays produced by isolated supernovae cannot explain the production of LiBeB. But then Parizot and Drury (1999c), Parizot (2000, 2001) have shown that superbubbles nicely solve the LiBeB issue. Indeed superbubbles are *the* place where most of the heavy elements are released (through massive stars winds and supernovae ejecta), and at a rate roughly *constant* in time (that is almost independent of the overall Galactic composition)[3].

8.1.2 Cosmic-Ray Composition Anomalies

For the same reason that superbubbles host most of the massive stars, they explain a composition anomaly observed in cosmic-rays. Namely the ratio ^{22}Ne/^{20}Ne is $\sim$5 times higher in cosmic-rays than in the average interstellar medium (Maehl et al. 1975, Garcia-Munoz et al. 1979, Binns et al. 2001). As acceleration mechanisms don't discriminate between isotopes, this point to an overabundance of ^{22}Ne in the sources. The only known big producers of this element are Wolf-Rayet winds (Völk and Forman 1982, Casse and Paul 1982).

[1] All the ratios are expressed in logarithmic units and with respect to the solar one, eg

$$[\mathrm{Fe/H}] = \log\left(\frac{([\mathrm{Fe}]\,/\,[\mathrm{H}])_\star}{([\mathrm{Fe}]\,/\,[\mathrm{H}])_\odot}\right)$$

[2] As secondary elements Y require their parents X to be produced first, there formation rate is proportional to [X] so that integrated on their production time-scale their concentration goes as [X]^2.

[3] Note that today the metallicity has raised everywhere in the Galaxy, so that the *current* rate of production of LiBeB does no longer really constrain the source of cosmic-rays: the issue was to sustain the same rate in the past.

But winds themselves are usually poor accelerators, so that cosmic-ray composition requires a sizeable fraction of the medium accelerated by supernova shocks to be ejecta from these massive stars (25%, Meynet et al. 2001; 18±5%, Higdon and Lingenfelter 2003; 20%, Binns et al. 2005). As superbubbles host most of the Wolf-Rayet stars, this again points to a close link between cosmic-rays and superbubbles.

Another composition anomaly has to be explained by any cosmic-ray production model, namely the fact that the ^{59}Ni/^{60}Ni ratio is almost zero in cosmic-rays. ^{59}Ni is produced by explosive nucleosynthesis and decays in ^{59}Co through electronic capture over $t_{\rm e} \simeq 10^5$ yr, so that necessarily most of the ^{59}Ni synthesized is *not* accelerated during the first 10^5 yr after the supernova explosion that produced it (Binns et al. 1999, Wiedenbeck et al. 1999). This can be explained if cosmic-rays are actually the result of a *sequence* of supernova shocks, separated by $\Delta t_{\rm SN} > t_{\rm e}$, as is possible in superbubbles (Higdon et al. 1998). However according to estimate (7.28) $\Delta t_{\rm SN}$ should be much lower than $t_{\rm e}$ in the largest OB clusters ($10^5 - 10^6\,M_\odot$), which would rule out rich superbubbles as a significant source of low-energy cosmic-rays. We believe that a more detailed modeling is required to fully explain this very constraining observation.

8.2 Effects of Multiple Shocks

As supernovae mostly occur within OB associations inside superbubbles (section 7.2.1), supernovae are highly correlated in space (they remain within the bubble, of size of a few 100 pc, see section 7.2.2) and in time (supernovae explode roughly every $\Delta t_{\rm SN} \sim 10^6$ yr, see section 7.2.4, and last for a few 10^5 yr, see section 7.2.2). Therefore regarding particle acceleration by supernova shocks one has to consider the possibility of *collective* effects inside superbubbles (Parizot et al. 2004). In this section we discuss the likeliness of multiple shock acceleration, review the two previous attempts to investigate it, and present our own approach and early results on that matter.

8.2.1 Probability of Multiple Shock Acceleration

Given all the arguments of section 7.2 there is little doubt that there are indeed many successive supernova shocks inside superbubbles. So the question regarding multiple shock acceleration is rather whether shocks are sufficiently frequent to re-accelerate cosmic-rays by the time they escape the superbubble. How well are cosmic-rays confined into superbubbles? We recall that cosmic-rays travel at almost the speed of light, and therefore can only be confined in a medium because of diffusion caused by turbulence, as discussed in section 7.3.2. Between two shocks separated by $\Delta t_{\rm S}$ cosmic-rays then travel a typical distance $x_{\rm diff} = \sqrt{6D\,\Delta t_{\rm S}}$ where D is the diffusion coefficient, which for magnetic turbulence is a function of the particle energy. This distance has

to be compared with the typical size of the acceleration region $x_{\rm accel}$. Using the diffusion coefficient $D(E)$ of equation (7.31) and equating $x_{\rm diff}$ and $x_{\rm accel}$, we obtain the maximum energy $E_{\rm cut}$ up to which cosmic-rays remain within the acceleration region between two shocks as

$$E_{\rm cut} \;=\; 10\,{\rm GeV}\;\left(\eta_T^3\right)\left(\frac{B}{10\;\mu{\rm G}}\right)\left(\frac{\lambda_{\rm max}}{10\;{\rm pc}}\right)^{-2}\left(\frac{\Delta t_S}{10^6\;{\rm yr}}\right)^{-3}\left(\frac{x_{\rm accel}}{150\;{\rm pc}}\right)^{6} \quad (8.1)$$

We note the strong dependence of $E_{\rm cut}$ on the parameters[4]. And most parameters are rather poorly constrained. As we have seen in section 7.3.1 B is probably of the order of 10 μG or more but this is still debatable. The turbulence scale $\lambda_{\rm max}$ could be up to one order of magnitude lower, rising $E_{\rm cut}$ by a factor 100. The size of the acceleration region is better constrained (but $E_{\rm cut}$ has the strongest dependence on it), it has been normalized here to the typical final extension of a supernova shock (see equation (7.23)). Finally the typical time between two shocks $\Delta t_{\rm S}$ appears to be a key parameter. Now we shall consider two kind of shocks, both strong primary supernova shocks and weak secondary induced shocks (see section 7.2.3). The typical time between two supernova shocks $\Delta t_{\rm SN}$ clearly depends on the OB association stars number and mass distribution, and varies during the superbubble life (see section 7.2.4). It is expected to range from 10^6 yr in small clusters to 10^3 yr in big clusters – where the above $E_{\rm cut}$ could be raised by a factor 10^9. Regarding weak shocks, the situation is less clear, but we expect $\Delta t_{\rm S}$ to be substantially lower than the duration of a supernova shock (equation (7.20)), maybe of the order of $10^3 - 10^4$ yr, depending on how clumpy the superbubble is. Anyway weak shocks favour higher values of $E_{\rm cut}$. In conclusion we believe that $E_{\rm cut} = 10$ GeV is a conservative estimate of the energy below which particles accelerated by one shock will most certainly experience re-acceleration by another shock. Depending on the actual superbubbles parameters, this could actually affect the whole spectrum of cosmic-rays.

Now what is the probability for a particle accelerated by one supernova shock to energy E to encounter *many* other successive supernova shocks? Assuming that the time between every two shocks is the same (which is probably too schematic, especially for weak shocks), according to equation (8.1) the energy $E_{\rm cut}^{(N)}$ below which particles experience re-acceleration by N other successive identical shocks goes roughly as $E_{\rm cut}^{(N)} \propto N^{-3}$, so that 3 decades of cosmic-rays are "lost" every time one adds 10 shocks. This quantity is shown on figure 8.1. But in fact all the particles will increase their energy at each shock – and at a rate which is dependent on their current energy – and thus will escape the acceleration region more easily than that: the more cosmic-rays are re-accelerated, the less chance they have to be re-accelerated again. In conclusion we believe that only cosmic-rays of rather low energy (conservatively

[4]Which also strongly depends on the turbulence index β (assumed here to be 5/3) as in fact $E_{\rm cut} \propto B\,\lambda_{\rm max}^{(\beta-1)/(\beta-2)}\,\Delta t_S^{1/(\beta-2)}\,x_{\rm accel}^{2/(\beta-2)}$.

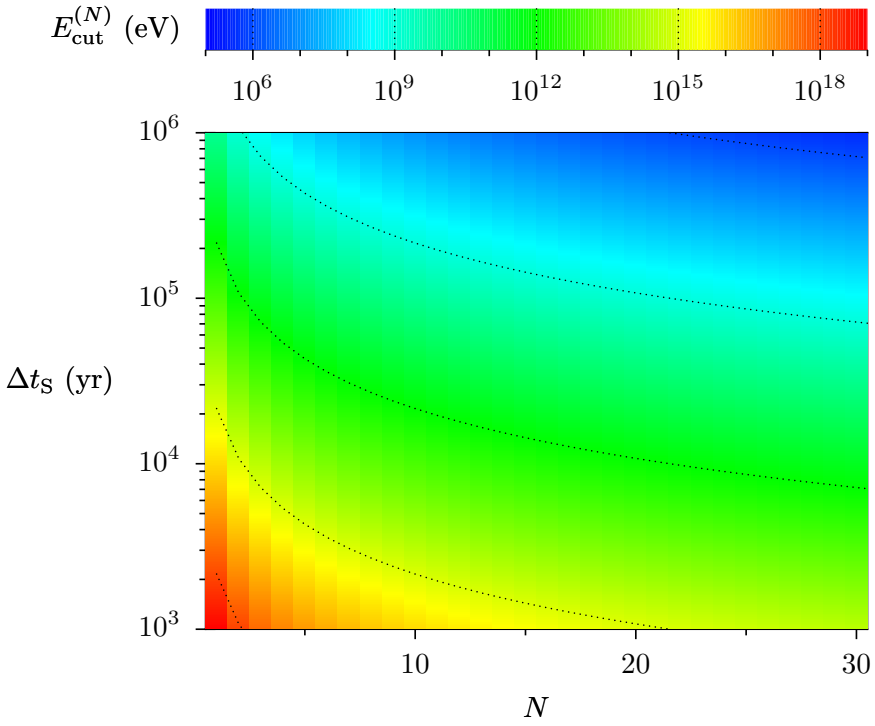

Figure 8.1: Cut-off energy for multiple shock acceleration.
The colour codes $E_{\rm cut}^{(N)} = N^{-3} E_{\rm cut}$ where N is the number of successive shocks and $E_{\rm cut}$ is given by equation (8.1) assuming $\eta_T = 1$, $B = 10\ \mu$G, $\lambda_{\rm max} = 10$ pc, $x_{\rm accel} = 150$ pc, so that the only remaining parameter is the typical time between two shocks $\Delta t_{\rm S}$. This represents a very rough estimate of the energy up to which cosmic-rays are likely to experience N successive shocks (cosmic-rays of higher energy will escape the system before).

up to the GeV) are likely to truly experience acceleration by repeated shocks as presented in chapter 3. A more precise answer would require first a more detailed study of the actual timeline of an OB association (as a function of its total mass), probably by the means of Monte-Carlo simulations.

8.2.2 Previous Approaches for Collective Acceleration

Two groups have already investigated multiple shock acceleration analytically in the context of superbubbles.

8.2.2.1 A Linear Model

Klepach et al. (2000) have studied test-particle acceleration by multiple spherical shocks (either winds termination shocks, either supernova shocks and winds external shocks). They have derived a transport equation for the mean dis-

tribution function $\langle f \rangle$ (the actual f can be strongly intermittent) and found that it leads to hard spectra, of index between 4 and 3 (in agreement with the general theoretical results presented in chapter 3). They applied their model to two regions of interests: OB associations, in which the maximum energy of cosmic-rays rises by more than one order of magnitude with respect to isolated stars (but it is still really difficult to reach the ankle, but maybe with very strong magnetic turbulence); and the Galaxy as a whole, in which multiple acceleration is not efficient (but maybe for low-energy cosmic-rays) as the diffusion coefficient is large. Their approach suffers from two major limitations: they don't consider cosmic-rays back-reaction (but see section 2.3), and they assume small winds filling factor to be able to make the calculations analytically (but see section 7.1.3.2).

8.2.2.2 A Non-Linear Model

Over the last 15 years Bykov and collaborators have developed a comprehensive kinetic model of production of cosmic-rays inside superbubbles (first presented in Bykov and Fleishman (1992) and Bykov and Fleishman (1993), reviewed and extended in Bykov (2001)).

They consider that particles are accelerated by a powerful energy release in the form of violent large-scale motions of the magnetized plasma inside the superbubble. Non-thermal particles eventually penetrate into the denser matter surrounding the bubble (supershell or cloud) and then suffer various interactions which lead to nucleosynthesis and high-energy emission. Their analytical treatment is statistical. The distribution function $N(\vec{x}, p, t)$ (such that $dN(\vec{x}, p, t) = 4\pi p^2 f(\vec{x}, p, t) dp$) of cosmic-rays averaged over an ensemble of turbulent motions and shocks (the shock ensemble is typically dominated by weak shocks, for which the ratio of particle acceleration over shock heating can be higher) satisfies the kinetic equation

$$\frac{\partial N}{\partial t} - \frac{\partial}{\partial \vec{x}} \left(\chi \frac{\partial N}{\partial \vec{x}} \right) = \frac{\hat{L} N}{\tau_{\rm sh} + B} + \frac{1}{p^2} \frac{\partial}{\partial p} \left(p^4 C \frac{\partial N}{\partial p} \right) + A \hat{L}^2 N + 2B \hat{L} \hat{P} N + Q \quad (8.2)$$

where $\hat{L}$ and $\hat{P}$ are integro-differential operators expressing respectively the action of a single shock and the effect of adiabatic decompression, χ, A, B, C are kinetic coefficients describing correlations between large scale turbulent motions and shocks (χ incorporates the microscopic diffusion coefficient $D(p)$ caused by magnetic turbulence), Q is the injection source term, $\tau_{\rm sh}$ is the characteristic acceleration time. The stationnary spectrum is given by

$$f(p) \propto \begin{cases} \left(\frac{p}{p_{\rm inj}} \right)^{-3} & p \leq p_\star \\ \left(\frac{p_\star}{p_{inj}} \right)^{s_1 - 3} \left(\frac{p}{p_{\rm inj}} \right)^{-s_1} & p \geq p_\star \end{cases} \quad (8.3)$$

where $s_1 = 3r/(r-1)$ is the canonical slope for a single linear shock and $p_\star$ is a time-dependent cut-off momentum (function of $\tau_{\rm sh}$). Again we see

that multiple shocks acceleration produces hard spectra (of slope between 4 and 3), especially at low energies. Note that in fact the actual distribution of accelerated particles is strongly intermittent, especially at low energies.

Test particle calculations have shown that the low energy branch of the particle distribution contains a substantial fraction of the free energy of the system after a few acceleration times, so that Bykov had to account for the back-reaction of the accelerated particles on the shocks turbulence. He thus added the (time-dependent) conservation equations for the transverse $T(k,\omega)$ and longitudinal $S(k,\omega)$ parts of the Fourier components of the turbulent velocity correlation tensor, getting a closed set of equations, allowing for a self-consistent solution. Note that because of the statistical approach this non-linear treatment is very different from ours: Bykov's model doesn't explicitly deal neither with cosmic-rays pressure (see sections 2.3.1 and 4.2.4) nor with shock modifications (see sections 2.3.2.1 and 4.3.2) as it doesn't actually deals explicitly with shocks structures. The asymptotic distribution $f(p)$ is still a power-law, but steeper than in the linear regime: its slope varies from 5 to 4 as cosmic-rays are initially injected at low (10 keV) or high (10 GeV) energies. Another remarkable result of the model is that 20% to 40% of the kinetic power released inside the superbubble can be transferred to low-energy particles on a time scale shorter than 10^6 yr. And finally the maximum energy of cosmic-rays is found to be around 10^{17} eV, that is compatible with the highest energy Galactic cosmic-rays.

8.2.3 On the Role of Internal and External Injection

A key point regarding acceleration by successive shocks is the presence, upstream of each shock (but maybe the very first), of a population of cosmic-rays accelerated by the last shock. Note that being already of (much) higher energy than the thermal plasma, these particles already match the conditions to see the shock as a discontinuity and be (re-)accelerated by the first order Fermi mechanism, that is, upstream cosmic-rays are all automatically injected in the new accelerator. Here we find it convenient to introduce a bit of new terminology: from now on we will call *external injection* the advection of pre-existing upstream high-energy particles, and *internal injection* the injection at the shock front from the thermal plasma (through thermal leakage, as presented in section 2.4). Internal injection is mostly controlled by η, the fraction of the incident fluid flux converted to cosmic-rays (see section 2.4.2); we will parametrize external injection by $\chi = P_{\rm cr}/P$ the ratio of the cosmic-rays and gas pressures (see section 2.3.1). In this final section we will discuss the relative importance of these two mechanisms.

8.2.3.1 Analytical Approach in the Linear Regime

Dorfi and Völk (1996) have already made a study of this kind in the context of elliptical galaxies. The average ISM in such galaxies is even hotter ($T = 10^6 - 3 \times 10^7$ K) and and of lower density ($n = 3 \times 10^{-3} - 10^{-4}$ cm^{-3}) than in superbubbles. Therefore superbubbles are somehow an intermediate case between the average ISM of spiral galaxies and the average ISM of elliptical galaxies. In these two extreme environments the situation is quite clear. In the average ISM of spiral galaxies supernova shocks are always strong shocks, so that we expect internal injection to be high and particle acceleration to be efficient; in the average ISM of elliptic galaxies supernova shocks are always weak shocks (with Mach numbers at the beginning of the Sedov phase between 2 and 7), so that we expect internal injection to be reduced and particle acceleration to be less efficient. Using test-particle two-fluids simulations, Dorfi and Völk have observed that indeed internal injection plays here a minor role: the amount of the supernova energy ultimately converted into cosmic-rays depends strongly on their external density. Comparing the energy flux of particles injected at the shock

$$F_{\rm inj}^{\rm int} = \eta \frac{1}{2} \rho_1 u_1 \left(u_1^2 - u_2^2 \right) \tag{8.4}$$

with the energy flux of particles advected to the shock

$$F_{\rm inj}^{\rm ext} = e_{\rm cr} u_1 = \frac{\chi P_1}{\gamma_{\rm cr} - 1} u_1 \tag{8.5}$$

they show analytically that injection dominates over advection above a shock Mach number $M_S^\star$ given by[5]

$$\begin{aligned} M_S^{\star 2} &= \frac{4\left(\gamma_g - 1\right)\left(\gamma_c - 1\right) + \left(\gamma_g + 1\right)^2 \delta}{8\gamma_g \left(\gamma_c - 1\right)} \\ &+ \frac{\left(\gamma_g + 1\right)\sqrt{16\left(\gamma_c - 1\right)^2 + 8\left(\gamma_g - 1\right)\left(\gamma_c - 1\right)\delta + \left(\gamma + 1\right)^2 \delta^2}}{8\gamma_g \left(\gamma_c - 1\right)} \end{aligned} \tag{8.6}$$

where $\delta = \chi/\eta$ is the relative importance of external versus internal injection. We have

$$M_S^{\star 2} \underset{\delta \gg 1}{\longrightarrow} \frac{\left(\gamma_g + 1\right)^2 \delta}{4\gamma_g \left(\gamma_c - 1\right)}. \tag{8.7}$$

Note also that $M_S^\star(\delta = 0) = 1$ which simply means that in the absence of upstream cosmic-rays internal injection dominates whatever the Mach number. The adiabatic index of the gas is taken to be γ_g=5/3. Dorfi and Völk assumed an adiabatic index γ_c=4/3 for the cosmic-rays "fluid", but this is actually the lower limit value, appropriate in the late acceleration phases, when cosmic-rays

[5]Note the missing δ in equation (10) of Dorfi and Völk.

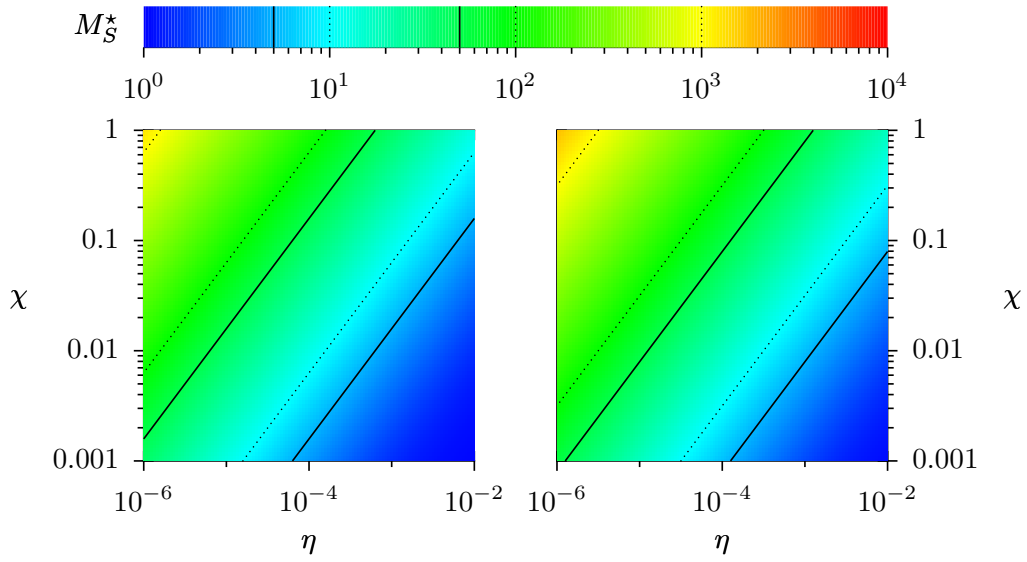

Figure 8.2: Critical Mach number for injection.
The colour codes the value of the theoretical critical Mach number $M_S^\star$ (given by equation (8.6)) as a function of the injection ratio η (internal injection) and of the upstream cosmic-rays pressure ratio χ (external injection). The lines denote a few constant Mach numbers, solid ones correspond to a typical strong shock ($M_S = 50$) and to a typical weak shock ($M_S = 5$) inside a superbubble. For pairs (η,χ) located at the bottom right of the line, injection is dominated by η, for pairs (η,χ) located at the top left of the line, injection is dominated by χ. The two plots correspond to the two limit values of the adiabatic index γ_c of the cosmic-rays: 5/3 at the left ($M_S^\star$ given by equation (8.9)), 4/3 at the right ($M_S^\star$ given by equation (8.8)).

have been accelerated to highly relativistic energies. In the early acceleration phases, when cosmic-rays are injected at non-relativistic energies, their index is close to 5/3 (see eg section 4.3.2). The corresponding limiting values of $M_S^\star$ are given by

$$\gamma_c = \frac{4}{3} \quad : \quad M_S^{\star 2} = \frac{1 + 8\delta + 4\sqrt{1 + \delta + 4\delta^2}}{5} \rightarrow \frac{16\delta}{5} \quad \delta \gg 1 \,; \tag{8.8}$$

$$\gamma_c = \frac{5}{3} \quad : \quad M_S^{\star 2} = \frac{1 + 4\delta + 2\sqrt{4 + 2\delta + 4\delta^2}}{5} \rightarrow \frac{8\delta}{5} \quad \delta \gg 1 \,. \tag{8.9}$$

These two cases are shown in figure 8.2. Assuming χ to be around 10^{-1} and η to be lower than 10^{-2}, so that $\delta \geq 10$, Dorfi and Völk find that in elliptical galaxies $M_S^\star \gtrsim 6$ and therefore conclude that injection at supernova shocks is always dominated by pre-existing cosmic-rays. We expect the same kind of values for χ and η in superbubbles, but here the shock Mach number ranges from $\simeq 5$ for weak secondary shocks to $\simeq 50$ for strong primary shocks

as discussed in section 7.2.3, so that the situation is less clear. As seen on figure 8.2, strong shocks of M_S=50 seem to be dominated by internal injection, but for low values of η (eg $\eta < 10^{-6}$ for χ=1%) or high values of χ (eg $\chi > 100\%$ for $\eta = 10^{-3}$). For weak shocks of M_S=5 the requirements on the value of χ for external injection to dominate are lowered by two orders of magnitude (eg $\chi > 1\%$ for $\eta = 10^{-3}$), so that they should be easily met in superbubbles.

Note that all this study holds in the linear regime, but might be substantially modified in the non-linear regime. First in the case of modified shocks the relevant Mach number for injection is the *sub-shock* one (see section 2.3.2.1). Assuming adiabatic heating in the precursor we have

$$M_{S,\mathrm{sub}} = \left(\frac{r_{\mathrm{sub}}}{r_{\mathrm{tot}}}\right)^{\frac{\gamma_g+1}{2}} M_{S,\mathrm{tot}} = \left(\frac{r_{\mathrm{sub}}}{r_{\mathrm{tot}}}\right)^{\frac{4}{3}} M_{S,\mathrm{tot}} \quad \text{for} \quad \gamma_g = \frac{5}{3}\,. \tag{8.10}$$

The ratio $r_{\mathrm{sub}}/r_{\mathrm{tot}}$ is not well constrained but is < 1 (and can easily be $< 1/2$) so that $M_{S,\mathrm{sub}}$ is substantially lower than the unmodified value (for $r_{\mathrm{sub}}/r_{\mathrm{tot}} = 1/2$: $M_{S,\mathrm{sub}} = 20$). Secondly η is actually time-dependent: it is lowered as the sub-shock is reduced (see Blasi's self-consistent recipe, equation (2.93)). We note that both effects tend to favour external injection.

8.2.3.2 Numerical Simulations in the Non-Linear Regime

In this final section we present the results of simulations aimed at determining the relative role of internal and external injection for supernova shocks propagating inside superbubbles. This constitutes a first step in the study of the effects of acceleration by multiple shocks in this environment, as one distinctive feature of this mechanism is precisely the pre-existence of "seed" cosmic-rays.

Units. The simulations presented in part II were not explicitly dimensioned, as we were mostly concerned in the overall evolution of the (modified) shocks and wanted to recover previous published results. Here we design simulations adapted to the superbubble environment, and explicit our system of units.

Each variable X is made non-dimensional as $X^\star = X/X_{\mathrm{ch}}$ where X_{ch} is the reference unit. When applying this transformation to the Euler equations (2.81), (2.82), (2.83) (or their modified versions (2.85), (2.82), (2.87)) the system still holds for the non-dimensional variables $X^\star$ provided the following conditions are met:

$$\begin{cases} u_{\mathrm{ch}} = x_{\mathrm{ch}}/t_{\mathrm{ch}} \\ P_{\mathrm{ch}} = \rho_{\mathrm{ch}} u_{\mathrm{ch}}^2 \\ e_{\mathrm{ch}} = P_{\mathrm{ch}} \end{cases} . \tag{8.11}$$

We can thus choose three independent units x_{ch}, t_{ch}, ρ_{ch} and then all other units u_{ch}, P_{ch}, e_{ch} are fixed according to (8.11). The cosmic-rays convection-

diffusion equation (2.65) adds the condition

$$D_{\rm ch} = x_{\rm ch}^2/t_{\rm ch} = x_{\rm ch}u_{\rm ch} = u_{\rm ch}^2 t_{\rm ch} \, . \tag{8.12}$$

We find it convenient to use the following set of units:

$$\begin{cases} x_{\rm ch} = 3 \times 10^{13} \, {\rm cm} \simeq 10^{-5} \, {\rm pc} \\ t_{\rm ch} = 3 \times 10^{5} \, {\rm s} \simeq 10^{-2} \, {\rm yr} \\ u_{\rm ch} = 10^{8} \, {\rm cm/s} = 1000 \, {\rm km/s} \\ \rho_{\rm ch} = 1 m_p/{\rm cm}^3 \simeq 1.7 \times 10^{-24} \, {\rm g/cm}^3 \\ P_{\rm ch} = e_{\rm ch} = 1.7 \times 10^{-8} \, {\rm erg/cm}^3 \\ D_{\rm ch} = 3 \times 10^{21} \, {\rm cm}^2/{\rm s} \simeq D_{\rm Bohm}(E = 1 \, {\rm GeV}, B = 10 \, \mu{\rm G}) \end{cases} . \tag{8.13}$$

We have then

$$P^\star = \frac{P}{P_{\rm ch}} \simeq 10^{-4} \left(\frac{n}{1 \, {\rm cm}^{-3}} \right) \left(\frac{T}{10^4 \, {\rm K}} \right) \tag{8.14}$$

so that in both the average ISM ($n \simeq 1 \, {\rm cm}^{-3}$, $T \simeq 10^4 \, {\rm K}$) and in a superbubble ($n \simeq 10^{-2} \, {\rm cm}^{-3}$, $T \simeq 10^6 \, {\rm K}$) we have $P^\star \simeq 10^{-4}$.

Strong shocks. We now focus our attention on superbubbles, and consider its ambient medium to be homogeneous and at rest, so we set the initial upstream state to be $\rho_1^\star = 10^{-2}$, $u_1^\star = 0$, $P_1^\star = 10^{-4}$. We set the (constant) Mach number of the shock to be $M_S = 50$ (using the "moving piston" initialization of section 4.1.2), so that its speed is $u_S = 6450$ km/s ($\beta_S = u_S/c = 0.0215$). Using equation (2.96) the mean downstream thermal momentum can be expressed as

$$\frac{p_{2,{\rm th}}}{{\rm m_p c}} \simeq 0.6 \frac{u_S}{c} \tag{8.15}$$

so that for a shock of $u_S \simeq 5000$ km/s we have $p_{2,{\rm th}} \simeq 10^{-2} \, {\rm m_p c}$. The acceleration time-scale at injection (equation (2.76)) is then $t_{\rm acc}^\star(p_{\rm inj}) \simeq 10^{-2}$. The minimum momentum of the numerical grid is set to $\log(p_{\rm inj}/{\rm m_p c}) = -2$. Given the computational cost of such simulations, and as we have observed that the cosmic-rays pressure evolves much more slowly after the bulk of cosmic-rays has become relativistic (that is has reached the GeV), we limit ourselves to a maximum momentum $p_{\rm max} = 10^2 \, {\rm m_p c} \simeq 10^2$ GeV. We assume Bohm-like diffusion $D(p) = D_0 \times (p/m_p c)^\alpha$ with $\alpha = 1$ and $B = 10 \, \mu$G so that $D_0^\star = 1$. According to the linear predictions we have then to set $t_{\rm end}^\star = 50$ only. The grid size is set so that $\Lambda = 10$ (see equation (5.4)), its resolution is set so that $\lambda = 0.1$ (see equation (5.3)). We activate AMR with 6 sub-levels. The momentum resolution is chosen to be 32 bins per decade.

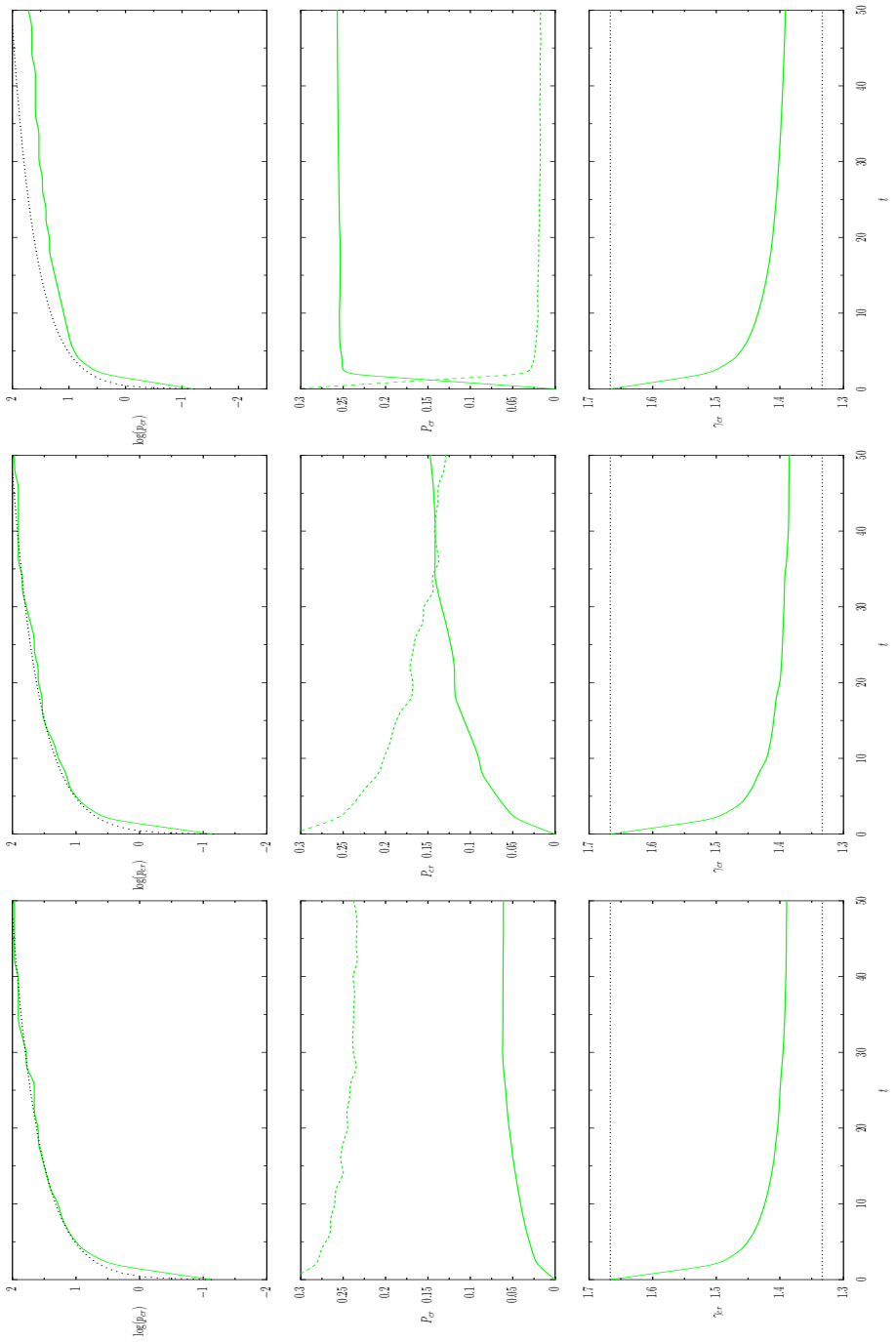

Figure 8.3: Evolution of cosmic-rays for a modified strong shock ($M_S = 50$) propagating in a superbubble with internal injection and no external injection. Plotted versus time are the maximum momentum $p_{\rm cr}$ (its theoretical linear evolution is added dotted, see equation (2.79)), pressure $P_{\rm cr}$ (the fluid pressure is added dashed) and adiabatic index $\gamma_{\rm cr}$ (the non-relativistic (5/3) and ultra-relativistic (4/3) values are added dotted). From left to right: $\xi = 3.00$ so that $\eta_0 \simeq 4 \times 10^{-4}$, $\xi = 2.88$ so that $\eta_0 \simeq 10^{-3}$, $\xi = 2.50$ so that $\eta_0 \simeq 10^{-2}$.

Effect of internal injection. Before discussing the role of external injection we show the importance of internal injection parameters on figure 50. Some key cosmic-rays parameters are plotted for three different levels of injection, as defined by equation (2.93). We see that although the values of ξ are very close and all reasonable, they lead to substantially different values of the initial injection rate η, which in turn lead to very different evolutions of the modified shock. In all cases the rate at which particles are accelerated is roughly the same (top and bottom plots), but the cosmic-rays and gas pressure evolution is totally different (middle plot): lowering ξ a bit changes the final pressure ratio $\chi(t_{\rm end})$ from roughly 1/4 to 12.

Role of external injection. To assess the relative role of internal and external injection we have run 20 simulations with different values of constant η and initial χ. We always inject cosmic-rays at $p_{\rm inj} = 2 \times 10^{-2}\ {\rm m_p c}$ (that is $\log(p_{\rm inj}/{\rm m_p c}) = -1.7$). Note that χ defines only the upstream cosmic-rays population normalization, we choose its initial slope to be the canonical one $s = 4$. At the end of each simulation we measure the downstream pressure of the gas and of the cosmic-rays[6]. The results are shown on figure 8.4. The observed vertical lines of constant $\chi_{\rm end}$ (that is of the same colour) at the right of the plot mean that, for a given η, $\chi_{\rm end}$ is the same whatever χ_0 is – so that the lower χ_0, the higher the increase of $P_{\rm cr}$ (that is bigger dots). Therefore in these cases injection is totally controlled by η. This effect is clearly seen for $\eta = 10^{-3}$ and $\eta = 10^{-4}$, but only marginally for $\eta = 10^{-5}$ and $\eta = 10^{-6}$ where one also see the effect of χ_0 in $\chi_{\rm end}$. Actually for high values of χ and low values of η we begin to observe the opposite phenomenon: for $\chi_0 \simeq 1$, $\chi_{\rm end}$ depends on χ_0 only as soon as $\eta \leq 10^{-4}$. Thus this plot allows to distinguish between the relative influence of η and χ_0 in the injection process. To make things more precise we have tried to draw contour lines indicating to which level η dominates over χ_0. At the bottom right of the 10%-line injection is totally controlled by η. As we cross lines from the bottom right to the top left the importance of χ_0 progressively increases. At the the top left of the 100%-line injection is now controlled by χ. The transition experimentally observed (dashed lines) is in good agreement with the transition theoretically predicted (dotted lines). We recall that the former comes from non-linear simulations whereas the latter calculation assumes the linear regime. We note that for a broad range of physical values of η and χ_0 injection turns out to be primarily driven by η, whereas we though that non-linear modifications might have favoured the effect of χ_0. We also note that the demarcation lines between η and χ are clearly not straight lines, so that these boundaries are not functions of the ratio $\delta = \chi_0/\eta$ alone as was naturally the case in the linear analysis of section 8.2.3.1.

When we explore the (η, χ_0) plane orthogonally, that is from the bottom left to the top right, we explore the effect of an overall increase of the total

[6]Note that as $P_{\rm g,down}(t_{\rm end}) > P_{\rm g,up}(t_0)$ it is possible to have $\chi_{\rm down}(t_{\rm end}) < \chi_{\rm up}(t_0)$.

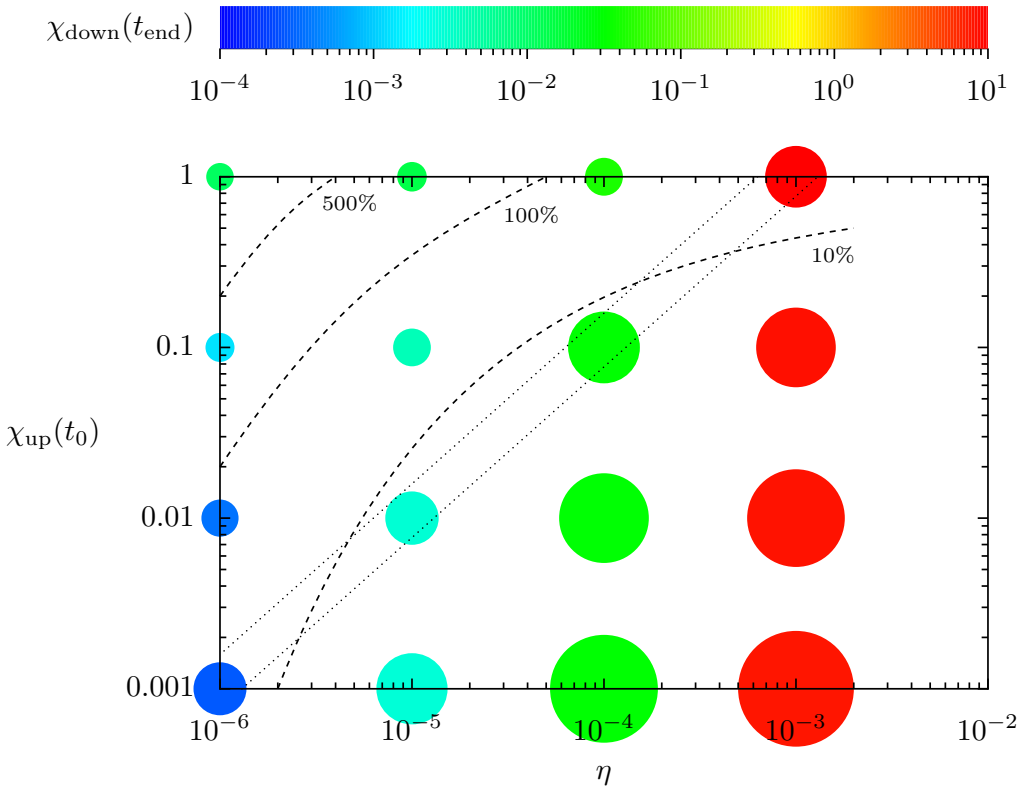

Figure 8.4: Numerical investigation of the relative role of internal and external injection for a strong supernova shock ($M_S = 50$) in a superbubble.
This plot shows the results of 16 numerical simulations made with various values of the (constant) injection fraction η (internal injection) and of the initial upstream cosmic-rays pressure ratio $\chi_0 = \chi_{\mathrm{up}}(t_0) = P_{\mathrm{cr,up}}(t_0)/P_{\mathrm{g,up}}(t_0)$ (external injection). The colour of each dot codes the final cosmic-rays pressure ratio just downstream of the shock $\chi_{\mathrm{end}} = \chi_{\mathrm{down}}(t_{\mathrm{end}}) = P_{\mathrm{cr,down}}(t_{\mathrm{end}})/P_{\mathrm{down}}(t_{\mathrm{end}})$, its size codes the cosmic-rays pressure enhancement $P_{\mathrm{cr,down}}(t_{\mathrm{end}})/P_{\mathrm{cr,up}}(t_0)$ (note that both scales are logarithmic). The dashed lines are tentative contours showing the relative influence of η and χ in the final cosmic-rays pressure. Their meaning is as follows: for any given η, as soon as χ_0 is below the line labelled $X\%$, χ_{end} doesn't vary by more than $X\%$ whatever the actual χ_0 is. The two straight dotted lines correspond to the $M_S^\star = 50$ lines in the two plots of figure 8.2, the band they draw is the transition region from η-dominated shocks to χ_0-dominated shocks predicted by the linear analytical model of section 8.2.3.1.

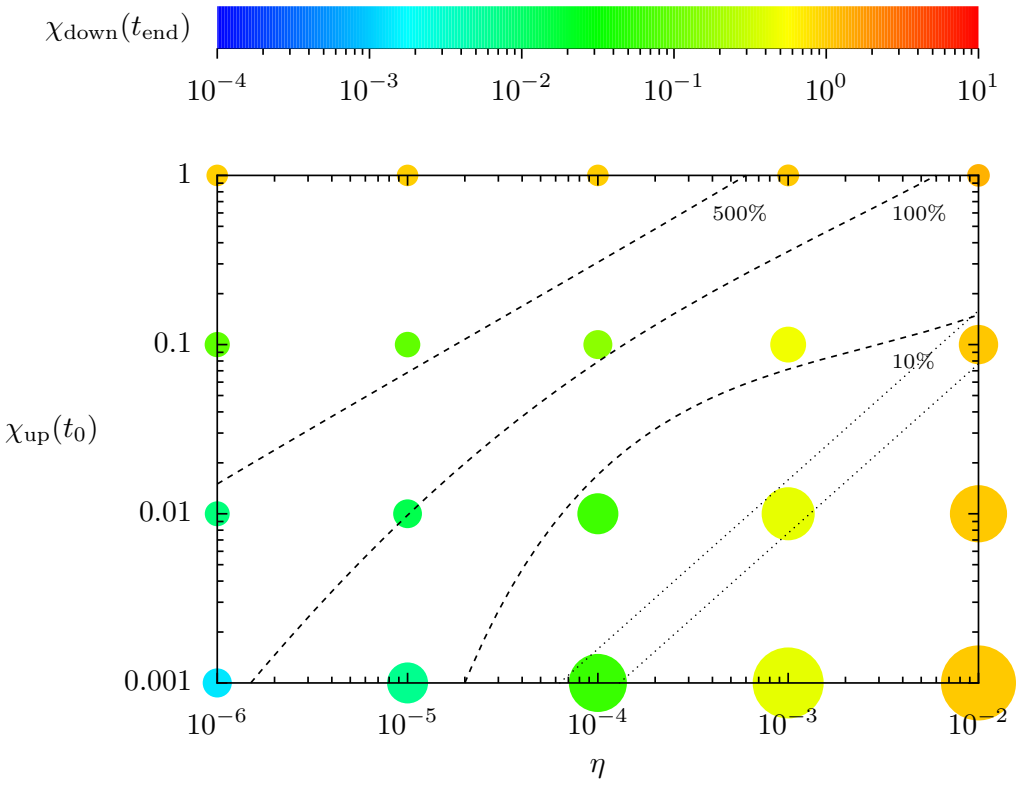

Figure 8.5: Numerical investigation of the relative role of internal and external injection for a weak supernova shock ($M_S = 5$) in a superbubble.
See figure 8.4 for details.

injection. As we already said with the ranges explored here this is actually mostly the effect of η. We note that $\chi_{\rm end}$ rises very fast as η rises, up to a point where the shock can actually no longer adapt itself: no data are present for $\eta = 10^{-2}$ because the shock was then always fully smoothed by cosmic-rays back-reaction in the very beginning of the simulation. And even for $\eta = 10^{-3}$ the cosmic-rays pressure is still rising rapidly at the end of the simulation: we have not reached a final quasi-steady state and it's not certain that such a state is possible. For $\eta \leq 10^{-4}$ however we have entered, by the end of the simulation, the quasi-steady state where $P_{\rm cr}$ still rises but now on very large time-scales. Therefore there seems to be some critical $\eta_c \sim 10^{-3}$ above which even through non-linear modifications a shock can't adapt itself to a constant injection of cosmic-rays at this rate. We recall that in the non-linear regime we expect η to be lowered in time. And we note that the inferred value of η_c is consistent with the results of test 3 of section 6.3.2.2.

Weak shocks. We have considered so far primary supernova shocks, of $M_S = 50$, but as shown in sections 7.2.3, 8.2.2.2, 8.2.3.1, secondary weak shocks might play an important role inside superbubbles. So we present now results for $M_S = 5$. Simulations design is the same as previously, but for the fact that now $u_S = 645$ km/s, so that we set $p_{\rm inj} = 2 \times 10^{-3}$ $\rm m_p c$ and $p_{\rm max} = 10^1$ $\rm m_p c \simeq 10^1$ GeV.

Results are shown on figure 8.5. We observe the same kind of $\eta - \chi$ domination pattern as on figure 8.4, translated towards the bottom right, that is higher η and lower χ (by roughly one order of magnitude). The cosmic-ray pressure is still controlled by internal injection for high η (around 10^{-2}), but the external level of cosmic-rays now plays an important role as soon as $\eta < 10^{-3}$ and $\chi > 10^{-3}$. Thus it is very likely that upstream cosmic-rays are an important ingredient of acceleration by weak shocks inside superbubbles. If the cosmic-ray pressure ratio χ is of the order of unity it may actually entirely control the acceleration process – which is then in fact mostly a re-acceleration process. Also we note that for a given set (η, χ), the cosmic-ray pressure enhancement (size of the dots) is systematically lower for a weak shock than for the strong one, but that the final cosmic-ray pressure ratio $\chi_{\rm end}$ (colour of the dots) can be higher for weak shocks when η is low, so that again weak shocks are probably more affected by repeated acceleration than strong shocks.

Limitations. Finally we would like to discuss the limitations of this very first simulations. First we recall that we have assumed a fixed cosmic-rays slope $s = 4$, for modified shocks the slope can be >4, and in the case of multiple acceleration it can be <4, up to 3. The actual shape of the spectrum is not necessarily that important in front of the total cosmic-rays pressure as far as the global dynamics are concerned, however this should be checked[7]. We aim at producing a more self-consistent modelling where the upstream cosmic-rays distribution accounts for both non-linear modifications and particle escape. Also we have assumed a fixed injection momentum $p_{\rm inj}$. For a truly modified shock $p_{\rm inj}$ is expected to be reduced, but only slightly, and as this is the lowest energy point of the spectrum this has probably a small effect on the total cosmic-rays pressure as soon as particles have been accelerated to high energies. Finally one might be concerned by the rather low maximum momentum and simulation end time. This has been mostly motivated by the computing cost of these simulations, however we believe that the maximum momentum is high enough to give precious indications on the way internal and external injection compete when a shock develops in a given medium.

[7]Preliminary results with $s = 3$ suggest that $\chi_{\rm end}$ might change substantially but that the overall η-χ_0 domination pattern remains the same.

References

Binns, W. R., Hink, P. L., Klarmann, J., Lijowski, M. L., Christian, E. R., von Rosenvinge, T. T., Cummings, A. C., Leske, R. A., Mewaldt, R. A., Stone, E. C., George, J. S., Wiedenbeck, M. E., and Yanasak, N. E. (1999). Measurements of the Isotopic Abundances of Galactic Cosmic Rays and their Implications for Cosmic Ray Origin. In Ramaty, R., Vangioni-Flam, E., Cassé, M., and Olive, K., editors, *LiBeB Cosmic Rays, and Related X- and Gamma-Rays*, volume 171, pages 96–103.

Binns, W. R., Wiedenbeck, M. E., Arnould, M., Cummings, A. C., George, J. S., Goriely, S., Israel, M. H., Leske, R. A., Mewaldt, R. A., Meynet, G., Scott, L. M., Stone, E. C., and von Rosenvinge, T. T. (2005). Cosmic-Ray Neon, Wolf-Rayet Stars, and the Superbubble Origin of Galactic Cosmic Rays. ApJ, 634:351–364.

Binns, W. R., Wiedenbeck, M. E., Christian, E. R., Cummings, A. C., Hink, P. L., Israel, M. H., Leske, R. A., Mewaldt, R. A., Stone, E. C., von Rosenvinge, T. T., and Yanasak, N. E. (2001). Neon Galactic Cosmic Ray Isotopic Abundances: Comparison with Wolf-Rayet Star Models and Meteoritic Abundances. In *International Cosmic Ray Conference*, volume 5 of *International Cosmic Ray Conference*, page 1683.

Bykov, A. M. (1999). Nonthermal Particles in Star Forming Regions. In Ramaty, R., Vangioni-Flam, E., Cassé, M., and Olive, K., editors, *LiBeB Cosmic Rays, and Related X- and Gamma-Rays*, volume 171 of *Astronomical Society of the Pacific Conference Series*, page 146.

Bykov, A. M. (2001). Particle Acceleration and Nonthermal Phenomena in Superbubbles. *Space Science Reviews*, 99:317–326.

Bykov, A. M. and Fleishman, G. D. (1992). On non-thermal particle generation in superbubbles. MNRAS, 255:269–275.

Bykov, A. M. and Fleishman, G. D. (1993). Superbubbles in galaxies: A new class of nonthermal sources. A&A, 280:L27–L29.

Casse, M., Lehoucq, R., and Vangioni-Flam, E. (1995). Production and Evolution of Light Elements in Active Star-Forming Regions. *Nature*, 373:318.

Casse, M. and Paul, J. A. (1982). On the stellar origin of the Ne-22 excess in cosmic rays. ApJ, 258:860–863.

Dorfi, E. A. and Völk, H. J. (1996). Supernova remnant dynamics and particle acceleration in elliptical galaxies. A&A, 307:715–725.

Garcia-Munoz, M., Simpson, J. A., and Wefel, J. P. (1979). The isotopes of neon in the galactic cosmic rays. ApJ, 232:L95–L99.

Higdon, J. C. and Lingenfelter, R. E. (2003). The Superbubble Origin of 22Ne in Cosmic Rays. ApJ, 590:822–832.

Higdon, J. C., Lingenfelter, R. E., and Ramaty, R. (1998). Cosmic-Ray Acceleration from Supernova Ejecta in Superbubbles. ApJ, 509:L33–L36.

Klepach, E. G., Ptuskin, V. S., and Zirakashvili, V. N. (2000). Cosmic ray acceleration by multiple spherical shocks. *Astroparticle Physics*, 13:161–172.

Maehl, R. C., Fisher, A. J., Hagen, F. A., and Ormes, J. F. (1975). Neutron-rich isotopes of cosmic rays with Z between 9 and 16. 202:L119–L123.

Meynet, G., Arnould, M., Paulus, G., and Maeder, A. (2001). Wolf-Rayet star nucleosynthesis and the isotopic composition of the Galactic Cosmic Rays. *Space Science Reviews*, 99:73–84.

Parizot, E. (2000). Superbubbles and the Galactic evolution of Li, Be and B. A&A, 362:786–798.

Parizot, E. (2001). Galactic Cosmic Rays and the Light Elements. *Space Science Reviews*, 99:61–71.

Parizot, E. (2005). Rayons cosmiques et rayonnement du cosmos. HDR.

Parizot, E. and Drury, L. (1999a). Spallative nucleosynthesis in supernova remnants. I. Analytical estimates. A&A, 346:329–339.

Parizot, E. and Drury, L. (1999b). Spallative nucleosynthesis in supernova remnants. II. Time-dependent numerical results. A&A, 346:686–698.

Parizot, E. and Drury, L. (1999c). Superbubbles as the source of 6Li, Be and B in the early Galaxy. A&A, 349:673–684.

Parizot, E., Marcowith, A., van der Swaluw, E., Bykov, A. M., and Tatischeff, V. (2004). Superbubbles and energetic particles in the Galaxy. I. Collective effects of particle acceleration. A&A, 424:747–760.

Reeves, H., Audouze, J., Fowler, W. A., and Schramm, D. N. (1973). On the Origin of Light Elements. ApJ, 179:909–930.

Reeves, H., Fowler, W. A., and Hoyle, F. (1970). Galactic Cosmic Ray Origin of Li, Be and B in Stars. *Nature*, 226:727.

Vangioni-Flam, E., Casse, M., Fields, B. D., and Olive, K. A. (1996). LiBeB Production by Nuclei and Neutrinos. ApJ, 468:199–206.

Völk, H. J. and Forman, M. (1982). Cosmic rays and gamma-rays from OB stars. ApJ, 253:188–198.

Wiedenbeck, M. E., Binns, W. R., Christian, E. R., Cummings, A. C., Dougherty, B. L., Hink, P. L., Klarmann, J., Leske, R. A., Lijowski, M., Mewaldt, R. A., Stone, E. C., Thayer, M. R., von Rosenvinge, T. T., and Yanasak, N. E. (1999). Constraints on the Time Delay between Nucleosynthesis and Cosmic-Ray Acceleration from Observations of 59Ni and 59Co. ApJ, 523:L61–L64.

Chapter 9

Radiation from Superbubbles

In this final chapter we review the observations of superbubbles, with an emphasis on their connection with cosmic-rays (see also the lecture of Marcowith (2007b)). Superbubbles are now commonly observed objects. However their identification suffers from two limitations: the uncertainties on their distances (often inferred from emission lines), and the extinction of optical to X radiation by interstellar dust. This is all the more problematic since real superbubbles actually exhibit many sub-structures that accumulate along the line of sight (see the case of the Cygnus superbubble in Uyaniker et al. (2001)).

This is a reason why the Magellanic clouds, hosting exceptional star forming regions, and for which the distance (55 kpc) and column density ($n_H \sim 10^{21}$ g/cm^2) are well known, have been extensively studied. In particular the Large Magellanic Cloud contains a remarkable superbubble, 30 Doradus (also known as the Tarantula nebula). This structure has been extensively observed at many wavelengths, yielding the gorgeous picture of figure 9.1. Its size is of about 250 pc (Walborn 1991), it is powered by the cluster R136, of size 40 pc and of mass $\sim 2 \times 10^4\ M_\odot$ (Walborn et al. 2002). Although a few supernova remnants candidates have been identified, only one has been firmly confirmed, N157B, at the border of the bubble (at the bottom right of figure 9.1). For those not familiar with superbubbles, we would like to introduce another remarkable representative: the Local Bubble (see figure 9.2 and the introduction of Frisch (2007)). We indeed all live within a big bubble of size $\sim$100 pc with an average density of 0.07 cm^{-3} and an average temperature of 10^6 K (the Sun is currently inside a cloud of higher density 0.2-0.3 cm^{-3} and lower temperature $6 - 7 \times 10^4$ K). This structure has been formed over the last few tens of millions of years, most probably due to the concomitant explosion of a few supernovae (the Geminga pulsar is likely the remnant of one of them).

In this final chapter we first present a general multi-wavelength panorama of superbubbles, distinguishing between thermal and non-thermal emission. We then focus on observations of supernova remnants inside superbubbles, which are unfortunately particularly difficult. Finally we summarize the indirect evidences for highly efficient cosmic-ray production into superbubbles.

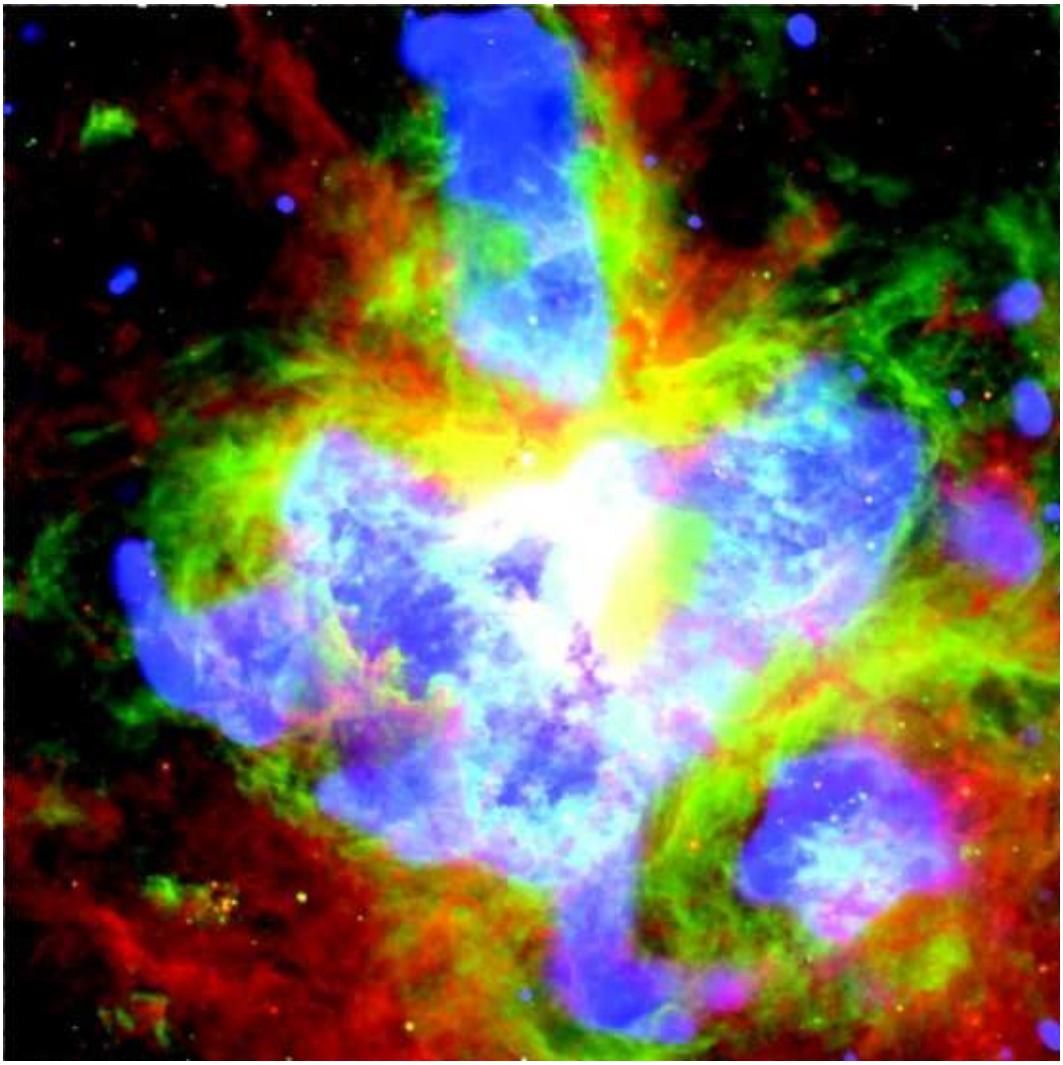

Figure 9.1: Multi-wavelength image of the 30 Doradus superbubble.

colour	instrument	band	composition	object
blue	Chandra ACIS	0.9-2.3 keV	10^6 K plasma	superbubble
green	MCELS	$H_\alpha = 656$ nm	10^4 K plasma	supershell
red	Spitzer IRAC	6.5-9.4 μm	dust & PAHs	supershell and molecular cloud

(figure from Townsley et al. (2006))

9.1 Observations of Superbubbles

The study of superbubbles began in the late 1970s, with the observation of the Cygnus superbubble (Cash 1979a, 1979b). Since then it has greatly benefited from the instrumental developments at all wavelengths, revealing progressively the complex physics of these objects.

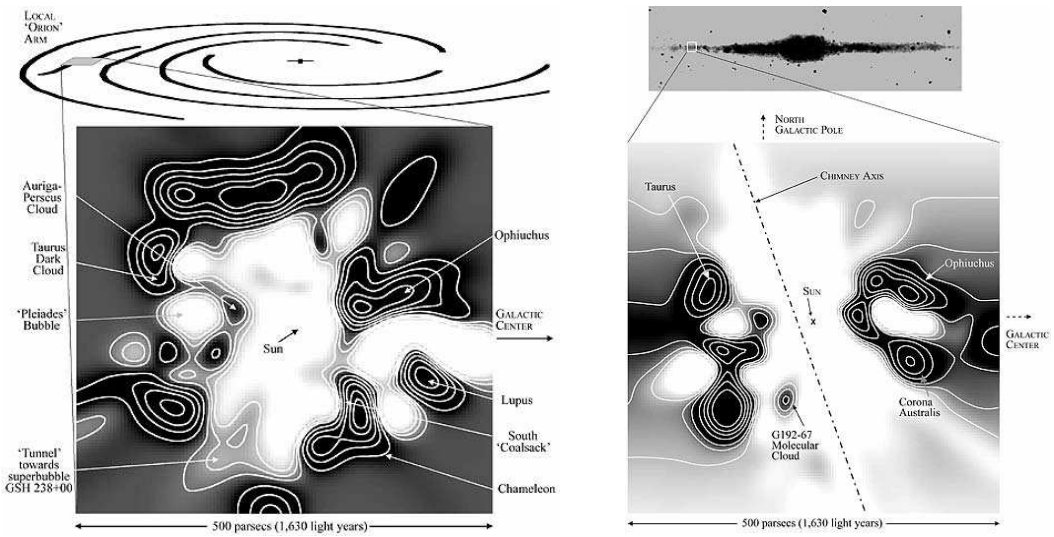

Figure 9.2: The Local Bubble.
White areas represent regions of very low density filled with hot ionized gas (the local superbubble), whereas dark areas reveal large condensations of cold and dense gas (giant molecular clouds). The left map is in the Galactic plane, the right map is a side view through the plane (figures from the press release of Robert Sanders announcing the mapping of Lallement et al. (2003)).

9.1.1 Thermal Emission

9.1.1.1 Radio Emission

Radio observations mostly trace the coldest part of the superbubbles, that is their boundaries, the supershells. For that purpose one mostly uses the hyperfine transition line of HI atoms (21 cm / 1.4 GHz) and the rotational transition lines of CO molecules (eg J=1-0 at 2.6 mm / 115 GHz). CO lines allow for an estimate of the velocity and thus of the distance by comparison to the Galaxy rotation curves. Then one can evaluate the size of the shell, and infer the total mass of swept-up ambient medium (see for instance Maciejewski et al. (1996) for an analysis of the Aquila supershell). One can also estimate the age of the structure, which requires modelling many effects such as the local Galactic density gradient or magnetic field (see section 7.1.3.3). Having such a complete description of the shell one can finally deduce the energy required to power the system (see Heiles 1979). A map of Galactic shells is presented on figure 9.3. We see that they are present everywhere, with a very high concentration in the Galactic plane (where their interior has a filling factor of roughly 50%). Note also the variety of sizes (the shapes are not accurate on this figure).

Finally we note that the synchrotron radio emission of the superbubble itself can hardly be detected because of the very low density (however a diffuse Galactic synchrotron emission is detected, see the survey of Reich et al. (2001)).

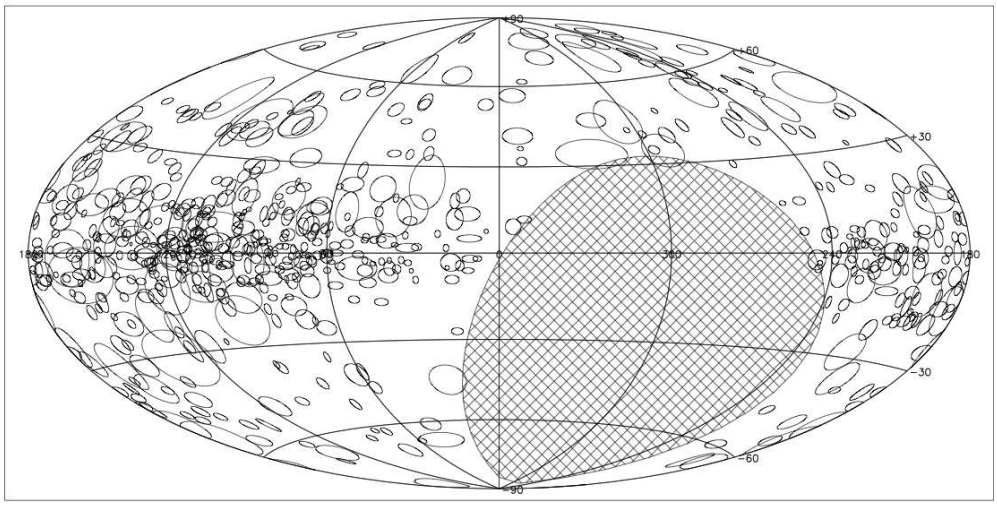

Figure 9.3: Map of Galactic HI shells.
(figure from Ehlerová and Palouš (2005), data from the Leiden-Dwingeloo HI survey of Hartmann and Burton (1997) (the shaded area is not accessible to the instrument))

9.1.1.2 Optical Emission

The first interest of the optical domain is of course the study of the stars powering the (not too old) superbubbles. Since the first observations of massive stars in the first half of the XXth century astronomers realized that they were not distributed uniformly but rather grouped. The first catalogues were made by Blaauw (1964) and Alter et al. (1966). The precise determination of the OB associations was rather delicate due to their large extension. The situation greatly improved in our neighbourhood with the launch of the astrometric telescope HIPPARCOS (de Zeeuw et al. 1999). Maps of the closest Galactic OB associations are shown on figure 9.4.

The optical and ultraviolet range is also the domain of a host of emission lines which can be used to probe the warm interstellar medium. UV photons produced by the massive stars are powerful enough to ionize the Hydrogen atoms, feeding the circumstellar medium with energetic electrons. These electrons produce recombination lines when captured back by an ion, and forbidden lines by collisionally exciting heavy ions which subsequently come back to their fundamental state[1]. In the optical range the [H_α], [H_β] recombination lines and the [OIII], [SII] forbidden lines probe the warm ionized ISM of $T \sim 10^4$ K. In the ultraviolet range the [CIV], [SiIV], [NV] lines probe higher temperatures of $T \sim 10^5$ K (the emission of hotter gas is in the X range, see section below). The study of the lines ratios provides the actual temperature and ionization

[1]This last process has very long timescales, so that it can be seen only in media tenuous enough so that collisional de-excitation is negligible.

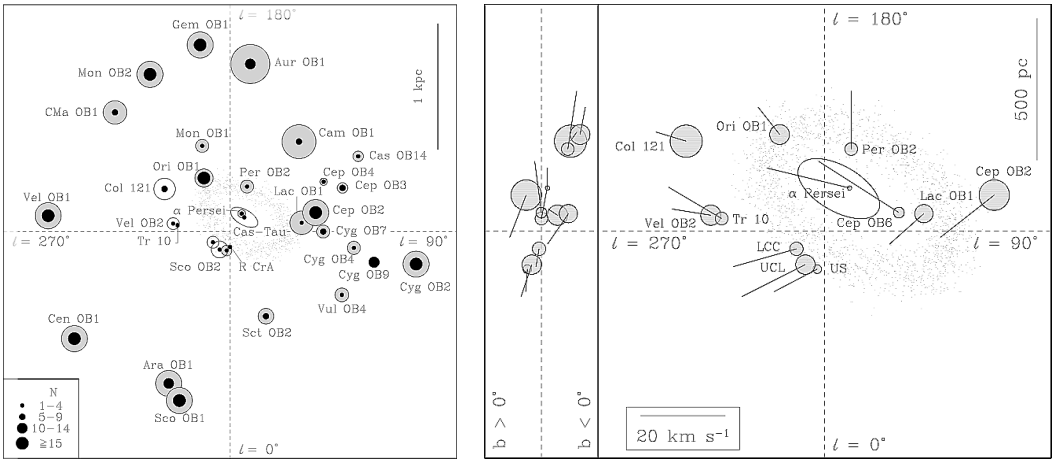

Figure 9.4: Maps of Galactic OB associations.
Left: pre-Hipparcos data within 1.5 kpc, right: post-Hipparcos data within 500 pc (figures from de Zeeuw et al. (1999)). Both maps are projections on the Galactic plane, the right one includes a Galactic cross-section on its left. The size of the circles represents the size of the association projected on the Galactic plane, on the left: enlarged by a factor 2 with respect to the distance scale, on the right: on the same scale as the distance scale. On the left map the size of the central dots indicates the degree of current or recent star formation activity, as given by the number N of stars more luminous than absolute magnitude $M_V \sim -5$. On the right map the lines represent the average streaming motions.

degree of the medium (see eg Madsen et al. 2006). The study of the lines width provides the local velocity of the medium (see section 9.2.2).

9.1.1.3 X Emission

Being very hot the superbubble interior mostly radiates in X-rays, between 0.1 and 1 keV (see eg the review of Townsley 2006). It produces atomic lines (from Oxygen to Iron) through K, L, M fluorescence transitions, as well as a Bremsstrahlung continuum. The overall X emission of a superbubble consists of a diffuse emission (from the hot plasma) as well as numerous discrete sources (massive stars, X-ray binaries, supernova remnants, pulsar nebulae). Thanks to the good resolution of the Chandra satellite the superbubbles content can now be studied in greater details (eg Townsley et al. 2003). The study of the X emission provides the temperature of the source as well as its metallicity. The observed temperatures are up to $10^7 - 10^8$ K in the center of the OB associations, decreasing to the average value of 10^6 K inside the superbubble. The X luminosity of the clusters are of the order of 10^{38} erg/s.

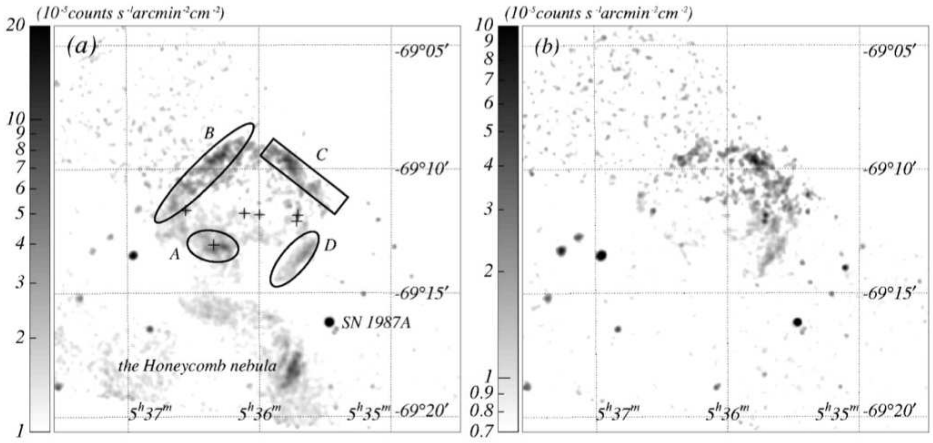

Figure 9.5: X-ray emission from the superbubble 30 Doradus C.
Images obtained with Chandra ACIS instrument in the 0.7 – 2.0 keV band (left) and in the 2.0 – 7.0 keV band (right). Solid lines show the four extended sources, plus signs represent point sources (figure from Bamba et al. 2004).

9.1.2 Non-Thermal Emission

Lately superbubbles have become at last important sources of non-thermal emission at high and very high energies.

9.1.2.1 X Emission

Diffuse non-thermal emission has been observed in X-rays above 1 keV by various instruments in a few objects: 30 Doradus (Townsley et al. 2003, Bamba et al. 2004, Townsley et al. 2006, see figure 9.5) and DEM L192 aka N51D (Cooper et al. 2004) in the LMC, NGC 6334 (Ezoe et al. 2006b, see figure 9.6) and possibly NGC 2024 (Ezoe et al. 2006a) in the Galaxy. Its exact origin is still uncertain. It can be either synchrotron emission either Bremsstrahlung, either from supernova remnants either from bigger structures. As for the thermal emission there is also a contribution from point sources, but at a low level ($< 10\%$ in 30 Doradus according to Townsley et al. (2006)).

The case of 30 Doradus C, a part of the Doradus complex (shown on figure 9.5 – but not apparent on figure 9.1) studied by Bamba et al. 2004, is particularly instructive. Non-thermal diffuse X emission is observed from four shell-like structures (of ~ 10 pc size), three of which have low thermal component. The photon index varies between 2.3 and 2.7. The spectrum is consistant with synchrotron radiation as extrapolated from the radio emission. But the total X luminosity 3×10^{35} erg/s is 10 times higher than the X luminosity of the SN 1006 supernova, so that if the emission is actually synchrotron it probably results from a succession of supernovae (the superbubble is already $\sim 10^7$ years old).

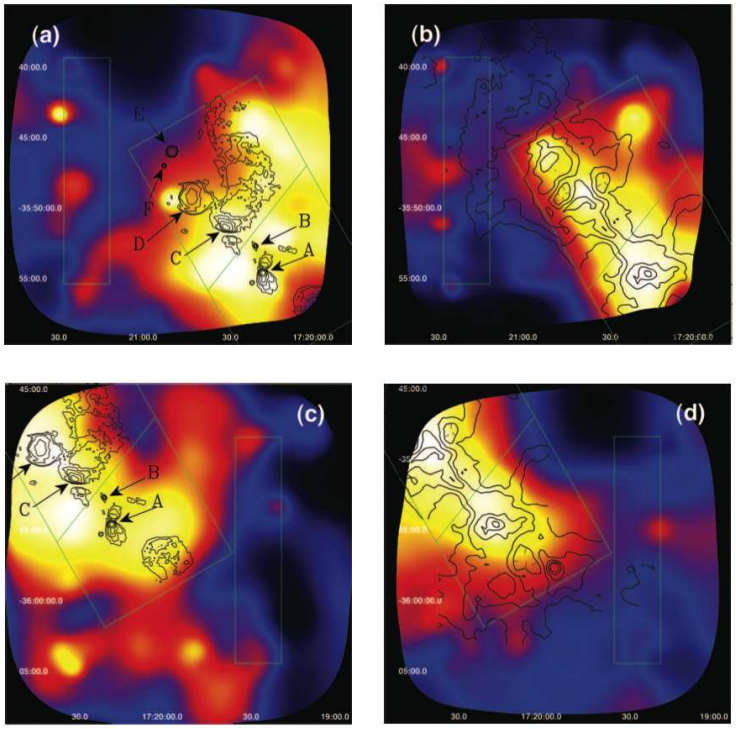

Figure 9.6: X-ray emission from the superbubble NGC 6334.
Images obtained with Chandra ACIS instrument in the 0.5 – 2.0 keV band (left) and in the 2.0 – 7.0 keV band (right) after removing point sources. Overlaid contours are OH 18 cm (left) and CO 1.3 mm (right) maps. Top and bottom panels correspond to the north and south observations respectively (figure from Ezoe et al. 2006b).

9.1.2.2 Gamma Emission

Since about 5 years superbubbles have been observed at very high energies, mostly thanks to the development of ground-based Cherenkov detectors.

One of the most successful region so far has been the Cygnus region. The EGRET instrument (0.1-10 GeV) on board the CGRO satellite has detected 8 unidentified sources and a diffuse emission in this region (Hartman et al. 1999). Note that all the EGRET sources are extended due to the low angular resolution of the instrument ($\sim 1^\circ$). The Hegra Cherenkov telescope (0.5-50 TeV) has found a TeV source (TeV J2032+4130) inside the Cygnus OB2 superbubble (Aharonian et al 2002, 2005). The source is extended over $\sim$ 2 pc, its spectrum is a power-law of index 1.9$\pm$0.6 and integrated flux above 1 TeV 3% of the Crab flux. The source is within the 95% confidence level of an EGRET source (3EG 2033-4118) and close to an ASCA extended source (see figure 9.7(a)). It has been recently confirmed by the Whipple observatory (see figure 9.7(b)). The origin of this emission is still unknown, it might be due to the interaction of massive stars winds (see section 7.1.3.2) or to the terminal

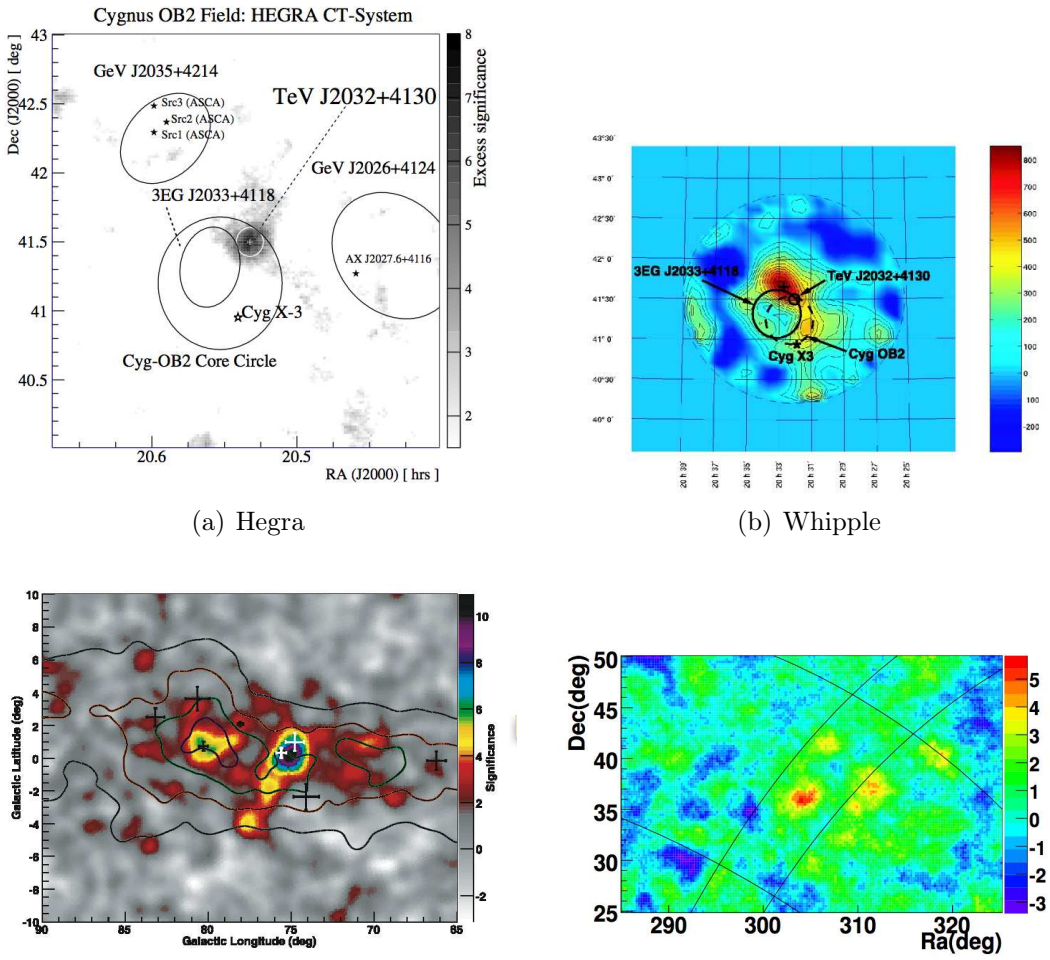

(a) Hegra (b) Whipple

(c) Milagro (d) Tibet AS-γ

Figure 9.7: γ-ray emission from the superbubble Cygnus OB2.
Top: TeV J2032+4130 observed by Hegra (figure from Aharonian et al. 2005) and by the Whipple Observatory (figure from Konopelko et al. 2007). Ellipses show the core of the OB association and the coincident EGRET source.
Bottom: MGRO J2019+37 observed by Milagro (figure from Abdo et al. 2007) and by the Tibet air shower array (figure from Amenomori et al. 2007). On the Tibet ASγ map lines stand for the Galactic latitude $b = \pm 3^\circ$ and longitude l =65°-85° to allow comparison. On the Milagro map contours show the matter density and crosses show the location of EGRET sources.

shock of a jet from the micro-quasar Cygnus X3. No X counterpart has been detected by Chandra (Butt et al. 2006), but XMM-Newton has observed a diffuse X emission (Horns et al. 2007). Recently the Milagro Cherenkov telescope ($\gtrsim$10 TeV) has also detected 2 sources and a diffuse emission in the TeV range (Abdo et al. 2007). The brightest source is MGRO J2019+37, spatially coincident with the EGRET source 3EG 2021-3716 (see figure 9.7(c)). How-

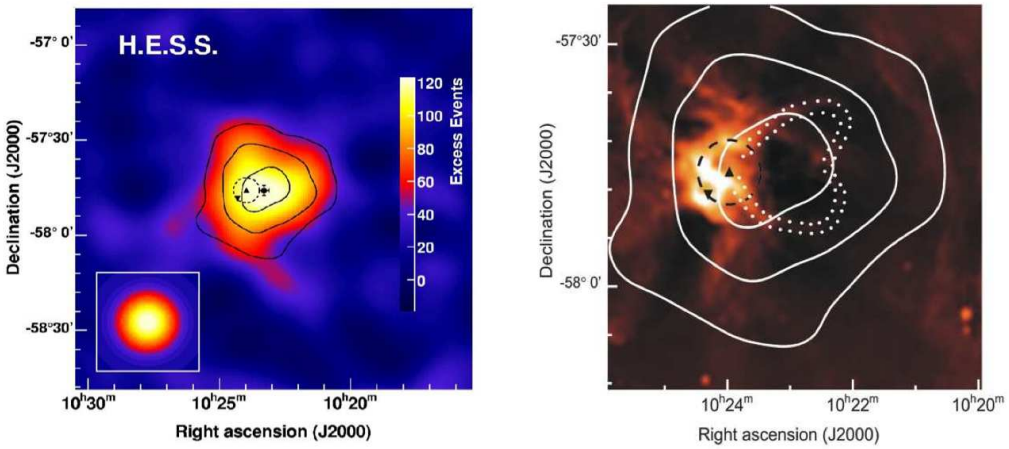

Figure 9.8: γ-ray emission from the OB association Westerlund 2. Left: HESS TeV map of the new source HESS 1023-575 (overlaid contours correspond to statistical significances of 5, 7, 9 σ). Right: HESS contours overlaid on a radio map (the "blister" surrounding a wind-blown bubble is indicated dotted). On both maps the dashed circle represents the Westerlund 2 cluster, and the two triangles mark Wolf-Rayet stars: WR 20a (upright) and WR 20b (reversed) (figures from Aharonian et al. 2007).

ever the MAGIC Cherenkov telescope (0.1-1 TeV) has observed no significant emission from this source in the energy range between EGRET and Milagro ones (Bartko et al. 2007). Although Milagro couldn't measure the spectral index, the integral flux above 100 GeV is likely to be a sizeable fraction of the Crab one. The Tibet air shower array (0.3-50 TeV) has recently confirmed this source (see figure 9.7(d)) and is currently measuring the index (Amenomori et al. 2007). Finally the SPI instrument on board the INTEGRAL satellite has also observed a diffuse emission of the 1.809 MeV line in the Cygnus region (Knödlseder et al. 2004). This emission is produced by the radioactive decay of ^{26}Al into ^{26}Mg. The broad line (of width $\Delta v = 550 \pm 210$ km/s) suggests turbulent motions.

The Galactic plane survey made by the HESS Cherenkov telescopes array (0.5-20 TeV) has discovered 14 new TeV sources, some of which are associated with massive stars formation regions (Aharonian et al. 2006). Of special interest is HESS J1023-575, a source coincident with the OB association Westerlund 2 in the HII complex RCW 49 aka NGC 3247 (Aharonian et al. 2007, Reimer et al. 2007). It has a power-law spectrum of index 2.53 ± 0.26 and a flux above 1 TeV of 1% of the Crab. The cluster contains young ($2-3\times10^6$ yr) massive stars, including 3 Wolf-Rayet stars, two of which (of mass $\sim 80\ M_\odot$ each) form a binary system (WR 20a). About 0.5% of the mechanical luminosity of WR 20a alone would suffice to power the gamma emission. However HESS J1023-575 is an extended source ($\sim$28 pc) and is centered slightly off

the cluster itself. It is in fact coincident with a large bubble-like structure seen in radio expanding from one side of the cluster. The origin of the high-energy emission is thus still uncertain. It can be due to colliding winds (through either leptonic or hadronic processes), collective wind effects, multiple shocks acceleration. Another interesting source is HESS J1813-069, coincident with a cluster of 14 red supergiants (Marcowith et al. 2007).

9.1.3 Expected Emission from the Irradiation of the Superbubble Neighbourhood

To end this section we would like to present briefly a few other signatures that are expected but not (yet) observed. Irradiation of the supershell and parent molecular cloud by cosmic-rays produced in the superbubble (especially those of low-energy, below the GeV) must be accompanied by a great variety of X and γ emission (see eg Tatischeff et al. 2001, Tatischeff 2003).

In X-rays a continuum is produced around a few tens of keV by inverse Bremsstrahlung (radiation of electrons at rest in the Coulombian field of fast ions) and non-thermal Bremsstrahlung (radiation of secondary electrons and positrons in the Coulombian field of the ambient ions), as well as a few lines such as the Iron Kα fluorescence line (at 6.4 keV for ambient atoms and 5.8-7.8 keV for fast atoms). In γ-rays a wide continuum is produced by non-thermal Bremsstrahlung, Inverse Compton and neutral pion decay, and many lines are produced through nuclear excitation (^{12}C at 4.44 MeV, ^{16}O at 6.13 MeV, ^{20}Ne at 1.63 MeV, ^{56}Fe at 0.845 MeV) and radioactive decay (^{26}Al at 1.809 MeV, ^{60}Fe at 1.173 MeV and 1.332 MeV).

Two nearby superbubbles ($d < 500$ pc) have been identified as promising targets. In the region of Orion OB1 Parizot and Knödlseder (1999) showed that the expected fluxes are too low to have been observed so far, but now close to the sensitivity of new instruments. And very recently a proposal lead by Terrier (2007) of observations of Perseus OB2 with Integral has been accepted. In that object an intense observed spallation activity (see more in section 9.3.2) has allowed for a precise normalization of the expected X-ray and γ-ray counterpart.

9.2 Detection of Supernovae

Unfortunately the observational signatures of supernovae in superbubbles are extremely faint. However they must be in (see sections 7.2.1 and 7.2.4)! And their energy is indeed required to power the observed superbubbles. For instance Oey (1996) studied the shell dynamics of a sample of 6 superbubbles in the LMC (DEM 25, 31, 50, 106, 226, 301). She found that all objects present a shell growth rate superior to the one obtained from the standard pressure-driven bubble model, and explained the discrepancy by acceleration

by supernova remnant impacts. Nevertheless the various attempts at the direct detection of supernova remnants inside superbubbles have not been very conclusive, as we show below.

9.2.1 Classical Radiative Signatures

First we recall that supernova remnants inside superbubbles are very extended structures and usually never enter the radiative phase[2] (see section 7.2.2), which makes their detection more difficult. Then the superbubble medium is such that the classical signatures of SNRs are weak (eg Chu 1997, Chen et al. 2000). A high-velocity SNR shock interacting with a cold and dense ambient ISM produces non-thermal radio emission, strong optical forbidden line emission (with notably an enhanced [SII]/H_α ratio), and bright X-ray emission (see section 2.5.1). But in superbubbles the situation is radically different. The radio emission is extremely low due to the low electrons density and is drowned out by the thermal emission from bright background HII regions – or from the radio emission of pulsar nebulae. The [SII] line strength is weakened because sulfur is photoionized to higher ionization stages by the intense UV radiation from the OB stars[3]. And the X-ray emission of SNRs is mixed with the high emission of the hot interior of the superbubble. To alleviate these problems Chu et al. (1994) suggested to make use of the UV interstellar absorption lines properties, but they found only two promising diagnostics.

Therefore direct evidence for supernova remnants inside superbubbles is very scarce. Comparing H_α/H_β and radio/H_α ratios in 30 Doradus Lazendic et al. (2003) have suggested two small radio sources to be non-thermal and therefore SNR candidates – however, no optical or X-ray counterpart were detected. Using high-resolution images and spectra Chu et al. (2004) still found no optical evidence supporting their identification as SNRs. High extinction can explain low optical and X-ray signatures, but would product high H_α/H_β and radio/H_α ratios that contradict observations and weaken the argument for non-thermal radio emission. Therefore there is no compelling evidence that either of the radio SNR candidates are truly SNRs. The only clear supernova remnant in 30 Doradus is N157B (located at the bottom right of figure 9.1). According to Chen et al. (2006) the fact that this remnant is expanding into the hot low-density interior of the superbubble formed by the OB association LH99 explains its exceptionally large physical size in both radio and X-rays ($\sim$20-30 pc), its relatively weak thermal emission and the lack of a rim-brightened outer blast wave.

[2]Which of course doesn't mean that they don't radiate at all, but simply that their radiation is too low to have an impact on their dynamical evolution.

[3]However Chen et al. (2000) claim that the filamentary shell morphologies observed with the [SII]/H_α ratio in the three superbubbles DEM L152, L192, L106 are produced by strong interstellar shocks, probably associated with supernovae.

9.2.2 Kinematic Detection

If the intensity and morphology of emissions from superbubbles don't allow for a clear detection of supernova remnants, it might still be possible to infer their presence through velocity measurements provided by the emission lines width. Chu and Kennicutt (1986) detected four unresolved large-velocity sources inside giant HII regions in M 101 using spectroscopy of H_α. Chu and Kennicutt (1994) mapped the complex velocity field in the 30 Doradus region. In the central core they have identified several fast-expanding shells with diameters of 2-20 pc and expansion velocities of 100-300 km/s. Their kinetic energy is of $0.5 - 10 \times 10^{50}$ erg each, and alltogether they contain roughly half of the kinetic energy in the 30 Doradus complex. These large and fast shells are coincident with the extended X-ray sources seen by Wang and Helfand (1991) and are very probably associated with supernova remnants embedded in the superbubble.

However Chu (1997), using a large sample of supernova remnants, showed that a detectable high-velocity H_α emission is neither necessary (as not all known remnants exhibit such clear kinematic features) nor sufficient (as wind-blown bubbles can produce the same effect) to confidently identify a SNR.

9.2.3 Interaction with Molecular Clouds

As we have seen in the last section all the signatures of supernova remnants are weak inside superbubbles, so that detecting a supernova remnant requires quite special conditions. A particular case of interest is the interaction of the remnant with a cloud denser than the superbubble interior, which can greatly enhance the emission from the remnant. This can be the case for a supernova exploding at the edge of the superbubble as it will collide with the supershell, but also for a supernova exploding well inside the superbubble if it encounters a dense cloud not swept away by the stellar winds (see section 7.1.3.2).

The effect of the inhomogeneity of the interstellar medium on the visibility of supernova remnants has been considered since the early developments of diffusive shock acceleration (Blandford and Cowie 1982). Chevalier (1999) has studied analytically the fate of supernova remnants exploding in molecular clouds. The main point is that the remnant enters the radiative phase sooner and at a smaller radius. The interaction of a supernova shock with a dense cloud has been investigated in details by the means of numerical simulations in 2D (eg Bedogni and Woodward 1990) then in 3D (eg Stone and Norman 1992). When hitting a cloud a supernova shock is both reflected (producing a bow shock) and transmitted (at lower speed). All the simulations showed the development of instabilities, which help the fragmentation and mixing of the cloud and enhance the radio emission. Orlando et al (2005, 2006) pointed out the role of thermal conduction and radiative losses and found that the hydrodynamic instabilities are never clearly visible in the X-ray band. Cosmic-ray acceleration was added in the simulations first using the two-fluids approxi-

mation with passive electrons (Jones and Kang 1993) then using a simplified kinetic approach with explicit electrons transport (Jun and Jones 1999). These studies confirmed the significant increase of the radio emission but showed that the presence of the cloud adds little to the net acceleration efficiency of the original shock. However using a different kinetic approach Bykov et al. (2000) found that evolved supernova remnants interacting with molecular clouds are efficient electron accelerators and sources of non-thermal X-ray and γ-ray emission. Recently Malkov et al. (2005) argued that diffusive shock acceleration is substantially affected by the different particle and Alfven wave propagation inside the partially ionized and dense cloud. They discussed possible applications to the recent TeV observations of the remnant RX J1713.7-3946 (figure 2.8) which is at the border of a molecular cloud. As pointed out by Aharonian et al. (1994) in the high-energy range the existence of dense targets for the cosmic-rays is particularly important for the hadronic π_0-decay process, the emission of which is proportional to the ambient medium density[4].

The first evidence for γ emission from supernova remnants interacting with dense clouds was reported by Pollock (1985): two COS-B sources are associated with two such remnants, G78.2+2.1 (γ Cygni) and G6.4-0.1 (W28). EGRET has detected four extended γ-ray sources that are candidates to be identified with the remnants γ Cygni, W28, W44 and IC 443 (Esposito et al. 1996), which interestingly all show evidences for interaction with molecular gas[5]. Chevalier (1999) showed that the multi-wavelength spectra of W44 and IC 443 (radio synchrotron, optical lines, non-thermal γ-rays) can be well modeled by the interaction of the radiative shell with molecular clumps. Bocchino and Bykov (2000) reported observations of hard X-ray emission from IC 443 coming from two localized features spatially correlated with bright molecular emission regions. Uchiyama et al. (2002) observed γ-Cygni and concluded that the bulk of γ-rays detected by EGRET likely comes from a radio-bright and X-ray-dim cloud at the border of the remnant. Rowell et al. (2007) recently reported HESS observations of γ emission coincident with the molecular clouds surrounding W28.

Now what is the situation inside superbubbles? Chu and Mac Low (1990) have observed diffuse X-ray emission not associated with known supernova remnants in 7 LMC HII complexes encompassing 10 OB associations (N44, N51D, N57A, N70, N154, N157 aka 30 Doradus, N158). Modeling these as superbubbles, they found that the X-ray luminosities expected from their hot interiors fall one order of magnitude below the observed values. They showed that supernovae close to the center of a superbubble add very little emission,

[4]However it has been realized that the observed γ-ray spectra usually can't be fitted by a pure π_0-decay spectrum and that some other component is needed: Bremsstrahlung and/or inverse Compton emission (eg Esposito et al. 1996, Sturner et al. 1997), so that the mere presence of clouds cannot resolve completely the ambiguity between electronic and hadronic emission.

[5]A good tracer of shock–cloud interaction is the OH maser emission, collisionally excited by H_2 molecules heated by the shock.

but that off-center supernovae hitting the ionized shell could explain the observed emission. Chu (1997) studied the environment of a large sample of supernovae. He argued that the X-ray bright superbubbles N51D and N44 are very probably powered by supernovae interacting with inner clouds or with the supershell – and he showed that the computed upstream density of such supernova shocks is consistent with the superbubble interior. Chen et al. (2000) studied the high-resolution morphology of the [SII]/H_α ratio in three superbubbles (DEM L152, L192, L106). They also concluded that the large expansion velocities and the large interior X-ray emission can be understood in terms of interior supernovae near the superbubble shell walls. However these again are very indirect proofs of the occurrence of supernovae inside superbubbles...

9.3 Indirect Signatures of Cosmic-Ray

The most obvious proof of the presence of high-energy particles inside superbubbles is of course the observation of non-thermal X and γ-ray emission from these objects, which is now firmly established as we have seen in section 9.1.2. However the exact nature of these particles and of the mechanism(s) that accelerate(s) them is still unclear – all the more so since many different accelerators are probably working together, in different objects or even within the same region. For instance, X-ray radiation from 30 Doradus C can be well interpreted as synchrotron radiation of TeV electrons accelerated in cumulative supernovae explosions (Bamba et al. 2004), but X-ray radiation from NGC 6334 seems more consistent with non-thermal Bremsstrahlung from moderately relativistic electrons (Ezoe et al. 2006b).

To end this chapter we would like to show how observations of thermal radiation and non-observations of non-thermal radiation can also be used to constrain the cosmic-rays properties inside superbubbles.

9.3.1 Energy Budget

An always interesting approach when studying an astrophysical object is to try to work out its global energy budget, regardless of the details of the (usually complex) physics: how much energy is provided by the sources, where does it end? In a superbubble energy is mostly provided as kinetic energy by the winds and explosions of the massive stars, and is expected to be stored in the thermal energy of the hot interior and in the kinetic energy of the dense swept-up supershell (radiative losses, although very important to us, are usually negligible).

Cooper et al. (2004) have reported an "energy crisis" in the superbubble DEM L192 (aka N51D). Through a careful analysis of the stellar content of the OB associations LH 51 and LH 54 powering the superbubble they evaluate the stellar winds energy release to $(5 \pm 1) \times 10^{51}$ erg and the supernovae energy release to $(13 \pm 4) \times 10^{51}$ erg, that is a total input of $(18 \pm 5) \times 10^{51}$ erg during

the ~ 3 Myr lifetime of the cluster. Using diagnostics of the superbubble and supershell composition by various instruments they infer their total thermal and kinetic energies to be respectively $(1.1 \pm 0.5) \times 10^{51}$ erg and $(4.7 \pm 1.0) \times 10^{51}$ erg, that is a total energy of $(6 \pm 2) \times 10^{51}$ erg stored inside the $120 \times 120 \times 200$ pc^3 superbubble. One sees that the computed input energy is $\sim$3 times higher than the observed energy. Therefore a sizeable fraction of the stars energy must be drained out of the superbubble. One mechanism that could be very efficient is the superbubble breaking out of the Galactic plane and pouring into the halo, but there is no indication of such a blow-out in DEM L192. Another mechanism is the evaporation of dense cooler gas at the interface between the supershell (or dense inner clouds) and the hot interior, but the radiative losses in DEM L192 can't be more than $\sim 1.5 \times 10^{51}$ erg. The most probable hypothesis left is that a substantial part of the winds and supernovae energy is not thermalized, but goes into non-thermal particles – and indeed the high-resolution spectra obtained by XMM-Newton contain a power-law component.

Smith and Wang (2004) have reported the same effect in the superbubble 30 Doradus C: the amount of energy currently present in the superbubble is significantly less then the expected energy input from the enclosed massive stars over their lifetime. The authors speculate that a substantial fraction of the input energy may be radiated in the far-infrared by dust grains mixed with the hot gas. However, thanks again to XMM-Newton, they also report that a power-law component contributes between one third and one half of the total luminosity observed – thus cosmic-rays are involved here too.

Thus, in the same way as one has to take into account cosmic-rays to model correctly the precise evolution of a supernova (see sections 2.3 and 2.5.2), one has very probably to take into account cosmic-rays to model correctly the precise evolution of a superbubble (see also the discussion of Oey 2007).

9.3.2 Chemistry and Low GeV Emission

As we have seen in section 8.1.1 cosmic-rays play an important role in the interstellar chemistry. This has been clearly observed in the Perseus OB2 superbubble (see Belikov et al (2002b, 2002a) and references therein for a general presentation of this object). Federman et al. (1996) have studied the production of OH and HD molecules through cosmic-rays ionization. Knauth et al. (2000) have reported an unusually low ^{7}Li/^{6}Li ratio in this region: $\sim$2 instead of 12.2 in the solar neighbourhood. The ^{6}Li enhancement is again explained by the interactions of (low-energy) cosmic-rays with ambient matter. Such an intense spallation activity should have high-energy emission counterparts (see section 9.1.3), especially in the GeV range due to the pion decay process. However EGRET hasn't detected any emission from Perseus OB2 (putting only upper limits). We have investigated this problem in an earlier research placement (Ferrand 2003). The situation is really problematic because the

Lithium ratio reported above requires a very high energy brought by cosmic-rays, of the order of 10^{54} erg. As the association is 7 Myr old the supernova and cosmic-rays activity is thought to have lasted for about 4 Myr. This gives an input power in cosmic-rays of roughly 8×10^{39} erg/s. Assuming a power-law cosmic-rays distribution of index of about 4, such a normalization leads to an easily detectable emission for EGRET. Adding an exponential cut-off to the cosmic-rays spectrum we found that it had to be as low as about 100 MeV for the GeV π_0 emission to remain below EGRET upper limits. Tatischeff et al. (1997) obtained the same kind of result in a study of the Orion region. This suggests that there is a very high flux of cosmic-rays in these superbubbles, but mostly in the form of low-energy cosmic-rays. We recall here that these low-energy cosmic-rays are the more likely to be well confined into superbubbles and thus to experience their specific processes such as repeated shock acceleration (see section 8.2).

Clearly observations at higher sensitivity in the GeV range would greatly help understanding the actual situation within superbubbles. Hopefully this window will be expanded by the LAT instrument (0.01-100 GeV, eg Michelson 2007) on board the GLAST satellite (eg Ritz 2007), to be launched in 2008.

References

Abdo, A. A., Allen, B., Berley, D., Blaufuss, E., Casanova, S., Chen, C., Coyne, D. G., Delay, R. S., Dingus, B. L., Ellsworth, R. W., Fleysher, L., Fleysher, R., Gebauer, I., Gonzalez, M. M., Goodman, J. A., Hays, E., Hoffman, C. M., Kolterman, B. E., Kelley, L. A., Lansdell, C. P., Linnemann, J. T., McEnery, J. E., Mincer, A. I., Moskalenko, I. V., Nemethy, P., Noyes, D., Ryan, J. M., Samuelson, F. W., Saz Parkinson, P. M., Schneider, M., Shoup, A., Sinnis, G., Smith, A. J., Strong, A. W., Sullivan, G. W., Vasileiou, V., Walker, G. P., Williams, D. A., Xu, X. W., and Yodh, G. B. (2007). Discovery of TeV Gamma-Ray Emission from the Cygnus Region of the Galaxy. ApJ, 658:L33–L36.

Aharonian, F., Akhperjanian, A., Beilicke, M., Bernlöhr, K., Börst, H., Bojahr, H., Bolz, O., Coarasa, T., Contreras, J., Cortina, J., Denninghoff, S., Fonseca, V., Girma, M., Götting, N., Heinzelmann, G., Hermann, G., Heusler, A., Hofmann, W., Horns, D., Jung, I., Kankanyan, R., Kestel, M., Kettler, J., Kohnle, A., Konopelko, A., Kornmeyer, H., Kranich, D., Krawczynski, H., Lampeitl, H., Lopez, M., Lorenz, E., Lucarelli, F., Magnussen, N., Mang, O., Meyer, H., Milite, M., Mirzoyan, R., Moralejo, A., Ona, E., Panter, M., Plyasheshnikov, A., Prahl, J., Pühlhofer, G., Rauterberg, G., Reyes, R., Rhode, W., Ripken, J., Röhring, A., Rowell, G. P., Sahakian, V., Samorski, M., Schilling, M., Schröder, F., Siems, M., Sobzynska, D., Stamm, W., Tluczykont, M., Völk, H. J., Wiedner, C. A., Wittek, W., Uchiyama, Y.,

Takahashi, T., and Collaboration, H. (2002). An unidentified TeV source in the vicinity of Cygnus OB2. A&A, 393:L37–L40.

Aharonian, F., Akhperjanian, A., Beilicke, M., Bernlöhr, K., Börst, H.-G., Bojahr, H., Bolz, O., Coarasa, T., Contreras, J., Cortina, J., Denninghoff, S., Fonseca, V., Girma, M., Götting, N., Heinzelmann, G., Hermann, G., Heusler, A., Hofmann, W., Horns, D., Jung, I., Kankanyan, R., Kestel, M., Kohnle, A., Konopelko, A., Kranich, D., Lampeitl, H., Lopez, M., Lorenz, E., Lucarelli, F., Mang, O., Mazin, D., Meyer, H., Mirzoyan, R., Moralejo, A., Oña-Wilhelmi, E., Panter, M., Plyasheshnikov, A., Pühlhofer, G., de los Reyes, R., Rhode, W., Ripken, J., Rowell, G. P., Sahakian, V., Samorski, M., Schilling, M., Siems, M., Sobzynska, D., Stamm, W., Tluczykont, M., Vitale, V., Völk, H. J., Wiedner, C. A., and Wittek, W. (2005). The unidentified TeV source (TeV J2032+4130) and surrounding field: Final HEGRA IACT-System results. A&A, 431:197–202.

Aharonian, F., Akhperjanian, A. G., Bazer-Bachi, A. R., Beilicke, M., Benbow, W., Berge, D., Bernlöhr, K., Boisson, C., Bolz, O., Borrel, V., Braun, I., Breitling, F., Brown, A. M., Chadwick, P. M., Chounet, L.-M., Cornils, R., Costamante, L., Degrange, B., Dickinson, H. J., Djannati-Ataï, A., Drury, L. O., Dubus, G., Emmanoulopoulos, D., Espigat, P., Feinstein, F., Fontaine, G., Fuchs, Y., Funk, S., Gallant, Y. A., Giebels, B., Gillessen, S., Glicenstein, J. F., Goret, P., Hadjichristidis, C., Hauser, M., Heinzelmann, G., Henri, G., Hermann, G., Hinton, J. A., Hofmann, W., Holleran, M., Horns, D., Jacholkowska, A., de Jager, O. C., Khélifi, B., Komin, N., Konopelko, A., Latham, I. J., Le Gallou, R., Lemière, A., Lemoine-Goumard, M., Leroy, N., Lohse, T., Martin, J. M., Martineau-Huynh, O., Marcowith, A., Masterson, C., McComb, T. J. L., de Naurois, M., Nolan, S. J., Noutsos, A., Orford, K. J., Osborne, J. L., Ouchrif, M., Panter, M., Pelletier, G., Pita, S., Pühlhofer, G., Punch, M., Raubenheimer, B. C., Raue, M., Raux, J., Rayner, S. M., Reimer, A., Reimer, O., Ripken, J., Rob, L., Rolland, L., Rowell, G., Sahakian, V., Saugé, L., Schlenker, S., Schlickeiser, R., Schuster, C., Schwanke, U., Siewert, M., Sol, H., Spangler, D., Steenkamp, R., Stegmann, C., Tavernet, J.-P., Terrier, R., Théoret, C. G., Tluczykont, M., Vasileiadis, G., Venter, C., Vincent, P., Völk, H. J., and Wagner, S. J. (2006). The H.E.S.S. Survey of the Inner Galaxy in Very High Energy Gamma Rays. ApJ, 636:777–797.

Aharonian, F., Akhperjanian, A. G., Bazer-Bachi, A. R., Beilicke, M., Benbow, W., Berge, D., Bernlöhr, K., Boisson, C., Bolz, O., Borrel, V., Braun, I., Brion, E., Brown, A. M., Bühler, R., Büsching, I., Boutelier, T., Carrigan, S., Chadwick, P. M., Chounet, L.-M., Coignet, G., Cornils, R., Costamante, L., Degrange, B., Dickinson, H. J., Djannati-Ataï, A., Drury, L. O., Dubus, G., Egberts, K., Emmanoulopoulos, D., Espigat, P., Farnier, C., Feinstein, F., Ferrero, E., Fiasson, A., Fontaine, G., Funk, S., Funk, S., Füßling,

M., Gallant, Y. A., Giebels, B., Glicenstein, J. F., Glück, B., Goret, P., Hadjichristidis, C., Hauser, D., Hauser, M., Heinzelmann, G., Henri, G., Hermann, G., Hinton, J. A., Hoffmann, A., Hofmann, W., Holleran, M., Hoppe, S., Horns, D., Jacholkowska, A., de Jager, O. C., Kendziorra, E., Kerschhaggl, M., Khélifi, B., Komin, N., Kosack, K., Lamanna, G., Latham, I. J., Le Gallou, R., Lemière, A., Lemoine-Goumard, M., Lohse, T., Martin, J. M., Martineau-Huynh, O., Marcowith, A., Masterson, C., Maurin, G., McComb, T. J. L., Moulin, E., de Naurois, M., Nedbal, D., Nolan, S. J., Noutsos, A., Olive, J.-P., Orford, K. J., Osborne, J. L., Panter, M., Pelletier, G., Petrucci, P.-O., Pita, S., Pühlhofer, G., Punch, M., Ranchon, S., Raubenheimer, B. C., Raue, M., Rayner, S. M., Reimer, A., Reimer, O., Ripken, J., Rob, L., Rolland, L., Rosier-Lees, S., Rowell, G., Sahakian, V., Santangelo, A., Saugé, L., Schlenker, S., Schlickeiser, R., Schröder, R., Schwanke, U., Schwarzburg, S., Schwemmer, S., Shalchi, A., Sol, H., Spangler, D., Spanier, F., Steenkamp, R., Stegmann, C., Superina, G., Tam, P. H., Tavernet, J.-P., Terrier, R., Tluczykont, M., van Eldik, C., Vasileiadis, G., Venter, C., Vialle, J. P., Vincent, P., Völk, H. J., Wagner, S. J., and Ward, M. (2007). Detection of extended very-high-energy gamma-ray emission towards the young stellar cluster Westerlund 2. A&A, 467:1075–1080.

Aharonian, F. A., Drury, L. O., and Völk, H. J. (1994). GeV/TeV gamma-ray emission from dense molecular clouds overtaken by supernova shells. A&A, 285:645–647.

Alter, G., Israel, B. Y., and Ruprecht, J. (1966). *Catalogue of star clusters and associations*. Prague: Astronomical Institute Czechoslovakia, 1966.

Amenomori, M., Ayabe, S., Bi, X. J., Chen, D., Cui, S. W., Danzengluobu, Ding, L. K., Ding, X. H., Feng, C. F., Feng, Z., Feng, Z. Y., Gao, X. Y., Geng, Q. X., Guo, H. W., He, H. H., He, M., Hibino, K., Hotta, N., Hu, H., Hu, H. B., Huang, J., Huang, Q., Jia, H. Y., Kajino, F., Kasahara, K., Katayose, Y., Kato, C., Kawata, K., Labaciren, Le, G. M., Li, A. F., Li, J. Y., Lu, H., Lu, S. L., Meng, X. R., Mizutani, K., Mu, J., Munakata, K., Nagai, A., Nanjo, H., Nishizawa, M., Ohnishi, M., Ohta, I., Onuma, H., Ouchi, T., Ozawa, S., Ren, J. R., Saito, T., Saito, T. Y., Sakata, M., Sako, T. K., Sasaki, T., Shibata, M., Shiomi, A., Shirai, T., Sugimoto, H., Takita, M., Tan, Y. H., Tateyama, N., Torii, S., Tsuchiya, H., Udo, S., Wang, B., Wang, H., Wang, X., Wang, Y. G., Wu, H. R., Xue, L., Yamamoto, Y., Yan, C. T., Yang, X. C., Yasue, S., Ye, Z. H., Yu, G. C., Yuan, A. F., Yuda, T., Zhang, H. M., Zhang, J. L., Zhang, N. J., Zhang, X. Y., Zhang, Y., Zhang, Y., Zhaxisangzhu, and Zhou, X. X. (2007). Study on TeV Gamma Ray Emission from Cygnus Region Using the Tibet Air Shower. In *ICRC'07 proceedings (pre-conference edition)*.

Bamba, A., Ueno, M., Nakajima, H., and Koyama, K. (2004). Thermal and

Nonthermal X-Rays from the Large Magellanic Cloud Superbubble 30 Doradus C. ApJ, 602:257–263.

Bartko, H., Bednarek, W., and Saito, T. (2007). Search for gamma-ray emission from unidentified EGRET sources located in the Cygnus region with the MAGIC telescope. In *ICRC'07 proceedings (pre-conference edition)*.

Bedogni, R. and Woodward, P. R. (1990). Shock wave interactions with interstellar clouds. A&A, 231:481–498.

Belikov, A. N., Kharchenko, N. V., Piskunov, A. E., Schilbach, E., and Scholz, R.-D. (2002a). Study of the Per OB2 star forming complex. II. Structure and kinematics. A&A, 387:117–128.

Belikov, A. N., Kharchenko, N. V., Piskunov, A. E., Schilbach, E., Scholz, R.-D., and Yatsenko, A. I. (2002b). Study of the Per OB2 star-forming complex. I. The Compiled Catalogue of kinematic and photometric data. A&A, 384:145–154.

Blaauw, A. (1964). The O Associations in the Solar Neighborhood. ARA&A, 2:213–246.

Blandford, R. D. and Cowie, L. L. (1982). Radio emission from supernova remnants in a cloudy interstellar medium. ApJ, 260:625–634.

Bocchino, F. and Bykov, A. M. (2000). Hard X-ray emission from IC443: evidence for a shocked molecular clump? A&A, 362:L29–L32.

Butt, Y. M., Drake, J., Benaglia, P., Combi, J. A., Dame, T., Miniati, F., and Romero, G. E. (2006). Deeper Chandra Follow-up of Cygnus TeV Source Perpetuates Mystery. ApJ, 643:238–244.

Bykov, A. M., Chevalier, R. A., Ellison, D. C., and Uvarov, Y. A. (2000). Nonthermal Emission from a Supernova Remnant in a Molecular Cloud. ApJ, 538:203–216.

Cash, W. and Charles, P. (1979a). The X-ray Superbubble in Cygnus. In *Bulletin of the American Astronomical Society*, volume 11 of *Bulletin of the American Astronomical Society*, page 723.

Cash, W. and Charles, P. (1979b). The X-ray Superbubble in Cygnus. In *Bulletin of the American Astronomical Society*, volume 11 of *Bulletin of the American Astronomical Society*, page 794.

Chen, C.-H. R., Chu, Y.-H., Gruendl, R. A., and Points, S. D. (2000). Hubble Space Telescope Wide Field Planetary Camera 2 Imaging of Shocks in Superbubbles. AJ, 119:1317–1324.

Chen, Y., Wang, Q. D., Gotthelf, E. V., Jiang, B., Chu, Y.-H., and Gruendl, R. (2006). Chandra ACIS Spectroscopy of N157B: A Young Composite Supernova Remnant in a Superbubble. ApJ, 651:237–249.

Chevalier, R. A. (1999). Supernova Remnants in Molecular Clouds. ApJ, 511:798–811.

Chu, Y.-H. (1997). Supernova Remnants in OB Associations. AJ, 113:1815–1832.

Chu, Y.-H., Gruendl, R. A., Chen, C.-H. R., Lazendic, J. S., and Dickel, J. R. (2004). An Optical and X-Ray Examination of Two Radio Supernova Remnant Candidates in 30 Doradus. ApJ, 615:727–731.

Chu, Y.-H. and Kennicutt, Jr., R. C. (1986). Kinematic detection of supernova remnants in giant H II regions. ApJ, 311:85–97.

Chu, Y.-H. and Kennicutt, Jr., R. C. (1994). Kinematic structure of the 30 Doradus giant H II region. ApJ, 425:720–737.

Chu, Y.-H. and Mac Low, M.-M. (1990). X-rays from Superbubbles in the Large Magellanic Cloud. ApJ, 365:510–521.

Chu, Y.-H., Wakker, B., Mac Low, M.-M., and Garcia-Segura, G. (1994). Ultraviolet interstellar absorption lines in the LMC: Searching for hidden SNRs. *Astronomical Journal*, 108:1696–1721.

Cooper, R. L., Guerrero, M. A., Chu, Y.-H., Chen, C.-H. R., and Dunne, B. C. (2004). Energy Crisis in the Superbubble DEM L192 (N51D). ApJ, 605:751–758.

de Zeeuw, P. T., Hoogerwerf, R., de Bruijne, J. H. J., Brown, A. G. A., and Blaauw, A. (1999). A HIPPARCOS Census of the Nearby OB Associations. AJ, 117:354–399.

Ehlerová, S. and Palouš, J. (2005). H I shells in the outer Milky Way. A&A, 437:101–112.

Esposito, J. A., Hunter, S. D., Kanbach, G., and Sreekumar, P. (1996). EGRET Observations of Radio-bright Supernova Remnants. ApJ, 461:820–827.

Ezoe, Y., Kokubun, M., Makishima, K., Sekimoto, Y., and Matsuzaki, K. (2006a). The Discovery of Diffuse X-Ray Emission in NGC 2024, One of the Nearest Massive Star-forming Regions. ApJ, 649:L123–L128.

Ezoe, Y., Kokubun, M., Makishima, K., Sekimoto, Y., and Matsuzaki, K. (2006b). Investigation of Diffuse Hard X-Ray Emission from the Massive Star-forming Region NGC 6334. ApJ, 638:860–877.

Federman, S. R., Weber, J., and Lambert, D. L. (1996). Cosmic Ray-induced Chemistry toward Perseus OB2. ApJ, 463:181–190.

Ferrand, G. (2003). Etude de l'émission haute énergie des superbulles galactiques. rapport de stage de fin d'études, Ecole Centrale Paris.

Frisch, P. C. (2007). The Local Bubble and Interstellar Material Near the Sun. *Space Science Reviews*, pages 124–134.

Hartman, R. C., Bertsch, D. L., Bloom, S. D., Chen, A. W., Deines-Jones, P., Esposito, J. A., Fichtel, C. E., Friedlander, D. P., Hunter, S. D., McDonald, L. M., Sreekumar, P., Thompson, D. J., Jones, B. B., Lin, Y. C., Michelson, P. F., Nolan, P. L., Tompkins, W. F., Kanbach, G., Mayer-Hasselwander, H. A., Mücke, A., Pohl, M., Reimer, O., Kniffen, D. A., Schneid, E. J., von Montigny, C., Mukherjee, R., and Dingus, B. L. (1999). The Third EGRET Catalog of High-Energy Gamma-Ray Sources. ApJS, 123:79–202.

Hartmann, D. and Burton, W. B. (1997). *Atlas of Galactic Neutral Hydrogen*. Atlas of Galactic Neutral Hydrogen, by Dap Hartmann and W. Butler Burton, pp. 243. ISBN 0521471117. Cambridge, UK: Cambridge University Press, February 1997.

Heiles, C. (1979). H I shells and supershells. ApJ, 229:533–537.

Horns, D., Hoffmann, A. I. D., Santangelo, A., Aharonian, F. A., and Rowell, G. P. (2007). XMM-Newton observations of the first unidentified TeV gamma-ray source TeV J2032+4130. A&A, 469:L17–L21.

Jones, T. W. and Kang, H. (1993). Cosmic-ray acceleration during the impact of shocks on dense clouds. ApJ, 402:560–573.

Jun, B.-I. and Jones, T. W. (1999). Radio Emission from a Young Supernova Remnant Interacting with an Interstellar Cloud: Magnetohydrodynamic Simulation with Relativistic Electrons. ApJ, 511:774–791.

Knauth, D. C., Federman, S. R., Lambert, D. L., and Crane, P. (2000). Newly synthesized lithium in the interstellar medium. *Nature*, 405:656–658.

Knödlseder, J., Valsesia, M., Allain, M., Boggs, S., Diehl, R., Jean, P., Kretschmer, K., Roques, J.-P., Schönfelder, V., Vedrenne, G., von Ballmoos, P., Weidenspointner, G., and Winkler, C. (2004). SPI/INTEGRAL Observation of 1809 keV Gamma-Ray Line Emission from the CYGNUS X Region. In Schoenfelder, V., Lichti, G., and Winkler, C., editors, *5th INTEGRAL Workshop on the INTEGRAL Universe*, volume 552 of *ESA Special Publication*, pages 33–37.

Konopelko, A., Atkins, R. W., Blaylock, G., Buckley, J. H., Butt, Y., Carter-Lewis, D. A., Celik, O., Cogan, P., Chow, Y. C. K., Cui, W., Dowdall, C.,

Ergin, T., Falcone, A. D., Fegan, D. J., Fegan, S. J., Finley, J. P., Fortin, P., Gillanders, G. H., Gutierrez, K. J., Hall, J., Hanna, D., Horan, D., Hughes, S. B., Humensky, T. B., Imran, A., Jung, I., Kaaret, P., Kenny, G. E., Kertzman, M., Kieda, D. B., Kildea, J., Knapp, J., Kosack, K., Krawczynski, H., Krennrich, F., Lang, M. J., LeBohec, S., Moriarty, P., Mukherjee, R., Nagai, T., Ong, R. A., Perkins, J. S., Pohl, M., Ragan, K., Reynolds, P. T., Rose, H. J., Sembroski, G. H., Schrödter, M., Smith, A. W., Steele, D., Syson, A., Swordy, S. P., Toner, J. A., Valcarcel, L., Vassiliev, V. V., Wagner, R. G., Wakely, S. P., Weekes, T. C., White, R. J., Williams, D. A., and Zitzer, B. (2007). Observations of the Unidentified TeV gamma-Ray Source TeV J2032+4130 with the Whipple Observatory 10 m Telescope. ApJ, 658:1062–1068.

Lallement, R., Welsh, B. Y., Vergely, J. L., Crifo, F., and Sfeir, D. (2003). 3D mapping of the dense interstellar gas around the Local Bubble. A&A, 411:447–464.

Lazendic, J. S., Dickel, J. R., and Jones, P. A. (2003). Supernova Remnant Candidates in the 30 Doradus Nebula. ApJ, 596:287–298.

Maciejewski, W., Murphy, E. M., Lockman, F. J., and Savage, B. D. (1996). The Aquila Supershell: A Remnant of Multiple Supernovae. ApJ, 469:238–245.

Madsen, G. J., Reynolds, R. J., and Haffner, L. M. (2006). A Multiwavelength Optical Emission Line Survey of Warm Ionized Gas in the Galaxy. ApJ, 652:401–425.

Malkov, M. A., Diamond, P. H., and Sagdeev, R. Z. (2005). On the Gamma-Ray Spectra Radiated by Protons Accelerated in Supernova Remnant Shocks near Molecular Clouds: The case of Supernova Remnant RX J1713.7-3946. ApJ, 624:L37–L40.

Marcowith, A. (2007b). Les supernovae comme sources des rayons cosmiques II. Les régions de formation d'étoiles massives et les superbulles [brouillon]. Ecole de Gif sur les rayons cosmiques de haute énergie.

Marcowith, A., Gallant, Y. A., and Komin, N. (2007). H.E.S.S. sources possibly associated with massive star clusters. In *ICRC'07 proceedings (pre-conference edition)*.

Michelson, P. F. (2007). The Large Area Telescope. In Ritz, S., Michelson, P., and Meegan, C. A., editors, *American Institute of Physics Conference Series*, volume 921 of *American Institute of Physics Conference Series*, pages 8–12.

Oey, M. S. (1996). The Dynamics of Superbubbles in the Large Magellanic Cloud. ApJ, 467:666–675.

Oey, M. S. (2007). Towards resolving the evolution of multi-supernova superbubbles. In Elmegreen, B. G. and Palous, J., editors, *IAU Symposium*, volume 237 of *IAU Symposium*, pages 106–113.

Orlando, S., Bocchino, F., Peres, G., Reale, F., Plewa, T., and Rosner, R. (2006). Crushing of interstellar gas clouds in supernova remnants. II. X-ray emission. A&A, 457:545–552.

Orlando, S., Peres, G., Reale, F., Bocchino, F., Rosner, R., Plewa, T., and Siegel, A. (2005). Crushing of interstellar gas clouds in supernova remnants. I. The role of thermal conduction and radiative losses. A&A, 444:505–519.

Parizot, E. and Knödlseder, J. (1999). Gamma-Ray Line Emission from Superbubbles. *Astrophysical Letters Communications*, 38:345–348.

Pollock, A. M. T. (1985). The probable identification of two COS-B gamma-ray sources with molecular clouds compressed by supernova remnants. A&A, 150:339–342.

Reich, P., Testori, J. C., and Reich, W. (2001). A radio continuum survey of the southern sky at 1420 MHz. The atlas of contour maps. A&A, 376:861–877.

Reimer, O., Hinton, J., Hofmann, W., Hoppe, S., Masterson, C., and Raue, M. (2007). HESS J1023-575: Non-thermal Particle Acceleration Associated with a Young Stellar Cluster. In Ritz, S., Michelson, P., and Meegan, C. A., editors, *American Institute of Physics Conference Series*, volume 921 of *American Institute of Physics Conference Series*, pages 220–222.

Ritz, S. (2007). Overview of the GLAST Mission and Opportunities. In Ritz, S., Michelson, P., and Meegan, C. A., editors, *American Institute of Physics Conference Series*, volume 921 of *American Institute of Physics Conference Series*, pages 3–7.

Rowell, G., Brion, E., Reimer, O., Aharonian, F., Goret, P., Djannati-Atai, A., Moriguchi, Y., and Fukui, Y. (2007). Discovery of TeV Gamma-Ray Emission in the W28 Region from HESS Observations and Multiwavelength Comparisons. In *ICRC'07 proceedings (pre-conference edition).*

Smith, D. A. and Wang, Q. D. (2004). Confronting the Superbubble Model with X-Ray Observations of 30 Doradus C. ApJ, 611:881–891.

Stone, J. M. and Norman, M. L. (1992). The three-dimensional interaction of a supernova remnant with an interstellar cloud. ApJ, 390:L17–L19.

Sturner, S. J., Skibo, J. G., Dermer, C. D., and Mattox, J. R. (1997). Temporal Evolution of Nonthermal Spectra from Supernova Remnants. ApJ, 490:619–632.

Tatischeff, V. (2003). X- and Gamma-Ray Line Emission Processes. In Motch, C. and Hameury, J.-M., editors, *EAS Publications Series*, volume 7 of *EAS Publications Series*, page 79.

Tatischeff, V., Ramaty, R., and Mandzhavidze, N. (1997). Constraints from Pion Production on the Spectral Hardness of the Low Energy Cosmic Rays In Orion. In Dermer, C. D., Strickman, M. S., and Kurfess, J. D., editors, *Proceedings of the Fourth Compton Symposium*, volume 410 of *American Institute of Physics Conference Series*, page 1054.

Tatischeff, V., Thibaud, J.-P., Kiener, J., Cassé, M., and Vangioni-Flam, E. (2001). Gamma-ray line emission from 7Li and 7Be production by cosmic-rays. In Gimenez, A., Reglero, V., and Winkler, C., editors, *ESA SP-459: Exploring the Gamma-Ray Universe*, pages 105–108.

Terrier, R. (2007). X-ray and gamma-ray counterpart of the observed spallation activity in the Per OB2 Cloud. Integral Proposal 520064.

Townsley, L. K. (2006). Not Your Grandmother's HII Regions: An X-ray Tour of Massive Star-forming Regions. In *Bulletin of the American Astronomical Society*, volume 38 of *Bulletin of the American Astronomical Society*, page 345.

Townsley, L. K., Broos, P. S., Feigelson, E. D., Brandl, B. R., Chu, Y.-H., Garmire, G. P., and Pavlov, G. G. (2006). A Chandra ACIS Study of 30 Doradus. I. Superbubbles and Supernova Remnants. AJ, 131:2140–2163.

Townsley, L. K., Feigelson, E. D., Montmerle, T., Broos, P. S., Chu, Y.-H., and Garmire, G. P. (2003). 10 MK Gas in M17 and the Rosette Nebula: X-Ray Flows in Galactic H II Regions. ApJ, 593:874–905.

Uchiyama, Y., Takahashi, T., Aharonian, F. A., and Mattox, J. R. (2002). ASCA View of the Supernova Remnant gamma Cygni (G78.2+2.1): Bremsstrahlung X-Ray Spectrum from Loss-flattened Electron Distribution. ApJ, 571:866–875.

Uyaniker, B., Fürst, E., Reich, W., Aschenbach, B., and Wielebinski, R. (2001). The Cygnus superbubble revisited. A&A, 371:675–697.

Walborn, N. R. (1991). The Starburst Region 30 Doradus. In Haynes, R. and Milne, D., editors, *The Magellanic Clouds*, volume 148 of *IAU Symposium*, pages 145–153.

Walborn, N. R., Maíz-Apellániz, J., and Barbá, R. H. (2002). Further Insights into the Structure of 30 Doradus from the Hubble Space Telescope Instruments. AJ, 124:1601–1624.

Wang, Q. and Helfand, D. J. (1991). An X-ray image of the violent interstellar medium in 30 Doradus. ApJ, 370:541–550.

Conclusion [en]

We have presented a study of the acceleration of cosmic-rays by supernova shock waves in superbubbles. We hope that this thesis has elucidated the situation inside these objects, where cosmic-ray production is probably underlooked and under-documented. We hope to have convinced the reader that cosmic-ray production in the Galaxy cannot be investigated properly if one does not take into account the way their progenitors, namely massive stars, evolve.

Our main production is a new code for the study of time-dependent non-linear DSA. It is based on the kinetic approach, coupling the hydrodynamical evolution of a thermal plasma with the diffusive transport of supra-thermal particles. As such, it falls under the legacy of the pioneers (Falle and Giddings, Duffy) and of the masters (Kang and Jones) of the genre. Although it relies on known methods it is a fully original implementation, which confirms that this approach is effective (in particular we have confirmed the use of an implicit routine in nested grids to handle particle diffusion). Our code has been validated against analytical results in the linear regime and against other simulations in the non-linear regime. It has been optimized as much as possible, resorting to techniques of Adaptive Mesh Refinement and parallelization to lower the cost of numerical resolution in the space and the energy dimension respectively. To the best of our knowledge it is the second tool of this kind currently operational in the world, and the only one in France and Europe (however at least two other numerical tools address the same problem using different approaches). The development of the code took some time, as realistic problems were numerically more difficult than anticipated – and even now the computational cost of simulations can still be very high, which limits the exploration of very high energies. The advantage is that we now have a clear and complete understanding of how our tool works. We have begun to address new science with it, in the context of superbubbles. We have performed the first investigations of time-dependent non-linear DSA by repeated shocks, confirming the hardening of the spectrum. We have begun to disentangle the effects of internal injection (new cosmic-rays produced at the shock front) and external injection (existing cosmic-rays advected to the shock front). In superbubbles the former seems to marginally dominate in strong shocks, but the latter might play an important role in weak shocks (as already argued by Bykov).

Although already quite a big tool, our code would benefit from better physics in many aspects. Our first concern is geometry: all the original results presented here have been obtained in a 1D slab geometry, we shall extend this to a spherical geometry. Going directly to full 3D seems clearly over-ambitious, but it shouldn't be too difficult to study acceleration in 1D spherical symmetry (see the appendix regarding hydrodynamics). An important effect of geometry is escape of particles upstream of the shock, which limits the maximum energy that cosmic-rays can achieve. Another key element of the DSA mechanism, especially regarding this important issue of the maximum energy, is the magnetic turbulence, which is not well understood. It is conveniently prescribed in our simulations through the diffusion coefficient. The next step would be to explicitly add waves transport, in order to solve the full problem in a self-consistent way. And finally of course it would be of great interest to add radiation into our code, as cosmic-rays induce broad-band emission which is well observed. We believe that the hadronic emission would be fairly easy to add (all the more so since we have already worked on that issue previously), the leptonic emission on the other hand would require a separate treatment of electrons as radiative losses impact their dynamics. We could also add the emission of the thermal plasma, especially if we want to investigate the interaction of a supernova remnant with a molecular cloud (which enhances emission, especially of protons). Note that these three major axes can be incremented progressively, and that they are actually fully coupled. To end the discussion on the future developments of our model, we would like to stress that another interesting approach would be to actually *downsize* it, trying to extract what is truly essential to non-linear DSA, with the aim of building a simple model that gives the global picture – as Ellison and Berezhko have already done. We would also like to explore the semi-analytical model of Blasi, which seems to complement nicely our own work.

Regarding superbubbles and multiple shocks, our code as it stands can still give useful insights into cosmic-ray production. We are currently completing the study of the effect of an upstream population of cosmic-rays on injection. We intend to run simulations of multiple shocks dedicated to superbubbles, where the upstream cosmic-ray pressure will evolve in a self-consistent manner. However we recall that the inter-shock treatment critically depends on the model of cosmic-rays transport inside the superbubble, which is rather poorly constrained. Here we feel the need to get better input data, in particular regarding the typical time between two shocks (strong or weak) and the bubble escape energy as a function of the number of shocks. This will probably require more careful analyse of the morphology and timeline of an OB association.

Conclusion [fr]

Nous avons présenté une étude de l'accélération des rayons cosmiques par les ondes de choc des restes de supernovae dans les superbulles galactiques. Nous souhaitons avoir clarifié la situation dans ces objets, où la production de rayons cosmiques est probablement sous-estimée et sous-documentée. Nous espérons avoir convaincu le lecteur qu'il n'est pas possible d'appréhender pleinement la production des rayons cosmiques dans la Galaxie sans tenir compte de la façon dont évoluent leurs progéniteurs, les étoiles massives.

Notre principale production est un nouveau code pour l'étude de l'ADOC non-linéaire et dépendante du temps. Il est basé sur l'approche cinétique couplant l'évolution hydrodynamique du plasma et le transport diffusif des particules supra-thermiques. Il s'inscrit ainsi dans la lignée des précurseurs (Falle et Giddings, Duffy) et des maîtres (Kang et Jones) du genre. Bien qu'il s'appuie sur des techniques connues, il constitue une implémentation entièrement originale, ce qui confirme la pertinence de cette approche (en particulier nous avons confirmé l'utilité de schémas implicites sur des grilles emboîtées pour la diffusion des particules). Notre code a été validé par comparaison à des résultats analytiques dans le régime linéaire et à d'autres simulations dans le régime non-linéaire. Il a été optimisé autant que possible, en ayant recours aux techniques de grille adaptative et de parallélisation. A notre connaissance c'est le second outil actuellement opérationnel de ce type au monde, et le seul en France et en Europe (toutefois au moins deux autres outils numériques répondent au même problème par des méthodes différentes). Le développement du code a pris du temps, car les problèmes réalistes se sont avérés plus difficiles que prévu – et encore à ce jour les simulations peuvent avoir un coût très élevé en temps de calcul, ce qui limite l'exploration des très hautes énergies. Le point positif est que nous avons maintenant une compréhension profonde et complète de notre outil. Nous avons commencé à explorer de nouveaux aspects avec lui, dans le cadre des superbulles. Nous avons réalisé les premières études de l'ADOC non-linéaire par chocs successifs, confirmant le raidissement du spectre. Nous avons commencé à démêler les effets de l'injection interne (nouveaux rayons cosmiques produits au choc) et de l'injection externe (rayons cosmiques existants advectés au choc). Dans les superbulles la première semble dominer marginalement pour les chocs forts, mais la seconde pourrait jouer un rôle important pour les chocs faibles (comme l'affirme Bykov).

Bien que notre code soit déjà un outil assez complexe, la physique de nom-

breux aspects gagnerait à être développée. Nos premiers efforts porteraient sur la géométrie : tous les résultats originaux présentés dans cette thèse ont été obtenus en géométrie plane 1D, ils devraient être étendus à la géométrie sphérique. Passer directement en 3D semble clairement trop ambitieux, mais il ne devrait pas être trop difficile d'étudier l'accélération de particules en 1D à symétrie sphérique (voir l'annexe pour la partie hydrodynamique). Un effet géométrique important est l'échappement des particules en amont du choc, qui limite l'énergie maximale des rayons cosmiques. Un autre élément clef de l'ADOC, notamment en ce qui concerne cette question importante de l'énergie maximale, est la turbulence magnétique, qui n'est pas bien comprise. Elle est simplement paramétrée dans nos simulations via le coefficient de diffusion, l'étape suivante serait d'ajouter explicitement le transport des ondes, de manière à résoudre le problème complet de façon auto-cohérente. Et finalement il serait bien sûr très intéressant d'ajouter le rayonnement dans notre code, puisque les rayons cosmiques induisent une émission multi-longueurs d'onde bien observée. Nous pensons que l'émission hadronique serait assez facile à ajouter (d'autant que nous avons déjà travaillé sur ce sujet auparavant), l'émission leptonique en revanche nécessiterait un traitement séparé des électrons car leurs pertes radiatives ont un impact sur leur dynamique. Nous pourrions aussi ajouter l'émission du plasma thermique, surtout si nous voulons étudier l'interaction d'un reste de supernova avec un nuage moléculaire (qui augmente l'émission, notamment des protons). Notons que ces trois axes majeurs peuvent être améliorés par étapes, et qu'ils sont en fait entièrement couplés. Pour achever cette discussion sur les développements futurs de notre modèle, nous voudrions signaler qu'une autre approche intéressante serait en fait de le réduire, en essayant d'extraire ce qui est vraiment essentiel dans l'ADOC non-linéaire, dans le but de construire un modèle simple qui donne l'essentiel – comme l'ont déjà fait Ellison et Berezhko. Dans cette optique nous aimerions également explorer le modèle semi-analytique de Blasi, qui semble complémentaire de notre approche.

En ce qui concerne les superbulles, notre code permet déjà d'obtenir des résultats utiles sur la production des rayons cosmiques. Nous sommes en train de compléter l'étude de l'effet d'une population amont de rayons cosmiques sur l'injection. Nous prévoyons de réaliser des simulations de chocs multiples dédiées aux superbulles, où la pression amont des rayons cosmiques évoluera de façon auto-cohérente. Toutefois nous rappelons que le traitement de l'entre-chocs dépend de façon critique du modèle de transport dans la superbulle, lequel est assez mal contraint. A ce stade nous éprouvons le besoin d'avoir de meilleures données d'entrée, notamment concernant l'intervalle de temps typique entre deux chocs (forts comme faibles) et l'énergie d'échappement de la bulle en fonction du nombre de chocs. Cela nécessitera probablement une analyse plus approfondie de la morphologie et de la chronologie d'une association OB.

Appendix A

Simulations in Spherical Geometry

The code has been presented in part II in 1D slab geometry, it works in 3D symmetrical spherical geometry too (1D effective), provided we take into account the geometry of the finite-volume cells, which are now spherical shells. This is appropriate to the simulation of supernova remnants (see section 2.1.1.3). We have successfully adapted our hydrodynamical module and reproduced Truelove and McKee (1999) analytical results, the next step will be to investigate cosmic-ray acceleration and shock modifications in this geometry.

A.1 Numerical Scheme

In 3D the conservative formulation of section 4.1 still holds with the velocity being now a 3-component vector $\vec{u}$ and the pressure a 9-component tensor $\overleftrightarrow{P}$, so that the conservation of impulsion now reads

$$\frac{\partial \rho \vec{u}}{\partial t} + \vec{\mathrm{div}} \left(\overleftrightarrow{P} + \rho \vec{u} \vec{u} \right) = \vec{0} \,. \tag{A.1}$$

In symmetrical spherical geometry we have $\vec{u} = (u_x, 0, 0)$ and $\overleftrightarrow{P} = P \overleftrightarrow{I}$, so that equation (A.1) reduces to a single scalar equation

$$\frac{\partial u_x}{\partial t} + \mathrm{div} \left(P + \rho u_x^2 \right) = \frac{2P}{x} \tag{A.2}$$

where the divergence operator reads

$$\mathrm{div} \left(. \right) = \frac{1}{x^2} \frac{\partial}{\partial x} \left(x^2 . \right) \,. \tag{A.3}$$

Therefore the formalism of section 4.1 still holds simply replacing u by the radial velocity u_x in equations (4.2) and (4.3) and adding a source term

$$\vec{Q} = \begin{pmatrix} 0 \\ 2P/x \\ 0 \end{pmatrix} \tag{A.4}$$

to equation (4.1).

Using the finite-volume approach of equation (4.4) with the second-order reconstruction of equation (4.7), equation (4.5) then becomes

$$\frac{V_i X_i^{n+1} - V_i X_i^n}{\delta t} = +S_{i-\frac{1}{2}} F_{i-\frac{1}{2}}^{n+\frac{1}{2}} - S_{i+\frac{1}{2}} F_{i+\frac{1}{2}}^{n+\frac{1}{2}} + Q_i^n \tag{A.5}$$

with the fluxes factors

$$S_{i\pm\frac{1}{2}} = \frac{3x_{i\pm\frac{1}{2}}^2}{x_{i\pm\frac{1}{2}}^3 - x_{i\pm\frac{1}{2}}^3} \tag{A.6}$$

and the source term

$$Q_i^n = 3\bar{P}_i^n \frac{x_{i+\frac{1}{2}}^2 - x_{i-\frac{1}{2}}^2}{x_{i+\frac{1}{2}}^3 - x_{i-\frac{1}{2}}^3} + \sigma_i^n \left(2 - 3c_i \frac{x_{i+\frac{1}{2}}^2 - x_{i-\frac{1}{2}}^2}{x_{i+\frac{1}{2}}^3 - x_{i-\frac{1}{2}}^3}\right) \tag{A.7}$$

(see Falle 1991 and Downes et al. 2002). We recall that $x_{i-1/2}, x_{i+1/2}$ are the borders of cell i and that c_i is its center, defined so that

$$\int_{V_i} (x - c_i)\, dV = 0 \tag{A.8}$$

(if $\rho = ct$ this is the "center of mass") which gives

$$c_i = \frac{3}{4} \frac{\left(x_{i+\frac{1}{2}}^4 - x_{i-\frac{i}{2}}^4\right)}{\left(x_{i+\frac{1}{2}}^3 - x_{i-\frac{1}{2}}^3\right)}\,. \tag{A.9}$$

We consider spherical shells of constant width $\delta x = x_{i+1/2} - x_{i-1/2}$ which is the numerical space resolution.

Particle acceleration works in the same way as in section 4.2 with minor changes for geometrical factors, for instance a centred divergence now reads

$$\mathrm{div}_i\,(A) = \frac{(c^2 A)_{i+1} - (c^2 A)_{i-1}}{c_i^2 \delta x} \tag{A.10}$$

(see equation (A.3)).

The AMR mechanism also works in the same way as in section 5.2[1]. Without cosmic-rays the grids hierarchy is designed as follows: we choose the resolution δx at the finest level N and set the resolution at level $n = 0 \ldots N-1$ to be $(\delta x)_n = 2^{N-n} \times \delta x$, we choose the size of the base grid Δx and set the size of level $n = 1 \ldots N$ to be $(\Delta x)_n = 2^{N-n} \times 0.001\, \Delta x$. The condition $(\Delta x)_n < \Delta x$ then determines the number of sub-grids N.

And finally parallelization in momentum, as presented in section 6.2.2, is of course unaffected by space geometry.

[1]Note that, as it's working in the local shock rest frame, the AMR mechanism of Kang et al. (2001) is not suitable for spherical geometry. For that matter Kang and Jones (2006) have developed a new version of their code dedicated to spherical geometry, working in a frame co-moving with the expanding shock.

A.2 Supernova Setup

To initialize a supernova shock we set the initial ejecta profile at some small non-zero time t_0 as done in Truelove and McKee (1999): a mass $M_{\rm ej}$ with total kinetic energy $E_{\rm sn}$ is deposited around the origin with a free expansion velocity profile

$$u(x) = \frac{x}{t_0} \quad 0 \le x \le x_{\rm ej} \tag{A.11}$$

and some power-law density profile of index n (which optionally starts only after a central uniform core of size $x_{\rm core}$)

$$\rho(x) = \frac{M_{\rm ej}}{\frac{4}{3}\pi x_{\rm ej}^3}\, f\left(\frac{x}{x_{\rm ej}}\right) \quad \text{with} \quad f(w) = \begin{cases} f_0 & 0 \le w \le x_{\rm core}/x_{\rm ej} \\ f_n w^{-n} & x_{\rm core}/x_{\rm ej} \le w \le 1 \end{cases} . \tag{A.12}$$

The total mass of the blast is

$$M_{\rm ej} = \int_0^{x_{\rm ej}} \rho(x) 4\pi x^2 dx \tag{A.13}$$

so that

$$f_n = \frac{1 - n/3}{1 - (n/3)\, r_{\rm core}^{3-n}} \tag{A.14}$$

(and by continuity $f_0 = f_n (x_{\rm core}/x_{ej})^{-n}$). The total energy of the blast is

$$E_{\rm sn} = \int_0^{x_{\rm ej}} \frac{1}{2}\rho(x) u^2(x) 4\pi x^2 dx = \alpha \frac{1}{2} M_{\rm ej} u_{\rm ej}^2 \tag{A.15}$$

with

$$\alpha = \frac{3-n}{5-n} \frac{1 - (n/5) x_{\rm core}^{5-n}}{1 - (n/3) x_{\rm core}^{3-n}} \tag{A.16}$$

so that

$$u_{\rm ej} = u(x_{\rm ej}) = \sqrt{\frac{2E_{\rm sn}}{\alpha M_{\rm sn}}} . \tag{A.17}$$

The initial blast radius is then simply

$$x_{\rm ej} = u_{\rm ej} \times t_0 . \tag{A.18}$$

Note that for a steep index $n > 5$ the blast must have a core-envelop structure ($x_{\rm core} > 0$) for its total mass and energy to remain finite.

A.3 Analytical Model

Truelove and McKee (1999) explain that whenever the initial conditions introduce three independent dimensional parameters, the Euler equations admit a solution in dimensionless form containing no dependence on the characteristic

parameters – they call it a *unified* solution. This means that a single simulation needs to be made to treat all the choices of parameters. This is the case for a supernova remnant as long as the ambient pressure can be neglected with respect to the ram pressure of the blast. In that case the initial conditions only introduce three independent parameters: the ejecta energy $E_{\rm sn}$, the ejecta mass $M_{\rm ej}$, the ambient density $\rho_{\rm ism} = n_{\rm ism} \times \mu m_p$ (we consider here a multiplicity $\mu = 1.4$). These three parameters can be combined in a unique way to form characteristic scales of length, time and mass:

$$x_{\rm ch} = M_{\rm ej}^{1/3}\, \rho_{\rm ism}^{-1/3} \simeq 3.07\,{\rm pc}\, \left(\frac{M_{ej}}{1\,M_\odot}\right)^{\frac{1}{3}} \left(\frac{n_{ism}}{1\,{\rm cm}^{-3}}\right)^{-\frac{1}{3}} \tag{A.19}$$

$$t_{\rm ch} = E_{\rm sn}^{-1/2} M_{\rm ej}^{5/6} \rho_{\rm ism}^{-1/3} \simeq 423{\rm yr}\, \left(\frac{E_{\rm sn}}{10^{51}\,{\rm erg}}\right)^{-\frac{1}{2}} \left(\frac{M_{\rm ej}}{1\,M_\odot}\right)^{\frac{5}{6}} \left(\frac{n_{\rm ism}}{1\,{\rm cm}^{-3}}\right)^{-\frac{1}{3}} \tag{A.20}$$

$$M_{\rm ch} = M_{\rm ej} \tag{A.21}$$

from which one can derive additional scales such as a velocity scale

$$u_{\rm ch} = \frac{x_{\rm ch}}{t_{\rm ch}} = E_{\rm sn}^{1/2} M_{\rm ej}^{-1/2} \simeq 7090\,{\rm km/s}\, \left(\frac{E_{\rm sn}}{10^{51}\,{\rm erg}}\right)^{\frac{1}{2}} \left(\frac{M_{\rm ej}}{1\,M_\odot}\right)^{-\frac{1}{2}} . \tag{A.22}$$

Any variable A is then made dimensionless as $A^\star = A/A_{\rm ch}$.

With the hypothesis and notations presented here, and using the blast initialization presented in section A.2, Truelove and McKee have computed analytically the approximate shock trajectories $x_S^\star(t^\star)$, $u_S^\star(t^\star)$ for both the forward (Sb) and reverse (Sr) shock and for various values of the density index n. Note that $u_{Sb}^\star$ and $u_{Sr}^\star$ are quantities calculated in the upstream rest frame, the reverse shock velocity is also calculated in the frame of the unshocked ejecta just ahead of it, that is

$$\tilde{u}_{Sr} = \frac{x_{Sr}}{t} - u_{Sr} . \tag{A.23}$$

Their results for $n = 0$ (a uniform blast) and $n = 7$ (the kind of blast expected for a SNIa) are shown in tables A.1 and A.2 [2] ($t_{\rm ST}$ and $t_{\rm PD}$ correspond respectively to the onset of the Sedov-Taylor and of the pressure-driven phase, see equations (2.10) and (2.15)).

[2] Note the sign error in Truelove and McKee (1999) for both $u_{Sb}^\star$ and $\tilde{u}_{Sr}^\star$ in the case $n = 7$ for $t < t_{\rm ST}$.

	$0 \leq t^\star < t^\star_{\rm ST}$	$t^\star_{\rm ST} \leq t^\star < t^\star_{\rm PD}$
$x^\star_{Sb}$	$2.01t^\star \left(1 + 1.72t^{\star 3/2}\right)^{-2/3}$	$(1.42t^\star - 0.254)^{2/5}$
$u^\star_{Sb}$	$2.01 \left(1 + 1.72t^{\star 3/2}\right)^{-5/3}$	$0.569\,(1.42t^\star - 0.254)^{-3/5}$
	$0 \leq t^\star < t^\star_{\rm ST}$	$t^\star_{\rm ST} \leq t^\star < 2.2$
$x^\star_{Sr}$	$1.83t^\star \left(1 + 3.26t^{\star 3/2}\right)^{-2/3}$	$t^\star\,(0.779 - 0.106t^\star - 0.533 \ln t^\star)$
$\tilde{u}^\star_{Sr}$	$5.94t^{\star 3/2} \left(1 + 3.26t^{\star 3/2}\right)^{-5/3}$	$0.533 + 0.106t^\star$

Table A.1: Approximate shock trajectories for $n = 0$ (from Truelove and McKee 1999)

	$0 \leq t^\star < t^\star_{\rm ST}$	$t^\star_{\rm ST} \leq t^\star < t^\star_{\rm PD}$
$x^\star_{Sb}$	$1.06t^{\star 4/7}$	$(1.42t^\star - 0.312)^{2/5}$
$u^\star_{Sb}$	$0.606t^{\star -3/7}$	$0.569\,(1.42t^\star - 0.312)^{-3/5}$
	$0 \leq t^\star < 0.36$	$0.36 \leq t^\star < 2.1$
$x^\star_{Sr}$	$0.841t^{\star 4/7}$	$t^\star\,(0.815 - 0.116t^\star - 0.511 \ln t^\star)$
$\tilde{u}^\star_{Sr}$	$0.361t^{\star -3/7}$	$0.511 + 0.116t^\star$

Table A.2: Approximate shock trajectories for $n = 7$ (from Truelove and McKee 1999)

A.4 Code Tests

We present here a few tests showing that our code can handle a spherical supernova remnant shock well.

We set $M_{\rm ej} = 10\ M_\odot$ and $E_{\rm sn} = 10^{51}$ erg. We consider two density profiles: a uniform blast ($n = 0$, $x_{\rm core} = 0$) and a power-law blast ($n = 7$, $x_{\rm core} = 0.1 x_{\rm ej}$). We consider a uniform ambient medium of density $n_{\rm ism} = 1\,{\rm cm}^{-3}$ (and temperature $T = 10^4$ K) and at rest ($u = 0$). Then according to Truelove and McKee the free-expansion phase lasts until $t_{\rm ST} \simeq 1400$ yr in the case $n = 0$ and until $t_{\rm ST} \simeq 2100$ yr in the case $n = 7$ (and for both cases the non-radiative phases last until $t_{\rm PD} \simeq 30\,000$ yr). We choose $t_0 = 1$ yr which is small enough to be a negligible time offset. The initial blast velocity is then $u_{\rm ej} \simeq 4000$ km/s (so that $M_S \simeq 270$) in the case $n = 0$ and $u_{\rm ej} \simeq 30\,000$ km/s (so that $M_S \simeq 1900$) in the case $n = 7$. In each case we run the simulation until $t_{\rm end} = 8\,000$ yr, which requires a grid of size $x_{\rm max} = 12$ pc. We use a resolution of $\delta x = 4.10^{-5}$ pc (so that the initial blast spreads over $\sim$100 cells in the case $n = 0$ and $\sim$300 cells in the case $n = 7$). We activate AMR, the number of sub-grids is $N = 4$.

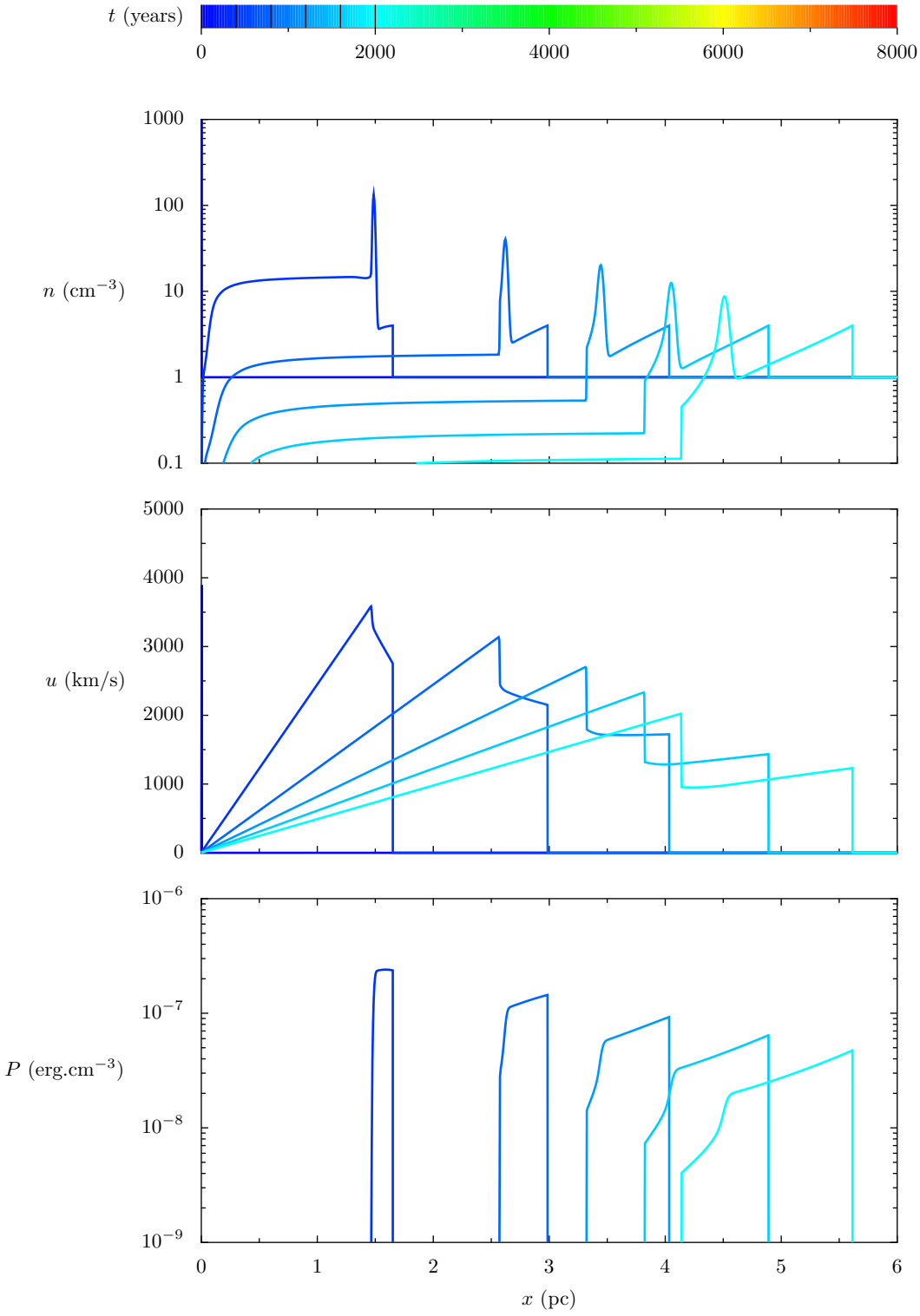

Figure A.1: Space profiles of a supernova shock as a function of time for a uniform blast ($n = 0$) – early phases.

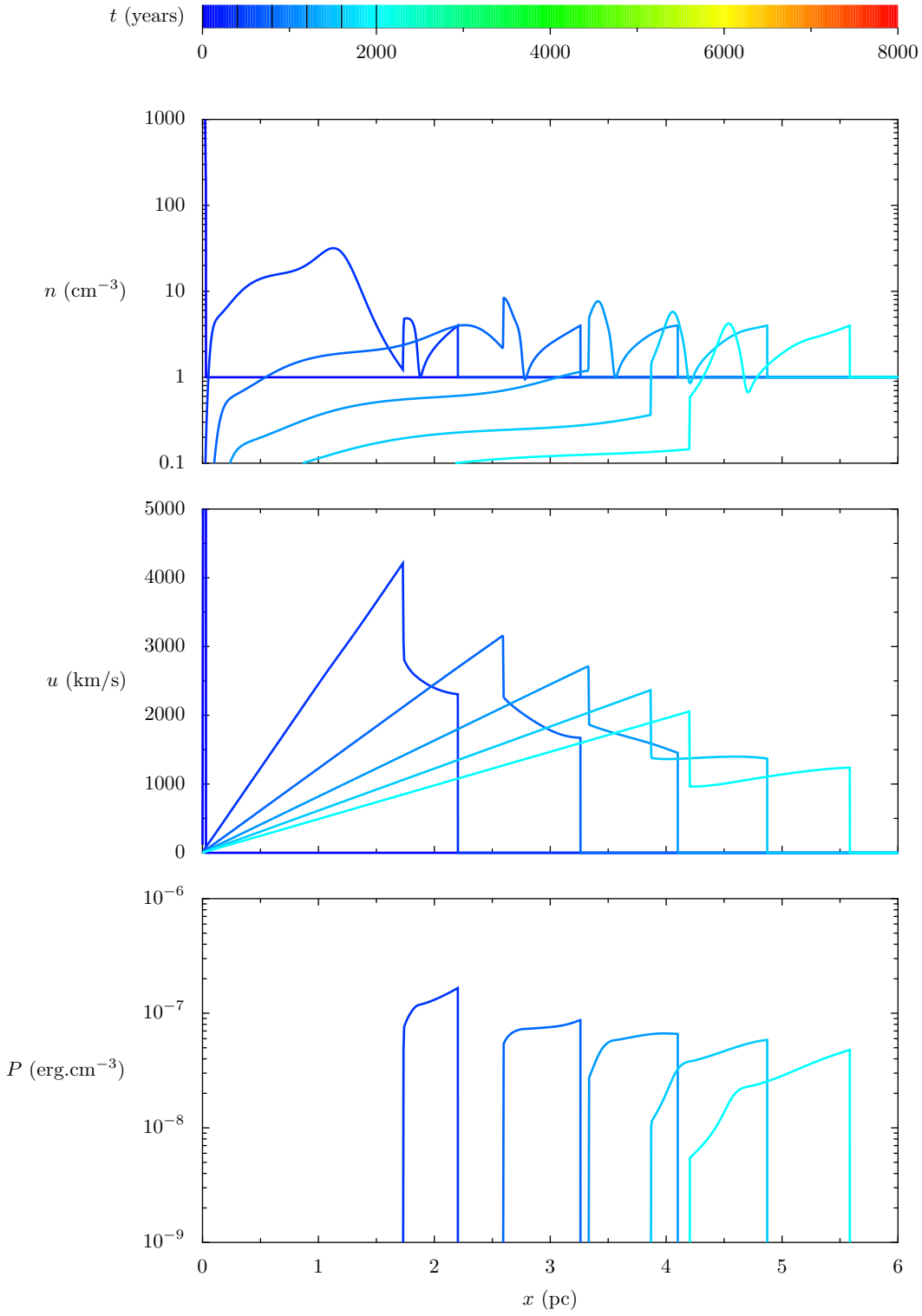

Figure A.2: Space profiles of a supernova shock as a function of time for a power-law blast ($n = 7$) – early phases.

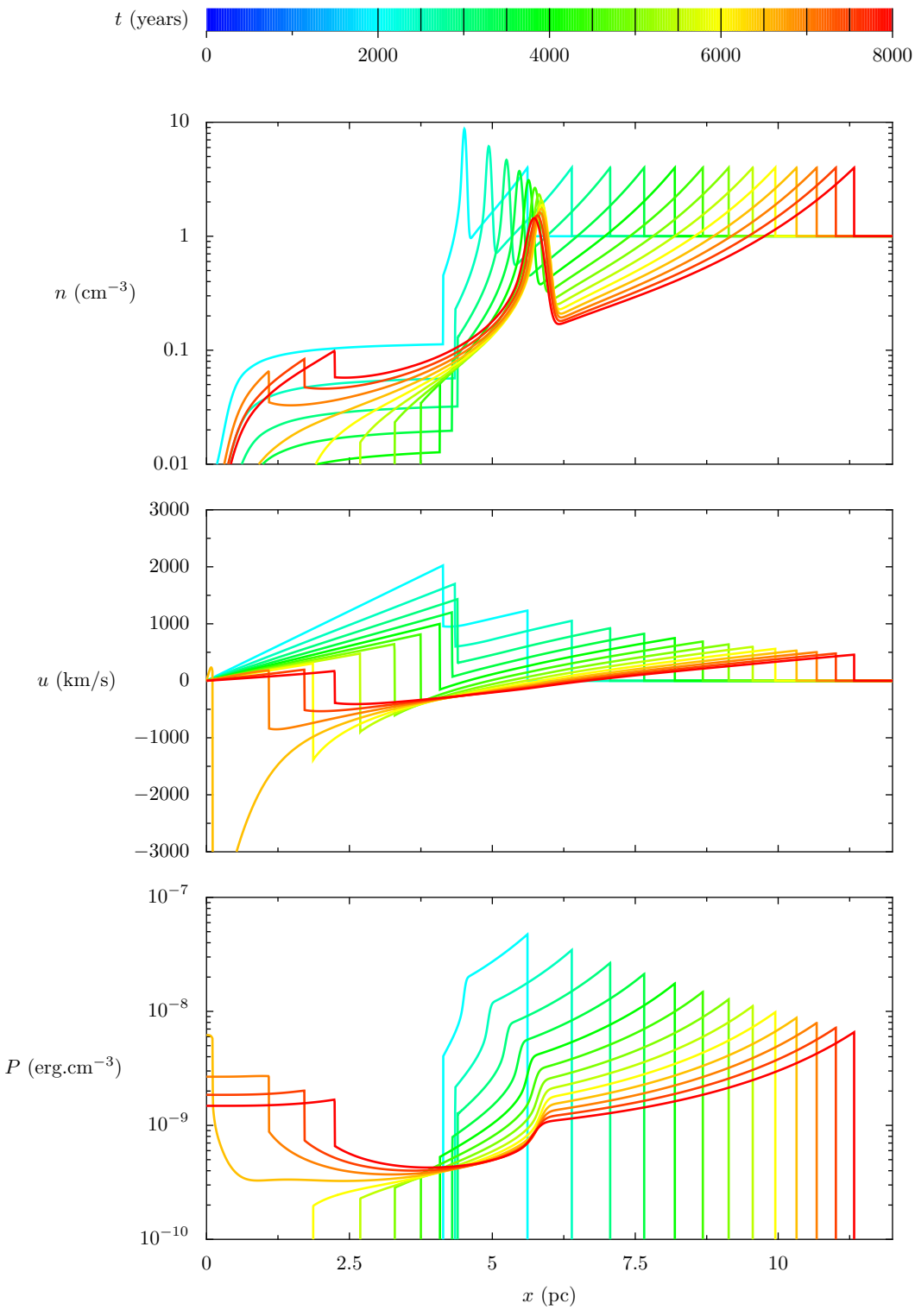

Figure A.3: Space profiles of a supernova shock as a function of time for a uniform blast ($n = 0$) – self-similar phase.

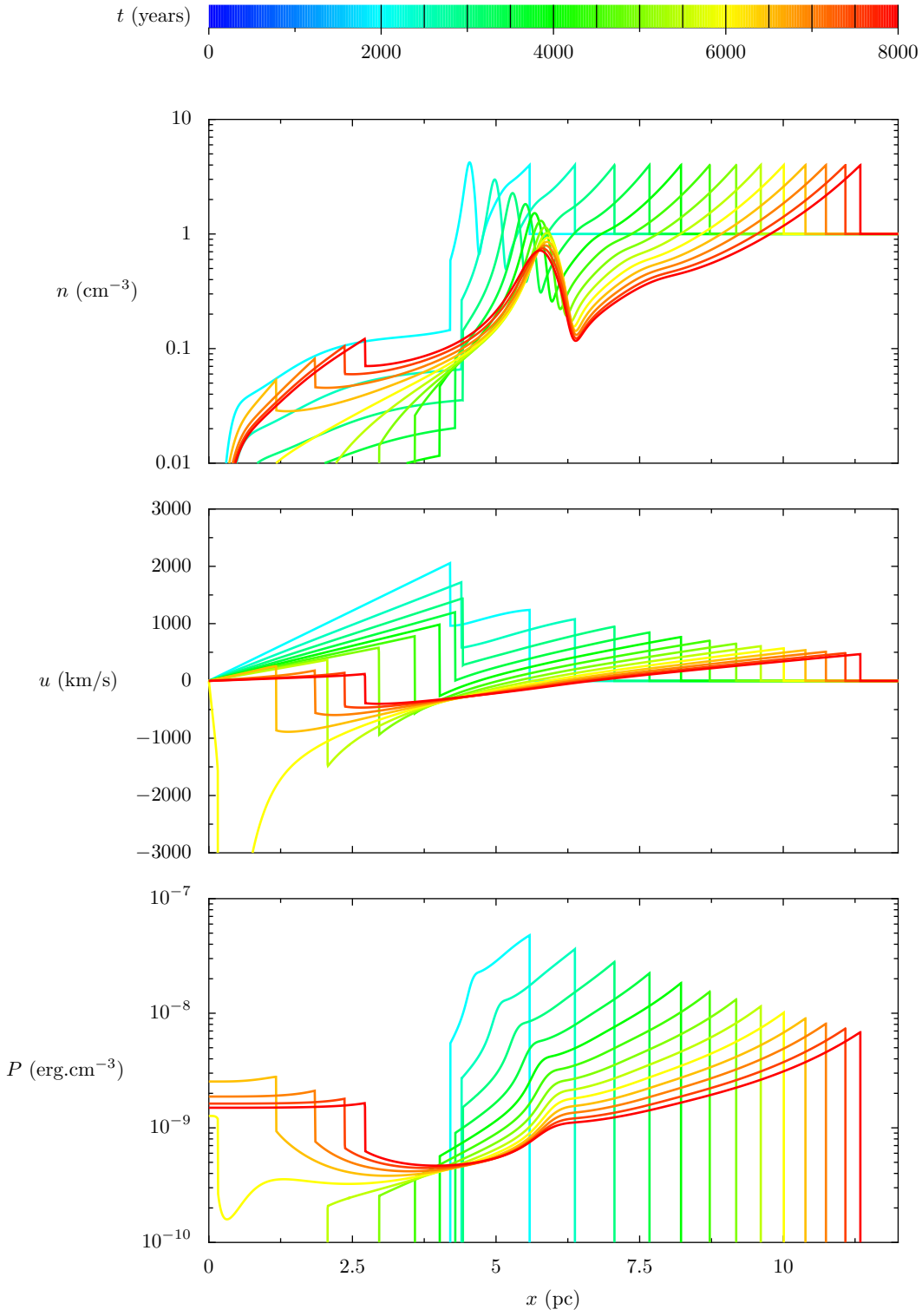

Figure A.4: Space profiles of a supernova shock as a function of time for a power-law blast ($n = 7$) – self-similar phase.

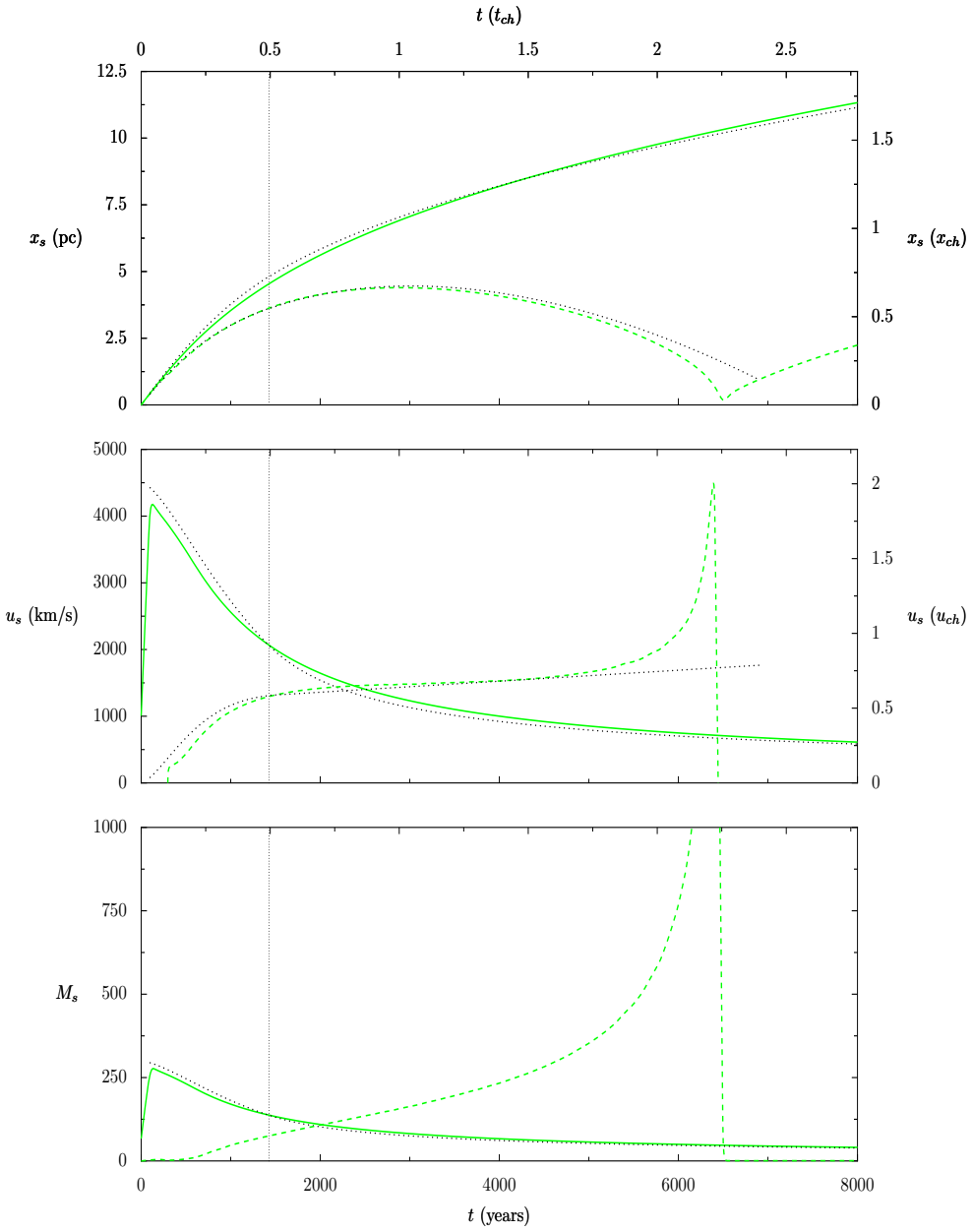

Figure A.5: Time evolution of supernova shocks for a uniform blast ($n = 0$). The evolution of the forward and reverse shocks are shown in solid and dashed lines respectively. The velocity (and the Mach number) is measured in the local upstream frame (see equation (A.23) for the reverse shock). Dotted are added the results from the model of Truelove and McKee (1999) given in table A.1. The right scales are in their characteristic scales (see equations (A.19),(A.20),(A.22)): $x_{\rm ch} \simeq 6.6$ pc, $t_{\rm ch} \simeq 2880$ yr, $u_{\rm ch} \simeq 2240$ km/s. The transition time $t_{\rm ST} = 0.495\, t_{\rm ch} \simeq 1430$ yr between the free-expansion and Sedov phases (see equation (2.10)) is indicated by a vertical dotted line.

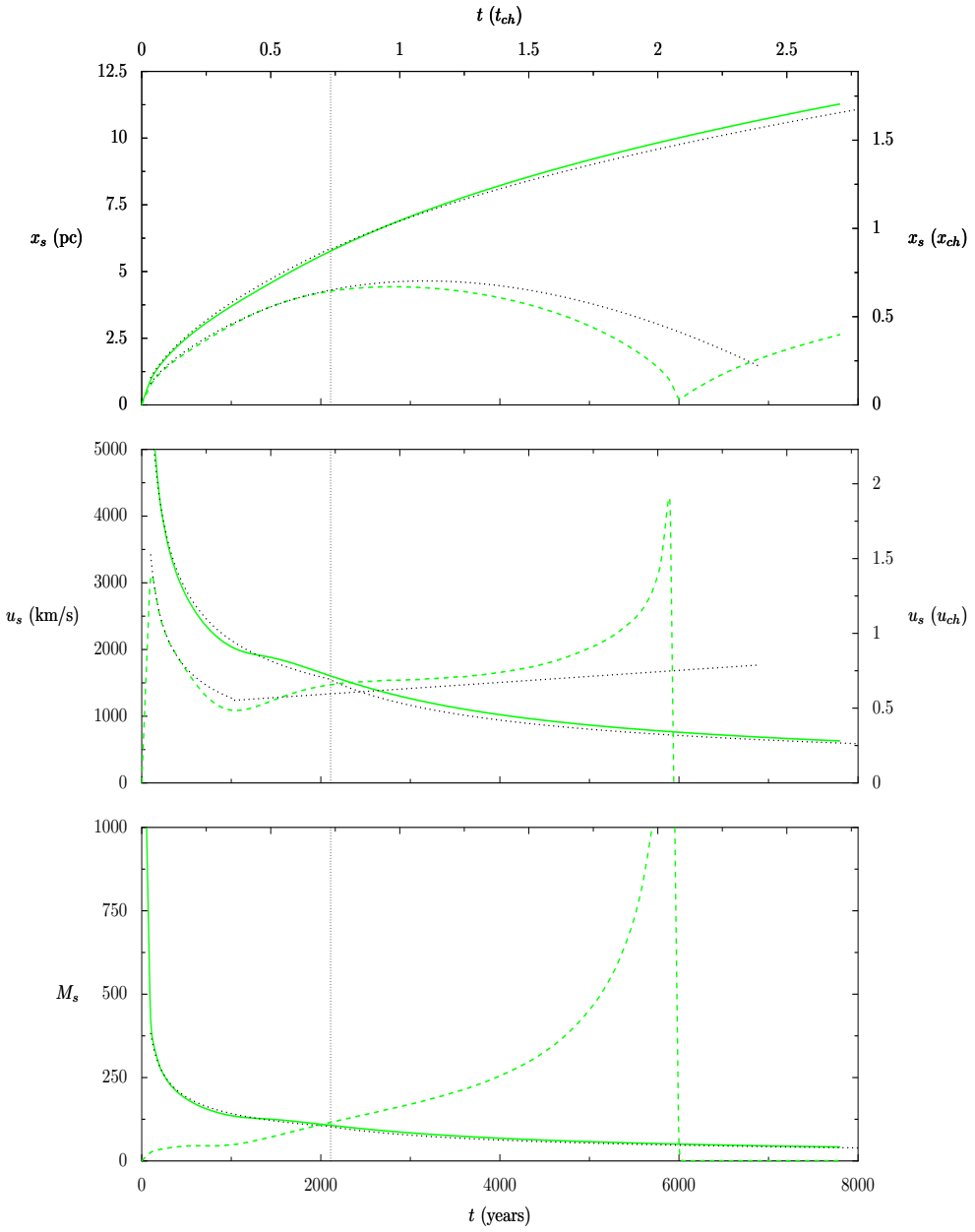

Figure A.6: Time evolution of supernova shocks for a power-law blast ($n = 7$). Same as figure A.5 for the $n = 7$ case. Data from the corresponding model of Truelove and McKee (1999) are given in table A.2. The transition time is now $t_{\rm ST} = 0.732\, t_{\rm ch} \simeq 2110$ yr.

The results are shown on figures A.1 to A.6. On odd figures $n = 0$ (uniform blast), on even figures $n = 7$ (power-law blast). In each case the first two figures show the hydrodynamical profiles at different times, first in the free expansion phase (A.1, A.2), then in the Sedov phase (A.3, A.4). We clearly see the three discontinuities: the forward shock (a strong shock of $r = 4$), the contact discontinuity (on the density and pressure profiles, but not on the velocity profile), the reverse shock (which indeed after some time goes back to the center where it rebounds). The global behaviour of the remnant doesn't depend much on n, however the actual shape of the three discontinuities during the early phases does. In that respect our results agree with the results of Dwarkadas and Chevalier (1998) (see their figure 3). The last two figures (A.5, A.6) show the shocks evolution as a function of time. On these figures Truelove and McKee's model has been added dotted to allow for comparison. We see that the code reproduces the analytical predictions well, but at the very begin and close to the reverse shock rebound. This rebound is more problematic as the reverse shock is accelerating very fast towards the center of the remnant where a very strong rarefaction has occured. And note that as the AMR grids hierarchy tracks only the forward shock, the curves concerning the reverse shock don't benefit from the same resolution (it is $2^4 = 16$ times lower). Note that our code could therefore not be presently be used to investigate acceleration at the reverse shock, which is often not considered, although it might play some role too (see eg Ellison et al. 2005). This would require the single initial grids hierarchy to be progressively splitted in two.

A.5 On the Role of Geometry

To end this appendix we would like to discuss briefly the importance of the shock geometry regarding the acceleration of cosmic-rays (see also the simulations of Kang and Jones 2006).

There are a few new features in the spherical case, with respect to the slab case. First the surface swept-up by the shock, and thus the rate at which ambient matter is shocked, is not constant, but constantly increases with time. As a consequence the shock speed is not constant but continuously decreases with time (an effect which could easily be mimicked in slab geometry). Also adiabatic decompression occurs immediately downstream of the shock, where a strong rarefaction occurs in the early phases. At each point it passes through the shock builds some cosmic-rays spectrum of index s (in the linear regime), particles advected downstream of the shock then suffer only adiabatic losses that shift the spectrum as a whole (see section 3.1.1), keeping the same index s, which reflects the state of the shock at the time it passed there. In spherically symmetric geometry the supernova remnant can thus be seen as a set of shells of particles having the same distribution $f(p)$. When the remnant finally merges in the ambient medium these shells are progressively "unpeeled". The resulting spectrum has been worked out by Bogdan and Völk (1983) who call this the

"onion shell" model. Remarkably it is still a power-law, just a bit steeper than the canonical one: s =4.1 instead of 4. The assumption of spherical symmetry thus naturally allows to take into account the shock evolution. To some point this could already be mimicked in the 1D slab version of our code by prescribing a time-dependent shock velocity (through forcing a time-dependent piston velocity).

Spherical symmetry, although addressing 3D geometry, is still 1D effective. The next step (probably a huge step in terms of computing power) would be to go to full 3D. This would in particular allow for a correct treatment of the hydrodynamical instabilities that may affect the three discontinuities. In particular it is well known that the contact discontinuity between the ejecta and the shocked matter is unstable: the two media actually penetrate each other due to the Rayleigh-Taylor instability. The development of this instability has been studied by Blondin and Ellison (2001) by the means of 2D (axi-symmetric) and 3D simulations, varying the effective adiabatic index of the gas to mimic the acceleration of particles (see section 4.3.2). They concluded that the instability itself doesn't significantly depend on the shock compression ratio, but that because the width of the region between the contact discontinuity and the forward shock shrinks significantly when this ratio rises (see section 2.5.2.1) the instability is more likely to affect the shock itself. The way a cosmic-ray-modified shock would actually respond to hydrodynamical instabilities is an open question.

Finally we note that the quality of the geometrical model of the supernova remnant has a direct impact on the relevance of broad-band emission maps that may be computed from our simulations. In 1D effective geometry one can address the interaction of the shock with an ambient medium of varying density, but in very special configurations only. Realistic shock-clouds interactions (and the associated hadronic emission) would require a complete 3D modelling.

References

Blondin, J. M. and Ellison, D. C. (2001). Rayleigh-Taylor Instabilities in Young Supernova Remnants Undergoing Efficient Particle Acceleration. ApJ, 560:244–253.

Bogdan, T. J. and Völk, H. J. (1983). Onion-shell model of cosmic ray acceleration in supernova remnants. A&A, 122:129–136.

Downes, T. P., Duffy, P., and Komissarov, S. S. (2002). Relativistic blast waves and synchrotron emission. MNRAS, 332:144–154.

Dwarkadas, V. V. and Chevalier, R. A. (1998). Interaction of Type IA Supernovae with Their Surroundings. ApJ, 497:807–823.

Ellison, D. C., Decourchelle, A., and Ballet, J. (2005). Nonlinear particle acceleration at reverse shocks in supernova remnants. A&A, 429:569–580.

Falle, S. A. E. G. (1991). Self-similar jets. MNRAS, 250:581–596.

Kang, H. and Jones, T. W. (2006). Numerical studies of diffusive shock acceleration at spherical shocks. *Astroparticle Physics*, 25:246–258.

Kang, H., Jones, T. W., LeVeque, R. J., and Shyue, K. M. (2001). Time Evolution of Cosmic-Ray Modified Plane Shocks. ApJ, 550:737–751.

Truelove, J. K. and McKee, C. F. (1999). Evolution of Nonradiative Supernova Remnants. ApJS, 120:299–326.

Author: Gilles Ferrand
Title: Study of the Acceleration of Cosmic-Rays by Supernovae Remnants Shock Waves in Galactic Superbubbles
Date: 18 December 2007

PhD Advisor: Alexandre Marcowith
University: TOULOUSE III - Paul Sabatier
Institute: Centre d'Etude Spatiale des Rayonnements,
9 avenue du Colonel Roche, BP 44346,
31028 Toulouse Cedex 4, FRANCE
Field: High-Energy Astrophysics

Abstract: In this thesis we study the acceleration of cosmic-rays, high-energy particles pervading the Universe. Galactic cosmic-rays are believed to be produced by *diffusive shock acceleration* in supernovae remnants. The linear theory explains the formation of power-law spectra, but it has to be amended because of the back-reaction of cosmic-rays. We focus our attention on *repeated* acceleration by successive shocks, which hardens the spectra, and relies on the transport of cosmic-rays *between* the shocks.

For this study we have developped a numerical tool which couples the hydrodynamical evolution of the plasma with the kinetic transport of the cosmic-rays. We have validated it against previous results. To resolve all the space- and time-scales induced by the energy-dependent diffusion of cosmic-rays we have implemented an adaptive mesh refinement technique. To save more computational power we have also parallelized our code, in the energy dimension. This enables us to present the first numerical simulations of non-linear acceleration by multiple shocks.

We apply our tool to superbubbles, the big hot tenuous structures surrounding OB associations, as this is probably the place where most supernovae explode – leading to substantial modifications of the standard model of the production of Galactic cosmic-rays. More precisely we have begun to investigate the effects of multiple shocks, through studying the role of pre-existing cosmic-rays upstream of a blast wave. Finally we review the radiation from superbubbles with a view to efficient cosmic-ray production.

Keywords: supernovae, superbubbles, high-energy emission
cosmic-rays, diffusive shock acceleration
numerical simulations, AMR, parallelization

auteur : Gilles Ferrand
titre : Étude de l'accélération des rayons cosmiques par les ondes de choc des restes de supernovae dans les superbulles galactiques
date : 18 décembre 2007

---

directeur : Alexandre Marcowith
université : TOULOUSE III - Paul Sabatier
laboratoire : Centre d'Etude Spatiale des Rayonnements,
9 avenue du Colonel Roche, BP 44346,
31028 Toulouse Cedex 4, FRANCE
spécialité : High-Energy Astrophysics

---

résumé : Dans cette thèse nous étudions l'accélération des rayons cosmiques (RC), ces particules très énergétiques qui emplissent l'univers. Il est admis que les RC galactiques sont produits par *accélération diffusive par onde de choc* dans les restes de supernovae. La théorie linéaire explique la formation de spectres en loi de puissance, mais elle doit être modifiée du fait de la rétroaction des RC. Nous nous concentrons sur l'accélération *répétée* par chocs successifs, qui durcit les spectres, et qui dépend du transport des rayons cosmiques *entre* les chocs.

Pour cette étude nous avons développé un outil numérique qui couple l'évolution hydrodynamique du plasma et le transport cinétique des RC. Nous l'avons validé grâce à des résultats déjà connus. Pour résoudre toutes les échelles induites par la dépendance en énergie du coefficient de diffusion des RC nous avons implémenté une technique de grille adaptative. Pour réduire le temps de calcul nous avons aussi parallélisé notre code, dans la dimension d'énergie. Cela nous permet de présenter les premières simulations de l'accélération non-linéaire par chocs multiples.

Nous appliquons notre outil aux superbulles, les vastes structures chaudes et peu denses entourant les associations OB, car c'est probablement là que la plupart des supernovae explose en fait – ce qui induit des modifications substantielles du modèle standard de production des RC galactiques. Plus précisément nous avons commencé à explorer les effets de chocs multiples, par une étude du rôle de RC pré-existants en amont d'une onde de choc. Pour finir nous passons en revue l'émission haute énergie des superbulles dans l'optique d'une production efficace de RC.

---

mots-clés : supernovae, superbulles, émission haute énergie
rayons cosmiques, acceleration diffusive par onde de choc
simulations numeriques, AMR, parallélisation